An investigation on the optoelectronic and thermoelectric properties of reactive evaporated degenerate and non degenerate p-type semiconducting compound selenide thin films for photovoltaic and thermoelectric applications

Thesis submitted to

Cochin University of Science and Technology

in partial fulfilment of the requirements
for the award of the degree of

Doctor of Philosophy

By

Urmila K. S

Solid State Physics Division
Department of Physics
Cochin University of Science and Technology
Kochi – 682022, Kerala, India

June 2016

An investigation on the optoelectronic and thermoelectric properties of reactive evaporated degenerate and non degenerate p-type semiconducting compound selenide thin films for photovoltaic and thermoelectric applications

Ph.D thesis in the field of Material Science

Submitted by:

Urmila K. S
Solid State Physics Division
Department of Physics
Cochin University of Science and Technology
Kochi – 682022, Kerala, India
Email: urmilaks7@gmail.com

Research Supervisor:

Dr. B. Pradeep
Professor
Solid State Physics Division
Department of Physics
Cochin University of Science and Technology
Kochi – 682022, Kerala, India
Email: bp@cusat.ac.in

June 2016

Department of Physics
Cochin University of Science and Technology
Kochi– 682022, Kerala, India

Dr. B. Pradeep

Professor

Certificate

*Certified that the work presented in the thesis entitled "**An investigation on the optoelectronic and thermoelectric properties of reactive evaporated degenerate and non degenerate p-type semiconducting compound selenide thin films for photovoltaic and thermoelectric applications**" is a bonafide record of research done by **Ms. Urmila K. S**, under my guidance and supervision at Department of Physics, Cochin University of Science and Technology, Kochi, Kerala, India. The work presented in this thesis has not been included in any other dissertation submitted previously for the award of any other degree, diploma, associateship or any other title or recognition from any University/Institution. All the relevant corrections and modifications suggested by the audience during the pre-synopsis seminar and recommended by the doctoral committee of the candidate has been incorporated in the thesis.*

Kochi - 682022
Date: 06.06.2016

Prof. B. Pradeep
(Research Supervisor)

Phone: +91 0484 2577404 **Fax:** +91 0484 2862459 **Email:** bp@cusat.ac.in

DECLARATION

*I hereby declare that the work presented in the thesis entitled "**An investigation on the optoelectronic and thermoelectric properties of reactive evaporated degenerate and non degenerate p-type semiconducting compound selenide thin films for photovoltaic and thermoelectric applications**" is based on the original research work done by me under the guidance and supervision of Dr. B. Pradeep, Professor, Department of Physics, Cochin University of Science and Technology, Kochi, Kerala, India. The work presented in this thesis has not been included in any other dissertation submitted previously for the award of any other degree, diploma, associateship or any other title or recognition from any University/Institution.*

Kochi - 682022 *Urmila K. S*

Date: 06.06.2016

Acknowledgement

Above all, I thank the Almighty GOD for having been with me throughout as a constant source of motivation and guiding strength and for enabling me to complete my research work successfully.

My foremost and utmost gratitude goes to my research supervisor Prof. B. Pradeep, who, in spite of all responsibilities and duties, found time to share his expertise and knowledge with me. It is my proud privilege to express my deep sense of gratitude for his gentle and inspiring guidance, expert advice, good suggestions, patience and understanding nature. I am extremely thankful to him for the encouragement, kindness and moral support extended to me during the tough times of my research work.

I extend my sincere thanks to Prof. S. Jayalekshmi, Head of the Department and all the former Heads of the Department for allowing me to use the facilities necessary for the work. I am extremely grateful to all the faculty members of the department for their helpful attitude and constant support. I am thankful to all the office staff, laboratory staff and library staff for their timely help and cooperation.

I specially appreciate the sincere support of Dr. Rachel Reena Philip, Assistant Professor, Department of Physics, Union Christian College, Aluva.

I am deeply indebted to her for the valuable advice, good comments, encouragement and constant prayers that have helped me a lot during the course of the study. I remember with utmost thanks the help, advice and kind support extended to me by Mrs. Rajani Jacob, Research Scholar, Department of Physics, Union Christian College, Aluva.

I am extremely grateful to all the scientists at University Grants Commission-Department of Atomic Energy (UGC-DAE) Consortium for Scientific Research, Indore, for allowing me to use the experimental facilities related to my work. Especially, I would like to thank, Dr. T. Shripathi for helping me with X-ray photoelectron spectroscopy (XPS) measurements, Dr. V. Ganesan for atomic force microscopy (AFM) measurements, Dr. G. S. Okram for thermoelectric power measurements, Dr. R. Rawat for electrical conductivity measurements and Dr. A. M. Awasthi for thermal conductivity measurements. I acknowledge all the scientists at Sophisticated Test and Instrumentation Centre (STIC) at Cochin University of Science and Technology (CUSAT), in particular, Dr. Shibu. M. Eappen for his timely assistance with energy dispersive analysis of X-rays (EDAX) and scanning electron microscopy (SEM) analysis.

I acknowledge the financial assistance from CUSAT in the form of research fellowship for the initial two years and UGC for providing research

fellowship in science for meritorious students (RFSMS) for the remaining years of my study.

I would like to express my sincere and special thanks to my seniors, Mrs. Namitha Asokan T and Mrs. Reena Rajan for the care and concern they have shown towards me and for helping me during the initial phase of my research work. I thank my labmates: Mr. Anuroop R, Mr. Abhilash A, Mr. Sreejith P and Mrs. Hiba Rahman E, for extending all sorts of help whenever necessary during the various stages of my research work. I owe a word of thanks to all the M.Sc and M.Phil students who joined our laboratory from time to time for their kind acts of love. I acknowledge the cooperative and helpful attitude of all my fellow research scholars in the department.

Words are not enough to express my love to my parents: My father and My mother. I express my deepest gratitude to them for their constant prayers, love, care, patience, encouragement to pursue my interests and continuing support to complete my research work. I recognize with sincere appreciation all my relatives and friends for the generous and kind support they offered me to make my study a success. Last but not the least, I would like to thank everyone who was important to the successful completion of my research work.

Urmila K. S

Dedicated

to

My Parents.....

Preface

The use of energy in our day to day life has grown exponentially and conserving energy to meet the world's escalating energy demands is the need of the hour. During the past decade there is a heightened awareness all over the world that the production costs of energy from coal, oil and natural gas is increasingly higher and at the same time the energy technologies involving their use are contributing to a serious rise in the greenhouse gases in the environment and a consequent global warming. As a result, more attention is focused on the utilization of clean energy technologies, especially solar energy which has a great potential to meet a large fraction of world's energy demands using **photovoltaics (PV)**. The heart of the PV system that efficiently convert sunlight directly into electricity through photovoltaic effect is the solar cell - originally developed for space applications in the 1950s, are now used in consumer products, mounted on roofs of houses or assembled into large power stations.

The leading technology in the commercial production of solar cells is based on silicon wafers. However the expensive nature of crystalline silicon is not likely to meet the substantial cost reductions that are necessary for large scale production of solar cells. This scenario has paved way for the entry of thin film solar cell modules into the solar market with the idea of fabricating cheaper solar cells. However, substantial research and technological advancements in thin film PV cells has started with the advent of the chalcogenide compounds – compounds comprising of heavier chalcogens (especially sulphides, selenides

and tellurides). In particular, the thin film PV built on the chalcogenide materials such as CdTe, CdS, $Cu(In,Ga)(S,Se)_2$ has become a product of high demand in the past years and its production keeps growing. But extensive research is necessary to further develop these PV materials and to make them competitive with the other state-of-the-art materials.

On the other hand, out of the world's huge primary energy consumption, more than 60% of the installed primary energy is dissipated as waste heat into the environment. This invokes serious environmental hazards such as increase in CO_2 emissions and consequently an alarming rise in atmospheric temperature. Therefore the efficient reuse of waste heat is urgently required to save our society and to sustain the world's enormous energy consumption. The environmental concern over the existing refrigerants is another serious issue. The outcome of widespread research on the reuse of discarded heat and viable alternate refrigerant resulted in the development of **thermoelectrics (TE)** which uses a thermoelectric module - a device that converts heat into electricity through Seebeck effect or electricity into cooling through Peltier effect. It is interesting to note that, most of the well established and emerging TE materials are based on chalcogenide compounds in the form of crystals, thin films or alloys. The prime candidates of TE technology are based on tellurides such as Bi_2Te_3, PbTe, SnTe and so on. But Te is scarce and expensive and it becomes necessary to opt for better alternatives that can replace Te based TE devices in the near future.

Today, it is thus fair to say that the achievements made by chalcogenide compounds in the field of PV and TE have been remarkable. In this point of view, chalcogenide compounds, either in bulk or thin film form, demand more systematic investigations and optimizations of their properties for use in solar cells and TE devices. **Accordingly, the main focus of the present thesis is to perform a comprehensive characterization of the structural, compositional, morphological, optical, electrical and thermoelectric power properties of certain degenerate and non degenerate p-type semiconducting compound selenide thin films prepared by reactive evaporation under optimized depositions conditions so as to gain a better understanding of the materials in view of their use in solar cells and TE devices.** Systematic studies are carried out to calculate the optical band gap (E_g), absorption coefficient (α), photosensitivity (PS), Seebeck coefficient (S) and thermoelectric figure of merit (ZT) of the compounds under investigation in an attempt to evaluate their potential for PV and TE technology and to provide a platform to highlight their unique capabilities. The thesis is organized in ten chapters. The contents of each chapter are summarized below:

Chapter 1 of the thesis presents an **introduction to chalcogens and chalcogenides** and their applications in various fields of science and technology. A brief overview of PV and TE is followed by definitions and an introduction to the prominent chalcogenide based PV and TE materials. The various factors that influence the selection of materials for PV and TE applications are discussed, followed by a literature review on the conventional and emerging chalcogenide based PV and TE materials that are used in the fabrication of solar cells and TE modules. In addition, the necessities for developing new and better PV and TE

materials that can compete with the present state-of-the-art materials are discussed. The future prospects in chalcogenide semiconductor research for PV and TE applications are also given. The end of the chapter clarifies the motivation behind the choice of the thesis topic and explains the objectives of the thesis.

Chapter 2 outlines the basic **principles of semiconductors** relevant to the work. The chapter includes an overview, salient properties and applications of semiconductors, theories related to energy band structure, classification of semiconductors, evaluation of charge carrier concentration and position of Fermi level, optical and electrical properties.

Chapter 3 elaborates the **theory of reactive evaporation** and the experimental setup used for the preparation of thin films under study. Comprehensive descriptions of the **experimental techniques** used for the characterizations of the as-prepared thin films are dealt with in detail, along with a brief account of relevant theory behind each technique.

Chapter 4 deals with the binary compound, **copper selenide** – a group I-VI semiconductor well recognized for its PV properties and recently recalled by the TE society for its fascinating TE properties. This chapter begins with a literature review on various compositions of copper selenide thin films prepared by various techniques. Later on, an elaborate study is carried out on the preparation, optimization of deposition parameters and characterization of the structural, compositional, morphological, optical, electrical and thermoelectric power properties of reactive evaporated p-type polycrystalline copper selenide thin films of composition **Cu_7Se_4** – a rare phase of copper selenide, whose

properties are not yet explored to date. Some of the salient features of the as-prepared Cu_7Se_4 thin film are its high charge carrier concentration ≈ 10^{21} cm^{-3}, high electrical conductivity ≈ 7.5×10^3 Scm^{-1}, low value of Seebeck coefficient ≈ 11.6 μVK^{-1}, high near infrared reflection and inverted bell type transmission curve – typical characteristics of a degenerate semiconductor. Experimental evidences and interpretations in favour of the degenerate behaviour of the prepared film are discussed in detail. The photoluminescence exhibited by the film at room temperature is another interesting feature. Certain important material parameters such as mean free path, relaxation time, Fermi energy, effective mass and electron affinity are calculated by correlating the results of Hall and thermoelectric power measurements. The possible applications of the prepared film in solar control coatings, microwave shielding coatings and radiation filters are suggested. The ZT ≈ 1.6 at 425 K exhibited by the as-prepared Cu_7Se_4 thin film is comparable to that of today's efficient TE materials. This could possibly make it suitable for high temperature TE applications, on further optimization. The major findings of the work are briefed at the end of the chapter.

Chapter 5 describes the ternary compound, **copper indium selenide** – a group I-III-VI semiconductor with chalcopyrite structure and an efficient absorber layer material for solar cells. A brief description and literature review of the compound is presented, followed by the preparation, optimization of deposition parameters and characterization of the structural, compositional, morphological, optical, electrical and thermoelectric power properties of reactive evaporated p-type polycrystalline **slightly Cu rich $CuInSe_2$** thin films. The main highlights of this chapter includes; calculation of distortion parameter, anion

displacement, anion-cation bond lengths and bond length mismatch of the film, evaluation of refractive index, extinction coefficient and dielectric constant of the film using Swanepoel's method, analysis of spectral dependence of the refractive index of the film using Wemple and DiDomenico model and subsequent calculation of single oscillator energy, dispersion energy, moments of optical spectra, oscillator strength and refractive index at infinite wavelength, estimation loss factor, quality factor and optical conductivity of the film in view of its use in the design of optical devices, identification of defect levels in the film by electrical conductivity measurements, characterization of defect levels and their influence on the photoconductivity of the film and the effect of phonon drag on low temperature thermoelectric power measurements. The as-prepared $CuInSe_2$ thin film exhibits $E_g \approx 1.07$ eV, $\alpha \approx 10^5$ cm^{-1} and PS ≈ 0.6, quite suitable for PV applications and reasonably good $S \approx 3309$ μVK^{-1} and ZT ≈ 1.1 at 48 K, suitable for low temperature TE applications. These results suggest the potential of $CuInSe_2$ for PV and TE applications, on further optimization. The conclusions drawn from the work are summarized at the end of the chapter.

Chapter 6 is about the binary compound, **indium selenide** – a group III-VI layered semiconductor suitable for photovoltaic and switching applications. This chapter commences with an introduction to indium selenide, which comprises; literature review on various compositions of indium selenide prepared by various techniques, phase diagram of In-Se system showing the formation energy range of various phases of InSe and the necessity to prepare single phase or phase pure InSe. Later on, the chapter details the preparation, optimization of deposition parameters and characterization of the structural, compositional, morphological, optical, electrical and thermoelectric power

properties of reactive evaporated p-type polycrystalline phase pure indium selenide thin films of composition **InSe** – about which reports are very scarce in literature. The as-prepared phase pure InSe thin film exhibits $E_g \approx 1.35$ eV, $\alpha \approx 10^5$ cm^{-1} and PS ≈ 0.4, quite suitable for PV applications and a reasonably good S ≈ 2626 μVK^{-1} and ZT ≈ 0.97 at 38 K, suitable for low temperature TE applications, thereby proving its potential in PV and TE technologies, on further optimization. The major conclusions drawn from the work are given at the end of the chapter.

Chapter 7 introduces a novel ternary compound, **indium antimony selenide** – an interesting group III-V-VI semiconductor that integrates the properties of In_2Se_3 and Sb_2Se_3 which are excellent PV and TE materials. However, systematic investigations on indium antimony selenide are not sufficient in literature. Therefore, this chapter undertakes a detailed examination of the preparation, optimization of deposition parameters and characterization of the structural, compositional, morphological, optical, electrical and thermoelectric power properties of reactive evaporated p-type polycrystalline **$InSbSe_3$** thin film in view of its use in solar cells and TE devices. The as-prepared $InSbSe_3$ thin film possesses $E_g \approx 1.52$ eV, $\alpha \approx 10^5$ cm^{-1} and PS ≈ 4.8, optimum values for PV applications and S ≈ 6342 μVK^{-1} and ZT ≈ 1.1 at 46 K, favourable for low temperature TE applications which are not so far been reported in literature to date. Moreover, the film shows low dielectric loss, high quality factor and very good optical conductivity ≈ 7.8×10^{14} s^{-1} at 1.55 eV, adequate for optoelectronic applications. Hence thin films of $InSbSe_3$ demand further research to make them competitive with the other state-of-the-art PV and

TE materials. The chapter concludes with the major conclusions drawn from the work.

Chapter 8 deals with the binary compound, **tin selenide** – a group IV-VI layered semiconductor widely studied for PV and high temperature TE applications. This chapter begins with an introduction and literature review on tin selenide prepared by various techniques, followed by the preparation, optimization of deposition parameters and characterization of the structural, compositional, morphological, optical, electrical and thermoelectric power properties of reactive evaporated p-type polycrystalline tin selenide thin films of composition **SnSe** with special emphasis on its low temperature TE properties. The as-prepared SnSe thin film shows $E_g \approx 1.2$ eV, $\alpha \approx 10^5$ cm^{-1} and PS ≈ 1.5, suitable for PV applications. The main highlight of this chapter is the high S ≈ 7863 μVK^{-1} and good ZT ≈ 1.2 exhibited by the film at low temperatures ≈ 42 K, which is not so far been reported in literature to date. The chapter concludes that SnSe which is an emerging high temperature TE material can also be considered for low temperature TE applications, on further optimization. The major findings of the work are summarized at the end of the chapter.

Chapter 9 describes a novel ternary compound, **tin antimony selenide -** a group IV-V-VI semiconductor that incorporates the properties of SnSe and Sb_2Se_3 which are excellent PV and TE materials. This chapter reports for the first time the preparation, optimization of deposition parameters and characterization of the structural, compositional, morphological, optical, electrical and thermoelectric power properties of reactive evaporated p-type polycrystalline **$Sn_2Sb_4Se_8$** thin films - a common crystalline phase of the Sn-Sb-

Se or TAS system but never before explored for its properties. The as-prepared $Sn_2Sb_4Se_8$ thin films reveals $E_g \approx 1.54$ eV, $\alpha \approx 10^5$ cm^{-1} and PS ≈ 8.4, optimum values for PV applications. The main focus of the chapter is the high Seebeck coefficient S ≈ 30174 μVK^{-1} and good ZT ≈ 1.3 exhibited by the film at 52 K, which opens up the possible use of the film for cryogenic TE applications. Thus the $Sn_2Sb_4Se_8$ thin film under study is found to be a prospective material for PV and TE applications and hence the TAS system and their thin films require further investigation and optimization of properties for use in PV and TE devices. The major findings of the work are briefed at the end of the chapter.

Chapter 10 summarizes the results and highlights of the research presented in the thesis and discuss the scope for future studies based on the major findings of the work.

List of Publications

Journal Publications

[1] **K. S. Urmila**, T. A. Namitha, R. R. Philip and B. Pradeep, "Reactive evaporated $InSbSe_3$ thin films for photovoltaic and thermoelectric applications", **Phys. Status Solidi A** (Communicated).

[2] **K. S. Urmila**, T. A. Namitha, R. R. Philip and B. Pradeep, "Characterization of reactive evaporated p-type $Sn_2Sb_4Se_8$ thin films- a prospective material for photovoltaic and thermoelectric applications", **J. Mater. Sci. Mater. Electron** (Communicated).

[3] **K. S. Urmila**, T. A. Namitha, J. Rajani, R. R. Philip and B. Pradeep, "Optoelectronic properties and Seebeck coefficient in SnSe thin films", **J. Semiconductors** (Accepted).

[4] T. A. Namitha, **K. S. Urmila** and B. Pradeep, "Structural, optical, transient photoconductivity studies and low temperature thermoelectric power measurements on reactively evaporated lead selenide thin films", **J. Mater. Sci. Mater. Electron** 27, 5646 (2016).

[5] **K. S. Urmila**, T. A. Namitha and B. Pradeep, "Thermoelectric figure of merit in degenerate Cu_7Se_4 and non degenerate InSe thin films", **Int. J. Recent. Res. Rev** 9, 13 (2016).

[6] **K. S. Urmila**, T. A. Namitha and B. Pradeep, "Analysis of structural parameters and low temperature electrical conductivity and thermoelectric power in slightly Cu rich p-type $CuInSe_2$ thin films", **Int. J. Recent. Res. Rev** 8, 1 (2015).

[7] **K. S. Urmila**, T. A. Namitha and B. Pradeep, "Characterization of defect levels and their influence on the photoconductivity of p-type $CuInSe_2$ thin films", **Int. J. Recent. Res. Rev** 8, 10 (2015).

[8] **K. S. Urmila**, T. A. Namitha, R. R. Philip and B. Pradeep, "Optical and low temperature thermoelectric properties of phase pure p-type InSe thin films", **Appl. Phys. A** 120, 675 (2015).

[9] T. A. Namitha, **K. S. Urmila**, J. Rajani, R. R. Philip, G. S. Okram, V. Ganesan and B. Pradeep, "Optical and electrical properties and phonon drag effect in low temperature TEP measurements of $AgSbSe_2$ thin films", **J. Semiconductors** 35, 0520011 (2014).

[10] **K. S. Urmila**, T. A. Namitha, R. R. Philip, V. Ganesan, G. S. Okram and B. Pradeep, "Structural, optical, electrical and low temperature thermoelectric properties of degenerate polycrystalline Cu_7Se_4 thin films", **Phys. Status Solidi B** 251, 689 (2014).

[11] R. Jacob, R. Geethu, T. Shripathi, G. S. Okram, V. Ganesan, B. Pradeep, **K. S. Urmila** and R. R. Philip, "Optoelectronic and low temperature thermoelectric effects in the OVC n-$CuIn_3Se_5$ thin films", **Phys. Status Solidi A** 209, 2195 (2012).

[12] R. Geethu, J. Rajani, T. Shripathi, G. S. Okram, V. Ganesan, T. Shilpa, A. Fathima, P. V. Sreenivasan, **K. S. Urmila**, B. Pradeep and R. R. Philip, "Optoelectronic and thermoelectric properties in Ga doped β-PbS_2 nanostructured thin films", **Appl. Surf. Sci** 258, 6257 (2012).

[13] J. Rajani, R. Geethu, T. Shripathi, G. S. Okram, V. Ganesan, B. Pradeep, **K. S. Urmila** and R. R. Philip, "Structural, optical, electrical and low temperature thermoelectric studies on the ordered vacancy compound $AgGa_3Se_5$", **Phys. Status Solidi B** 249, 1271 (2012).

Conference Publications

[1] **K. S. Urmila**, T. A. Namitha and B. Pradeep, "$InSbSe_3$ thin films – a prospective absorber layer material for thin film solar cells", **AIP Conf. Proc** (Communicated).

[2] T. A. Namitha, **K. S. Urmila** and B. Pradeep, "Optical investigations on polycrystalline $Pb_{3.58}Sb_{4.42}Se_{10}$ thin film", Proceedings of the fourth international conference on frontiers in nanoscience and technology **- COCHIN NANO 2016**, Kochi, Kerala, 20th-23rd February 2016, p. 171.

[3] **K. S. Urmila**, T. A. Namitha, and B. Pradeep, "$Sn_2Sb_4Se_8$ thin films-a novel chalcogenide for energy applications", Proceedings of the international conference on materials for the millennium - **MATCON 2016**, Kochi, Kerala, 14^{th}-16^{th} January 2016, p. 664.

[4] **K. S. Urmila**, T. A. Namitha and B. Pradeep, "Structural and optical characterization of reactive evaporated tin diselenide thin films", **IOP Conf. Series. Mater. Sci. Eng** 73, 0120581 (2015).

[5] T. A. Namitha, **K. S. Urmila** and B. Pradeep, "Electrical and photoconductivity studies on $AgSbSe_2$ thin films", **IOP Conf. Series. Mater. Sci. Eng** 73, 0120131 (2015).

[6] R. Anuroop, **K. S. Urmila** and B. Pradeep, "Composition dependent properties of copper indium selenide thin films prepared by reactive evaporation technique", Proceedings of the international conference on energy harvesting, storage and conversion - **IC-EEE 2015**, Kochi, Kerala, 5^{th}-7^{th} February 2015, p. 74.

[7] **K. S. Urmila**, T. A. Namitha and B. Pradeep, "SnSe thin films - a prospective material for thermoelectric applications", Proceedings of the national conference on advanced materials - **NCAM 2014**, Thrissur, Kerala, 16^{th}-17^{th} October 2014, p. 35.

[8] G. Simi, T. A. Namitha, **K. S. Urmila**, R. Anuroop and B. Pradeep, "Structural and electrical studies of reactively evaporated lead selenide thin film", Proceedings of the national conference on advanced materials

- **NCAM 2014**, Thrissur, Kerala, 16th- 17th October 2014, p. 34.

[9] **K. S. Urmila**, T. A. Namitha, J. Rajani, R. R. Philip and B. Pradeep, "Photoconductivity in reactively evaporated copper indium selenide thin films", **AIP Conf. Proc.** 1576, 69 (2014).

[10] T. A. Namitha, **K. S. Urmila** and B. Pradeep, "Structural and optical studies on $AgSbSe_2$ thin films", **AIP Conf. Proc.** 1576, 60 (2014).

[11] J. Rajani, R. R. Philip, N. Sheeba, A. Anitha, B. N. Sinitha, B. Pradeep, **K. S. Urmila** and G. S. Okram, "Optoelectronic and low temperature thermoelectric studies on nanostructured thin films of silver gallium selenide", **AIP Conf. Proc.** 1576, 83 (2014).

[12] **K.S. Urmila**, T.A. Namitha, R.R. Philip and B. Pradeep, "Optoelectronic properties of phase pure InSe thin films", Proceedings of the international conference on advanced functional materials - **ICAFM 2014**, Thiruvananthapuram, Kerala, 19th- 21st February 2014, p. 328.

[13] **K. S. Urmila**, T. A. Namitha, and B. Pradeep, "Preparation and electrical characterization of copper selenide thin films", Proceedings of the national conference on advances in materials science: macro to nano scales-**NCAMS 2012**, Aluva, Kerala, 16th-17th March 2012, p. 37.

[14] T. A. Namitha, **K. S. Urmila** and B. Pradeep, "Optical and electrical characterization of silver selenide thin films", Proceedings of the national conference on advances in materials science: macro to nano scales –

NCAMS 2012, Aluva, Kerala, 16th-17th March 2012, p. 31.

[15] **K. S. Urmila**, T. A. Namitha, and B. Pradeep, "Preparation and optical characterization of indium selenide thin films", Proceedings of the national seminar on trends in physical sciences – **TRIPS 2011**, Kalady, Kerala, 21st-22nd July 2011, p. 23.

[16] **K. S. Urmila**, T. A. Namitha and B. Pradeep, "Photoluminescence study of copper selenide thin films", **AIP Conf. Proc.** 1391, 770 (2011).

[17] **K. S. Urmila**, T. A. Namitha and B. Pradeep, "Preparation and optical characterization of copper selenide thin films", Proceedings of the international conference on contemporary trends in optics and optoelectronics - **XXXV OSI Symposium 2011**, Thiruvananthapuram, Kerala, 17th-19th January 2011, p. 543.

[18] T. A. Namitha, **K. S. Urmila**, B. Pradeep, S. Dhanya and R. R. Philip, "Optical characterization of lead selenide thin films prepared by reactive evaporation", Proceedings of the international conference on contemporary trends in optics and optoelectronics - **XXXV OSI Symposium 2011**, Thiruvananthapuram, Kerala, 17th-19th January 2011, p. 541.

CONTENTS

Chapter 1

Introduction to Chalcogens and Chalcogenides: Overview and Applications

Chapter 2

Semiconductor Principles

Chapter 3

Experimental Technique and Characterization Tools

Chapter 4

Preparation and Characterization of Degenerate Polycrystalline Cu_7Se_4 Thin Films

Chapter 5

Preparation and Characterization of Polycrystalline $CuInSe_2$ Thin Films

Chapter 6

Preparation and Characterization of Polycrystalline InSe Thin Films

Chapter 7

Preparation and Characterization of Polycrystalline $InSbSe_3$ Thin Films

Chapter 8

Preparation and Characterization of Polycrystalline SnSe Thin Films

Chapter 9

Preparation and Characterization of Polycrystalline $Sn_2Sb_4Se_8$ Thin Films

Chapter 10

Summary and Scope for Future Studies

Chapter 1

Introduction to Chalcogens and Chalcogenides: Overview and Applications

1.1 Introduction

The metal chalcogenide systems comprising of inorganic compounds of oxygen, sulphur, selenium and tellurium with metals and semimetals form an interesting and infinite area of research. To date, several reviews are available on the physical, chemical and electronic properties, crystal structure, preparation techniques and applications of metal chalcogenide systems. In the past few decades, a vast amount of research has been dedicated to these materials due to their wide spectrum of properties and potential applications in the field of electronics, optics, magnetics, photovoltaics, thermoelectrics and so on. Today, more and more complicated compounds based on these systems are being investigated especially for their photovoltaic and thermoelectric properties with much ease owing to the availability of sophisticated characterization tools and viable preparation routes.

This chapter, chooses selected important topics for discussion which includes: fundamentals of chalcogen chemistry and their compounds, systematic description of metal chalcogenides in terms of their key properties, review of state-of-the-art and emerging metal chalcogenide materials for photovoltaic and thermoelectric applications along with the criteria for material selection, comprehensive coverage of achievements, complications and future prospects in the area of chalcogenide based photovoltaics and thermoelectrics. The motivation and objectives of the present work is also described.

1.2 Chalcogens

The term chalcogen was proposed by Werner Fischer- a German inorganic chemist in 1930 to refer to the elements in Group 16 of the periodic table. This group is also known as the oxygen family. It consists of the elements oxygen (O), sulphur (S), selenium (Se), tellurium (Te), polonium (Po) and ununhexium (Uuh). The word chalcogen – meaning ore former is derived from a combination of the Greek word chalcos meaning ore and the Latinised Greek word genes meaning produced [1].

The physical properties of the chalcogens vary dramatically. For example, oxygen is a gaseous non-metal while sulphur and selenium are solid non-metals. Tellurium is a solid metalloid, polonium is a solid metal and ununhexium is a synthetic element. In addition, electronegativity, ionization energy and electron affinity are high for lighter chalcogens whereas density, melting point, boiling point, atomic radii and ionic radii are high for heavier chalcogens. Chalcogens shows allotropy and polymorphism and exhibits a common oxidation state of -2. The chemical properties of chalcogens are similar, to some extent, owing to their same number of valence electrons. But

regarding toxicity, lighter chalcogens are typically nontoxic, while the heavier chalcogens are typically toxic [1]. The significant intermolecular interactions displayed by Se and Te are very useful in crystal engineering for creating novel materials with extended structures.

Table 1.1 gives a brief description on the properties and applications of the members of the chalcogen family with special emphasis on selenium – the chalcogen chosen in the present study.

Table 1.1 The Chalcogen Family: Properties and Applications

Element	Properties	Applications
Oxygen (O)	Oxygen is one of the life sustaining elements on earth. It is a colourless, odourless and tasteless gas and the 3rd most abundant element in the universe. Oxygen has allotropes (O_2, O_3, O_4 and O_8), isotopes (^{16}O, ^{17}O, ^{18}O) and radioisotopes (^{14}O, ^{15}O). Oxidation states are -2, -1 and 0.	Used in water treatment, manufacture of iron, steel, and other chemicals, oxidizer in rocket fuel, medicinal purposes, petroleum refining etc [1] .

Sulphur (S)	Sulphur is a bright yellow crystalline solid. It can be found in elemental form or in the form of sulphide minerals, sulphate minerals or sulphosalt minerals. It is the 10^{th} most abundant element in the universe. It has over 30 allotropes (S_6, S_7, S_8, S_{12}, S_{18}) and 25 isotopes (^{32}S, ^{33}S, ^{34}S, ^{36}S). The radioisotope is ^{35}S. Oxidation states are +6, +5, +4, +3, +2, +1,-1 and -2.	Used in gunpowder, concrete, fireworks and chemicals. It is used directly as a fungicide and insecticide, used in the vulcanization of natural rubber and to change the pH of soil [1].
Selenium (Se)	Selenium is the 67^{th} most abundant element in the earth's crust. It is a solid non-metal with photoconducting properties. Usually selenium is an amorphous, brick-red powder. When melted rapidly, it turns to vitreous black Se which is a brittle, lustrous solid. When heated at 180 °C, it turns to gray selenium - the most stable form of selenium with appreciable photoconductivity. Some of the allotropes are: Se_6, Se_7 and Se_8. A few isotopes are: ^{72}Se, ^{74}Se, ^{75}Se, ^{76}Se, ^{77}Se, ^{78}Se, ^{79}Se, ^{80}Se and ^{82}Se. Oxidation states: +6, +4, +2, +1 and -2.	Due to the semiconducting properties, selenium finds applications in DC power surge protectors, rectifiers, thermoelectric devices and solar cells. It is also used in the toning of photographic prints and as gamma source in radiography [1].

Tellurium (Te)	Tellurium is a silvery white metalloid. It is the 8th rarest element on earth. It has 5 stable isotopes (^{122}Te, ^{123}Te, ^{124}Te, ^{125}Te, ^{126}Te), 3 radioactive isotopes (^{120}Te, ^{128}Te, ^{130}Te) and 38 nuclear isomers. It has the oxidation states: +6, +5, +4, +2 and -2.	Used in photoreceptors, phase change memory chips, optical disks, acousto-optic modulators, far-IR detectors, solar cells and thermoelectric devices. It is also used in metallurgy and to colour ceramics [1].
Polonium (Po)	Polonium is a silvery solid metal which is highly radioactive. It is one of the 10th rarest metals on earth. It exists in two metallic allotropes and has 33 radioactive isotopes (^{208}Po, ^{209}Po, ^{210}Po). Oxidation states are: +6, +5, +4, +2 and -2.	Used as an alpha particle generator for research. It is used as an alloy with beryllium to act as a neutron source for nuclear weapons. It is also used in nuclear batteries and antistatic devices [1].

Ununhexium (Uuh)	Ununhexium is the temporary name of an unconfirmed chemical element with atomic number 116. Due to its position in the periodic table, it is expected to show properties similar to Te and Po. It has very short half life and is highly unstable and hence decomposes very quickly into other elements when formed. Ununhexium do not occur naturally on earth, it is entirely synthesised in laboratories.	Ununhexium do not have any known applications and only little is known about it [1].

1.3 Chalcogenides

The term chalcogenide is used to address the compounds of chalcogens with elements such as arsenic (As), silver (Ag), bismuth (Bi), copper (Cu), cadmium (Cd), iron (Fe), gallium (Ga), germanium (Ge), indium (In), lead (Pb), sodium (Na), antimony (Sb), silicon (Si), tin (Sn), thallium (Tl), zinc (Zn) etc [1]. Strictly speaking, the term chalcogenide is commonly reserved for sulphides, selenides, and tellurides, rather than oxides. Chalcogenides are used in pigments, catalysts, xerography, lubricants, solar cells, thermoelectric devices and so on. During the last decades, applications of semiconducting thin films based on metal chalcogenides in photovoltaic and thermoelectric industry have been very impressive.

The relevant properties and applications of a few well known metal oxides and sulphides are summarized in Table 1.2 and 1.3 respectively. Table 1.4 and 1.5 describes a few well known metal selenides and tellurides respectively along with their properties and applications.

Table 1.2 Metal Oxides: Properties and Applications

Metal Oxides		
Compound	**Properties**	**Applications**
Zinc Oxide (ZnO)	Crystal system : Cubic, Hexagonal Optical band gap : 3.3 eV (Direct) Conductivity type : n-type Wide band gap, high optical transmission, thermal and chemical stability, high electron mobility and conductivity, photoluminescence and ferromagnetism.	Potential window layer material in solar cells. It is used in liquid crystal displays (LCDs), gas sensors, transducers, light emitting diodes (LEDs), thin film transistors, medicine, rubber and ceramic industry and in ultrasonic oscillators [2].
Cadmium Oxide (CdO)	Crystal system : Cubic Optical band gap : 2.2 eV (Direct) Conductivity type : n-type Transparent conducting material.	Widely used in LCDs, pigments, photodiodes, infrared (IR) detectors, phototransistors, transparent electrodes, antireflection coatings and photovoltaic cells [3].

Aluminium Oxide (Al_2O_3)	Crystal system : Trigonal Optical band gap : 6.4 eV (Direct) Conductivity type : n-type High dielectric constant, mechanical strength, chemical inertness, high melting point and good transparency.	Used in optical waveguides, paints and sodium vapour lamps. It is also used as a catalyst, abrasive and filler for plastics. It can act as a passivation layer for solar cells and organic LEDs [4].
Indium Tin Oxide (In_2O_3/SnO_2 or ITO)	Crystal system : Hexagonal Optical band gap : 4 eV (Direct) Conductivity type : n-type Common choice of transparent conducting oxide with high optical transparency and conductivity.	Mainly used as transparent conducting electrode in organic LEDs, flat panel displays (FPDs) and solar cells. Thin films of ITO are used in gas sensors [5].
Fluorine Tin Oxide (F:SnO_2 or FTO)	Crystal system : Tetragonal Optical band gap : 3.6 eV (Direct) Conductivity type : n-type FTO is inexpensive, chemically and thermally stable and hence a possible alternative to ITO. It has high visible transparency and high conductivity.	Promising material for use in thin film solar cells, touch screen displays, dielectric layers in low emissivity coatings for windows, gas sensors, LCDs and other electro-optical applications [6].

Table 1.3 Metal Sulphides: Properties and Applications

Metal Sulphides		
Compound	**Properties**	**Applications**
Copper Sulphide (Cu_2S)	Crystal system : Cubic, Hexagonal Optical band gap : 2.3 eV (Direct) Conductivity type : p-type Exhibits near ideal solar control properties: Transmission in IR region, low visible reflection < 10% and high near infrared (NIR) reflection > 15%.	Promising absorber layer material in solar cells. Used in photodetectors, conducting electrodes, solar control coatings, laminated glazing and microwave shielding [7].
Cadmium Sulphide (CdS)	Crystal system : Cubic, Hexagonal Optical band gap : 2.2 eV (Direct) Conductivity type : n-type High resistivity. Shows considerable cathodoluminescence and good electroluminescence.	Conventional buffer layer material in high efficiency solar cells. Used in photoresistors, solid state lasers, transistors, LCDs and photoconductors [8].
Indium Sulphide (In_2S_3)	Crystal system : Tetragonal Optical band gap : 2.1 eV (Direct) Conductivity type : n-type High resistivity and large band gap – a possible alternative to CdS.	Used as a buffer layer material in solar cells and it is also widely used in the photoelectrochemical cells [9].

Copper Indium Sulphide ($CuInS_2$)	Crystal system : Cubic, Tetragonal Optical band gap : 1.5 eV (Direct) Conductivity type : p-type Non toxic semiconducting material with near optimum band gap for harvesting solar energy and high absorption coefficient (10^5 cm^{-1}).	Promising absorber layer material for solar cells. It is an excellent visible light responsive photocatalyst [10].
Copper Zinc Tin Sulphide (Cu_2ZnSnS_4)	Crystal system : Tetragonal Optical band gap : 1.5 eV (Direct) Conductivity type : p-type Optimum band gap for solar energy conversion and high absorption coefficient (10^5 cm^{-1}) - a possible alternative to $CuInS_2$.	Used as an absorber layer material in solar cells and it is also widely used in the thermoelectric devices [11].

Table 1.4 Metal Selenides: Properties and Applications

Metal Selenides		
Compound	**Properties**	**Applications**
Tin Selenide (SnSe)	Crystal system : Orthorhombic Optical band gap : 1.2 eV (Direct) Conductivity type : p-type Layered semiconductor with optimum band gap, high absorption coefficient (10^5 cm^{-1}), low thermal conductivity and reasonable electrical conductivity.	Used in solar cells as an absorber layer material. Used in memory switching devices, thermoelectric devices, radiation detectors and photoelectrochemical cells [12].
Cadmium Selenide (CdSe)	Crystal system : Cubic, Hexagonal Optical band gap : 1.7 eV (Direct) Conductivity type : n-type Transparent to IR light, highly photosensitive and highly luminescent.	Used as a buffer layer material in solar cells. It is used in photoconductors, transistors, γ-ray detectors, polarizors and also in biomedical imaging [13].

Zinc Selenide (ZnSe)	Crystal system: Cubic, Hexagonal Optical band gap: 3.1 eV (Direct) Conductivity type : n-type IR optical material with a remarkably wide range of transmission, emits blue light when used in LEDs and diode lasers.	Used as a window layer material in solar cells. Used in X-ray and γ-ray detectors, IR optics, photoluminescent and electroluminescent devices [14].
Copper Indium Selenide ($CuInSe_2$)	Crystal system : Tetragonal Optical band gap : 1.1 eV (Direct) Conductivity type : p-type Near optimum band gap for solar energy conversion, high absorption coefficient (10^5 cm^{-1}), highly stable and reasonable work function.	Prominent absorber layer material for efficient low cost solar cells [15].
Copper Indium Gallium Selenide ($CuInGaSe_2$)	Crystal system : Tetragonal Optical band gap: 1.7 eV (Direct) Conductivity type : p-type Optimum band gap, high absorption coefficient (10^5 cm^{-1}) - an alternative to $CuInSe_2$.	Potential absorber layer material for solar cells. It is widely used in flexible and light weight solar panels [16].

Table 1.5 Metal Tellurides: Properties and Applications

Metal Tellurides		
Compound	**Properties**	**Applications**
Bismuth Telluride (Bi_2Te_3)	Crystal system : Trigonal Optical band gap : 0.2 eV (Direct) Conductivity type : p-type/n-type Narrow band gap semiconductor. High electrical conductivity, low thermal conductivity and reasonably high Seebeck coefficient.	Thermoelectric material for power generation and refrigeration. It is used in IR opto-electronics, laser diodes and thermal sensors [17].
Cadmium Telluride (CdTe)	Crystal system : Cubic Optical band gap : 1.45 eV (Direct) Conductivity type : p-type Near optimum band gap for solar energy conversion, high absorption coefficient (10^5 cm^{-1}), highly stable, and transparent in the IR region.	Used as an absorber layer material in solar cells. Used in the detection of X-rays, γ-rays, α particles and β particles. It is also used in sensors, lasers, IR optical windows and thermoelectric devices [18].

Lead Telluride (PbTe)	Crystal system : Cubic Optical band gap : 0.3 eV (Direct) Conductivity type : p-type Narrow band gap, high carrier mobility, good stability and low thermal conductivity.	Used in IR detectors, solar panels, IR lasers, thermoelectric devices and LEDs. It is used in spacecraft and power applications [19].
Indium Telluride (In_2Te_3)	Crystal system : Cubic, Hexagonal Optical band gap : 1.1 eV (Direct) Conductivity type : n-type High electrical resistivity.	Widely used in radiation detectors, switching and memory devices, gas sensors, electrode in capacitors and micro batteries and also as a buffer layer material in solar cells [20].
Copper Indium Telluride ($CuInTe_2$)	Crystal system : Tetragonal Optical band gap: 1.04 eV (Direct) Conductivity type : p-type Optimum band gap and absorption coefficient (10^5 cm^{-1}) for use in solar cells.	Promising absorber layer material for solar cells and potential material for use in thermoelectric devices [21].

Thus the favourable optical and electrical properties have ascertained a promising commercial future for chalcogenides (either in single crystal or thin film form) in the areas of photovoltaics, infrared optics, thermoelectrics, laser technology, metallurgy and so on. In the present context, main focus is given on the application and future prospects of chalcogenide semiconductors in photovoltaic and thermoelectric industry.

1.4 Photovoltaics

Among the various technologies developed for harnessing the solar energy, the most efficient are the photovoltaic (PV) systems that convert radiant energy from the sun directly into electricity by means of solar panels composed of a number of solar cells. Today, over 91% of solar cells produced worldwide are based on expensive crystalline silicon wafers, also referred to as first generation PV. However, the crystalline silicon technologies are not likely to meet the substantial cost reductions that are necessary for large scale production of solar cells. This scenario has paved way to cost effective polycrystalline thin film solar cells (TFSCs) also referred to as second generation PV to enter the PV market replacing silicon. The third generation PV (nanocrystal solar cell, photoelectrochemical cell, polymer solar cell, dye sensitized solar cell) and fourth generation PV (hybrid inorganic crystals within a polymer matrix) covers the future technologies and are not yet commercialized.

1.5 Chalcogenide based photovoltaic materials: a review

Counting from 1980, several heterojunctions and homojunctions with improved conversion efficiencies have been successfully fabricated with the

chalcogenide semiconducting compounds. To date, the prominent members among the chalcogenide based thin film PV technologies are CdTe and $Cu(In,Ga)(S,Se)_2$ and they have gained nearly 17% of PV market share in 2011 [22]. However, the recent achievements in chalcogenides and their applications in solar cells are based on a long history of research and technological development. The following section gives a review on a few prominent chalcogenide based photovoltaic materials.

1.5.1 $CuInS_2$

$CuInS_2$ has the potential to reach high conversion efficiencies due to its large absorption coefficient of 10^5 cm^{-1} and direct band gap of 1.5 eV, which matches well with the solar spectrum. Therefore $CuInS_2$ based solar cells are promising for large scale applications in the field of photovoltaic energy conversion. $CuInS_2$ can de doped as either p-type or n-type which is obviously a desirable property for the fabrication of homojunctions [10].

1.5.2 $CuInSe_2$

The toxicity of cadmium and scarcity of Te has led to lots of work on the preparation of $CuInSe_2$ – a leading absorber layer material for solar cells. Some of the notable peculiarities of $CuInSe_2$ are its near optimum band gap for solar energy harvesting (1.1 eV), high absorption coefficient (10^5 cm^{-1}), stable device performance, potential for forming both homojunctions and heterojunctions as it can be doped either as p-type or n-type and allows band gap engineering [15].

1.5.3 $Cu(In,Ga)(S,Se)_2$

$Cu(In,Ga)(S,Se)_2$ - an alloy of $Cu(In,Ga)S_2$ and $Cu(In,Ga)Se_2$, is one of the most interesting and versatile absorber layer material for large scale production of efficient, low cost TFSC which is expected to revolutionize the PV industry. The advantages of incorporating Ga in $CuIn(S,Se)_2$ is that Ga increases the optical band gap of the $Cu(In,Ga)(S,Se)_2$ layer to 1.7 eV as compared to pure $CuIn(S,Se)_2$ with band gap between 1.1 eV to 1.5 eV, thus increasing the open circuit voltage. Also, relative abundance of Ga compared to In lowers the cost of production [16].

1.5.4 $Cu_2ZnSn(S,Se)_4$

The kesterite - $Cu_2ZnSn(S,Se)_4$ is a prospective absorber material for low cost solar cells and have recently gained appreciable commercial success. It is superior to the prominent PV materials namely CdTe and $Cu(In,Ga)(S,Se)_2$, in the sense that, the constituent elements of $Cu_2ZnSn(S,Se)_4$ are non toxic and earth abundant and hence only 0.1% of the available raw material is sufficient to produce enough power. The optimum band gap (1.5 eV) and high absorption coefficient (10^5 cm^{-1}) of $Cu_2ZnSn(S,Se)_4$ are favourable for efficient solar energy conversion [11].

1.5.5 CdTe

CdTe is a very good absorber layer material for TFSCs due to its optimum band gap (1.45 eV) and high absorption coefficient (10^5 cm^{-1}) suitable for solar energy conversion. CdS can be doped either p-type or n-type

and it is chemically stable [18]. Hence CdTe has been considered as one of the most promising candidates for the development of cost effective solar cells.

1.6 Emerging chalcogenide photovoltaic technologies

Investigations on chalcogenide thin film solar cells based on novel cell configurations are being carried out by the researchers worldwide. Table 1.6 presents some of the emerging chalcogenide thin film PV technologies with solar cell parameters: open circuit voltage (V_{OC} in Volts), short circuit current (J_{SC} in $mAcm^{-2}$), fill factor (FF), efficiency (η in %) and active area in cm^2.

Table 1.6 A few emerging chalcogenide thin film PV technologies

Heterojunction	V_{OC}	J_{SC}	FF	η	Active area	Reference
p-Cu_2S/n-CdS	0.58	5.8	0.73	10.9	0.06	[23]
p-PbS/n-CdS	0.28	20.93	0.53	3.1	0.65	[24]
p-SnS/n-$Zn_{0.83}Mg_{0.17}O$	0.27	12.1	0.64	2.1	0.04	[25]
p-Sb_2S_3/n-CdS	0.6	6.12	0.35	1.3	0.03	[26]
p-$Cu_{1.9}Se$/n-CdS	0.46	18.7	0.63	5.4	1	[27]
p-SnSe/n-CdS	0.6	5.51	0.29	0.96	0.08	[28]
p-$Ag(In_{0.2,}Ga_{0.8})Se_2$/n-CdS	0.87	14.5	0.58	8	0.42	[29]
p-CdTe/n-Bi_2Te_3	0.65	26.9	0.61	10.6	0.07	[30]

To summarize, the literature survey presented on the chalcogenide based photovoltaics shows that the chalcogenide semiconductors are being successfully applied as efficient absorber and buffer layer materials in today's

leading polycrystalline thin film solar cells. The substantial increase in the efficiency of chalcogenide based thin film solar cells from 4% (1963) to 22.8% (2014) indicate that this PV material system are promising candidates to future photovoltaics and hence demands further research with due importance.

1.7 Future prospects of chalcogenide photovoltaics

Today, the module production cost of both CdTe and $Cu(In,Ga)(S,Se)_2$ technologies is about 0.85 $/W at an efficiency of 11%. With an anticipated module lifespan of 30 years and an energy payback time of one year, these modules can assure a cost reduction of 0.5 $/W at an increased efficiency of 15% in the coming years [31]. As per literature reports the world energy consumption is projected to be about 30 TW by 2050. Based on aforesaid estimates, it can be concluded that, chalcogenide thin film PV technologies with an annual growth rate of 30% over the last 5 years can definitely provide nearly 10 TW of energy for terrestrial applications in the near future [32]. These technologies have room for further improvement and can substantially add to the world's power supply.

1.8 Thermoelectrics

Thermoelectrics represent a novel method of power generation and refrigeration for specific applications. The interest in thermoelectrics began in the mid 1990s when it was predicted that the energy conversion process in thermoelectric (TE) energy converters is reversible. The term reversible suggests that a thermoelectric energy converter can be applied either to convert the input thermal power directly to electric power for lighting and operating electrical equipment or to convert the input electric power directly to thermal

power for heating or refrigerating. The former process is called as thermoelectric power generation and the latter process is called as thermoelectric refrigeration [33]. The basic mechanisms and the fundamentals of thermoelectric power generation and refrigeration are discussed in the following sections. In general, thermoelectric energy converters have the following advantages and disadvantages [34]:

Advantages

- Lack of moving parts, maintenance free and long operating life.
- Direct conversion of energy, clean and silent operation.
- Absence of materials that need to be replenished.
- Provides up to 100,000 hours of steady state operation.
- High power density and physical ruggedness.
- Small size, lightweight and flexible shape offers easy portability.
- Easy and convenient to reverse from heating to cooling and vice-versa.

Disadvantages

- Relatively high cost and low power efficiency.
- Thermoelectric generators have high output resistance and adverse thermal features.
- Thermoelectric coolers can dissipate only a limited amount of heat flux and are relegated to applications with low heat flux.

1.8.1 Thermoelectric effect

In 1821, Thomas Johann Seebeck - a German Physicist, observed that when two dissimilar materials (either electrical conductors or semiconductors) are joined together with the junctions held at different temperatures (T and T+ΔT), then a voltage (ΔV) is developed proportional to the temperature difference (ΔT). This phenomenon is termed as the Thermoelectric effect. The ratio of the voltage developed (ΔV) to the temperature gradient (ΔT) is called the thermoelectric power or Seebeck coefficient (S) and it is given by

$$S = \frac{\Delta V}{\Delta T} \tag{1.1}$$

The Seebeck coefficient is an intrinsic property of the materials. It is very low for metals (a few μVK^{-1}) and high for semiconductors (a few 100 $\mu V K^{-1}$). The thermoelectric effect includes three separately identified effects: the Seebeck effect, Peltier effect and Thomson effect, each of which are depicted in Fig 1.1(a), (b) and (c) respectively [34].

- **The Seebeck effect:** Discovered by Thomas Johann Seebeck in 1821. The Seebeck effect is the electromotive force (EMF) caused by the temperature gradient across two dissimilar conducting metals which form a closed loop.

- **The Peltier effect:** Discovered by Jean Charles Peltier in 1834. The Peltier effect is the temperature difference caused at the junctions of dissimilar conductors with the passing of current. He found that the heat adsorption or generation at the junction of two different materials

depends on the polarity of the current and that reversing this polarity will change the direction of transfer.

- **The Thomson effect:** Discovered by William Thomson in 1851. The Thomson effect is the electric current caused by a temperature gradient in a single homogeneous conductor. It is defined as the rate of heat generated or absorbed in a single current carrying conductor in the presence of a temperature gradient.

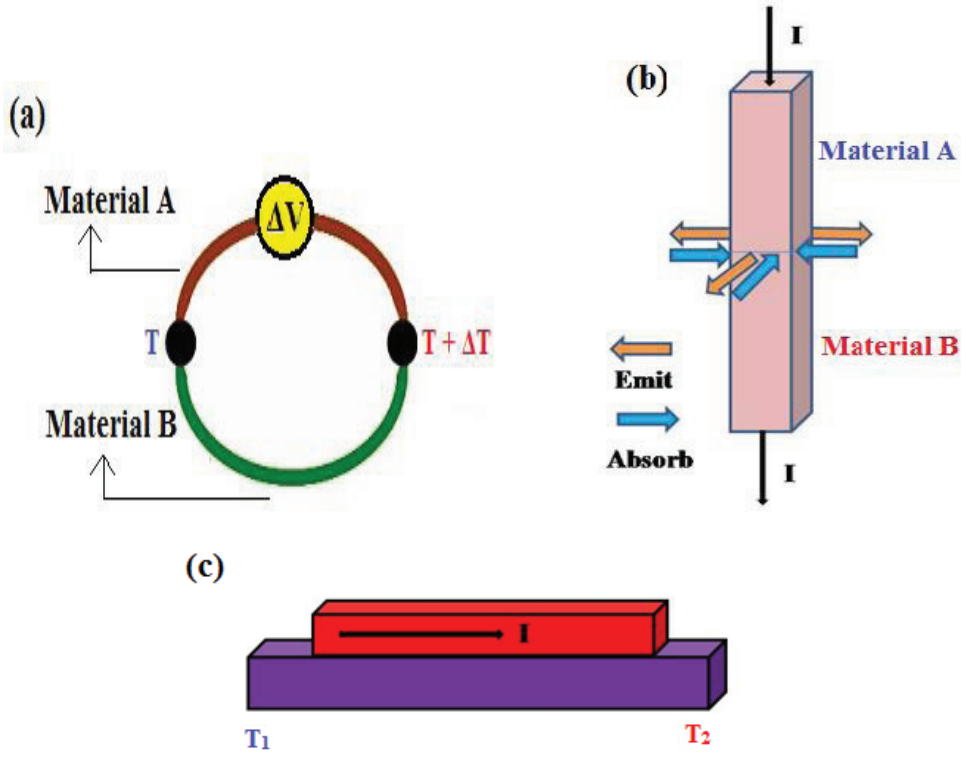

Fig 1.1 Thermoelectric effect includes (a) Seebeck effect (b) Peltier effect and (c) Thomson effect

1.8.2 Thermoelectric power generation

It is well known that, of the world's enormous energy consumption, about 70% of the consumed energy is dissipated untapped into the atmosphere as heat. The waste heat from home heating, automotive exhaust and industrial processes, brings about an increase in CO_2 emissions, followed by a rise in atmospheric temperature. On the other hand, the increase in the production of large scale integration (LSI) devices and solar cells, generates considerable amounts of waste silicon from semiconductor industries, which leads to serious environmental contamination [35].

Therefore, in order to reduce CO_2 emissions to counteract greenhouse effects and to minimize the environmental hazards due to silicon waste, a positive attitude towards the industrial reuse of waste heat and waste silicon is urgently required to sustain the huge growth in energy consumption on a global scale. Consequently, intensive research has been carried out worldwide to implement technologies that can recover and effectively utilize the waste heat into useful energy at low cost. The final outcome of the research is the discovery of a direct thermal energy to electric energy conversion technique termed as thermoelectric power generation - the most promising technology for reclaiming waste heat.

When a temperature gradient is applied to a material, the mobile charge carriers at the hot end tend to diffuse to the cold end. The build up of charge carriers results in a net charge (negative for electrons, positive for holes) at the cold end, producing an electrostatic potential (voltage). An equilibrium is thus reached between the chemical potential for diffusion and the electrostatic repulsion due to the build up of charge. This property known as Seebeck effect,

is the basis of thermoelectric power generation. The solid state device that converts the temperature difference directly into electrical energy is called as a thermoelectric generator (TEG) [33]. The basic configuration of a thermoelectric generator is shown in Fig 1.2.

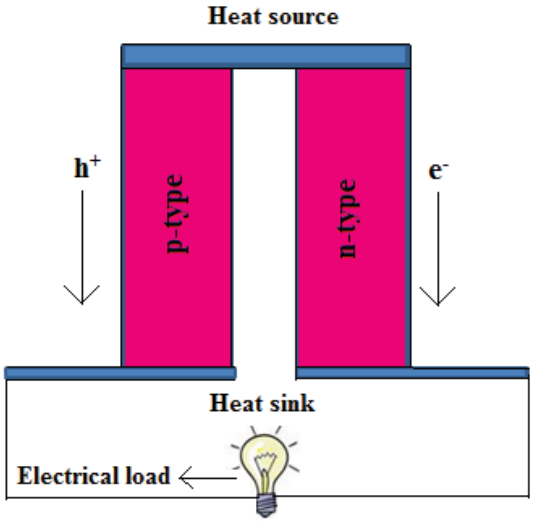

TEG consists of the following components:

- Heat source (hot side).
- p-type and n-type semiconductor stack or TE module (optimized for Seebeck effect) sandwiched between metalized ceramic substrates.
- Heat sink (cold side).
- Electrical load (output voltage).

Fig 1.2 Thermoelectric generator

One side of the TEG is heated by the waste heat from the industrial furnaces and automobile engines and acts as the heat source. The other side of the device acts as the heat sink and is kept at a temperature below that of the heat source. Thus a temperature gradient is set up between the upper and lower surfaces of two sides of the device. The temperature gradient results in heat flow and consequently diffusion of charge carriers between the hot and cold sides. This generates electric power to an electrical load having a terminal voltage and terminal current. The electric power generated in the device is equal to the product of the Seebeck coefficient (S), the current (I) and the

temperature gradient (ΔT). The ohmic heating in the resistances of the two semiconductors dissipates a fraction of the generated electric power. The remaining fraction is the electrical power output to the electrical load [33]. TEG can be used for various purposes and a few of them are listed below [34]:

Applications

- To harvest the waste heat from industries and automobiles.
- To power equipments in remote uninhabited locations.
- To provide backup power for solar PV.
- To power portable communication transmitters.
- To power electronic sensors and microcontrollers.

1.8.3 Thermoelectric refrigeration

Beginning around 1990, a combination of factors – notably environmental concerns regarding refrigerant fluids and interest in cooling electronics has led to renewed activity in the science and technology of alternative refrigeration. The most well established of these technologies is the thermoelectric refrigeration. This technology becomes more practical and cost effective than the conventional refrigeration system, especially, in situations where thermal energy must be transferred away from a solid or liquid on a small scale.

As already mentioned, a unique aspect of thermoelectric energy conversion is that the direction of energy flow is reversible. Hence, if the electrical load shown in Fig 1.2 is removed and a DC power supply is substituted, then the TE module absorbs heat at one end of the device and emits

heat at the opposite end. This pheneomenon is known as the Peltier effect. The removal of thermal energy (ranging from milliwatts to several thousand watts) from a medium, device or component by applying a voltage of constant polarity to the junction between dissimilar electrical conductors or semiconductors is called as thermoelectric refrigeration. The solid state device that uses electrical power to pump heat and produce refrigeration using the principle of Peltier effect is called as a thermoelectric refrigerator (TER) or Peltier heat pump [33]**.** The basic configuration of a thermoelectric refrigerator is shown in Fig 1.3.

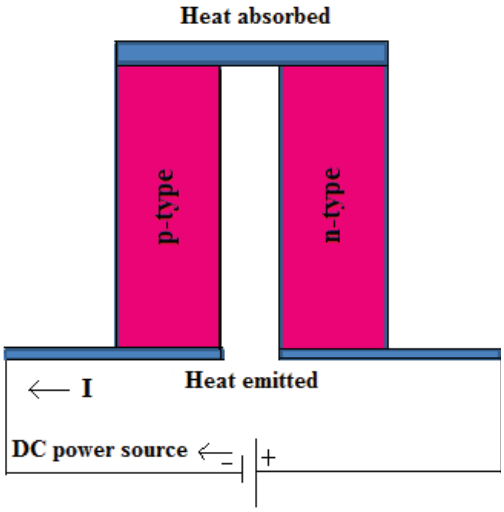

Fig 1.3 Thermoelectric refrigerator

TER consists of the following components:

- Negative electrode or heat source (hot side) where heat is absorbed.
- p-type and n-type semiconductor stack or TE module (optimized for Peltier effect) sandwiched between two large electrodes.
- Positive electrode or heat sink (cold side) where heat is emitted.
- DC power source.

The negative electrode is placed in contact with the component, device or medium to be cooled, while the positive electrode is connected to a heat sink that radiates or dissipates thermal energy into the external environment. When a DC voltage source is connected between the electrodes, the negatively

charged side becomes cooler while the positively charged side becomes warmer thereby implementing thermoelectric refrigeration [33]. TER can be used for various purposes and a few of them are listed below [34]:

Applications

- Used for localized spot cooling for sensitive components in computers.
- Used in satellites to moderate the extreme temperatures.
- To cool digital cameras so as to minimize thermal noise.
- To extract water from air in dehumidifiers and for cooling of car seats.
- Used as heat sinks for microprocessors.
- Used in portable coolers and climate controlled jackets.

1.8.4 Thermoelectric power factor and figure of merit

The efficiency of a thermoelectric (TE) material is represented by a dimensionless quantity called figure of merit (ZT) and it is given by

$$ZT = \frac{S^2 \sigma T}{k} \tag{1.2}$$

where S is the Seebeck coefficient, σ is the electrical conductivity, T is the absolute temperature and k is the total thermal conductivity given by

$$k = k_L + k_E \tag{1.3}$$

where k_L and k_E are the lattice and electronic contributions respectively. As per Eq (1.2), an efficient thermoelectric material must have large Seebeck coefficient, high electrical conductivity and low thermal conductivity. Large Seebeck coefficient is necessary to produce the required voltage, high electrical

conductivity is essential to minimize Joule heating and low thermal conductivity helps to retain heat at the junctions and maintain a large temperature gradient. This means that the numerator ($S^2\sigma$, often called as thermoelectric power factor P) has to be maximized and the denominator (thermal conductivity k) has to be minimized. Thermoelectric power factor is determined by the electronic properties of the material and is optimized as a function of carrier concentration of nearly 10^{19} cm^{-3}, through doping, to give largest ZT. The main contribution to k has its origin in the vibrational properties of the lattice, i.e., phonons [33]. For commercial application, TE materials must have value of ZT above 2. For example, to efficiently recover waste heat ZT = 1.5 is needed [36] and to match a refrigerator ZT = 3 is desirable [37]. However, materials with ZT $\geq$ 1 are considered as promising materials for TE applications [34]. To date, most of the state-of-the-art TE materials possess ZT between 1 and 2 and further enhancement in ZT is still an ongoing subject of research.

Compounds with thermoelectric power factor $\approx 10^{-3}$ $Wm^{-1}K^{-2}$ and thermal conductivity below 3 $Wm^{-1}K^{-1}$ are considered as good thermoelectric materials [38]. Semiconductors are found to be the materials of choice for thermoelectric application with S $\approx$ 100 μVK^{-1} which is high compared to that of metals which is typically 10 μVK^{-1}. In addition, semiconductors have a higher ratio of electrical conductivity (10^{-3} Sm^{-1}) to thermal conductivity (10 $Wm^{-1}K^{-1}$) when compared to metals ($\sigma=10^7$ Sm^{-1} and $k=10^2$ $Wm^{-1}K^{-1}$). These properties of semiconductors contribute to a greater ZT for thermoelectric applications [39].

1.9 Chalcogenide based thermoelectric materials: a review

At present, the trend in search for new TE materials based on layered chalcogenides comprising of heavy elements is being actively developed. This is because these class of compounds exhibit complicated crystalline lattices and low thermal conductivity due to effective scattering of phonons. Among the chalcogens, tellurium based alloys are commercialized for medium temperature TE devices while TE devices based on sulphides and selenides are still a subject of research. This review illustrates, a selected number of chalcogenides that are actively being researched for their TE properties.

1.9.1 Bi_2Te_3

Bi_2Te_3 (both p-type and n-type) and their alloys are known to be the best conventional materials for thermoelectric modules for power generation as well as refrigeration over the temperature range from 200 K to 400 K [40]. Bi_2Te_3 is a V-VI compound semiconductor with a narrow band gap and layered crystal structure. It is a semimetal alloy having high σ, high S and low k. The anisotropic nature and complex hexagonal crystal structure of Bi_2Te_3 owes for its favourable TE properties [41]. Bulk p-type and n-type Bi_2Te_3 based materials have the highest ZT ≈ 1.41 and 1.13 respectively at room temperature [42]. Tan et al [43] has observed a maximum S ≈ -287 μV per degree celsius at 54 °C for RF magnetron sputtered n-Bi_2Te_3 thin film. Moreover, ZT close to unity was reported by Goncalves et al [44] for thermal evaporated optimized thin films of n-Bi_2Te_3 (S = -250 μVK^{-1}, $S^2\sigma = 4.87 \times 10^{-3}$ W m^{-1} K^{-2}) at room temperature. Recently Zhou et al [45] showed that p-Bi_2Te_3 nanofilms could be good candidates for TE nanomaterials with ZT ≈ 2.5 at 300 K when compared to p-Bi_2Te_3 films with ZT ≈ 1 at 300 K.

1.9.2 PbTe

PbTe is a narrow band gap IV–VI compound semiconductor with cubic structure. It holds the best performance in TE power generation in the mid temperature range from 500 K to 900 K. The p-PbTe is an outstanding high temperature TE material with ZT ≈ 2 at high temperatures due to its complex band structure [46]. Pei et al [47] has reported on nanostructed p-type PbTe:Na system with ZT ≈ 1.4 at 750 K whereas Biswas et al [48] has reported on nanostructed p-type PbTe:SrTe system with ZT ≈ 2.2 at 915 K. PbTe nanocomposites exhibit relatively large S ≈ 325 μVK^{-1} at 300 K [49] when compared to PbTe thin films (S ≈ 160 μVK^{-1} at 300 K) [50]. Moreover, $Pb_{0.97}Mn_{0.03}Te$ alloys exhibit ZT as high as 1.6 at 700 K [51] and $Ag_{0.8}Pb_{22.5}SbTe_{20}$ exhibits ZT ≈ 1.5 at 700 K [52]. There is a continued interest among researchers in enhancing the TE properties of PbTe based systems and the various approaches adopted for achieving high ZT in PbTe based systems has been discussed by Rawat et al [46].

1.9.3 SnTe

SnTe which is a lead free rock salt analogue of PbTe is recently been recognized as a potentially attractive TE material. It is a narrow band gap IV-VI layered semiconductor with three distinct crystal phases namely, α-SnTe (rhombohedral), β-SnTe (cubic) and γ-SnTe (octahedral) existing at low, room and high temperatures respectively [53]. During the past few decades, SnTe was considered as a poor TE material because of its low value of Seebeck coefficient (S ≈ 20 μVK^{-1} at 300 K for SnTe thin film), poor ZT, high hole concentration arising from inherent Sn vacancies in the lattice and very high σ and k [54]. Xu et al [55] observed S ≈ 50 μVK^{-1} for p-SnTe crystals and an S ≈

-200 μVK^{-1} for n-SnTe crystals at 300 K whereas Ivanov et al [56] observed a very low value of S for SnTe thin films (S ≈ 20 μVK^{-1}) at 300 K. Later it was experimentally proved that SnTe based materials could be applied as ideal alternatives for p-type lead chalcogenides for high temperature TE power generation by introducing a few key concepts such as Sn self compensation (reduce hole concentration), co-doping (enhance S and ZT) and endotaxial nanostructuring (reduce k) [57]. Applying these conceptions, researchers were successful in improving the TE performance of p-type samples of $In_{0.0025}Sn_{0.9975}Te$ (ZT ≈ 1.1 at 873 K) [58], $Sn_{0.97}In_{0.015}Cd_{0.015}Te$ (ZT ≈ 1.4 at 923 K) [59] and $SnTe_{0.985}I_{0.015}$ (ZT ≈ 0.6 at 700 K) [60].

1.9.4 Cu_2Te

Cu_2Te is a highly degenerate p-type semiconductor with high carrier concentration (10^{20} cm^{-3}) and high electrical conductivity at 300 K. It is a narrow band gap I-VI compound semiconductor with orthorhombic crystal structure [61]. At 300 K, Cu_2Te single crystals shows high S ≈ 370 μVK^{-1} than Cu_2Te thin films (S ~ 10 μVK^{-1}) [53]. Kurosaki et al [62] reported an ZT ≈ 0.03 at 634 K for Cu_2Te and a slightly enhanced ZT ≈ 0.38 at 592 K for $CuTl_9Te_5$ whereas Sklyarchuk et al [63] reported S ≈ 130 μVK^{-1} at 800 K for a Cu_2Te alloy. The presence of Ag and Ga can enhance the thermoelectric performance of Cu_2Te to a maximum ZT ≈ 1 at 900 K for $Cu_{1.98}Ag_{0.2}Te$ [64] and ZT ≈ 1 at 840 K for $CuGaTe_2$ [65].

1.9.5 Sb_2Te_3

Sb_2Te_3 is a narrow band gap V-VI compound semiconductor with trigonal crystal structure. Sb rich Sb_2Te_3 thin film possess S ≈ 536 $\mu V\ K^{-1}$ at

300 K, almost six times higher than stoichiometric Sb_2Te_3 thin film 90 $\mu V K^{-1}$. Also, Zhang et al [66] observed that by altering Sb content, various Seebeck coefficients would be acquired in Sb rich Sb_2Te_3 films thereby moulding them appropriate for TE devices. Fang et al [67] observed $S \approx 123 \mu V K^{-1}$ for RF magnetron sputtered Sb_2Te_3 thin film and Aabdin et al [68] observed $S \approx 130 \mu V K^{-1}$ for Sb_2Te_3 thin film deposited by molecular beam epitaxy respectively. On the other hand, alloys of Sb_2Te_3, namely, $AgSn_4SbTe_6$ ($ZT \approx 1$ at 710 K) holds great promise as an efficient p-type TE material at medium temperature [69].

1.10 Emerging chalcogenide thermoelectric technologies

It is obvious from the aforementioned review that, compounds and alloys based on tellurides are considered as classic TE materials with high value of ZT. However, tellurium is least abundant on earth's crust when compared to the other chalcogens, namely, sulphur and selenium. Hence intensive research efforts are directed towards finding TE materials based on sulphides and selenides, using earth abundant and toxic Pb free elements that can ensure high ZT and better TE performance. Research efforts devoted in this direction has led to the successful development of novel TE materials based on sulphides and selenides with ZT values almost comparable to commercialized TE materials whose constituents are non toxic and earth abundant. A few among them are summarized in Table 1.7 along with their ZT values.

Table 1.7 A few emerging chalcogenide based TE materials with their ZT values

TE material	ZT	Reference
n-Bi_2S_3	0.5 at 723 K	[70]
p-SnS	0.19 at 823 K	[71]
p-Cu_2S	1.9 at 970 K	[72]
p-$AgBi_3S_5$	0.2 at 573 K	[73]
p-Bi_2Se_3	0.096 at 523 K	[74]
p-Ag_2Se	0.6 at 300 K	[75]
p-Cu_2Se	1.5 at 1000 K	[76]
p-SnSe	2.6 at 923 K	[77]

It is noteworthy that the ZT values attained so far for these compounds is an outcome of decades of meticulous research on the simultaneous tuning of their thermoelectric power factor and thermal conductivity. It is of no doubt that chalcogenide material systems have a bright prospect in TE applications as they exhibit continued improvement in their ZT values.

1.11 Future prospects of chalcogenide thermoelectrics

During the last decade, the dramatic improvement in the ZT values above 1 or even 2 attained in chalcogenide TE materials provide overwhelming optimism for their future progress in TE power generation and refrigeration. However, despite of extensive research activities, chalcogenide TE materials, other than Bi_2Te_3 and their alloys, have not yet led to widespread market applications due to their relatively low ZT values. This is because simultaneous

tuning of independent thermoelectric parameters, such as, electrical conductivity, Seebeck coefficient and thermal conductivity to improve ZT is very difficult and it remains as the utmost challenge in this field [33]. Consequently, scientists are trying to theorize and experiment on novel materials based on chalcogenides by employing various preparative methods to realize higher ZT in chalcogenides in the upcoming years [78]. In this perspective, Chen et al [79] and Han et al [80] have reviewed the recent progress on prospective TE materials based on novel complex chalcogenides and Venkatasubramanian et al [81] have highlighted the potential application of thin film approach on chalcogenides so as to enhance ZT and has reported on a Bi_2Te_3/Sb_2Te_3 superlattice with an enhanced ZT of 2.4 at 300 K. Therefore through nanotechnology, chemical doping and engineering of electronic structure of metal chalcogenides, it is expected that TE power generation based on this material system can guarantee nearly 720 MW power annually in the near future.

1.12 Motivation and Objectives of the present study

Motivation: In the 21st century, we are facing serious challenges in energy and environment. The energy crisis due to decline in coal, oil and natural gas and global warming due to the increase in carbon dioxide emissions has enhanced interest in photovoltaics (PV) which is a clean and renewable source of energy. On the other hand, efficient conversion of waste heat energy from automobiles and industrial process directly into electricity (Seebeck effect) or alternative conversion of electricity to produce effective cooling (Peltier effect) has led to remarkable progress in the field of thermoelectrics (TE) which is a clean and transformative energy conversion technology. Thus

PV and TE, together, represent one of the main components of future sustainable energy scenarios.

Over the past few years, incredible achievements were made on PV and TE materials research. Among the various materials investigated, the chalcogenide based compound semiconductors (either in bulk, thin film or nanocomposite form) have demonstrated promising PV and TE performances and they are one among the critical materials for today's leading PV and TE technologies. The chalcogenide based compound semiconductors exhibits versatile optical and electrical characteristics, which can in principle be manipulated and tuned for a specific need in a given PV or TE device. Also, the reasonably low temperature for preparation and high tolerance to defects and impurities make them highly relevant for future developments in PV and TE. As already discussed, these compounds are nearing to PV and TE energy conversion efficiencies as that of the state-of-the-art PV and TE materials and thereby providing an overwhelming optimism for future progress in the area of chalcogenide based PV and TE.

To date, investigations on toxic Cd free materials for thin film solar cells, toxic Pb and scarce Te free materials for thermoelectric modules for power generation and refrigeration based on chalcogenides are an ongoing field of research. However, the development of solar cells and thermoelectric modules based on earth abundant and non toxic novel chalcogenide materials that can offer reasonably high PV efficiency and TE figure of merit is still a challenging task for the researchers. Therefore, in order to develop viable modules for future PV and TE applications, exhaustive research efforts towards the improvement of energy conversion efficiencies, stabilities and production

scalability of chalcogenide semiconductors becomes necessary. In this point of view, there is an urgent need for a better understanding of the structural, optoelectronic, photovoltaic and thermoelectric properties of the developed materials and optimization of PV and TE properties of developing novel materials based on chalcogenide material system. These key aspects has motivated us to choose chalcogenide semiconductors in thin film form, prompted by the various advantages of thin film materials over their bulk counterparts, as the topic of research.

Objectives: In the present scenario, it would be a great advantage to find a material (free of Cd, Pb and Te) that promise equally good PV performance like that of conventional CdS, InS, ZnS and good TE performances similar to the prime telluride candidates such as PbTe, Bi_2Te_3, Cu_2Te. Hence, in this thesis, we focus on compound semiconducting thin films based on selenides - a prominent member of the chalcogen family which is well known for its semiconducting and photoconducting properties with relative abundance ten times more than tellurium. The objective of the thesis is to document, understand and explore the structural, compositional, morphological, optical, electrical and thermoelectric properties of the as-prepared compound semiconducting selenide thin films in view of their PV and TE applications. In general, the present research work has two different directions: The further development and investigation of existing (binary and ternary) compound semiconducting selenide thin films for PV and TE applications and second the exploitation of compound semiconducting selenide thin films of novel composition with optimum fulfilment of PV and TE requirements. The main objectives of the present study are as follows:

- To present an overview on the present status, breakthroughs, advances and future challenges in the field of chalcogenide based PV and TE research.

- To review the present state-of-the-art chalcogenide PV and TE materials along with a few emerging chalcogenide technologies and looks at future prospects.

- To prepare compound semiconducting selenide thin films by reactive evaporation which is a variant of Gunther's three temperature method - a widely used technique in semiconductor processing that provides crystalline thin films of high purity.

- To optimize the deposition parameters such as substrate temperature, source temperature and impingement rate (flux rate) of evaporants so as to obtain good quality thin films of required composition.

- To characterize the structural, compositional, morphological, optical, electrical and thermoelectric properties of the as-prepared thin films by various experimental techniques in view of their applications in solar cells and thermoelectric devices.

- To analyze the obtained theoretical and experimental results on the crystal structure, elemental composition, surface morphology, optical band gap, dispersion parameters, optical constants, photoconductivity, photoluminescence, charge carrier transport properties, Seebeck coefficient, electrical conductivity, thermal conductivity and thermoelectric figure of merit of the as-prepared thin films and to compare these results with literature reports (if any).

- To develop novel materials that exhibit interesting PV and TE properties which on further investigation and optimization holds the promise to be commercialized in the near future.

References

[1] M. Bouroushian, Electrochemistry of metal chalcogenides, ed. by F. Scholz (Springer, Berlin, 2010), pp. 1-76.

[2] M. Sahal, B. Hartiti, A. Ridah, M. Mollar and B. Mari, Microelectron. J. 39, 1425 (2008).

[3] H. H. Afify, N. M. Ahmed, M. Y. Tadros and F. M. Ibrahim, J. Elec. Sys. Info. Technol 1, 119 (2014).

[4] N. V. Nguyen, O. A. Kirillov, W. Jiang, W. Wang, J. S. Suehle, P. D. Ye, Y. Xuan, N. Goel, K. W. Choi, W. Tsai and S. Sayan, Appl. Phys. Lett 93, 0821051 (2008).

[5] M. Thirumoorthi and J. T. J. Prakash, J. Asian. Ceramic. Soc 4, 124 (2016).

[6] Z. Y. Banyamin, P. J. Kelly, G. West and J. Boardman, Coatings 4, 732 (2014).

[7] F. I. Ezema, M. N. Nnabuchi and R. U. Osuji, Trends. Appl. Sci. Res 1, 467 (2006).

[8] P. P. Hankare, P. A. Chate and D. J. Sathe, Solid. State. Sci 11, 1226 (2009).

[9] N. Barreau, J. C. Bernede, S. Marsillac and A. Mokrani, J. Cryst. Growth 235, 439 (2002).

[10] M. V. Yakushev, A. V. Mudryi, I.V. Victorov, J. Krustok and E. Mellikov, Appl. Phys. Lett 88, 0119221 (2006).

[11] W. Xinkun, L. Wei, C. Shuying, L. Yunfeng and J. Hongjie, J. Semicond 33, 0220021 (2012).

[12] R. Indirajith, M. Rajalakshmi, R. Gopalakrishnan and K. Ramamurthi, Ferroelectrics 413, 108 (2011).

[13] R. I. Chowdhury, M. S. Islam, F. Sabeth, G. Mustafa, S. F. U. Farhad, D. K. Saha, F.A. Chowdhury, S. Hussain and A.B. M. O. Islam, Dhaka. Univ. J. Sci 60, 137 (2012).

[14] S. Venkatachalam, Y. L. Jeyachandran, P. Sureshkumar, A. Dhayalraj, D. Mangalaraj, S. K. Narayandass and S. Velumani, Mater. Charact 58, 794 (2007).

[15] N. M. Shah, C. J. Panchal, V. A. Kheraj, J. R. Ray and M. S. Desai, Sol. Energy 83, 753 (2009).

[16] T. Yamaguchi, K. Tsujita, S. Niiyama and T. Imanishi, Adv. Mater. Phys. Chem 2, 106 (2012).

[17] J. Dheepa, R. Sathyamoorthy and A. Subbarayan, J. Cryst. Growth 274, 100 (2005).

[18] J. P. Enriquez, N. R. Mathews, G. P. Hernandez and X. Mathew, Mater. Chem. Phys 142, 432 (2013).

[19] L. Kungumadevi and R. Sathyamoorthy, Adv. Cond. Mater. Phys 763209, 1 (2012).

[20] B. R. Kumar and T. S. Rao, Chalcogenide. Lett 8, 83 (2011).

[21] K. R. Murali, P. Muthusamy and A. Panneerselvam, J. Mater. Sci. Mater. Electron 24, 3412 (2013).

[22] A. L. Donne, A. Scaccabarozzi, S. Tombolato, S. Marchionna, P. Garattini, B. Vodopivec, M. Acciarri and S. Binetti, Int. Scholar. Res. Notices. Renew. Energy 830731, 1 (2013).

[23] R. Saraf, Int. Org. Sci. Res. J. Elec. Electron. Eng 2, 47 (2012).

[24] D. H. Yeon, S. M. Lee, Y. H. Jo, J. Moon and Y. S. Cho, J. Mater. Chem. A 2, 20112 (2014).

[25] T. Ikuno, R. Suzuki, K. Kitazumi, N. Takahashi, N. Kato and K. Higuchi, Appl. Phys. Lett 102, 1939011 (2013).

[26] J. E. Garcia, D. Becerra, M. T. S. Nair and P. K. Nair, Thin Solid Films 569, 28 (2014).

[27] W. S. Chen, J. M. Stewart and R. A. Mickelsen, Appl. Phys. Lett 46, 1095 (1985).

[28] J. E. Garcia, E. B. Salgado, M. T. S. Nair and P. K. Nair, Proc. Mater. Res. Soc 1670, 1 (2014).

[29] K. Yamada, N. Hoshino and T. Nakada, Sci. Technol. Adv. Mater 7, 42 (2006).

[30] R. Tang, Z. Wang, W. Li, L. Feng, J. Zhang, L. Wu, B. Li, G. Zeng and W. Wang, Sol. Energy. Mater. Sol. Cells 121, 92 (2014).

[31] R. Scheer and H. W. Schock, Chalcogenide photovoltaics: Physics, technologies and thin film devices (Wiley, USA, 2011), pp. 1-2.

[32] M. Hosenuzzaman, N. A. Rahim, J. Selvaraj, M. Hasanuzzaman, A. B. M. A. Malek and A. Nahar, Renewable. Sustainable. Energy. Rev 41, 284 (2015).

[33] J. R. Szczech, J.M. Higgins and S. Jin, J. Mater. Chem 21, 4037 (2011).

[34] T. M. Tritt and M. A. Subramanian, Mater. Res. Soc. Bulletin 31, 188 (2006).

[35] M. K. S. Bhutta, A. Omar and X. Yang, Economic. Res. Int 474230, 1 (2011).

[36] Y. Pei, X. Shi, A. Lalonde, H. Wang, L. Chen and G. J. Snyder, Nature 473, 66 (2011).

[37] J. Yang and F. R. Stabler, J. Electron. Mater 38, 1245 (2009).

[38] T. K. Reynolds, J. G. Bales, R. F. Kelley and F. J. DiSalvo, Chemistry, physics and materials science of thermoelectric materials: Beyond bismuth telluride, ed. by M. G. Kanatzidis, S. D. Mahanti and T. P. Hogan (Springer, Berlin, 2003), pp. 19-34.

[39] Z. H. Dughaish, Physica B 322, 205 (2002).

[40] Y. Lan, A. J. Minnich, G. Chen and Z. Ren, Adv. Funct. Mater 20, 357 (2010).

[41] L. M. Goncalves, C. Couto, P. Alpuim, D. M. Rowe and J. H. Correia, Mater. Sci. Forum 514-516, 156 (2006).

[42] O. Yamashita, S. Tomiyoshi and K. Makita, J. Appl. Phys 93, 368 (2003).

[43] J. Tan, K. Kalantarzadeh, W. Wlodarski, S. Bhargava, D. Akolekar, A. Holland and G. Rosengarten, Proc. Int. Soc. Optics. Photonics 5836, 711 (2005).

[44] L. M. Goncalves, C. Couto, P. Alpuim, A. G. Rolo, F. Volklein and J. H. Correia, Thin Solid Films 518, 2816 (2010).

[45] G. Zhou and D. Wang, Sci. Report 5, 1 (2015).

[46] P. K. Rawat, B. Paul and P. Banerji, Mater. Process. Energy 1, 840 (2013).

[47] Y. Pei, A. LaLonde, S. Iwanaga and G. J. Snyder, Energy Environ. Sci 4, 2085 (2011).

[48] K. Biswas, J. He, I. D. Blum, C. I. Wu, T. P. Hogan, D. N. Seidman, V. P. Dravid and M. G. Kanatzidis, Nature 489, 414 (2012).

[49] J. Martin, L. Wang, L. Chen and G. S. Nolas, Phys. Rev B 79, 1153111 (2009).

[50] S. S. Patil and P. H. Pawar, Chalcogenide Lett 9, 133 (2012).

[51] Y. Pei, H. Wang, Z. M. Gibbs, A. D. LaLonde and G. J. Snyder, Nature. Public. Group. Asia. Mater 4, 1 (2012).

[52] M. Zhou, J. F. Li and T. Kita, J. American. Chem. Soc 130, 4527 (2008).

[53] O. Madelung, Semiconductors data handbook (Springer, Berlin, 2004), pp. 567- 568.

[54] A. Banik, U. S. Shenoy, S. Anand, U.V. Waghmare and K. Biswas, Chem. Mater 27, 581 (2015).

[55] L. Xu, H. Q. Wang and J. C. Zheng, J. Electron. Mater 40, 641 (2011).

[56] V. A. Ivanov, V. F. Gremenok, H. G. Seidi, S. P. Zimin and E. S. Gorlachev, Nanosys. Phy. Chem. Math 4, 816 (2013).

[57] G. Tan, L. D. Zhao, F. Shi, J. W. Doak, S. H. Lo, H. Sun, C. Wolverton, V. P. Dravid, C. Uher and M. G. Kanatzidis, J. American. Chem. Soc 136, 7006 (2014).

[58] Q. Zhang, B. Liao, Y. Lan, K. Lukas, W. Liu, K. Esfarjani, C. Opeil, D. Broido, G. Chen and Z. Ren, Proc. Nat. Acad. Sci 110, 13261 (2013).

[59] G. Tan, F. Shi, S. Hao, H. Chi, L.D. Zhao, C. Uher, C. Wolverton, V. P. Dravid and M. G. Kanatzidis, J. American. Chem. Soc 137, 5100 (2015).

[60] M. Zhou, Z. M. Gibbs, H. Wang, Y. Han, C. Xin, L. Li and G. J. Snyder, Phys. Chem. Chem. Phys 16, 20741 (2014).

[61] K. Neyvasagam, N. Soundararajan, A. Soni, G. S. Okram and V. Ganesan, Phys. Status Solidi B 245, 77 (2008).

[62] K. Kurosaki, K. Goto, A. Kosuga, H. Muta and S. Yamanaka, Mater. Trans 47, 1432 (2006).

[63] V. M. Sklyarchuk and Y. O. Plevachuk, Semiconductors 36, 1123 (2002).

[64] S. Ballikaya, H. Chi, J. R. Salvador and C. Uher, J. Mater. Chem. A 1, 12478 (2013).

[65] Z. Ye, J. Y. Cho, M. M. Tessema, J. R. Salvador, R. A. Waldo, H. Wang and W. Cai, J. Solid. State. Chem 201, 262 (2013).

[66] Z. Zhang, Y. Wu, H. Zhang, Z. Zeng and Z. Hu, J. Mater. Sci. Mater. Electron 26, 1619 (2015).

[67] B. Fang, Z. Zeng, X. Yan and Z. Hu, J. Mater. Sci. Mater. Electron 24, 1105 (2013).

[68] Z. Aabdin, N. Peranio, M. Winkler, D. Bessas, J. Konig, R. P. Hermann, H. Bottner and O. Eibl, J. Electron. Mater 41, 1493 (2012).

[69] M. K. Han, J. Androulakis, S. J. Kim and M. G. Kanatzidis, Adv. Energy. Mater 2, 157 (2012).

[70] W. Liu, C. F. Guo, M. Yao, Y. Lan, H. Zhang, Q. Zhang, S. Chen, C. P. Opeil and Z. Ren, Nano Energy 4, 113 (2014).

[71] Y. M. Han, J. Zhao, M. Zhou, X. X. Jiang, H. Q. Leng and L. F. Li, J. Mater. Chem A 3, 4555 (2015).

[72] L. Zhao, X. Wang, F. Y. Fei, J. Wang, Z. Cheng, S. Dou, J. Wang and G.J. Snyder, J. Mater. Chem A 3, 9432 (2015).

[73] L. J. Zhang, B. P. Zhang, Z. H. Ge, C. G. Han, N. Chen and J. F. Li, Intermetallics 36, 96 (2013).

[74] K. Kadel, L. Kumari, W. Z. Li, J. Y. Huang and P. P. Provencio, Nanoscale. Res. Lett 6, 57 (2011).

[75] H. Wang, W. Chu, D. Wang, W. Mao, W. Pan, Y. Guo, Y. Xiong and H. Jin, J. Elec. Mater 40, 624 (2011).

[76] H. Liu, X. Shi, F. Xu, L. Zhang, W. Zhang, L. Chen, Q. Li, C. Uher, T. Day and G. J. Snyder, Nature. Mater 11, 422 (2012).

[77] L. D. Zhao, S. H. Lo, Y. Zhang, H. Sun, G. Tan, C. Uher, C. Wolverton, V. P. Dravid and M. G. Kanatzidis, Nature 508, 373 (2014).

[78] J. F. Li, W. S. Liu, L. D. Zhao and M. Zhou, Nature. Publishing. Group. Asia. Mater 2, 152 (2010).

[79] Z. G. Chen, G. Han, L. Yang, L. Cheng and J. Zou, Prog. Nat. Sci. Mater. Int 22, 535 (2012).

[80] C. Han, Z. Li and S. Dou, Chinese. Sci. Bulletin 59, 2073 (2014).

[81] R. Venkatasubramanian, E. Siivola, T. Colpitts and B. O. Quinn, Nature 413, 597 (2001).

Chapter 2

Semiconductor Principles

2.1 Introduction

Semiconductors are an integral part of today's leading technology. The history of research on semiconductors is a long one, extending over more than a century. The products found on the basis of semiconductor devices such as computers, communication systems, displays, lasers and LEDs has become a part of our day to day life. Thus fundamental research on semiconductor physics and devices is vital for the development of modern society.

This chapter highlights a few important theoretical and experimental concepts on semiconductors that are relevant to the proposed work. This includes: an overview, salient properties and applications of semiconductors, theories related to energy band structure, classification of semiconductors, evaluation of charge carrier concentration and position of Fermi level, optical properties with special emphasis on absorption process, photoconductivity and

photoluminescence, electrical properties with special focus on the fundamental charge carrier transport parameters, Hall effect and thermoelectric effect.

2.2 Semiconductors: Overview and Applications

The first semiconductor effect was observed in Ag_2S by Michael Faraday in 1833 where he noticed a decrease in the resistance of Ag_2S with increase in temperature, a behaviour different from that of a conductor. Later, rectifying effect was realized in PbS by F. Braun in 1873, photoconducting effect was observed in Se by W. Smith in 1874 and Hall effect was detected in thin sheets of conducting or semiconducting materials by E.H. Hall in 1879 [1]. After these major breakthroughs, semiconductors were introduced as an interesting class of compounds in basic and applied solid state research. Semiconductors are defined as materials whose electrical properties are intermediate between those of metals and insulators, or alternately, defined as materials with band gap less than 3 eV. Materials with zero band gap are metals and that with band gap greater than 3 eV are insulators. But the frequent use of terms such as semiconducting diamond (band gap 6 eV) and semi insulating GaAs (band gap 1.5 eV) are exceptions to these definitions [2].

Semiconductors exist in a variety of crystal structures with different chemical compositions. Some of the better known semiconductors are: Elemental semiconductors (Si, Ge, P, Se, Te and carbon in the form of C_{60} or nanotubes), semiconductors comprising binary (GaAs, InP, CdS), ternary ($CuAlO_2$, $CuInSe_2$, BiSbTe) and quaternary (Cu_2ZnSnS_4, $CuInGaSe_2$, $AgInGaSe_2$) compounds and alloys, organic semiconductors (polyacetylene, poly diacetylene), magnetic semiconductors (EuS and CdMnTe), layered

semiconductors (PbI_2, MoS_2, GaSe), amorphous semiconductors (a-Si:H), liquid semiconductors (mixtures of As, Se and Te) and crystalline solids such as single crystals of Si [2].

In addition to the aforesaid semiconductors, there exist several other semiconductors that show attractive properties. For example, SbSI and $AgGaS_2$ are interesting semiconductors that exhibit low temperature ferroelectric properties and non linear optical properties respectively. The well known $CuInSe_2$ crystallizes in chalcopyrite structure and As_2Se_3 is a semiconductor in both the crystalline and glassy states. La_2CuO_4 is a semiconductor but it becomes a superconductor when alloyed with Sr to form $(LaSr)_2CuO_4$ [2]. Thus semiconductors are by no means simple and have some rather subtle properties.

Some of the salient properties of a semiconductor are as follows [1]

- Resistivity in the range 10^{-3} Ω cm to 10^{8} Ω cm which is in between to that of a conductor (10^{-8} Ω cm to 10^{-6} Ω cm) and insulator (10^{14} Ω cm to 10^{22} Ω cm).

- Negative temperature coefficient of resistance which means that resistance decreases with increase in temperature resulting in an increase in electrical conductivity.

- High Seebeck coefficient, both positive and negative relative to a given metal and high thermoelectric figure of merit.

- Sensitivity to light - producing photoelectric effects.

- Develops Hall voltage on passing current in the presence of a magnetic field applied in a perpendicular direction.

- Exhibits an optical band gap between 0 eV and 3 eV which is small compared to that of insulators (6 eV). This property determines the wavelength of radiation which can be emitted or absorbed by the semiconductor and hence helps to construct devices such as LEDs and lasers.

- To meet specific applications, optical band gap of a semiconductor can be tuned by adding impurities into the lattice which is often referred to as doping.

Today semiconductors are the foundation of modern electronics, medical research and space exploration. Semiconductors are successfully being applied in rectifiers, LEDs, photoconductors, high speed computer chips, calculators, telephones, transistors, thyristors, integrated circuits, robotics, photodiodes, lasers, solar cells, thermoelectric modules, electrical power systems, amplifiers, oscillators, radiation detectors and image sensors for aerospace and defence applications,. In medical science research, semiconductors are extensively investigated for their use in monitoring, imaging and instrumentation systems [3]. Thus semiconductor science and technology is a rapidly growing as well as an ongoing area of research that can open up new ventures in various fields of science and technology in terms of performance and productivity.

2.3 Energy band structure

The understanding of the behaviour of electrons in solids is one of the keys to understand materials. During the past hundred years, three approaches have been developed to explain the electronic properties of materials. First one

is the continuum theory, which considered only the macroscopic properties and interrelated experimental data. Later Paul Drude proposed the classical free electron theory, according to which free electrons in metal, drift as a response to an external force and interacts with certain lattice atoms. This theory explained Ohm's law, electrical conductivity, thermal conductivity, optical properties, malleability and ductility of metals but was inadequate to explain certain phenomena such as electronic specific heat, electrical conductivity of semiconductors and insulators, paramagnetic susceptibility, ferromagnetism, photoelectric effect, Compton effect and black body radiation [1].

Therefore, a further refinement in understanding the properties of materials was accomplished by the use of quantum theory. The first application of quantum mechanics to the motion of electrons in solids was the treatment of the electrical conduction mechanism in metals by A. Sommerfeld. The only difference between this and the earlier theories, based on the classical theory of electrons, was that the energy levels which the various electrons can occupy are determined by wave mechanics [1]. According to Sommerfeld's quantum free electron theory, the valence electrons of the constituent atoms are free to move in a field free space, throughout the volume of the specimen, except at the boundary of the solid as shown in Fig 2.1.

Fig 2.1 Sommerfeld model for potential energy V(x) of electrons in a crystalline solid

The potential energy due to the field of all nuclei and all other electrons is assumed to be a constant everywhere inside the metal except at the boundary of the solid. The energy of the free electron as a function of wave vector is given by

$$E = \frac{\hbar^2 k^2}{2m} \tag{2.1}$$

where k is the wave vector given by

$$k = \frac{p}{\hbar} = \frac{2\pi}{\lambda} \tag{2.2}$$

where λ is the wavelength associated with the free electron and p is the momentum. In this theory, the allowed energy levels for the valence electrons lie very close together and their values extend from nearly the bottom of the potential trough in which the electron move to indefinitely high values; i.e., the energy spectrum is quasi continuous as shown in Fig 2.2, whereas for the other electrons the energy levels are assumed to be undisturbed and are just the atomic energy levels [4].

The Sommerfeld theory explains successfully the phenomena of specific heat, electrical conductivity, thermionic emission, thermal conductivity and paramagnetism. But it could not explain why some solids are good conductors of electricity, some are semiconductors and some others are insulators.

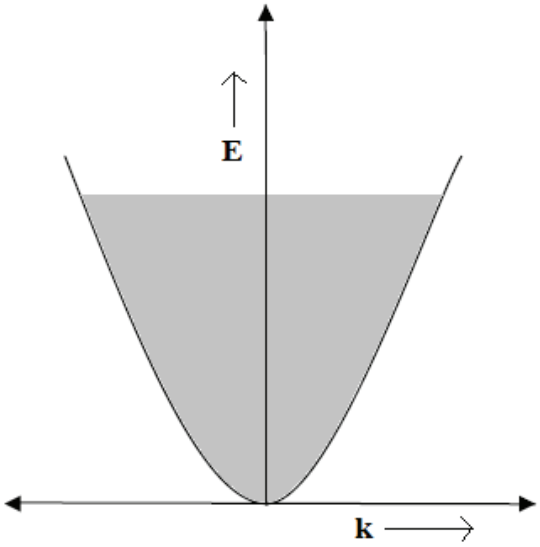

Fig 2.2 Energy (E) versus wave vector (k) for a free electron

Later, a much more defined theory, known as Bloch theory was discussed by F. Bloch to describe the motion of electrons in crystalline solids [1]. According to which, the electrons are no longer free instead they undergo frequent collisions with atomic nuclei. In such a case, the concept of a constant potential in the interior of the solid is replaced by a periodic potential with periodicity same as that of the concerned lattice. It is schematically represented in Fig 2.3.

Fig 2.3 Periodic potential V(x) due to atomic core in a crystalline solid

The motion of the electron through periodic potential is solved by reducing the problem to one body problem by using the following assumptions [1]

- The nuclei at the lattice sites are perfectly at rest. The interaction between the electrons and phonons are thus neglected.

- Interactions between the electrons are ignored. Every electron is in a potential field, which is due to the positive nuclei and an averaged charge distribution of the other electrons. The strong fields of nuclei are thus more or less screened by the electrons.

The conclusions derived by considering the motion of an electron in a periodic potential are:

- The energy spectrum of an electron in a periodic potential is discontinuous and it consists of a number of allowed energy bands separated by forbidden regions in which no energy levels are allowed.

- The energy E is a periodic function in the wave vector k.

The E – k variation on the basis of band theory of solids is given in Fig 2.4. The discontinuities in the curve occur at $k = \frac{n\pi}{a}$, where a is the lattice constant and n = ±1, ±2, ±3 etc..... Except for these k values, the electrons in a crystal behave like free electrons. These k values define the boundaries of first, second, third, etc.....brillouin zones [4].

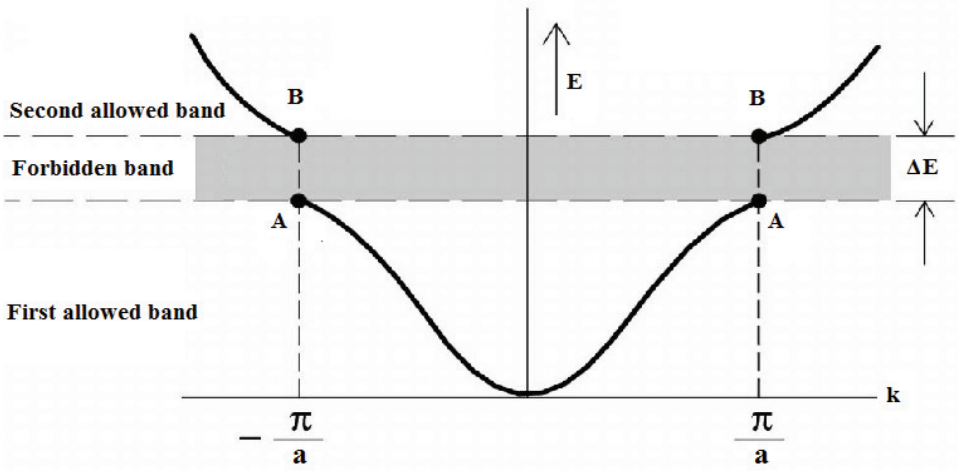

Fig 2.4 E-k variation on the basis of band theory of solids

Fig 2.5 shows the energy band for an insulator, say diamond which is a crystalline form of carbon with bonding same as that of Si and Ge. The energy levels are plotted as a function of the interatomic distance (a).

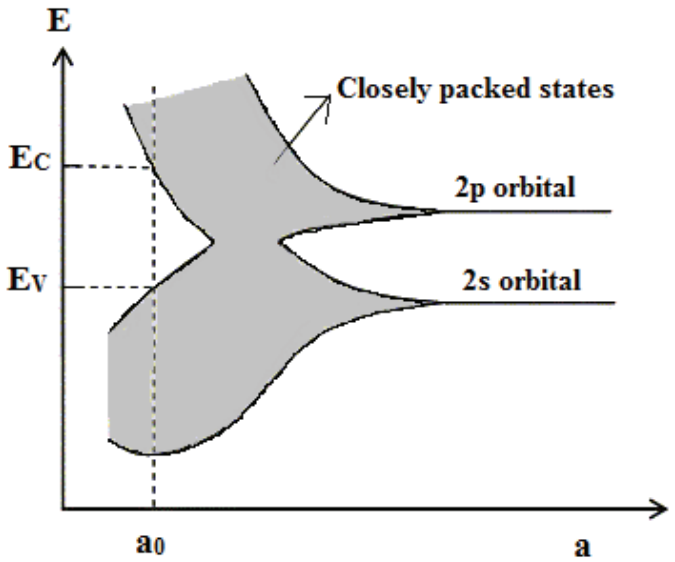

Fig 2.5 Energy band for diamond versus interatomic distance

The isolated, free carbon atoms contain six electrons, which occupy the 1s, 2s and 2p orbitals in pairs. Fig 2.5 indicates only the energy of an electron occupying the 2s and 2p orbital. As the interatomic distance (a) is reduced, there is an overlap of the electron wave functions occupying the adjacent atoms. This leads to a splitting of the energy levels consistent with the Pauli exclusion principle. The splitting results in an energy band containing 2N states in the 2s band and 6N states in the 2p band, where N is the number of atoms in the crystal. As the interatomic distance is further reduced, the 2s and 2p energy bands merge and split again into two bands containing 4N states each. At the equilibrium interatomic distance (a_0), the two bands are widely separated. The lower band which is completely filled with electrons is termed as the valence band. The upper band which is empty is termed as the conduction band. The separation between the uppermost filled level (i.e. valence level E_V) and the first empty level above the valence band (i.e. conduction level E_C) is termed as band gap (E_g) [5]. According to the band theory of solids, the presence of a forbidden band or energy gap is the main difference in the electronic structure of conductors, semiconductors and insulators.

2.4 Classification of solids

On the basis of energy bands, the solids can be classified as follows [5]

- **Conductors:** In a conductor (Cu, Ag), the conduction band is either partially filled or the valence band overlaps with the conduction band. So there is no band gap. Thus the electrons and vacant energy states are intermixed within the bands so that the electrons move freely within the conduction band under the influence of an electric field. Hence the conductors have high electrical conductivity (10^8 Scm^{-1} to 10^6 Scm^{-1}).

- **Semiconductors:** In a semiconductor (Si and Ge), at absolute zero of temperature, the valence band is completely filled and the conduction band is absolutely empty. So the semiconductors behave as an insulator at very low temperature. But as the temperature is increased the valence electrons crosses over to the conduction band and the electrical conductivity increases. The electrical conductivity of semiconductors lies between 10^{-8} Scm^{-1} to 10^{3} Scm^{-1}. Semiconductors have a much smaller band gap less than or equal to 3 eV.

- **Insulators:** In an insulator (Diamond), at absolute zero of temperature, the valence band is completely filled and the conduction band is absolutely empty. The electrical conductivity of insulators lies between 10^{-14} Scm^{-1} to 10^{-22} Scm^{-1}. The insulators are characterized by a large band gap greater than 3 eV. These materials do not allow the flow of current through them. Fig 2.6 represents the energy band structure of (a) Conductor (b) Semiconductor and (c) Insulator.

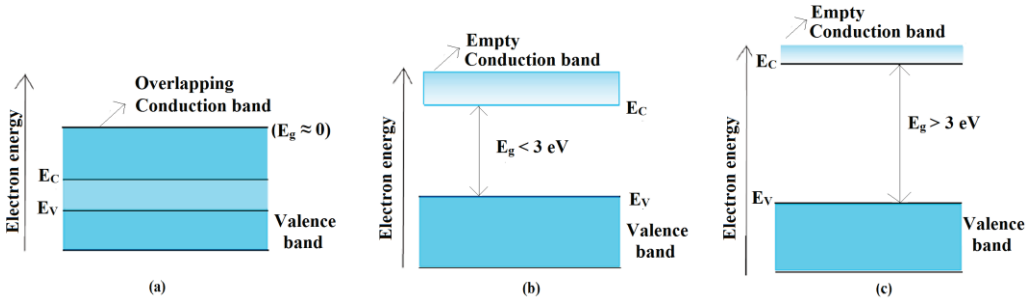

Fig 2.6 Energy band structure of (a) Conductor (b) Semiconductor and (c) Insulator

2.5 Classification of semiconductors

The importance of semiconductors is that the conductivity and band gap of these materials can be modified by the introduction of impurities which strongly affect their electrical and optical properties. The process of adding impurities in semiconductors in a precisely controlled manner is termed as doping [6]. Depending on the nature of impurities added, the semiconductors are classified as intrinsic semiconductor and extrinsic semiconductor.

2.6 Intrinsic semiconductor

The intrinsic semiconductors are pure or undoped semiconductors whose electrical conductivity is solely determined by thermally generated charge carriers [6]. Examples: Si, Ge, GaP, GaAs, InSb, etc. The bonding in Si atoms and the energy level diagram of an intrinsic semiconductor is shown in Fig 2.7 and Fig 2.8 respectively.

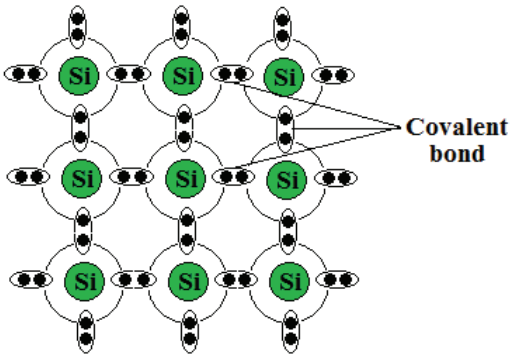

Fig 2.7 2D representation of a pure Si crystal

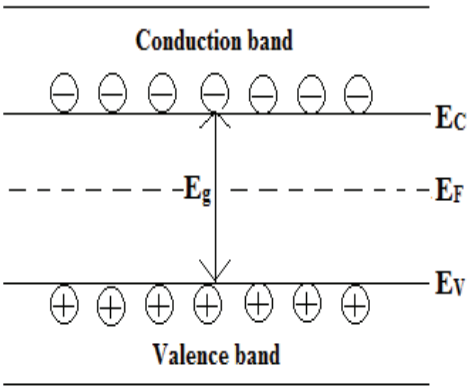

Fig 2.8 Energy level diagram of an intrinsic semiconductor

It is clear from Fig 2.7 that all the four valence electrons of each of the Si atoms form four covalent bonds with neighbouring four Si atoms. As a result no electron is free to cause conduction at 0 K. Hence pure Si is an insulator at 0 K. But as the temperature increases above 0 K, valence electrons get sufficient thermal energy to break away their covalent bonds, generating electron-hole pairs. These electrons and holes move in opposite directions under the influence of an external electric field and constitutes current [6].

At 0 K, the intrinsic semiconductor behaves as an insulator, because at 0 K the valence band is completely filled and the conduction band is completely empty. As temperature increases, electrons in valence band get sufficient thermal energy to jump to conduction band leaving behind an equal number of holes in valence band as shown in Fig 2.8. Thus electrons in conduction band and holes in valence band behave as free charge carriers and increase the conductivity of the material. The Fermi level (E_F) lies in the middle of the band gap (E_g) [6].

2.6.1 Variation of electrical conductivity with temperature

Conductivity due to holes in valence band is given by $\sigma_p = pe\mu_p$ (2.3)

Conductivity due to electrons in conduction band is given by $\sigma_n = ne\mu_n$ (2.4)

Total conductivity is given by $\sigma = e\left(n\mu_n + p\mu_p\right)$ (2.5)

where p and n denote the number of holes in valence band and number of electrons in conduction band respectively. μ_p and μ_n are the mobility of hole and electron respectively. For an intrinsic semiconductor, $n = p = n_i$ where n_i is the intrinsic charge carrier concentration.

Therefore Eq (2.5) becomes $\sigma = en_i(\mu_n + \mu_p)$ (2.6)

Assuming mobilities to be independent of temperature, temperature dependence of conductivity arises due to the variation of n_i with temperature, where

$$n_i = \frac{2(2\pi K_B T)^{3/2}}{h^3}(m_n^* m_p^*)^{3/4} \exp\left(-\frac{E_g}{2K_B T}\right) \quad (2.7)$$

where m_p^* and m_n^* are the effective mass of hole and electron respectively, E_g is the band gap, K_B is the Boltzmann constant, h is the Plank's constant and T is the absolute temperature.

Using Eq (2.7) in Eq (2.6) gives

$$\sigma = e(\mu_n + \mu_p)\frac{2(2\pi K_B T)^{3/2}}{h^3}(m_n^* m_p^*)^{3/4} \exp\left(-\frac{E_g}{2K_B T}\right) \quad (2.8)$$

Thus the final expression for the variation of electrical conductivity with temperature is

$$\ln\sigma = \left(-\frac{E_g}{2K_B}\right)\frac{1}{T} + \frac{3}{2}\ln T + \text{ Constant} \quad (2.9)$$

The plot of $\ln\sigma$ versus 1/T is a straight line whose slope gives an estimate of band gap of the semiconductor [6].

2.6.2 Hole concentration in valence band

The number of holes in the energy range E and E+ dE is

$$dp = D(E)[1 - f(E)]dE \quad (2.10)$$

The density of states D(E) of holes is given by

$$D(E) = \frac{4\pi}{h^3}\left(2m_p^*\right)^{3/2}\left(E_V - E\right)^{1/2} \tag{2.11}$$

Probability of finding a hole in the energy state E, assuming $E < E_F$, is given by

$$1 - f(E) \approx \exp\left(\frac{E - E_F}{K_B T}\right) \tag{2.12}$$

Using Eq (2.11) and Eq (2.12) in Eq (2.10), we get

$$dp = \frac{4\pi}{h^3}\left(2m_p^*\right)^{3/2}\left(E_V - E\right)^{1/2} \exp\left(\frac{E - E_F}{K_B T}\right) dE \tag{2.13}$$

On integrating Eq (2.13) from $E = -\infty$ to $E = E_V$ and on further simplification, we get the hole concentration in valence band as [6]

$$p = N_V \exp\left[-\left(\frac{E_F - E_V}{K_B T}\right)\right] \tag{2.14}$$

where N_V represents the effective density of states of holes at valence band edge and is given by

$$N_V = 2\left(\frac{2\pi m_p^* K_B T}{h^2}\right)^{3/2} \tag{2.15}$$

2.6.3 Electron concentration in conduction band

The number of free electrons in the energy range E and E+ dE is

$$dn = D(E) f(E) dE \tag{2.16}$$

The density of states D(E) of electrons is given by

$$D(E) = \frac{4\pi}{h^3}\left(2m_n^*\right)^{3/2} E^{1/2} \tag{2.17}$$

and f(E) is the Fermi distribution function given by

$$f(E) = \frac{1}{\exp\left(\frac{E - E_F}{K_B T}\right) + 1} \tag{2.18}$$

Therefore, using Eq (2.17) and Eq (2.18) in Eq (2.16) gives

$$dn = \frac{4\pi}{h^3}\left(2m_n^*\right)^{3/2}\left(E - E_c\right)^{1/2} \frac{1}{\exp\left(\frac{E - E_F}{K_B T}\right) + 1} dE \tag{2.19}$$

On integrating Eq (2.19) from $E = E_C$ to $E = \infty$ for energies greater than E_C and on further simplification, we get the electron concentration in conduction band as [6]

$$n = N_C \exp\left[-\left(\frac{E_C - E_F}{K_B T}\right)\right] \tag{2.20}$$

where N_C represents the effective density of states of electrons at conduction band edge and is given by

$$N_C = 2\left(\frac{2\pi m_n^* K_B T}{h^2}\right)^{3/2} \tag{2.21}$$

2.6.4 Position of Fermi level

For an intrinsic semiconductor, $n = p = n_i$

Therefore from Eq (2.14) and Eq (2.20), we get

$$N_V \exp\left[-\left(\frac{E_F - E_V}{K_B T}\right)\right] = N_C \exp\left[-\left(\frac{E_C - E_F}{K_B T}\right)\right] \quad (2.22)$$

On simplification Eq (2.22) gives the position of Fermi level E_F as

$$E_F = \frac{E_C + E_V}{2} + \frac{K_B T}{2} \ln\left(\frac{N_V}{N_C}\right) \quad (2.23)$$

Using Eq (2.15) and Eq (2.21) in Eq (2.23), we get

$$E_F = \frac{E_C + E_V}{2} + \frac{3}{4} K_B T \ln\left(\frac{m_p^*}{m_n^*}\right) \quad (2.24)$$

At 0 K,

$$E_F = \frac{E_C + E_V}{2} \quad (2.25)$$

i.e., Fermi level lies in the middle of conduction band and valence band. This is true at all the other temperatures provided $m_p^* = m_n^*$. However, in general $m_p^* > m_n^*$ and the Fermi level is slightly raised as temperature exceeds 0 K [6].

2.7 Extrinsic semiconductor

The extrinsic semiconductors are impurity or doped semiconductors in which suitable impurity atoms called dopants are added so as to modify its electrical and optical properties. The impurity atoms frequently used to dope pure Si or Ge are the elements of group III and group V of the periodic table. The dopants are added in the ratio of 1 in 10^6 atoms to 1 in 10^8 atoms of the semiconducting material [6]. Such small quantities of dopants can greatly

affect the electrical conductivity. Depending on the type of impurity added, extrinsic semiconductors are classified as p-type semiconductor and n-type semiconductor.

2.7.1 p-type semiconductor

Consider a trivalent impurity atom, say boron in a Si crystal as shown in Fig 2.9. If such an impurity atom is introduced into Si, it forms three covalent bonds with the neighbouring three Si atoms while the fourth bond is not completed due to the deficiency of one electron. Thus the trivalent impurity atom has a tendency to accept one electron from a neighbouring Si atom to form the fourth covalent bond. Due to thermal agitation, an electron in the neighbouring Si atom gets transferred to complete the fourth bond. This process leaves behind a hole on the Si atom as shown in Fig 2.9. The hole thus generated acts as the current carrier. Thus each trivalent impurity atom can accept an electron from a neighbouring Si atom to produce a hole in the semiconductor. Therefore such impurities are known as acceptors or p-type impurities and the semiconductor containing such impurity atoms is known as a p-type semiconductor. In these semiconductors, holes are the majority charge carriers and the thermally generated electrons are the minority charge carriers [6]. The conductivity of a p-type semiconductor is given by $\sigma_p = pe\mu_p$. Examples: Cu_2O, Cu_2S and CdSe.

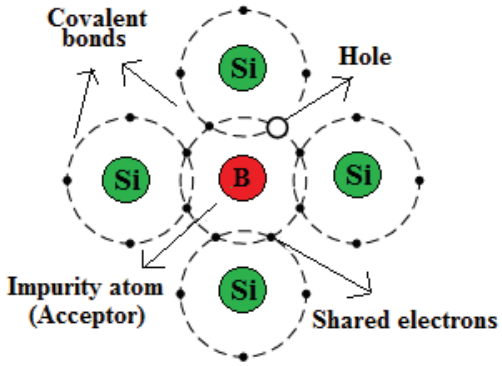

Fig 2.9 Trivalent impurity atom boron (B) in a Si crystal

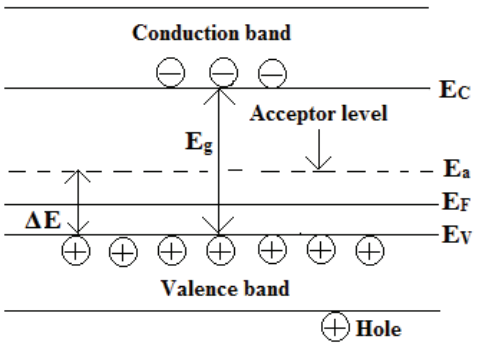

Fig 2.10 Energy level diagram of a p-type semiconductor

The energy level diagram of a p-type semiconductor is shown in Fig 2.10. The acceptor impurity atoms occupy the acceptor level E_a which lie above the valence band. An electron can be easily transferred from valence band to E_a by providing a small amount of energy called activation energy ΔE (0.046 eV to 0.16 eV for Si and 0.01 eV for Ge). This creates a hole in valence band which acts as the charge carrier. For T > 0 K, a part of the acceptors is ionized by acquiring electrons from valence band, thus creating holes in valence band which cause p-type conduction [6]. Let p, n, N_a^- represent hole concentration in valence band, electron concentration in conduction band and concentration of ionized acceptors respectively, then $p \approx n + N_a^-$. Neglecting n in comparison with N_a^-, we get

$$p \approx N_a^- \tag{2.26}$$

where

$$p = N_V \exp\left[-\left(\frac{E_F - E_V}{K_B T}\right)\right] \tag{2.27}$$

and $$N_a^- = N_a \exp\left[\left(\frac{E_F - E_a}{K_B T}\right)\right] \quad (2.28)$$

Using Eq (2.27) and Eq (2.28) in Eq (2.26), we obtain the position of Fermi level E_F as

$$E_F = \frac{E_a + E_V}{2} - \frac{K_B T}{2} \ln\left(\frac{N_a}{N_V}\right) \quad (2.29)$$

The expression given by Eq (2.29) is valid only at moderate temperatures where n can be neglected. Thus, as shown in Fig 2.10, in a p-type semiconductor, E_F lies near the middle of acceptor level and at the top of valence band at moderate temperatures. Using Eq (2.29) in Eq (2.27), we get p as [6]

$$p = \left(N_a N_V\right)^{1/2} \exp\left(-\frac{\Delta E}{2K_B T}\right) \quad (2.30)$$

where $\Delta E = E_V - E_a$ represent the ionization energy of acceptors.

2.7.2 n-type semiconductor

Consider a pentavalent impurity atom, say antimony in a Si crystal as shown in Fig 2.11. If such an impurity atom is introduced into Si, four of its five valence electrons forms four covalent bonds with the neighbouring four Si atoms while the fifth valence electron remains loosely bound to its nucleus. Due to thermal agitation, this fifth electron gets easily detached from its nucleus and becomes free to conduct as shown in Fig 2.11. This free electron acts as the current carrier. Thus each pentavalent impurity atom donates an electron to Si which enhances the conductivity of pure Si. Therefore such impurities are known as donors or n-type impurities and the semiconductor

containing such impurity atoms is known as an n-type semiconductor. In these semiconductors, electrons are the majority charge carriers and the thermally generated holes are the minority charge carriers [6]. The conductivity of an n-type semiconductor is given by $\sigma_n = ne\mu_n$. Examples: ZnO, CdS and Ag_2Se.

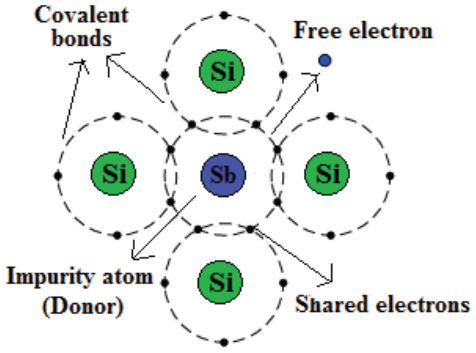

Fig 2.11 Pentavalent impurity atom antimony (Sb) in a Si crystal

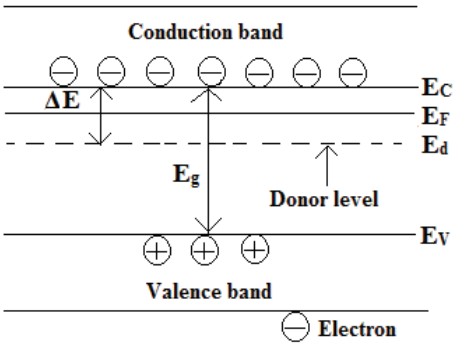

Fig 2.12 Energy level diagram of an n-type semiconductor

The energy level diagram of an n-type semiconductor is shown in Fig 2.12. The donor impurity atoms occupy the donor level E_d which lie below the conduction band. An electron can be easily transferred from E_d to conduction band by providing a small amount of energy called activation energy ΔE (0.03 eV for Si and 0.01 eV for Ge). This electron in the conduction band acts as the current carrier. For $T > 0$ K, a part of the donors is ionized and contribute electrons to conduction band, which cause n-type conduction. Also some of the electrons in valence band may jump to conduction band leaving behind holes in valence band [6]. Let p, n, N_d^+ represent hole concentration in valence band, electron concentration in conduction band and concentration of ionized donors respectively, then $n \approx N_d^+ + p$. Neglecting p in comparison with N_d^+, we get

$$n \approx N_d^+ \tag{2.31}$$

where $$n = N_C \exp\left[-\left(\frac{E_C - E_F}{K_B T}\right)\right] \quad (2.32)$$

and $$N_d^+ = N_d \exp\left[-\left(\frac{E_F - E_d}{K_B T}\right)\right] \quad (2.33)$$

Using Eq (2.32) and Eq (2.33) in Eq (2.31), we obtain the position of Fermi level E_F as

$$E_F = \frac{E_d + E_C}{2} + \frac{K_B T}{2} \ln\left(\frac{N_d}{N_c}\right) \quad (2.34)$$

The Eq (2.34) is valid only at moderate temperatures and not valid for T = 0 K and T→∞. Thus, as shown in Fig 2.12, in an n-type semiconductor, E_F lies near the middle of the donor level and bottom of conduction band at moderate temperatures. Using Eq (2.34) in Eq (2.32), we get n as [6]

$$n = \left(N_d N_C\right)^{1/2} \exp\left(-\frac{\Delta E}{2K_B T}\right) \quad (2.35)$$

where $\Delta E = E_C - E_d$ represent the ionization energy of donors.

2.7.3 Degenerate and non degenerate semiconductor

If the doping level is moderate, then the impurities introduce discrete, non interacting acceptor energy states in p-type material or discrete, non interacting donor energy states in n-type material [7]. Such semiconductors are known as non degenerate semiconductors, whose energy band diagrams and properties are already discussed in the earlier sections.

If the doping level is high (10^{25} atoms m^{-3} to 10^{26} atoms m^{-3}), then the distance between the impurity atoms decrease and they begin to interact with

each other. When this occurs, in the case of a p-type semiconductor, the single discrete acceptor energy level will split into a band of energies. As acceptor concentration increases and becomes comparable to N_V, the band of acceptor state widens and overlaps with the top of valence band. As acceptor concentration exceeds N_V, then the Fermi level E_F lies within valence band. These types of semiconductors are called as p-type degenerate semiconductors. Thus heavy p-type doping (p^+ doped) causes lowering of E_F into valence band, which is depicted in Fig 2.13 (a). Here energy states between valence band and E_F are empty, thus hole concentration in valence band is large [7]. The value of E_F is given by the Joyce-Dixon approximation as [8]

$$E_F = E_V - K_B T\left[\ln\frac{p}{N_V} + \frac{1}{\sqrt{8}}\frac{p}{N_V}\right] \tag{2.36}$$

In the case of an n-type semiconductor, the single discrete donor energy level will split into a band of energies. As donor concentration increases and becomes comparable to N_C, the band of donor state widens and overlaps with the bottom of conduction band. As donor concentration exceeds N_C, then the Fermi level E_F lies within the conduction band. These types of semiconductors are called n-type degenerate semiconductors. Thus heavy n-type doping (n^+ doped) causes E_F to enter into conduction band, which is depicted in Fig 2.13 (b). Here energy states between E_F and conduction band are filled with electrons, thus electron concentration in conduction band is large [7]. The value of E_F is given by the Joyce-Dixon approximation as [8]

$$E_F = E_C + K_B T\left[\ln\frac{n}{N_C} + \frac{1}{\sqrt{8}}\frac{n}{N_C}\right] \tag{2.37}$$

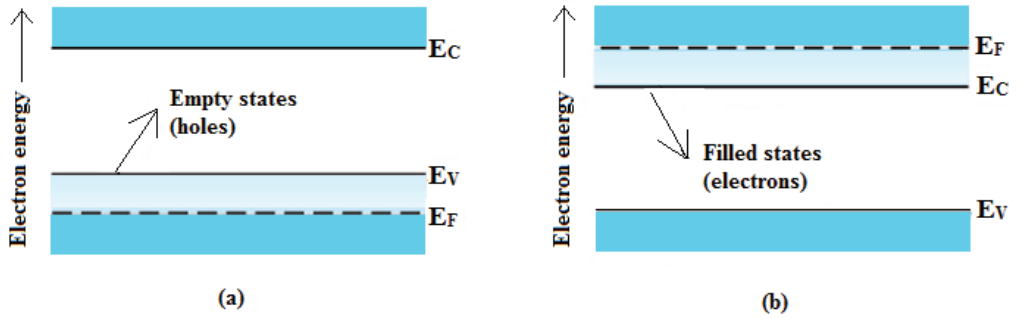

Fig 2.13 Energy band diagram of heavily doped (a) p-type semiconductor and (b) n-type semiconductor

In general degenerate semiconductors are heavily doped semiconductors that cease to show the typical traits of a semiconductor and act more like a metal than as a semiconductor. However, degenerate semiconductor has fewer charge carriers than a true metal so that its behaviour is intermediate between semiconductor and metal. Therefore degenerate semiconductor is also termed as semi metal and finds applications in high power and high frequency devices [6].

2.8 Optical properties: Absorption process

The optical properties of a semiconductor can be defined as any property that involves interaction between electromagnetic radiation and the semiconductor in the region of optical frequencies. The systematic investigations on the optical properties have lead to the development of several optical and optoelectronic devices for laboratory and industrial applications. The optical properties can be divided into electronic properties and lattice properties. The electronic properties concern process involving the electronic states of a solid while the lattice properties involve the vibrations of lattice. As

far as practical applications are concerned, electronic properties receive most attention in semiconductors. Hence, in the present context, only the electronic properties are dealt in detail with special focus on the absorption process. Absorption studies provides a simple means for the evaluation of absorption edge, optical band gap energy, optical transitions which may be direct or indirect, allowed or forbidden and also the nature of the semiconductor thereby providing a wealth of information about the electronic band structure of a semiconductor [4]. In semiconductors, a number of absorption processes takes place independently and they are discussed in the following sections.

2.8.1 Fundamental absorption

Fundamental absorption involves the transition of electrons from valence band to conduction band. It is the most important absorption process and hence referred to as fundamental absorption. The absorption coefficient (α) associated with fundamental absorption is large, about 10^5 cm^{-1}. The absorption coefficient determines how far into a material light of a particular wavelength can penetrate before it is absorbed. It depends on the material and also on the wavelength of light which is being absorbed. Semiconductor materials have a sharp edge in their absorption coefficient, since light which has energy below the band gap does not have sufficient energy to excite an electron into the conduction band from the valence band and hence this light is not absorbed [4].

In fundamental absorption, an electron absorbs a photon from the incident beam and jumps from the valence band into the conduction band. The photon energy must be greater than or equal to the energy gap.

Therefore, the frequency must be

$$\nu \geq \left(\frac{E_g}{h} \right) \tag{2.38}$$

The frequency $\nu_0 = \frac{E_g}{h}$ is referred to as the absorption edge. In the transition process, the total energy and the momentum of the electron-photon system must be conserved. Therefore

$$E_f = E_i + h\nu \tag{2.39}$$

and

$$k_f = k_i + q \tag{2.40}$$

where E_i and E_f are the initial and final energies of the electron in the valence band and conduction band respectively and k_i and k_f are the corresponding electron momenta. The vector q is the wave vector for the absorbed photon. Since the wave vector of a photon in the optical region is negligibly small, the momentum condition reduces to

$$k_f = k_i \tag{2.41}$$

i.e., the momentum of the electron alone is conserved [4]. This selection rule means that only vertical transitions in k-space are allowed between the valence band and conduction band. Such a transition is called direct transition and is represented in Fig 2.14(a).

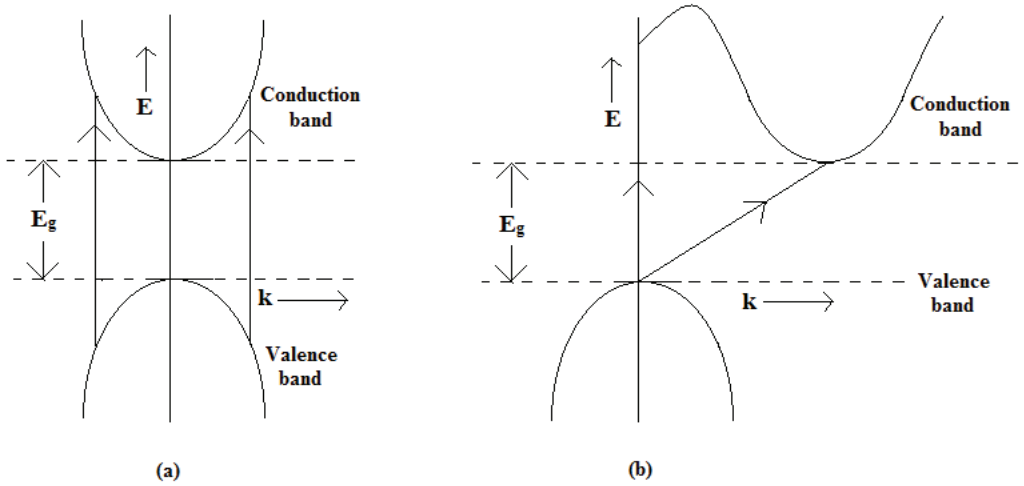

Fig 2.14 Energy band diagram with (a) Direct band gap (b) Indirect band gap

The semiconductors that exhibit direct transitions are called direct band gap semiconductors. Here the bottom of the conduction band lies at k = 0, and hence directly above the top of the valence band [4]. Electrons near the top of the valence band make transitions to states near the bottom of the conduction band, consistent with the selection rule. Direct band gap semiconductors are characterized by high value of α in the relevant energy range for photovoltaics and hence suitable to fabricate thin film solar cells. In these materials, most of the sunlight is absorbed within a small range beneath the surface. Examples: InAs, InSb, GaAs, GaSb, ZnO, CdS, PbSe, CdTe, $CuInSe_2$ and Cu_2ZnSnS_4 [4]. The absorption coefficient (α) in direct allowed transitions is given by [9]

$$\alpha h\nu = A\left(h\nu - E_g\right)^{1/2} \tag{2.42}$$

where A is a constant involving the properties of bands and E_g is the energy band gap. In certain cases, the selection rules forbid direct transitions at k = 0,

but allow them at k ≠ 0. The absorption coefficient for such direct forbidden transition is given by [9]

$$\alpha h\nu = A\left(h\nu - E_g\right)^{3/2} \tag{2.43}$$

There are also indirect transitions, in which the bottom of the conduction band does not lie at the origin. Fig 2.14(b) shows the corresponding energy band diagram. In this case the electron cannot make a direct transition from the top of the valence band to the bottom of the conduction band because this would violate the selection rule ($k_f = k_i$). Such transitions take place by a two step process. The electron absorbs both a photon and a phonon respectively. The photon supplies the required energy while the phonon supplies the required momentum. The semiconductors that exhibit indirect transitions are called indirect band gap semiconductors [4]. These semiconductors are usually not used in thin film solar cells because more material (thick layers) is needed to absorb most of the sunlight and this increases material costs. Examples: Si, Ge, Sn, TiO_2, GaSe, GaP and AlGaP [4]. The absorption process for indirect allowed transition is given by [9]

$$\alpha h\nu = B\left(h\nu - E_g \pm E_p\right)^2 \tag{2.44}$$

where B is a constant containing parameters pertaining to the bands and the temperature and E_p is the phonon energy. The absorption coefficient for indirect forbidden transition is given by [9]

$$\alpha h\nu = B\left(h\nu - E_g \pm E_p\right)^3 \tag{2.45}$$

In the recombination process, an electron in the conduction band annihilates a hole in the valence band, emitting the excess energy as photon in a radiative process. This radiative recombination is possible in a direct band gap semiconductor but not possible in an indirect band gap semiconductor because photons cannot carry crystal momentum thereby violating conservation of crystal momentum. In an indirect band gap semiconductor, radiative recombination occurs only if the process involves the absorption or emission of a phonon, where the phonon momentum equals the difference between the momentum of electron and hole. The involvement of the phonon makes this process much less likely to occur in a given span of time. Hence radiative recombination is slower in indirect band gap materials than direct band gap materials. Therefore LEDs and laser diodes are made of direct band gap semiconductors [10].

2.8.2 Free charge carrier absorption

Free charge carriers, both electrons and holes absorb radiation without becoming excited into the other band. In absorbing a photon, the electron (or hole) makes a transition to another state in the same band, as shown in Fig 2.15. Such process is referred to as an intraband transition. The free charge carrier absorption takes place when $h\nu < E_g$ and frequently this absorption dominates the spectrum below the fundamental edge. For $h\nu > E_g$, both fundamental absorption and free charge carrier absorption occurs simultaneously [4].

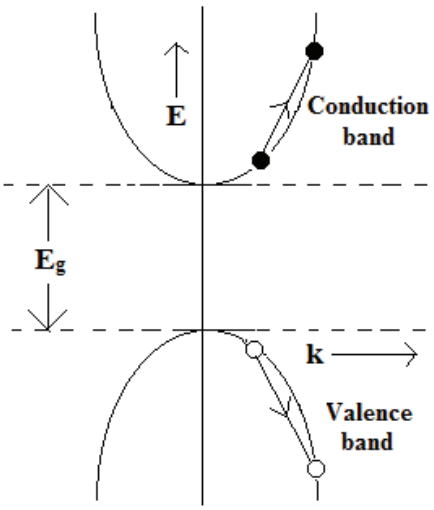

Fig 2.15 Free charge carrier absorption

2.8.3 Exciton absorption

In fundamental absorption, the excited electron becomes a free particle in the conduction band and the hole left in the valence band is also free. The electron and hole attract each other and may form a bound state referred to as an exciton [4] in which the two particles revolve around each other. The binding energy of exciton is nearly 0.01 eV and hence the exciton level falls slightly below the edge of the conduction band, as indicated in Fig 2.16.

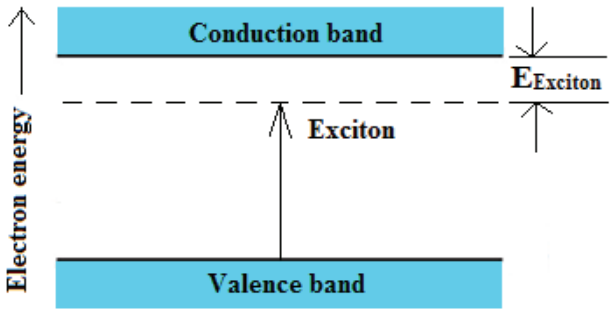

Fig 2.16 Exciton absorption

The exciton level is in the same neighbourhood as the donor level. The energy of the photon involved in exciton absorption is given by [4]

$$h\nu = E_g - E_{Exciton} \tag{2.46}$$

where $E_{Exciton}$ is the exciton binding energy. The exciton spectrum therefore consists of a sharp line, falling slightly below the fundamental edge. This line is often broadened by the interaction of the exciton with impurities or other similar effects, and may merge with the fundamental absorption band, although the peak of the exciton line remains clearly visible. Absorption of an exciton introduces complications into the fundamental absorption spectrum, particularly near the band edge and renders the determination of the energy gap in semiconductors more difficult. However, exciton absorption is important in the discussion of optical properties of insulators in the ultraviolet region of the spectrum [4].

2.8.4 Absorption involving impurities

The absorption process involving impurities often takes place in semiconductors. The type and degree of absorption depend on the type of impurities present and on its concentration. Fig 2.17 depicts the main classes of such process. Fig 2.17(a) shows the transition from the valence band to a neutral acceptor, which is analogous to the donor-conduction band transition. Fig 2.17(b) shows the case in which a neutral donor absorbs a photon and the electron makes a transition to a higher level in the impurity itself or in the conduction band. The transition to higher impurity levels appear as sharp lines in the absorption spectrum. Fig 2.17(c) represents a process in which an electron is excited from the valence band to an ionized donor or from an

ionized acceptor to the conduction band. Such process leads to absorption which is close to the fundamental absorption and are seldom resolved from it. Fig 2.17(d) illustrates an absorption process, involving transition from an ionized acceptor to an ionized donor [4]. The energy of the photon in this case is

$$h\nu = E_g - E_d - E_a \tag{2.47}$$

This leads to discrete structure in the absorption curve but this is often difficult to resolve because of its proximity to the fundamental edge [4].

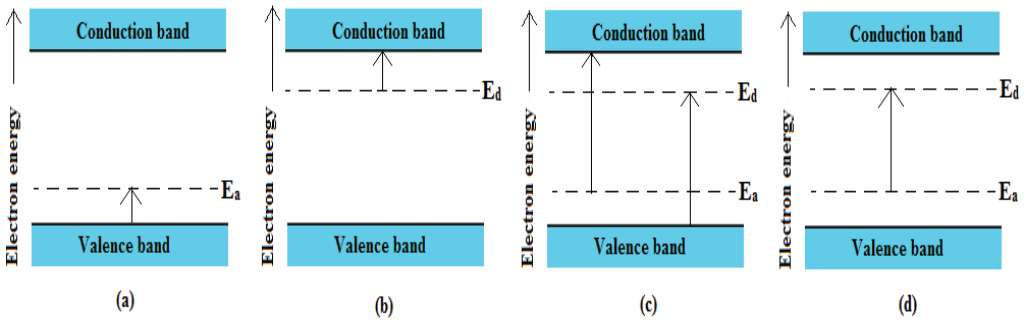

Fig 2.17 Various absorption process involving impurities

The impurities may also affect the absorption spectrum in another indirect ways. For instance, an exciton is often found to be trapped by an impurity. This may happen as follows: The impurity first traps an electron, and once this happens the impurity now charged attracts a hole through the Coulomb force. Thus both an electron and a hole are trapped by the impurity. The spectrum of this exciton is different from that of the free exciton because of the interaction with the impurity [4].

2.8.5 Photoconductivity

When a light beam of energy hν > E_g is incident on a semiconductor, the electrons gets excited across the energy gap. This leads to an increase in the number of free charge carriers (electrons and holes) and hence an increase in electrical conductivity. This phenomenon is termed as photoconductivity. CdS is an example of a good photoconducting material. In CdS, it is possible to change the conductivity by ≈ 10 orders of magnitude through charge carrier generation by light. These large changes in electrical conductivity can be utilized in a variety of device applications such as light meters, photodetectors, optically activated switches, infrared solid state detectors and information storage [4]. The concept of photoconductivity is illustrated by using a semiconductor slab shown in Fig 2.18.

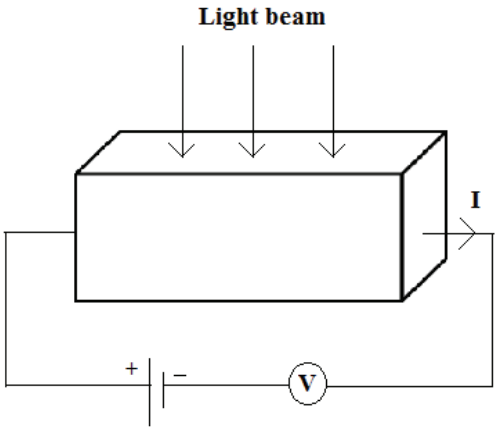

Fig 2.18 Basic experimental setup for photoconductivity

Before the light beam is turned ON, the conductivity is given by [4]

$$\sigma_0 = e\left(n_0\mu_n + p_0\mu_p\right) \tag{2.48}$$

where n_0 and p_0 are concentrations at equilibrium and σ_0 is the dark conductivity. When the light beam is turned ON, the free charge carrier concentrations increase by the amounts Δn and Δp and the current increases abruptly. Since electrons and holes are always created in pairs $\Delta n = \Delta p$. Thus conductivity is now

$$\sigma = \sigma_0 + e\Delta n\left(\mu_n + \mu_p\right) = \sigma_0 + e\Delta n\mu_p\left(1 + b\right) \tag{2.49}$$

where $b = \mu_n/\mu_p$ is the mobility ratio. The relative increase in conductivity is given by

$$\frac{\Delta\sigma}{\sigma_0} = \frac{e\Delta n\mu_p\left(1 + b\right)}{\sigma_0} \tag{2.50}$$

To measure photocurrents, photoexcited charge carriers are collected at the external electrodes. In the steady state, free charge carriers are continually created by the incident light. At the same time, the excited free charge carriers continually annihilate each other through electron-hole recombination. To produce a large photocurrent, it is desirable to have a long free charge carrier lifetime or a slow recombination time. If G is the rate of generation of electrons per unit volume due to photoexcitation then the photoexcited electron density in the steady state is given by

$$\Delta n = G\tau \tag{2.51}$$

where τ is the recombination time which is essentially the lifetime for a free charge carrier. Slow recombination rates are essential to the operation of photoconductors. G can be written as

$$G = \frac{\alpha dN\left(\nu\right)}{V} \tag{2.52}$$

where α is the absorption coefficient and d is the thickness of the semiconductor slab. N(ν) is the number of photons incident on the semiconductor slab per unit time and is given by

$$N(\nu) = \frac{I(\nu)A}{h\nu} \tag{2.53}$$

where A is the area of the semiconductor slab, I(ν)A is the incident power and hν is the photon energy. Combining Eq (2.51) and Eq (2.53), we get

$$\Delta n = \frac{\alpha I(\nu)}{h\nu}\tau \tag{2.54}$$

Using Eq (2.54) in Eq (2.50), we obtain the relative increase in conductivity as [4]

$$\frac{\Delta\sigma}{\sigma_0} = e\frac{\alpha I(\nu)\tau\mu_p(1+b)}{h\nu\sigma_0} \tag{2.55}$$

It is to be noted that $\frac{\Delta\sigma}{\sigma_0} \approx I(\nu)$ and also particularly that $\frac{\Delta\sigma}{\sigma_0} \approx \alpha(\nu)$, the fundamental absorption coefficient that is already discussed in section 2.8.1.

2.8.6 Luminescence

Once the electrons are excited by the absorption of radiation, the distribution of electrons is no longer in equilibrium. The electrons decay into lower states by emitting radiation. This emission is referred to as luminescence. Luminescence is therefore the inverse of absorption and it is a non equilibrium phenomena. It requires excitation by light, electron beams, current injection, etc., which create excess electrons, holes or both. The effects of electron-hole recombination give rise to recombination radiation or luminescence. ZnS, GaP, GaAs are examples for luminescent materials. The luminescent process is

widely used in television screens, semiconductor lasers and LEDs [4]. There are several types of luminescence mechanisms. The first classification is based on the source of excitation energy [4]. The most important excitation sources are as follows:

- Electroluminescence : Excitation by an electric field or current.
- Photoluminescence : Excitation by optical absorption.
- Cathodoluminescence : Excitation by high energy electron beam.
- Radioluminescence : Excitation by high energy radiation.
- Thermoluminescence : Charge carriers are first excited by some means and the electrons are frozen in their trapping states. Then thermal agitation assists the electrons to deexcite and release radiation.
- Incandescence : Electrons are straightaway excited thermally and then release radiation.

The second classification of luminescent processes pertains to the time that the light is emitted relative to the initial excitation [4]. They are of two types, namely:

- Fluorescence : Luminescence that takes place during the time of excitation.
- Phosphorescence : Luminescence that continues for some time even after the excitation.

2.9 Electrical properties: Charge carrier transport

The charge carrier transport phenomena are the foundation for determining the current-voltage characteristics of semiconductor devices. The basic semiconducting parameters which control the charge carrier transport properties are band gap energy, activation energy, Fermi energy, electrical conductivity, densities of charge carriers, concentration of donors and acceptors, effective mass and mobility of charge carriers, relaxation time, mean free path, Hall coefficient, thermoelectric power and so on. Therefore knowledge of these basic charge carrier transport parameters is necessary for a better understanding of the electrical properties of a semiconductor [10].

2.9.1 Charge carrier drift and charge carrier diffusion

The net flow of charge carriers (electrons and holes) in a semiconductor will generate current. The process by which these charged particles move is called charge carrier transport [11]. The two basic transport mechanisms are charge carrier drift and charge carrier diffusion.

An electric field applied to a semiconductor will produce a force on electrons and holes so that they will experience a net acceleration and net movement, provided there are available energy states in the conduction band and valence band. The motion of free charge carriers in a semiconductor caused by an electric field leads to a current. This transport mechanism is termed as charge carrier drift. The net drift of charge give rise to a drift current [11]. Hole drift current density is

$$J_p(drift) = pe\mu_p E \tag{2.56}$$

Electron drift current density is

$$J_n(drift) = ne\mu_n E \tag{2.57}$$

When a charge carrier density gradient is established by varying the doping density in a semiconductor or by applying a thermal gradient, the charge carriers move from regions where the charge carrier density is high to regions where the charge carrier density is low. This transport mechanism is termed as charge carrier diffusion. The net diffusion of charge give rise to a diffusion current [11]. Hole diffusion current density is

$$J_p(diffusion) = -eD_p \frac{\partial(\Delta p)}{\partial x} \tag{2.58}$$

Electron diffusion current density is

$$J_n(diffusion) = eD_n \frac{\partial(\Delta n)}{\partial x} \tag{2.59}$$

where $-\frac{\partial(\Delta p)}{\partial x}$ and $\frac{\partial(\Delta n)}{\partial x}$ are the rate of flow of holes and electrons respectively and D_p and D_n are the diffusion coefficient of hole and electron respectively. The diffusion coefficient gives an indication of how well an electron or hole moves in a semiconductor as a result of a density gradient [11]. Thus, total hole current is given by

$$J_p = J_p(drift) + J_p(diffusion) = pe\mu_p E - eD_p \frac{\partial(\Delta p)}{\partial x} \tag{2.60}$$

Total electron current is given by

$$J_n = J_n(drift) + J_n(diffusion) = ne\mu_n E + eD_n \frac{\partial(\Delta n)}{\partial x} \tag{2.61}$$

In general, the total current (I) is the sum of the hole and electron current densities multiplied with the cross sectional area (A) of the semicnductor, perpendicular to the direction of the charge carrier flow [11], i.e.,

$$I_{Total} = A\left(J_p + J_n\right) \tag{2.62}$$

When drift or diffusion of charge carriers takes place, the semiconductor is no longer in thermal equilibrium. As a result the concept of constant Fermi energy throughout the semiconductor is not valid. Therefore, the Fermi energy is allowed to vary throughout the material and is assigned a different Fermi energy, namely the Quasi-Fermi energies, F_p and F_n to holes and electrons respectively [10]. Then

$$J_p = \mu_p p \frac{dF_p}{dx} \tag{2.63}$$

$$J_n = \mu_n n \frac{dF_n}{dx} \tag{2.64}$$

2.9.2 Effective mass

According to band theory, electron mass (m_n) is variable with k and can be positive, negative and also infinite. In the free electron concept, m_n is a constant. The following consideration will lead to an effective electron mass m_n^* for electrons moving in a periodic potential field. The electron has a dualistic character i.e., particle and wave. Hence the velocity of electron can be described by its wave vector k [12].

If conduction electrons in the band theory are considered as wave packets of group velocity v_g described by k, then

$$v_g = \frac{2\pi}{h}\frac{dE}{dk} \tag{2.65}$$

If electrons are accelerated to a, then

$$a = \frac{2\pi}{h}\left(\frac{d^2E}{dk^2}\right)\left(\frac{dk}{dt}\right) \tag{2.66}$$

where a is the acceleration under an electric field F. Further

$$dE = eFdx = eF\left(\frac{2\pi}{h}\right)\left(\frac{dE}{dk}\right)dt \tag{2.67}$$

Using $\frac{dk}{dt} = \frac{2\pi eF}{h}$ in Eq (2.66) we get

$$a = \frac{4\pi^2}{h^2}\left(\frac{d^2E}{dk^2}\right)eF \tag{2.68}$$

For electrons moving in a field free space i.e., for free electrons

$$a = \frac{eF}{m} \tag{2.69}$$

Comparing Eq (2.68) and Eq (2.69) for acceleration of electrons respectively for the band theory and free electron cases, the electron mass (m) in the latter case becomes effective electron mass m_n^* and is given by [12]

$$m_n^* = \left(\frac{h^2}{4\pi^2}\right)\left(\frac{d^2E}{dk^2}\right) \tag{2.70}$$

It is interesting to note that m_n^* is a function of the directions in anisotropic solids and hence it is a tensor in a three dimensional case.

2.9.3 Electrical conductivity and mobility

Consider the motion of one typical conduction electron in an electric field E. The field exerts on the electron a force –eE. Due to collision with the medium, the electron experiences a frictional force $-\frac{m_n^* u}{\tau}$, where u is the electron drift velocity, m_n^* is the effective mass of the electron and τ is a constant called the collision time or relaxation time. Using Newton's law, we have [4]

$$m_n^* \frac{du}{dt} = -eE = m_n^* \frac{u}{\tau} \tag{2.71}$$

The effect of collision tends to reduce u to zero. Considering the steady state solution, i.e., where $\frac{du}{dt} = 0$, the appropriate solution to Eq (2.71) becomes [4]

$$u = -\frac{e\tau}{m_n^*} E \tag{2.72}$$

or the electron mobility μ_n becomes

$$\mu_n = \frac{u}{E} = -\frac{e\tau}{m_n^*} \tag{2.73}$$

It is defined as the velocity acquired by the current carrying particle per unit electric field. The negative sign indicates that μ_n is opposite to E because charge on the electron is negative. Then electrical conductivity becomes

$$\sigma = \frac{ne^2\tau}{m_n^*} \tag{2.74}$$

2.9.4 Relaxation time and mean free path

When an electron moves in the lattice, it collides with ions which have the effect of slowing down the momentum of the electron. Now let the electric field E be suddenly removed at some instant. Then u after this instant is governed by [12]

$$m_n^* \frac{du}{dt} = -eE = m_n^* \frac{u}{\tau} \tag{2.75}$$

The solution appropriate to the initial condition is now

$$u = u_0 e^{-t/\tau} \tag{2.76}$$

Showing that u approaches zero exponentially with a characteristic time τ. This behaviour is called a relaxation process. It is to be noted that τ is very small (10^{-14}s). Hence u relaxes to zero very rapidly. Therefore the relaxation time or collision time (τ) is defined as the average time between two successive collisions and is expressed as [12]

$$\tau = \frac{l}{u} \tag{2.77}$$

where l is termed as the mean free path and is defined as the average distance travelled by the electron between two successive collisions. Thus mobility and electrical conductivity becomes respectively as

$$\mu_n = \frac{el}{um_n^*} \tag{2.78}$$

$$\sigma = \frac{ne^2 l}{um_n^*} \tag{2.79}$$

2.9.5 Hall effect

When a magnetic field is applied perpendicular to a current carrying conductor, a voltage is developed across the specimen in a direction perpendicular to both the current and the magnetic field. This phenomenon is called as the Hall effect. The voltage so developed is called as the Hall voltage [13].

Consider a slab of material subjected to an electric field E_x along X-axis and a magnetic field H_z along Z-axis as shown in Fig 2.19.

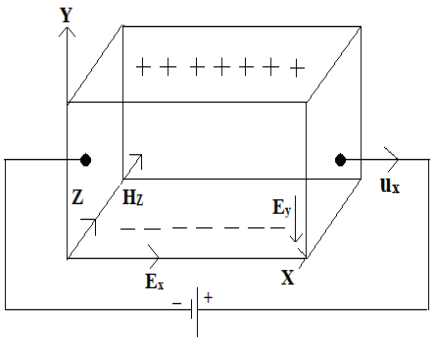

Fig 2.19 Origin of Hall effect and Hall field

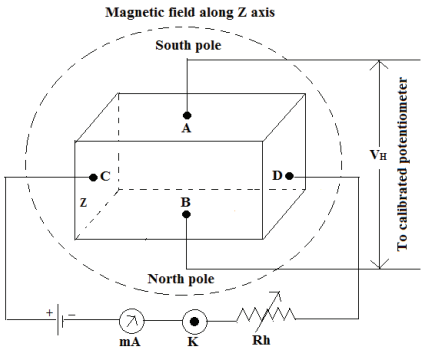

Fig 2.20 Experimental setup for the determination of Hall coefficient

Let J_x be the current density that flow in the direction of E_x. Suppose that I is the current carried by an electron of charge –e. The magnetic field H_z applied perpendicular to current will exert a transverse magnetic deflecting force on the electron which causes the electron to drift downward to the lower edge of the specimen. Consequently, lower surface of the slab collects a negative charge and the upper surface of the slab collects a positive charge. This excess of negative charge on the lower edge and the corresponding excess

of positive charge on the upper edge create a transverse electric field E_y known as Hall voltage or Hall field which opposes the transverse drifting of electrons. Finally an equilibrium is reached, when the force ($-eE_y$) due to accumulation of electrons becomes equal to the magnetic force (eu_xH_z) and so the flow of electrons stops. Then the net force on the electron F_y becomes zero [13]. Therefore in the steady state $F_y = 0$ i.e.,

$$-eE_y + eu_xH_z = 0 \tag{2.80}$$

From Eq (2.80), we get the Hall voltage as $E_y = u_xH_z$ (2.81)

Let n be the free electron density. Then the current density is given by

$$J_x = -neu_x \tag{2.82}$$

or
$$u_x = -\frac{J_x}{ne} \tag{2.83}$$

Using Eq (2.83) in Eq (2.81), we get

$$E_y = -\frac{J_xH_z}{ne} = R_HJ_xH_z \tag{2.84}$$

Here, $R_H = -\frac{1}{ne}$ is called as the Hall coefficient of the material [13].

As per Eq (2.73), mobility of the electron can be written as

$$\mu = \frac{u_x}{E_x} \tag{2.85}$$

or
$$u_x = \mu E_x \tag{2.86}$$

Using Eq (2.86) in Eq (2.84), we get $E_y = \mu E_xH_z$ (2.87)

Comparing Eq (2.84) and Eq (2.87), we get

$$R_H = \mu \frac{E_x}{J_x} \tag{2.88}$$

or

$$R_H = \mu \frac{1}{\sigma} \tag{2.89}$$

Here, σ is the electrical conductivity of the material [13]. Therefore

$$\mu = R_H \sigma \tag{2.90}$$

To determine R_H, consider the experimental setup as given in Fig 2.20. A suitable current I is passed through a specimen of breadth b and thickness d placed in X direction and a magnetic field H_z is applied in the Z direction. The current is adjusted by using a rheostat Rh. Two leads from A and B are connected to a potentiometer to measure the Hall voltage V_H. Then the current density is given by [13]

$$J_x = \frac{I}{bd} \tag{2.91}$$

Using Eq (2.91) in Eq (2.84), we get

$$E_y = -\frac{I}{nebd} H_z \tag{2.92}$$

or

$$E_y d = V_H = -\frac{I}{neb} H_z = R_H \frac{IH_z}{b} \tag{2.93}$$

This gives Hall coefficient,

$$R_H = \frac{V_H b}{IH_Z} \tag{2.94}$$

Thus R_H can be calculated by knowing I and H_z and by measuring V_H developed across the points A and B by means of a calibrated potentiometer

[13]. Hall effect measurement provides the following information about the solid [13]:

- The sign of charge carrier (R_H is positive if charge carriers are holes and R_H is negative if charge carriers are electrons).
- The concentration and mobility of charge carriers.
- To distinguish between a metal, semiconductor and insulator.
- By measuring Hall voltage and knowing the value of Hall coefficient, the unknown magnetic field can be measured.

2.9.6 Thermoelectric effect

When two dissimilar materials (either electrical conductors or semiconductors) are joined together with the junctions held at different temperatures (T and T+ΔT), then a voltage (ΔV) is developed proportional to the temperature difference (ΔT). This phenomenon is termed as the thermoelectric effect [14]. The ratio of the voltage developed to the temperature gradient is called the Seebeck coefficient (S) or the thermoelectric power (TEP) [14]. The Seebeck coefficient is low for metals (10 μV K^{-1}) and high for semiconductors (a few 100 μV K^{-1}). The Seebeck coefficient is positive for Zn and Cu and negative for Fe and Ni. The principles and applications of thermoelectric effect and the potential of a material for thermoelectric applications have already been discussed in chapter 1.

When a thermal gradient is applied in a semiconducting material, the charge carriers (electrons or holes) diffuse from hot side to cold side. The

charge carriers migrating to cold side leave behind their oppositely charged and immobile nuclei at hot side thus giving rise to a thermoelectric voltage. If the voltage developed at hot end is negative with respect to cold end then the charge carriers are holes and the semiconductor is of p-type and if it is positive with respect to cold end then the charge carriers are electrons and the semiconductor is of n-type. Thus TEP measurement gives us an idea about the nature of the semiconductor i.e., p-type or n-type [12]. Moreover, by correlating the results of TEP and Hall measurements, it becomes possible to deduce important material parameters such as Fermi energy, effective mass, mean free path and relaxation time, as follows:

The Seebeck coefficient is related to the Fermi energy for degenerate [15] and non degenerate semiconductors [16] respectively as

$$S = \frac{\pi^2 K_B{}^2 T}{3eE_F}\left(\frac{3}{2} + A\right) \tag{2.95}$$

$$S = \pm\frac{K_B}{e}\left[A + \frac{E_F}{K_B T}\right] \tag{2.96}$$

where A is the scattering parameter and can take the values A = -1/2 for acoustic phonon scattering, which is dominant at high temperatures T ≥ 300 K and also A = 3/2 for ionized impurity scattering, which is dominant at low temperatures T ≤ 300 K [12]. K_B is the Boltzmann constant, T is the absolute temperature, e is the electronic charge and E_F is Fermi energy.

The Seebeck coefficient is related to effective mass of degenerate [17] and non degenerate [12] semiconductors respectively as

$$S = \frac{8\pi^2 K_B{}^2 T}{3eh^2} m_p^* \left(\frac{\pi}{3p} \right)^{2/3} \tag{2.97}$$

$$S = \pm \frac{K_B}{e} \left[A + \ln \left[\frac{2(2\pi m_p^* K_B T)^{3/2}}{ph^3} \right] \right] \tag{2.98}$$

Substituting the value of p (hole concentration for p-type material) or n (electron concentration for n-type material), obtained from Hall measurements, accordingly in Eq (2.97) gives m_p^* and m_n^* respectively. Using these values of m_p^*or m_n^* and the values of μ_p or μ_n, in Eq (2.73) gives the relaxation time τ. On substituting the value of τ in Eq (2.77) gives the mean free path.

For degenerate semiconductors TEP increases with increase in temperature whereas for non degenerate semiconductors TEP decreases with increase in temperature. In materials of high to moderate resistivities, there is often a sharp increase in TEP towards low temperatures due to preferential scattering of charge carriers by phonons which travel from the hot to the cold end of the sample. The tendency of the phonon stream to scatter the charge carriers towards the hot end for electrons and to the cold end for holes, thus setting up an additional electric field causing a remarkable increase in TEP is termed as phonon drag [18]. This is observed at low temperatures. At higher temperature region, the phonon-phonon scattering tends to restore isotropic distribution of electrons, thereby reducing the effect of phonon drag on the charge carriers [12].

References

[1] R. A. Smith, Semiconductors (Academic, Calcutta, 1978), pp. 1-18.

[2] Y. Y. Peter and M. Cardona, Fundamentals of semiconductors: Physics and materials properties (Springer, Berlin, 2013), pp. 1-4.

[3] M. Grundmann, The physics of semiconductors: An introduction including nanophysics and applications (Springer, Berlin, 2010), pp. 519-768.

[4] M. A. Omar, Elementary solid state physics: Principles and applications (Addison Wesley, New Delhi, 2001), pp. 176-304.

[5] S. O. Pillai, Solid state physics (New Age International, New Delhi, 2001), pp. 477-483.

[6] R. K. Puri and V. K. Babbar, Solid state physics (S. Chand, New Delhi, 2003), pp. 199-227.

[7] J. M. M. Duart, R. J. M. Palma and F. A. Rueda, Nanotechnology for microelectronics and optoelectronics (Elsevier, USA, 2006), pp. 75-76.

[8] J. Singh, Semiconductor devices: Basic principles (Wiley, USA, 2007), pp. 76-77.

[9] J. Tauc, Amorphous and liquid semiconductors (Plenum, New York, 1974), pp. 159-220.

[10] A. Kitai, Principles of solar cells, LEDs and diodes: The role of the PN junction (Wiley, USA, 2011), pp. 34-35.

[11] D. A. Neamen and D. Biswas, Semiconductor physics and devices (Tata McGraw Hill, New York, 2007), pp. 132-196.

[12] A. Goswami, Thin film fundamentals (New Age International, New Delhi, 1996), pp. 193-278.

[13] R. Murugeshan, Modern physics (S. Chand, New Delhi, 2002), pp. 786-789.

[14] T. M. Tritt and M. A. Subramanian, Mater. Res. Soc. Bulletin 31, 188 (2006).

[15] H. Arabshahi and F. Sarlak, Res. J. Appl. Sci 6, 232 (2011).

[16] H. B. Kwok and R. H. Bube, J. Appl. Phys 44, 138 (1973).

[17] G. J. Snyder and E. S. Toberrer, Nature. Mater 7, 105 (2008).

[18] C. Herring, Phys. Rev 96, 1163 (1954).

Chapter 3

Experimental Technique and Characterization Tools

3.1 Introduction

Today thin film science and technology has become a subject of full fledged research. Thin film science covers a wide span of disciplines such as microelectronics, optics, photovoltaics, thermoelectrics, magnetics, aeronautics, space science, material science and so on. Thin film devices are preferred over their bulk counterparts due to their compactness, better performance, reliability, low cost of production and low package weight.

Thin film is defined as any object in solid, liquid or gaseous form with one of its dimensions negligibly small than the other two. It can also be defined as a thin layer deposited on a solid support called substrate by an atom by atom process. The structural, optical and electrical properties of thin films are sensitive not only to their structure and thickness but also to the deposition

parameters such as rate of deposition, substrate temperature, environmental conditions, residual gas pressure in the system, purity of the material to be deposited, inclusion of foreign matter in the deposit, inhomogeneity of the film and so on.

This chapter gives a brief mention of the various thin film deposition techniques and elaborates the theory of reactive evaporation - a variant of Gunther's three temperature technique along with the experimental setup used for the preparation of thin films under study, followed by the procedures adopted for cleaning the substrates and evaporators. The entire process involved in the deposition of thin film is dealt with in detail. Also, comprehensive descriptions of the experimental tools used for the characterizations of the as-prepared thin films are given along with a brief account of relevant theory behind each technique.

3.2 Thin film deposition techniques

Thin films of metals, semiconductors, insulators and dielectrics can be prepared by a variety of deposition techniques [1] as described in Table 3.1.

Table 3.1 Classification of thin film deposition techniques

Thin Film Deposition Techniques

Physical Methods | Chemical Methods

Evaporation	Sputtering	Liquid Phase	Gas Phase
Resistive heating	Glow discharge sputtering	Electrolytic deposition	Chemical vapour deposition (CVD)
Flash evaporation	Asymmetric AC sputtering	Electroless deposition	Photochemical vapour deposition (PCVD)
Arc evaporation	Bias sputtering	Anodic oxidation	
Laser evaporation	RF sputtering	Liquid phase epitaxy	
Electron beam evaporation	Ion beam sputtering	Chemical bath deposition (CBD)	Plasma enhanced chemical vapour deposition (PECVD)
Reactive evaporation	Triode sputtering	Spray pyrolysis	
Exploding wire technique	Reactive sputtering	Sol gel method	
Molecular beam epitaxy	Magnetron sputtering	Langmuir blodget method	Thermal growth

In general, thin film deposition techniques can be broadly classified into physical vapour deposition (PVD) and chemical vapour deposition (CVD).

3.2.1 Physical Vapour Deposition (PVD)

The physical vapour deposition (PVD) is an atomistic deposition process in which the material to be deposited is vaporized from a solid or liquid source in the form of atoms or molecules and transported in the form of a vapour through vacuum or low pressure gaseous (or plasma) environment to the substrate, where it condenses. In this method, the transport of vapours from source to substrate and deposition takes place by physical means. This is achieved by carrying out the deposition in a vacuum of magnitude such that the mean free path of ambient gas molecules is greater than the dimensions of the deposition chamber and source to substrate distance [1]. PVD provides thin films of wide range of compositions and crystalline structures with high purity and crystallinity. However, the need for vacuum facilities makes the experimental setup of PVD more complex and expensive. PVD technique is broadly classified into evaporation and sputtering.

Evaporation is one of the most widely used techniques for the deposition of thin films of extreme purity and crystallinity. In this method the solid material is vaporized by heating it to sufficiently high temperatures and then condensing it onto a substrate to form a thin film [1]. The variants of evaporation are given in Table 3.1.

In evaporation method, the heating of evaporant can be carried out either directly or indirectly. In direct heating, the evaporant is supported on a filament basket or boat (generally made of refractory materials such as W, Mo, Ta) which is heated by passing electric current. In indirect heating, the evaporant is taken in crucibles made of glass, quartz, graphite which are heated

indirectly by supporting them in a metal basket [1]. The four stages of film formation by vacuum evaporation technique are as follows:

- Transformation of the material from solid or liquid state to gaseous state.
- Transfer of gaseous particles from source to substrate.
- Deposition of the particles on the substrate surface.
- Rearrangement of the particles over the substrate surface.

The deposition of the films occurs at low pressure (10^{-5} Torr) and hence a vacuum chamber is required. When evaporation is made in vacuum, the evaporation temperature is considerably lowered, formation of oxides and incorporation of impurities in the film is reduced, ensures straight line propagation of particles from source to substrate and hence films with desired pattern can be produced with appropriate masking.

The rate of evaporation of atoms or molecules from a clean surface of unit area in vacuum is given by the Hertz-Knudsen equation

$$N_e = \frac{3.513\times10^{22} P_e}{\sqrt{MT}} \text{ molecules cm}^{-2}\text{ s}^{-1} \qquad (3.1)$$

where P_e is the equilibrium vapour pressure in Torr of the evaporant under saturated vapour conditions at a temperature T, M is the molecular weight of the species [1]. The liberated particles travel along a straight line with their thermal velocities until they encounter collisions with ambient gas molecules.

The number of particles scattered by collision with ambient gas molecules is given by

$$N_s = 1 - \exp\left(\frac{-d}{l}\right) \tag{3.2}$$

where d is the source to substrate distance and l is the mean free path [1]. For a given temperature T, the mean free path is given by

$$l = \frac{5 \times 10^{-3}}{P} \text{ cm} \tag{3.3}$$

where P is the pressure in Torr [1]. The mean free path should be greater than the source to substrate distance in order to minimize collision with stray molecules. The mean free path for air at 25°C and pressure in the range 10^{-4} Torr to 10^{-6} Torr is about 50 cm to 5000 cm, respectively. Thus pressure lower than 10^{-5} Torr is necessary to ensure a straight line path for most of the evaporated species and source to substrate distance of 10 cm to 50 cm in a vacuum chamber. The impingement rate (rate at which the atoms arrive at the substrate surface) is expressed as

$$\frac{dN_m}{A_r dt} = \frac{N_a \rho_m d'}{M_m} \text{ molecules cm}^{-2}\text{ s}^{-1} \tag{3.4}$$

where ρ_m is the density (gm cm^{-3}) and M_m is the molar mass (gm mol^{-1}) of the material to be evaporated, d' is rate of deposition (cm s^{-1}) and A_r is the area of the substrate surface (cm^2) [1]. The rate of deposition of the vapour on the substrate depends on the evaporation rate, source geometry, its position relative to the substrate and the condensation coefficient. For the ideal case of deposition from a clean, uniformly emitting point source onto a plane substrate, the rate of deposition varies as $\cos\theta/r^2$ given by Knudsen's cosine law, where r

is the radial distance of the substrate from the source and θ is the angle between the radial vector and the normal to the substrate [1]. The thickness distribution is given by

$$\frac{t}{t_0} = \frac{1}{\left[1+\left(\frac{x}{h}\right)^2\right]^{3/2}} \tag{3.5}$$

where t_0 is the thickness of the deposit where the vapours fall normally and t is the thickness at a distance x from this point and h is the normal distance of the point source from the substrate [1]. For evaporation from a small area onto a parallel plane substrate, the deposition rate is $\cos^2\theta/r^2$ and the thickness distribution is given by [1]

$$\frac{t}{t_0} = \frac{1}{\left[1+\left(\frac{x}{h}\right)^2\right]^{2}} \tag{3.6}$$

Fig 3.1 shows the variation of thickness of the thin film along the length of the substrate. It shows that the thickness of the film at distance x will be slightly less than that at x=0.

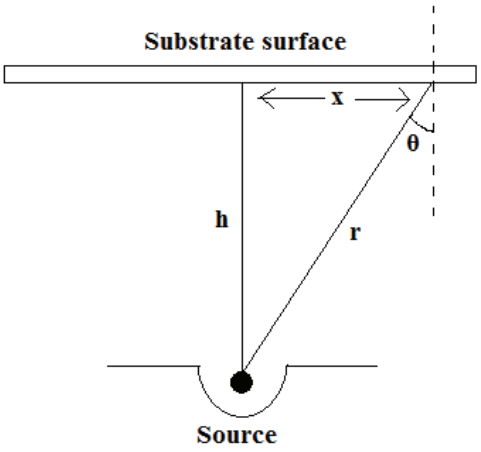

Fig 3.1 Variation of thickness of thin film along the length of substrate

Sputtering is another category of PVD technique in which the vapour species are produced by mechanically knocking out the atoms or molecules from the surface of a solid material by bombarding it with energetic and nonreactive ions. The ejection process is known as sputtering and it occurs as a result of momentum transfer between the impinging ions and the atoms of the target being bombarded. The sputtered species can be condensed on a substrate to form a thin film [1]. The variants of sputtering are given in Table 3.1.

3.2.2 Chemical Vapour Deposition (CVD)

The chemical vapour deposition (CVD) is a process which involves a heterogeneous chemical reaction at the surface of a substrate without requiring vacuum as an essential condition for deposition. In CVD process, the continuously flowing carrier gas and chemical reactions induced by temperature or concentration gradients between the substrate and the surrounding gas ambient are responsible for the transfer of the vapour to the

substrate, i.e., transfer of vapour from source to substrate and deposition takes place by chemical means [1]. The chemical reaction in CVD are activated by the application of light, heat, radio frequency (RF) field, X-ray radiation, glow discharge, electron bombardment or by the catalytic activity of the substrate surface. The CVD technique is classified into liquid phase and gas phase.

Liquid phase CVD is a process whereby constituents of the liquid phase (solution which contains the material to be deposited in the form of ions) react chemically near or at the substrate surface to form a thin film.

Gas phase CVD is a process whereby constituents of the gas phase (gas which contains the material to be deposited in the form of atoms) react chemically near or at the substrate surface to form a thin film. The variants of liquid phase CVD and gas phase CVD are given in Table 3.1.

In the present work, thin films are prepared by reactive evaporation- a variant of Gunther's there temperature method which is discussed in detail in the following sections.

3.3 Gunther's three temperature method

When multicomponent alloys or compounds are thermally evaporated, the components may evaporate at different rates because of their different vapour pressures thereby producing non stoichiometric films. A satisfactory method of preparing alloys and compound semiconducting thin films with precisely controlled composition is to evaporate each component from separate sources at suitable rates and allow them to impinge on a substrate kept at an elevated temperature. Such a method is referred to as Gunther's three temperature technique. For the formation of the stoichiometric binary

compound, generally three temperatures, i.e., substrate temperature and two evaporator temperatures are to be fixed and hence the process is called three temperature method [2].

The basic principle of Gunther's three temperature method is that for many binary systems there exist a stoichiometric interval with a limited degree of freedom in selecting the individual components and substrate temperatures for the formation of a particular compound film [2]. According to this method, the continuous condensation of a given vapour on a substrate is possible only if critical supersaturation is exceeded, i.e., continuous condensation of a particular vapour at a given deposition rate is possible only if the temperature of the substrate drops below a critical temperature or if a critical supercooling is reached. Since these critical values are functions of the interfacial energies, they should differ in magnitude for different kinds of vapour and surface conditions. Furthermore, if different vapours are present in the vapour phase, they may interact with each other and influence the above mentioned critical values of supersaturation or supercooling. But at a particular substrate temperature and critical value of incident flux, sufficient molecules of the compound are formed on the substrate and nucleation and progressive condensation of the compound occurs [2]. This technique is simple when compared to other methods because with proper experimental conditions it provides films of high purity and crystallinity. Moreover films with a wide range of compositions and crystalline structures can be obtained, because evaporation is one of the techniques most often used in semiconductor processing and thin film depositions.

3.3.1 Fundamental theory

The sticking coefficient β of a given vapour on a given substrate, or the condensation flux N_K exceeds zero only if the ratio p/p_e of the actual vapour pressure p and the equilibrium pressure p_e exceeds a critical value q_c [2].

$$N_K > 0 \text{ if } \frac{p}{p_e} > q_c \tag{3.7}$$

The pressure p in the Eq (3.7) is also related to the substrate temperature T. If the equilibrium temperature of the vapour is T' with $T' > T$, then the value of p' given by

$$p' = p\left(\frac{T}{T'}\right)^{1/2} \tag{3.8}$$

is to be inserted instead of p in Eq (3.7). It is more convenient to use the numbers N_+ or N_e which denotes the number of incident or emitted particles per unit time and area. Then from thermodynamic theory N_e can be written as

$$N_e = \frac{\alpha p_e}{(2\pi m K_B T)^{1/2}} \tag{3.9}$$

where α is the condensation coefficient, m is the atomic weight and K_B is the Boltzmann constant [2]. The condition (3.7) may be rewritten as

$$N_K > 0 \text{ if } \left(\frac{N_+}{N_e}\right) > \left(\frac{N_+}{N_e}\right)_c \tag{3.10}$$

At a given substrate temperature T, the equilibrium value N_e is given by

$$N_e = C\frac{\exp\left(\frac{-\Delta G_v}{K_B T}\right)}{(2\pi m K_B T)^{1/2}} \tag{3.11}$$

where p_e = constant × exp ($-\Delta G_v/K_B T$) and ΔG_v is the vaporization energy [2]. The condition for progressive condensation at a given substrate temperature involves exceeding a critical incident flux, i.e.,

$$N_K = 0 \text{ if } N_+ \le N_{+c}(T) \tag{3.12}$$

$$N_K > 0 \text{ if } N_+ > N_{+c}(T) \tag{3.13}$$

where N_{+c} is the critical value of incident flux. If the flux exceeds N_{+c}, the condensation flux rises rapidly and approaches its maximum value given by

$$N_{K\max} = \alpha(N_+ - N_e) \tag{3.14}$$

This behaviour is shown schematically in Fig 3.2. The slope of the function $N_K = f(N_+)$ depends on the mechanism of nucleation and can vary from one case to another. The ratio $(p/p_e)_*$ corresponds to the beginning of nucleation due to surface diffusion [2].

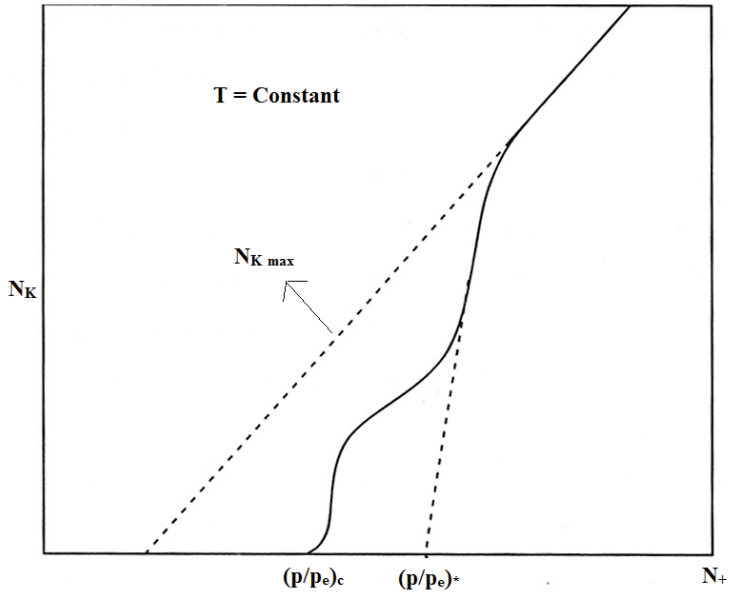

Fig 3.2 Variation of condensation flux N_K with flux N_+ of incident particles

Assuming a constant incident flux N_+ for vapour particles on a substrate, the condition for progressive condensation can be expressed in terms of a critical temperature T_c as follows

$$N_K = 0 \text{ if } T \geq T_c(N_+) \tag{3.15}$$

$$N_K > 0 \text{ if } T < T_c(N_+) \tag{3.16}$$

where

$$T_c = \frac{\Delta G_v}{K_B \ln\left(\frac{q_c C}{p}\right)} = \frac{T_c}{\left(1 + \frac{\ln q_c}{\ln\left(\frac{C}{p}\right)}\right)} \tag{3.17}$$

where q_c is the critical supersaturation, T_e is the equilibrium temperature corresponding to N_+. Thus by analogy with Fig 3.2, the condensation can be schematically represented as a function of the substrate temperature in the manner of Fig 3.3 i.e., after dropping below the critical temperature T_c, condensation sets in spontaneously and quickly approaches a maximum [2].

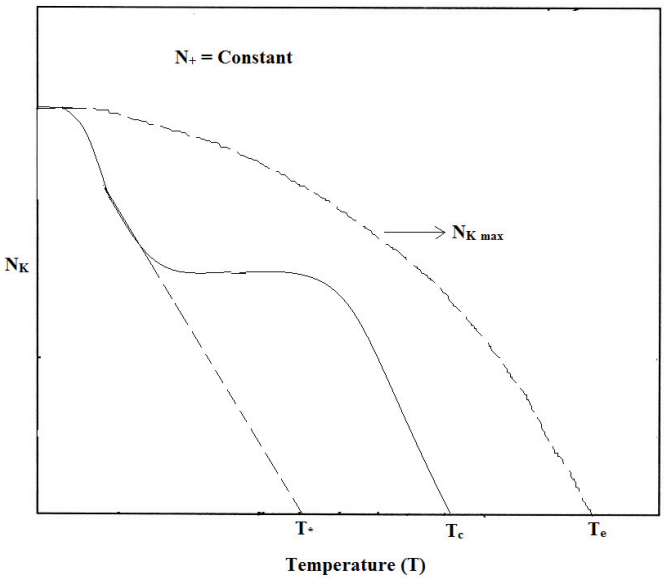

Fig 3.3 Variation of condensation flux N_K with substrate temperature T

During deposition and condensation of the first monolayer of the incident vapour on an unlike substrate, the interfacial forces and consequently the critical values q_c and the ratio T_c/T_e may change due to supersaturation or subcooling, reaching constant values when the deposited layer itself acts as substrate. Considering continuous deposition, where the condensation of the first monolayer is only a negligible part of the process as a whole, all further considerations will be related to these equilibrium values, i.e., to the critical values for supersaturation or subcooling which are related to like substrates [2].

3.3.2 Condensation phenomenon occurring with binary vapours

Consider the vapour phase consisting of two components A and B, both being incident on the substrate under consideration. As in the cases of high vacuum deposition, vapour density may be low enough to neglect collisions between particles of the components A and B in the vapour phase. Interactions can take place between such particles within the adsorbed stage on the substrate surface [2]. These interactions due to the strong attractive forces between particles A and B, lead to the formation of molecules

$$A + B \rightarrow AB \tag{3.18}$$

of a stable compound AB. Here AB stands for all possible compounds $A_m B_n$. An estimate of the interaction probability on the surface gives a density of adsorbed molecules AB, which is proportional to the product ($n_A n_B$) of the adsorbed particles A, B, and a mean diffusion coefficient D.

$$n_{AB} = \text{constant} \times n_A n_B D \tag{3.19}$$

The density n_i of the adsorbed particles is given by

$$n_i = \left(\frac{N_{+i}}{\omega} \right) \exp\left(\frac{\Delta G_a}{K_B T} \right) \; i = A, B \tag{3.20}$$

where ΔG_a is the interfacial energy with the substrate and ω is the transmission frequency [2]. Since n_i is proportional to the actual vapour pressure p, or the incident flux N_+ of the particular vapour, the density n_{AB} should also be proportional to the product of incident fluxes (N_{+A} N_{+B}) or vapour pressures (p_A p_B). Let p_{eA}, p_{eB} and p_{eAB} be the equilibrium pressures of the components A,

B and the compound AB respectively. Here p_{eAB} corresponds to the dissociation pressure of the compound and is equivalent to the pressure p_e (i/AB) of the volatile component i in equilibrium with the compound [2]. In most cases, this value is much lower than the equilibrium pressure p_{ei} of the pure component i. Thus, the critical values of one component i in the presence of the other component j should vary as

$$N_{+ci}(j) << N_{+ci} \text{ if } P_e\left(\frac{i}{AB}\right) << P_{ei} \tag{3.21}$$

$$T_{ci}(j) > T_{ci} \tag{3.22}$$

with respect to incident fluxes N_+. This behavior is shown in Fig 3.4.

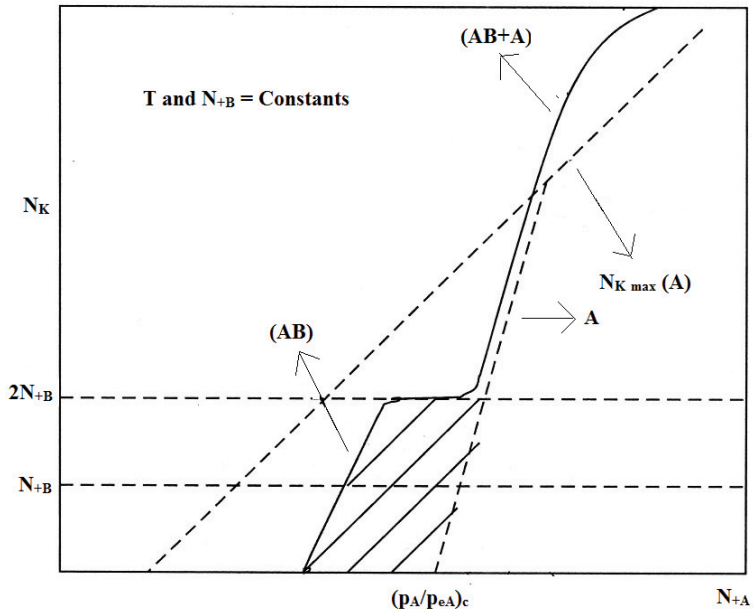

Fig 3.4 Condensation flux N_K with two incident components A and B

At a given substrate temperature T and for incident fluxes $N_{+B} < N_{+cB}$, no condensation of any kind is possible while the incident rate N_{+A} and the related adsorption density n_A are also very low. However, at a critical value $N_{+cA}(B)$ sufficient molecules AB are formed on the substrate, nucleation and progressive condensation of the compound AB starts and rapidly approaches the maximum flux [2]. Here, it is considerably lower than the analogous value N_{+cA} without the presence of B. This maximum value is reached when each impinging particle B reacts with one of the simultaneously impinging particles A. With further increase of N_{+A}, no increase of the condensation flux N_K is possible until, with $N_{+A} > N_{+cA}$, condensation of non interacting particles A takes place thereby further increasing the total condensation flux to $(N_{+B} + N_{+A} - N_e)$. In terms of substrate temperatures this is shown in Fig 3.5.

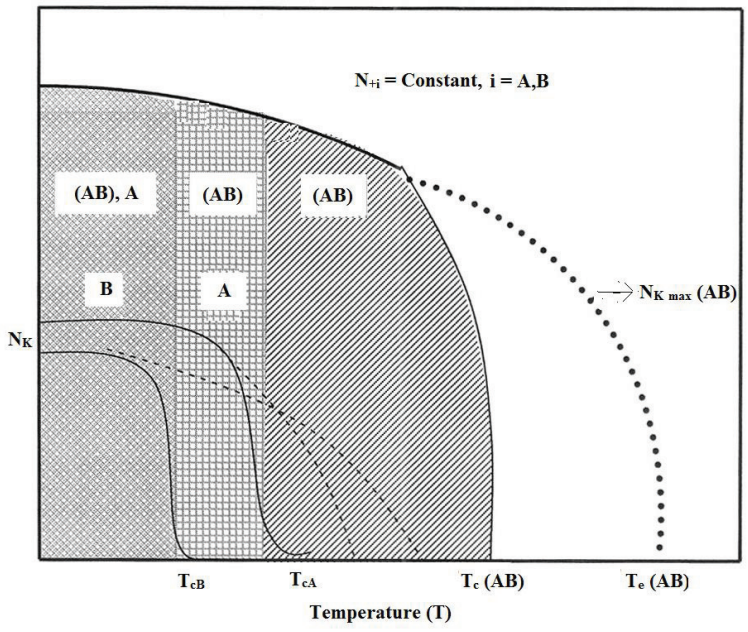

Fig 3.5 Condensation flux N_K as a function of temperature T with two incident components A and B

With decreasing substrate temperature, the condensation of the compound AB sets in at a certain critical value T_{cAB} until, with temperatures $T < T_{cA}$, additional condensation of the pure component A becomes possible, leading to a further increase of the condensation flux, with rapid approach to the final value [2]. In contrast to the conditions for single components, the critical values T_{cAB}, N_{+cAB} of the compound can be different from the equilibrium values since, according to Eq (3.19), the adatom densities of the two components, and not of the existing compound, govern the condensation flux. As indicated by Fig 3.4 and Fig 3.5, not only the condensation flux but also the composition of the condensed layers are affected by the given incident fluxes and substrate temperatures [2]. These relations are shown in Fig 3.6.

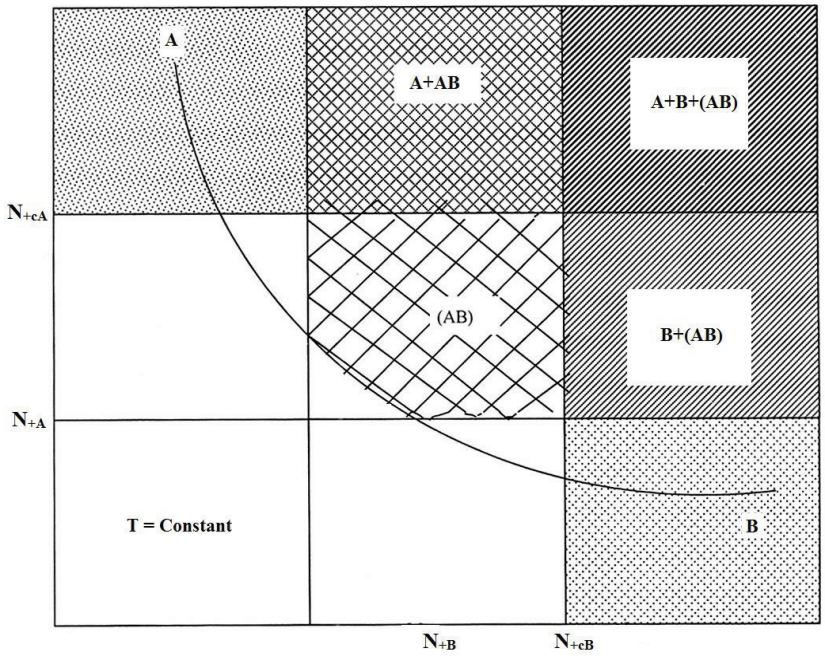

Fig 3.6 Condensation diagram for two incident components A and B

It is seen that well defined areas with layers of different compositions can exist as functions of the incident fluxes. There exists one region in particular where only pure compound layers of the composition AB are obtained while the unsaturated components are re-emitted in the vapour phase. This special region should occur in all cases, where the condition

$$p_e\left(\frac{i}{AB}\right) < p_{ei} \quad i = A, B \tag{3.23}$$

is satisfied i.e., a significant increase in adsorption energy due to the reaction A+B→AB is necessary. The area of the region is dependent on the substrate temperature T and increases with T, but this is possible only within a limited temperature range. Thus by selecting a method on the basis of above assumption, the deposition of exact stoichiometric compound layers by simultaneous evaporation of the single components should be possible [2]. The advantages and disadvantages of Gunther's three temperature method [2] are as follows:

3.3.3 Advantages and Disadvantages

Advantages

- The need to synthesize the compound from the elements prior to deposition which is a tedious and sometimes expensive metallurgical process is eliminated.

- High temperatures are frequently needed to evaporate high melting point carbides, nitrides and oxides and if resistive heating is used, the film will be contaminated due to evaporation of the source itself. This is

avoided in reactive evaporation.

- The decomposition of the compound upon heating in vacuum and the consequent lack of stoichiometry in the films are avoided.
- High rates of deposition of the compounds are possible.
- The lowest substrate temperature possible is dictated by the condensation temperature of the more volatile component (usually low for O_2, S_2, and Se_2) and as such this method can be used as an efficient technique for the preparation of amorphous films.
- Dopants can be evaporated simultaneously and a uniform dispersal of the dopant can be easily achieved.

Disadvantages

- The use of large volatile flux entails the loss of the volatile element.
- When high deposition rates are required, the use of large amounts of volatile flux leads to high volatile partial pressure (10^{-4} Torr to 10^{-2} Torr), which reduces the mean free path and also scatters the non volatile beam away from the substrate surface. Again the high pressure in the vacuum system reduces the evaporation rate of the non volatile component.
- Because of high volatile elemental pressure, some unreacted volatile element is likely to be entrapped in the growing film thereby changing the film properties, especially at low substrate temperatures.

- Determination of temperature of evaporators for achieving control over incident flux rate that will give rise to a particular composition of the compound can be done only by different trials.

3.4 Experimental technique

In the present study, reactive evaporation- a variant of Gunther's three temperature method, described in section 3.3, is used to prepare compound thin films. In the present work a conventional vacuum system operated in the range of 10^{-5} mbar is used to prepare thin films. The experimental setup, selection of substrates, procedure adopted for cleaning the substrates and evaporators and the detailed process of thin film deposition is presented in the following sections.

3.4.1 Vacuum system

The most important consideration for vacuum deposition techniques is the performance of a vacuum system [3] with a chamber or bell jar. The structure and properties of the film, may be influenced by the ultimate vacuum and residual gases and their partial pressures. In the present work, thin films are prepared in a conventional vacuum system with 12 inch glass bell jar, as shown in Fig 3.7.

The major components of a vacuum system are evaporation chamber, pumping system, vacuum gauges and power supplies. The pumping system consists of an oil diffusion pump [3] backed by an oil sealed rotary pump [3]. Diffusion pump requires a fore vacuum of 10^{-2} mbar which could be achieved by the rotary pump. A water cooled baffle is normally used with the diffusion

pump to keep the oil out of the system. Vacuum produced by this pumping system is better than 10^{-5} mbar.

Fig 3.7 Vacuum system

Inside the evaporation chamber there are provisions for three independent resistively heated sources with transformer capable of supplying 200 A current each. Also there are provisions for ion bombardment, substrate heating and substrate temperature measurements. The pirani gauges (low vacuum gauge) [3] and penning gauge (high vacuum gauge) [3] are used to measure the pressure inside the chamber. The normal pump down time to get ultimate vacuum is around 1 hour. Schematic diagram of the vacuum system used for the preparation of the thin films under study is given in Fig 3.8.

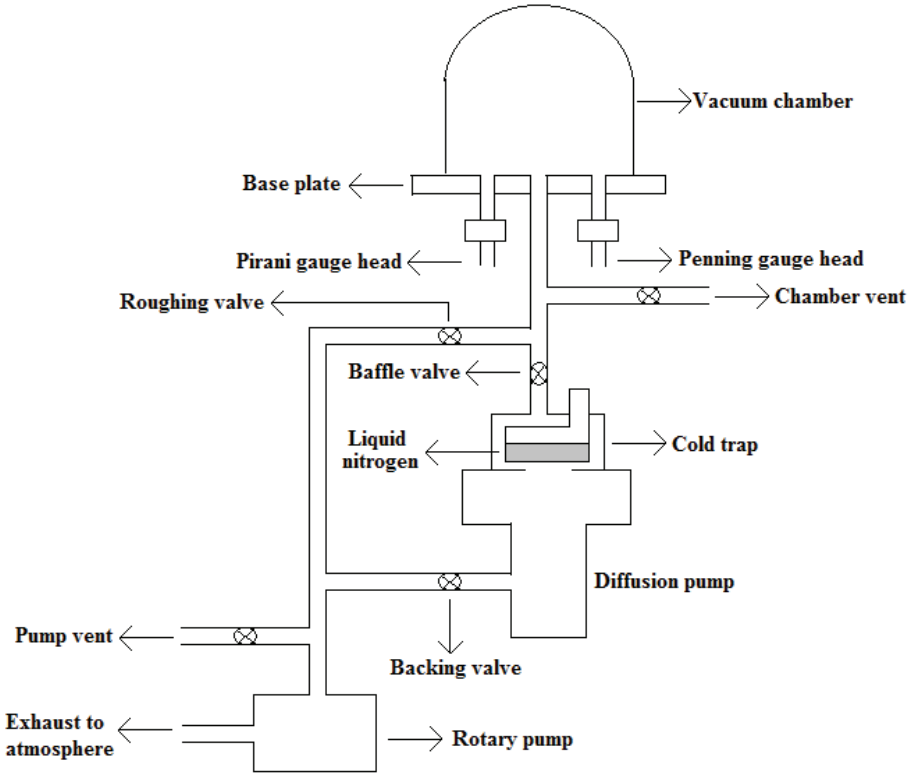

Fig 3.8 Schematic diagram of vacuum system

3.4.2 Selection of substrates

The nature and surface finish of the substrates are extremely important because they greatly influence the properties of the film deposited onto them. Glass, quartz and ceramic substrates are commonly used for polycrystalline thin films. Single crystal substrates of alkali halides, mica, MgO, Si, Ge etc are used for epitaxial growth. The most commonly used glass slides as substrates are of pyrex, soda lime glass, corning glass etc. An important parameter that is to be considered while selecting substrates is the temperature range up to which the substrate is stable. For about 450 $^{\circ}$C glass substrates are stable and for

temperature higher than 450 °C quartz substrates are used. In the present work, ultrasonically cleaned optically flat soda lime glasses are used as the substrates.

3.4.3 Cleaning of substrates

The adhesion of adatom to the substrate surface mainly depends on the cleanliness of the substrate. Thus for an efficient adhesion of atoms, the substrate surface should be very clean. Optically flat glass slides of 3.4 cm x 1.3 cm are used as the substrate. Initially the substrates are cleaned with an industrial detergent. After this they are thoroughly washed in running water followed by distilled water. The slides are then arranged in specially made holder immersed in double distilled water and are subjected to ultrasonic agitation for 15 minutes. This gives a scrubbing effect on the substrates and removes the dust particles which are still adhering to the surface. After cleaning with distilled water, the substrates are dried by blowing hot air onto it. After loading into the vacuum chamber, the substrates are further cleaned by ion bombardment.

3.4.4 Cleaning of evaporators

Contamination of the film is sure to happen if the sources used are not clean. In the present work, the evaporators used are: molybdenum boat (Metal source) and glass crucible kept in molybdenum basket (Chalcogen source). The sources are labelled in Fig 3.9. The molybdenum boat is initially dipped in nitric acid for removal of contaminants. Then it is washed in clean running water and in distilled water. It is then dried by the hot air blower and is connected in between the electrodes in the vacuum chamber. The glass crucible

is cleaned with acetone and is placed in a basket made of molybdenum wire whose ends are connected to the electrodes in the vacuum chamber.

3.4.5 Deposition of thin film

After loading the substrates and the elements for evaporation, the chamber is evacuated initially by the rotary pump. When the pressure inside the vacuum chamber is about 0.05 mbar, roughing valve is closed and the backing valve is opened and the diffusion pump is switched ON. The cooling system is also switched ON. After about 20 minutes the baffle valve is opened. Now the evacuation is done by diffusion pump backed by the rotary pump. After reaching a vacuum of the order of 10^{-5} mbar, substrate heating is started. For this a suitable current is passed through the heater coil. A chromel- alumel thermocouple is used to measure the temperature of the substrates.

High purity (99.999%) materials are used as evaporants. A molybdenum boat is used to evaporate metal. The chalcogen is evaporated from a glass crucible kept in a molybdenum basket. The temperature of the sources and hence the fluxes could be easily controlled by adjusting the currents through the molybdenum boat and molybdenum basket. Schematic diagram of the experimental setup for reactive evaporation is shown in Fig 3.9.

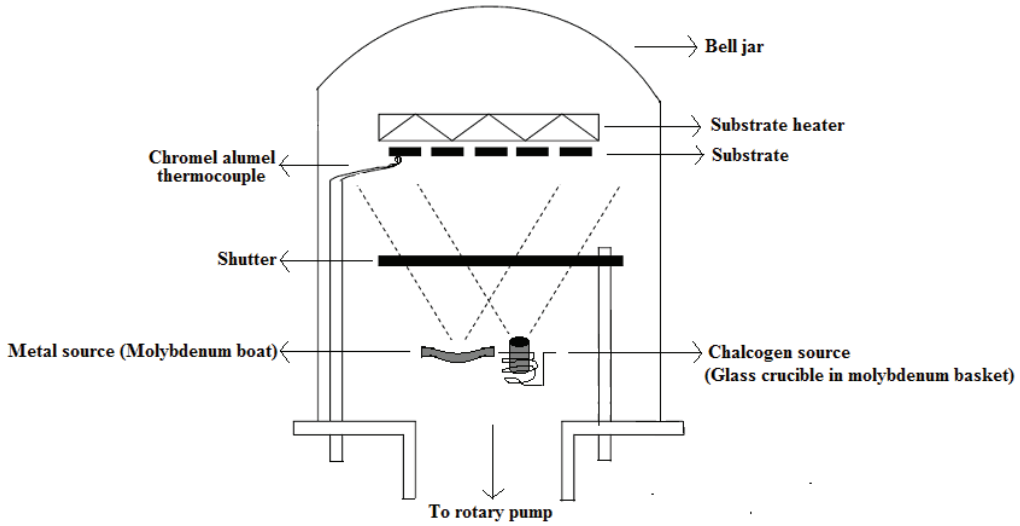

Fig 3.9 Schematic diagram of the experimental setup for reactive evaporation

When the substrates had attained the required temperature, it is maintained at that temperature for 20 minutes. At stable substrate temperature and low pressure, the current through the chalcogen source is switched ON keeping the shutter over both sources. The current is adjusted to a value precalibrated through different trials for obtaining a certain incident flux. After attaining a sufficient atmosphere of chalcogen, the current to the metal source is switched ON and adjusted to the precalibrated value to obtain the required flux. The shutter is then removed so as to allow the atoms of the evaporants from both the sources to reach the substrate and react at the substrate surface to form the compound thin film. Thus the rate of evaporation of the metal and chalcogen is controlled by the current through the sources. The unreacted elemental atoms or molecules will re-evaporate from the surface due to elevated temperature given to the substrate. Care is taken to keep the substrate and the source temperature stable throughout the time of deposition.

On completion of the deposition process, the shutter is put back in position over the sources and the power supply to the sources is switched OFF. The substrate temperature is maintained at the coating temperature for 5 min after deposition to stabilize the reactions. Later, the temperature is reduced stepwise to get good quality thin films. The chamber is opened only after the films are cooled to room temperature. The films thus obtained are handled with care to avoid contamination. Thus by a precise control and optimization of the deposition parameters such as substrate temperature and impingement rates of evaporants, it is possible to deposit stoichiometric compound thin films with extreme purity and crystallinity.

3.5 Characterization tools

The as-prepared thin films are systematically characterized for their structural, morphological, compositional, optical, electrical and thermoelectric properties by various characterization tools. The following section gives a detailed description of the various characterization tools used in the present study, along with a brief account of relevant theory behind each technique.

3.5.1 X-ray diffraction (XRD)

XRD is a versatile and non destructive technique used for the structural characterization of materials. It gives whole range of information about the crystal structure, crystallite size, orientation, chemical composition, stress, strain and defects in thin films.

Suppose that monochromatic X-rays impinge upon the atoms in a crystal lattice as shown in Fig 3.10. The crystal acts as a series of parallel reflecting planes. Each atom in the crystal acts as a scattering centre for X-rays.

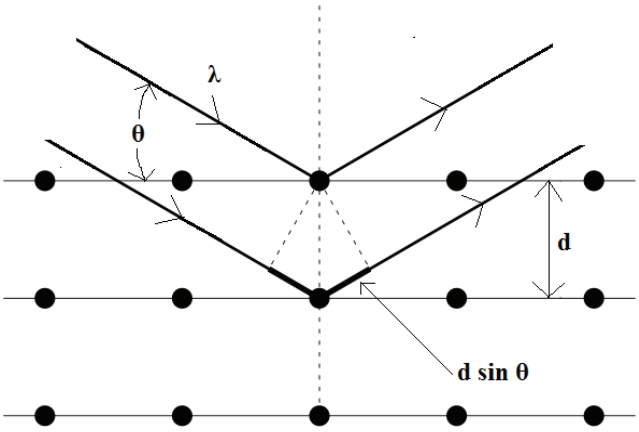

Fig 3.10 Reflection of monochromatic X-rays by successive planes of a crystal

The intensity of the reflected X-rays at certain angles will be maximum when the path difference between the two reflected waves from two different planes is an integral multiple of wavelength of X-ray. This condition is known as Bragg's law and it is expressed as

$$n\lambda = 2d\sin\theta \tag{3.24}$$

where n is the order of reflection, λ is the wavelength of X-ray, d is the interplanar spacing and θ is the glancing angle of incidence of X-rays (Bragg's angle). The reflection takes place for those values of d, θ and λ which satisfies Bragg's law. Bragg's law is the underlying principle of XRD technique [4].

In the present study, X-ray diffraction based on Bragg Brentano geometry [4] as shown in Fig 3.11 is used for diffraction studies. According to Bragg Brentano geometry, the sample is held in the path of monochromatic X-rays and is rotated about an axis, i.e., λ is fixed while θ varies [4]. The X-ray incident with a glancing angle θ on the thin film is detected by a detector at an angle 2θ with the incident direction of X-rays. Since the film and the detector

are rotated at angular velocities ω and 2ω, different sets of parallel atomic planes are exposed to incident radiations for different values of θ. But reflections take place only from those atomic planes for which d and θ satisfy the Bragg's law [4].

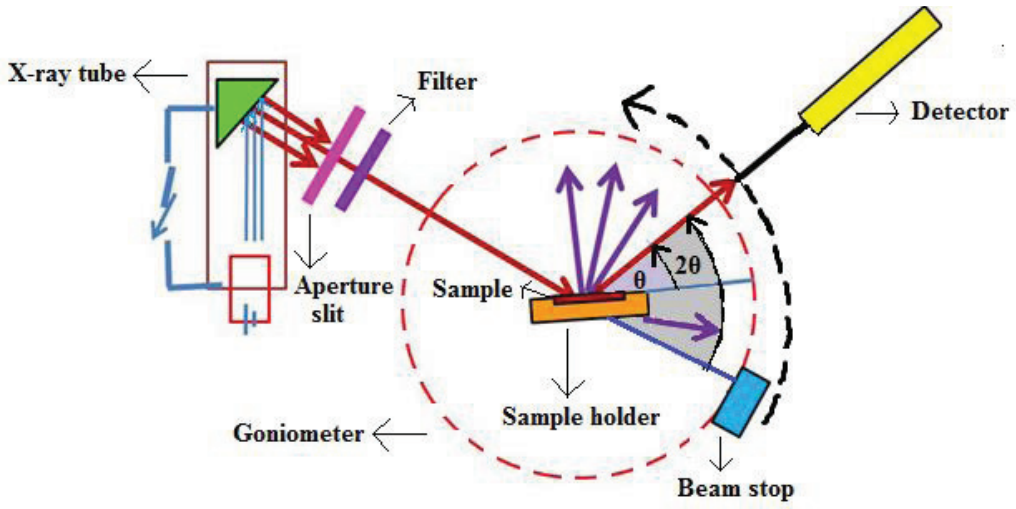

Fig 3.11 X-ray diffraction based on Bragg Brentano geometry

The samples are scanned at a suitable scan range and scan speed. When the scan process is over, the system generates a diffraction pattern (XRD profile) which is a plot of detector angle 2θ along the X axis and reflected intensities along the Y axis. The reflections from the atomic planes appear as diffraction peaks in the XRD profile. By noting the position of these peaks, the d values corresponding to these reflections are calculated using Eq (3.24). The d values are then compared with JCPDS (Joint Committee on Powder Diffraction Standards) data, to identify the phase (chemical composition), crystal structure and the (hkl) planes [4].

Knowing the crystal structure, the lattice parameters can be calculated by using the calculated d values and the corresponding (hkl) values. This helps to find out the distortion in the crystal lattice (distortion parameter), anion displacement and anion-cation bond lengths in the crystal. The crystallite size (D) can be calculated using Scherrer formula [5]

$$D = \frac{0.9\lambda}{\beta \cos\theta} \tag{3.25}$$

where λ is the wavelength of X-ray used, β is the full width at half maximum in radians and θ is the Bragg's angle. Using the value of crystallite size, various microstructural parameters such as dislocation density, number of crystallites per unit area and lattice strain in the sample can be estimated as follows:

- Dislocation density is given by [6]

$$\rho = \frac{1}{D^2} \tag{3.26}$$

- Number of crystallites per unit area is given by [7]

$$N = \frac{t}{D^3} \tag{3.27}$$

  where t is the thickness of the film.

- The lattice strain is given by [8]

$$S = \frac{1}{\sin\theta}\left[\frac{\lambda}{D} - \beta\cos\theta\right] \tag{3.28}$$

In the present work, the thin film samples are analyzed using Rigaku D MaxC X-ray diffractometer with CuK_α (1.5404 Å) as the radiation source. The accelerating voltage is 30 kV and the tube current is 20 mA.

3.5.2 Scanning electron microscopy (SEM)

SEM is one of the most useful and versatile technique used for the investigation of surface morphology, crystalline structure, grain size, orientation of crystallites and microstructural features of solid specimens. It provides a pictorial display of the surface texture of the sample with a high depth of focus. The scanning electron microscope images the sample surface by scanning it with a focused beam of high energy electrons in a raster scan pattern. These electrons interact with the atoms at or near the surface of the sample. As a result of the electron-sample interactions, various types of signals (secondary electrons, back scattered electrons, transmitted electrons, characteristic X-rays, electromagnetic radiations) are generated and are detected by specialized detectors. These signals reveal information about the surface morphology, crystalline structure, grain size, orientation of crystallites and microstructural features of the sample. In SEM, the scattered secondary electrons of energy less than 50 eV are primarily used for imaging the sample surface. These secondary electrons are formed by the interaction of the primary electron beam with the loosely bound electrons of the surface atoms [9]. Schematic diagram of scanning electron microscopy is shown in Fig 3.12.

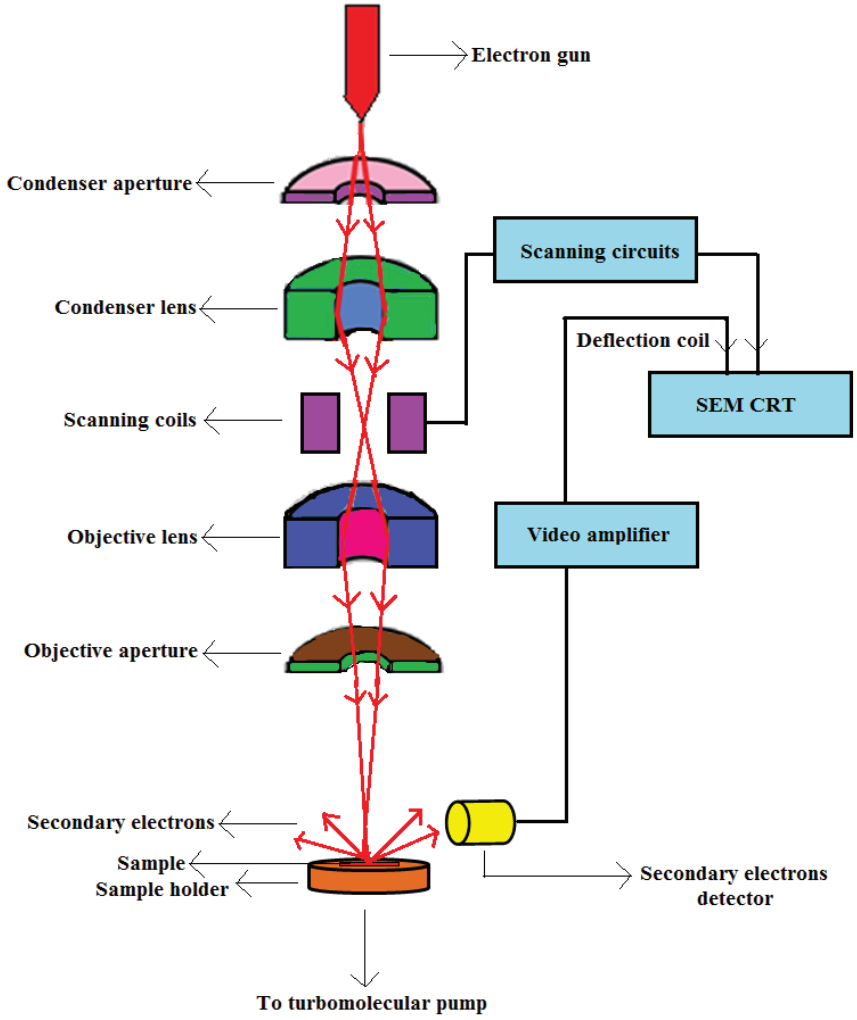

Fig 3.12 Schematic diagram of scanning electron microscopy

The basic instrument consists of an electron gun which produce electron beam of very small diameter of the order of 100 Å. A series of lens system produce a finely focussed electron beam on the specimen surface. The scanning coils at right angles to each other and connected to a scanning circuit,

deflects this electron beam and sweeps it over the sample surface in a rectangular zig zag raster scan pattern. The secondary electrons emitted as a result of the electron-sample interactions are detected by a secondary electron detector which is then amplified by a video amplifier and fed to a cathode ray tube (CRT). As the electron beam scans the sample surface there will be a change in the secondary electron emission according to the surface texture. The scanning picture observed on the CRT represents the image of the surface [9]. The CRT is scanned synchronously with the electron beam. The brightness of CRT is modulated by the signals which arise from the interaction of the electron beam with the sample surface which is probed. Thus the strength of this signal is translated into image contrast. The secondary electrons that are collected by the secondary electron detector are used as the contrast signal. The yield of secondary electrons depends on the nature of the sample surface and on its inclination with respect to the probing electron beam. In order to avoid scattering of the electron beam and the contamination of electron gun and other components, the SEM analysis is carried out in ultra high vacuum created by using a turbomolecular pump [9].

In the present work, SEM images of the thin film samples are recorded using a Cambridge instrument model no: S-360 machine.

3.5.3 Atomic force microscopy (AFM)

AFM is a very high resolution type of scanning probe microscopy used for the topographical imaging of materials. It has the ability to create two dimensional and three dimensional micrographs with resolution down to nanometer and angstrom scales. AFM can also be used to determine the root

mean square (RMS) value of surface roughness of the sample [10]. Schematic diagram of atomic force microscopy is shown in Fig 3.13.

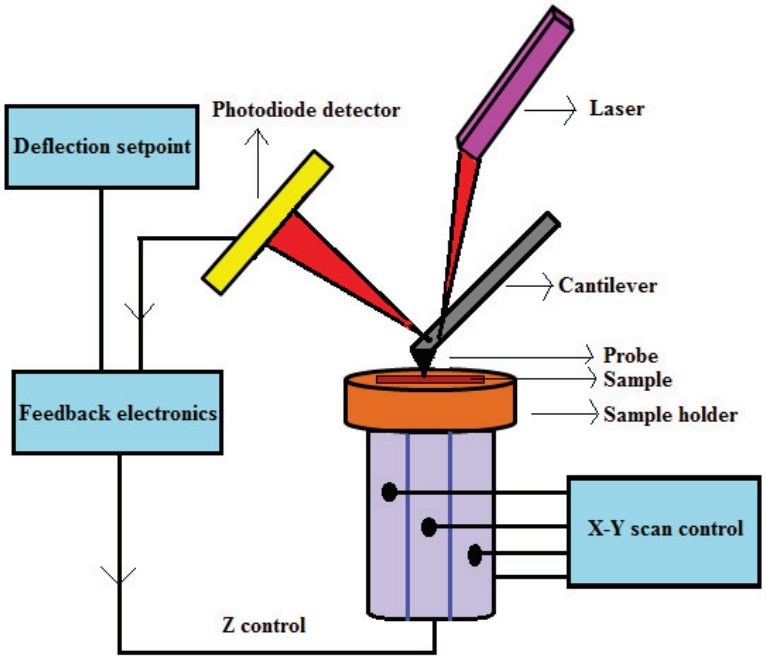

Fig 3.13 Schematic diagram of atomic force microscopy

The key element of AFM is its solid microscopic force sensor or cantilever which is typically silicon or silicon nitride with a tip radius of curvature of the order of nanometer. At the end of the cantilever, there is a sharp tip (probe) which is used to scan the surface of the sample. The sample is mounted on a tripod of three piezoelectric crystals (piezoelectric scanner) with each responsible for scanning in the X, Y and Z directions. The fine and precise movement of the piezoelectric scanner on the application of voltage ensures precise scanning. On the back of the cantilever, a laser beam is

positioned with a spot visible on the head's filter screen [10]. The feedback mechanism adjusts the tip to sample distance and thereby maintains a constant force between the tip and the sample. When the tip is brought close to the sample surface, the cantilever deflects due to the forces between the tip and the sample. This deflection is measured using the laser spot reflected from the top surface of the cantilever into a photodiode detector. Thus by scanning the sample surface with the cantilever and by recording the deflection of the cantilever, the local height of the sample is measured. The local sample height versus horizontal probe position generates two dimensional and three dimensional topographic images of the sample surface [10].

AFM can be operated either in contact mode or non contact (tapping) mode. In contact mode, the tip of the cantilever is dragged across the sample and the shape of the sample surface is imaged using the deflection of the cantilever. In non contact or tapping mode, the tip of the cantilever undergoes up and down oscillations at or near its resonance frequency. When the tip is close to the sample surface, the amplitude of oscillation changes due to the interaction of forces acting on the cantilever. The shape of the sample surface is imaged by measuring the change in the amplitude of oscillation of the cantilever [10].

In the present work, an AFM nanoscope E, Digital Instruments with a silicon nitride cantilever is used to probe different portions of the thin film sample surface in contact AFM mode.

3.5.4 Energy dispersive analysis of X-rays (EDAX)

EDAX which is also referred to as EDX or EDS is a non destructive technique used for identifying the elemental composition of the sample [11]. It identifies the constituent elements in the sample along with their atomic percentage. Usually, the EDAX system works as an integrated feature of a SEM and cannot be operated in its own without the latter. Hence the schematic diagram of EDAX is the same as that of SEM given in Fig 3.12.

In EDAX, the sample is first viewed by SEM, and a tiny spot (area of about 1 μm) on the sample surface is selected for compositional analysis. For EDAX, the electron beam is collimated into a size of about 1 μm cross section and it is focused on the sample surface exactly on the selected tiny spot to be analysed. The electron beam incident on the sample knocks out some of the electrons belonging to the inner shells of the atoms comprising the sample thereby leaving a vacant position in the inner shell. This vacancy is later filled by the jump of a high energy electron from an outer shell. The process of transfer of electron from a high energy outer shell to a low energy inner shell results in the emission of X-rays characteristic of atoms in the irradiated area, as shown in Fig 3.14, with energies that are unique to the ionized atom. These X-rays are used for EDAX analysis of the sample [11].

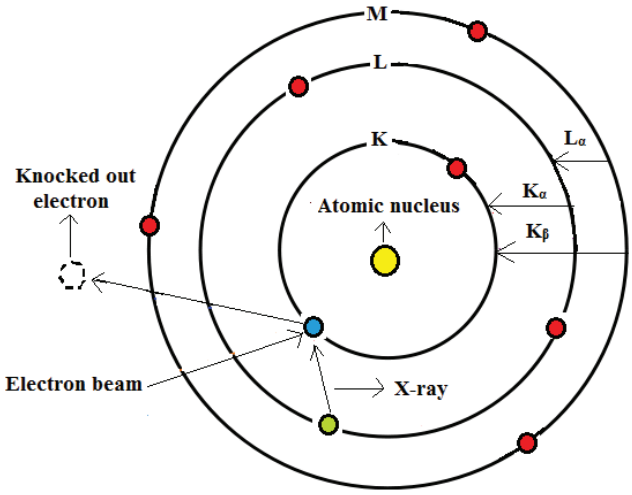

Fig 3.14 Principle of energy dispersive analysis of X-rays

By an analysis of energies of the emitted X-rays, the atoms from which the X-ray is emitted can be identified and from the count of the number of X-rays emitted, the concentration of atoms in the sample can be determined. The X-ray energies are measured by a semiconductor detector which initially generates a charge pulse proportional to the X-ray energy. Subsequently, it converts charge pulse into a voltage which is then amplified and digitalized [11].

The output of EDAX analysis is an EDAX spectrum- a plot of X-ray energy along the X axis and count of the number of X-rays emitted from the constituent element of the sample along the Y axis. EDAX spectrum shows how often each energy level receives X-rays. Each element in the sample has a unique atomic structure which results in a unique set of peaks in the EDAX spectrum. This helps in identifying the constituent elements of the sample. The more concentrated element in the sample will have a higher peak in the

spectrum [11]. EDAX spectrum also reveals the type of X-ray corresponding to each peak. For example, L_α peak corresponds to X-rays emitted by the transition of an electron from M shell to L shell whereas K_α peak and K_β peak corresponds to X-rays emitted by the transition of an electron from L shell to K shell and from M shell to K shell respectively [11]. These transitions are illustrated in Fig 3.14.

In the present work, EDAX measurement is done on different points of thin film samples using LINK 10000 Cambridge instruments and the average elemental ratio is taken to minimize error.

3.5.5 X-ray photoelectron spectroscopy (XPS)

XPS is a very useful non destructive spectroscopic technique used to get information about the elemental composition, empirical formula, chemical and electronic state of element present in the sample [12].

In XPS, the sample is irradiated by a source of monochromatic X-rays. The X-rays cause photoionisation of atoms in the sample which results in the emission of photoelectrons from the surface atoms. The binding energy of each core electron possessed by each surface atom is a characteristic of the individual atom to which it is bound. The elemental compositional analysis is done based on the information on the binding energy of the electrons in the sample [12]. Since energy of a particular X-ray wavelength is known, the electron binding energy of each of the emitted electron can be determined using the Einstein's relation

$$E_{Binding} = h\nu - E_{Kinetic} - \Phi \tag{3.29}$$

where $E_{Binding}$ is the binding energy of orbital electrons, $E_{Kinetic}$ is the kinetic energy of photoelectrons, hν is the energy of the X-ray photon and Φ is the work function of the spectrometer [12]. The principle of X-ray photoelectron spectroscopy is shown in Fig 3.15.

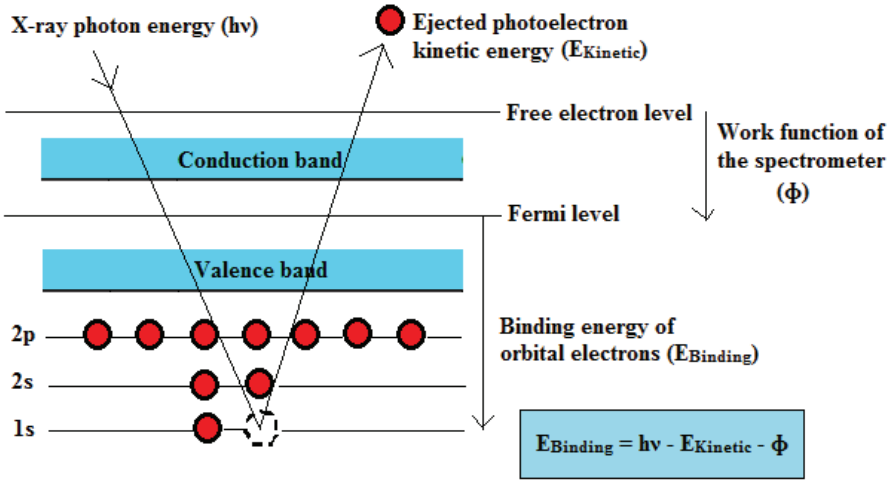

Fig 3.15 Principle of X-ray photoelectron spectroscopy

The output of XPS analysis is the XPS spectrum- a plot of binding energy of the electrons detected along the X axis and the number of electrons detected (count rate) along the Y axis. Each element produces a characteristic set of XPS peaks at characteristic binding energy values that directly identify each element that exist in or on the surface of the sample being analyzed. These characteristic peaks correspond to the electronic configuration of electrons within the atoms. The number of electrons detected in each of the characteristic peaks is directly related to the amount of element within the area irradiated. The composition of the sample is readily determined from the positions of the peaks in the XPS spectrum and the chemical bonding from

their positions or shifts and the shape of the XPS peaks [12]. Schematic diagram of X-ray photoelectron spectroscopy is shown in Fig 3.16.

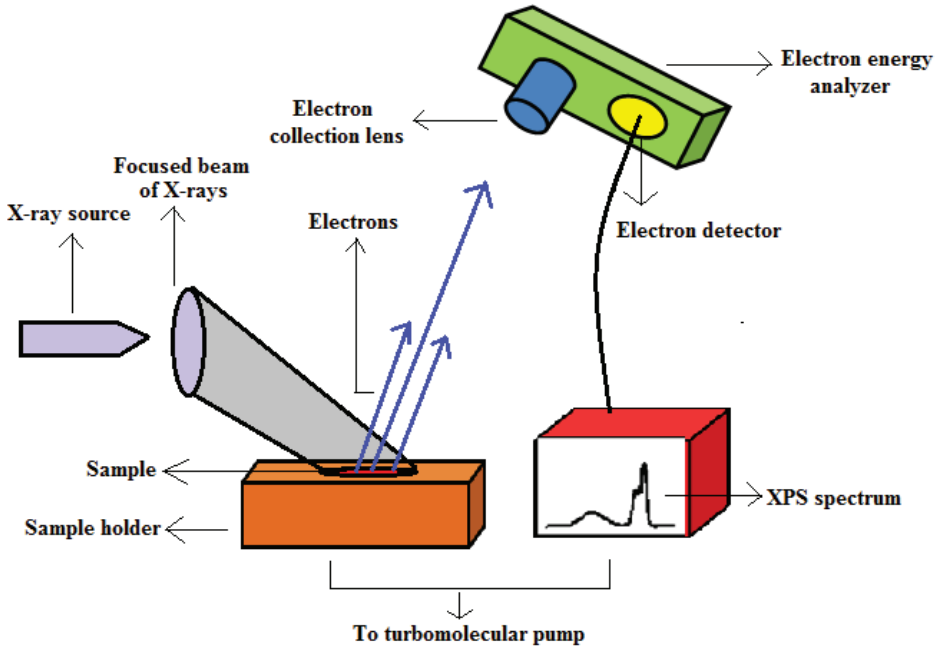

Fig 3.16 Schematic diagram of X-ray photoelectron spectroscopy

The basic instrument consists of a source of X-rays which produces monochromatic X-rays. The X-rays are focused onto the sample surface. Photoionisation then takes place on the sample surface and the resultant photoelectrons are collected by the electron collection lens of the electron energy analyzer. The function of electron energy analyzer is to disperse the photoelectrons emitted from the specimen according to their energies. Followed by energy dispersion, the photoelectrons are made to enter an electron detector. Here each incident photoelectron causes a secondary electron cascade giving an output pulse of upto 10^8 electrons with less than 0.1 μs. The

electron detector can then be operated by recording the count rate of electrons detected versus binding energy of the electrons detected. The output of electron detector is in the form of discrete pulses (XPS spectrum) and it is recorded on a computer. In order to avoid contamination, the XPS analysis is carried out in ultra high vacuum created by using a turbomolecular pump [12].

In the present work, XPS analysis is done on the thin film samples using an ESCA machine of VSW scientific instruments with Mg and Al twin anode X-ray source operated at an accelerating voltage of 15 kV and tube current 20 mA. AlK_{α} (1486.6 eV) is used as the source of radiation and the C1s peak is used for the calibration of photoelectron spectrometer.

3.5.6 Thickness measurement

Thickness is one of the most significant film parameters that strongly influence the film properties. The Stylus profiler is an advanced thin and thick film step height measurement tool capable of measuring step even below 100 Å with an accuracy of ±1 Å and maximum sensitivity of 20 Å. In this method, the thickness of the film is measured by scanning the step region in the film by a probe (stylus). The step can be achieved by masking a portion of the film at the time of deposition or by removing a part of the deposited film from the substrate. The high precision stage moves the sample beneath the diamond tipped stylus according to the user programmed scan length, speed and stylus force. Then the instrument electromechanically measures the thickness of the sample by monitoring the vertical motion of the stylus over the step [13]. Schematic diagram of stylus profiler is shown in Fig 3.17.

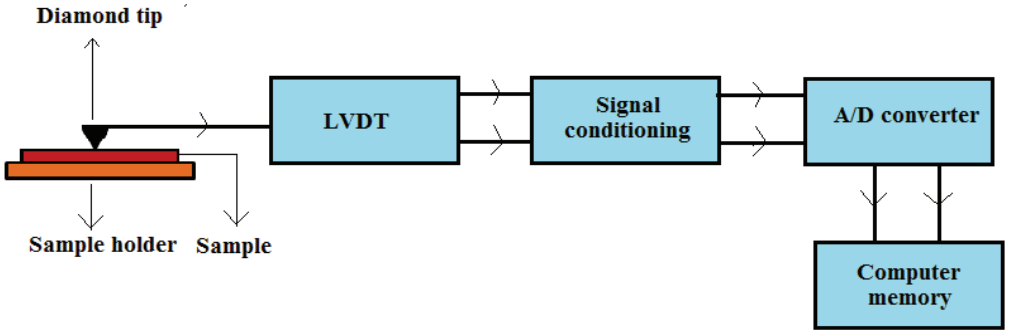

Fig 3.17 Schematic diagram of stylus profiler

The system known as talysurf consists of a diamond with a rounded or four sided pyramid tip or probe which can be mechanically driven over the sample. The stylus is mechanically coupled to the core of an LVDT (Linear Variable Differential Transformer). As the stage moves the sample, the stylus move over the sample surface. The stylus undergoes vertical translation due to variations on the sample surface. As the core position of LVDT changes, the electrical signals corresponding to the stylus movement are produced. The LVDT scales an AC reference signal proportional to the position change. This signal in turn is conditioned and converted to a digital format through a high precision integrating analog to digital converter. The digitalized signal from performing a single scan is stored in computer memory for display. The display provides an image of the sample surface by plotting the sample height against the lateral dimension. Once the image is levelled, it gives information regarding thickness of the sample [13].

In the present work, thicknesses of the thin film samples are measured using a Veeco Dektak 6M stylus profiler.

3.5.7 Determination of optical parameters

The study of the optical properties of solid is a powerful tool in elucidating the electronic and atomic structure of solids. The measurement of optical parameters (refractive index (n), extinction coefficient (r), absorption coefficient (α), real part (ε_1) and imaginary part (ε_2) of the complex dielectric constant) as a function of wavelength can provide a better understanding of the optical properties of the material because these parameters are the key factors that decide the application of a material in optical communication and device design. Hence the measurement of these quantities is performed by recording the optical absorption, transmission and reflection spectra of thin films using UV-Vis-NIR spectrophotometers. Schematic diagram of a UV-Vis-NIR spectrophotometer is shown in Fig 3.18.

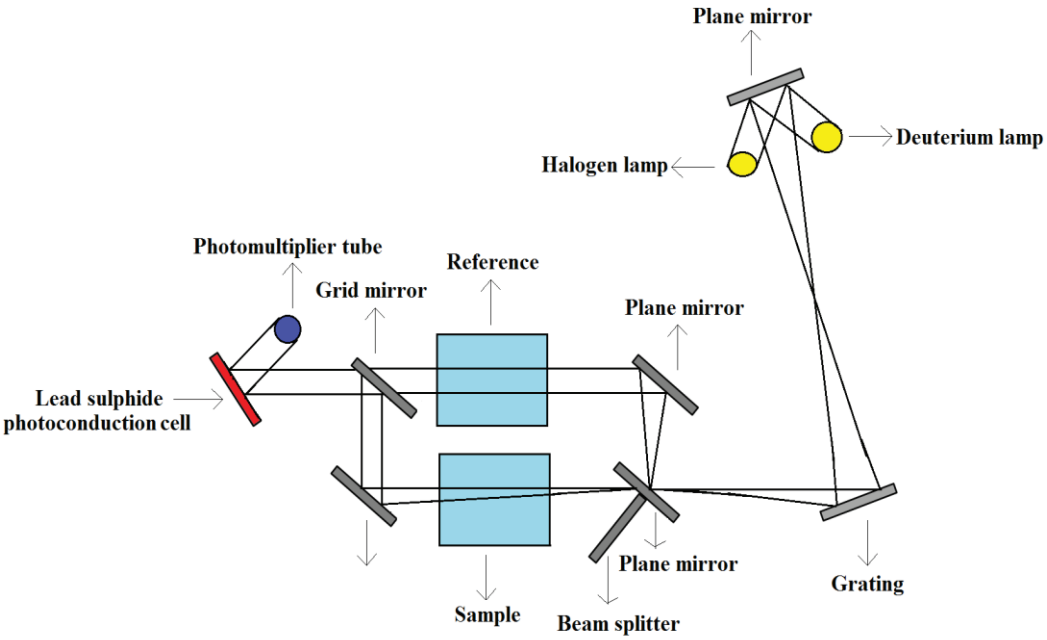

Fig 3.18 Schematic diagram of UV-Vis-NIR spectrophotometer

The spectrometer has two light sources, namely, a deuterium lamp (190 nm to 350 nm) and a halogen lamp (330 nm to 2500 nm) and two detectors, namely, a photomultiplier tube and a lead sulphide photoconduction cell. The light from the source is made to fall on the grating. The grating is rotated about an axis in such a way that the angle of incidence of the light beam from the light source gradually changes. The output beam from the grating will contain different wavelength which are spatially separated. At a particular angle of incidence of light on the grating, only one wavelength will pass through the slit such that the output from the slit will be monochromatic. Different wavelengths are obtained in accordance with different angle of incidence. The beam is split by means of a beam splitter. One of the beams passes through the reference and the other through the sample for which the spectrum is to be recorded. The phase and intensity of the transmitted beam from both the reference and sample are detected. The radiation in UV-Vis region is detected by the photomultiplier tube and the radiation in the NIR region is detected by the lead sulphide photoconduction cell. By comparing the data using a phase sensitive amplifier, the spectrum of the sample is displayed and recorded [14].

In absorption studies, the output of the spectrophotometer is an absorbance spectrum of the thin film sample - a plot of wavelength of incident light in nanometers along the X axis and absorbance (αt) of the sample along the Y axis. The absorbance spectrum is analyzed to determine the absorption coefficient (α), provided the thickness t of the sample is known. The optical band gap (E_g) of the thin film sample is be calculated using the Tauc relation

$$\alpha h\nu = A\left(h\nu - E_g\right)^n \tag{3.30}$$

for direct transitions, where n can take values 1/2 and 3/2 for direct allowed and direct forbidden transitions respectively [15]. Also

$$\alpha h\nu = A\left(h\nu - E_g \pm E_p\right)^n \tag{3.31}$$

for indirect transitions, where n can take values 2 and 3 for indirect allowed and indirect forbidden transitions respectively [15]. Here n is an integer that determines the type of electronic transition causing the absorption. If the plot of hν along the X axis and $(\alpha h\nu)^2$ along the Y axis gives a linear portion then the sample must possess a direct allowed transition and the value of X intercept of the tangent to the plot gives the band gap of the sample. Since the absorption edge occur at the wavelength corresponding to the band gap energy, the optical band gap E_g can be calculated from the absorption edge using the Planck relation [16]

$$E_g = \frac{hc}{e\lambda} \cong \frac{1242}{\lambda} eV \tag{3.32}$$

In transmission studies, the output of the spectrophotometer is a transmission spectrum of the thin film sample - a plot of wavelength of incident light in nanometers along the X axis and transmission (T%) of the sample along the Y axis.

Consider a system of an absorbing thin film on a thick finite transparent substrate as shown in Fig 3.19. Let the film has thickness t and complex refractive index $n^* = n\text{-}ir$, where n is the refractive index and r is the extinction coefficient. r can be expressed in terms of the absorption coefficient (α) and wavelength of light (λ) using the relation [17]

$$r = \frac{\alpha\lambda}{4\pi} \tag{3.33}$$

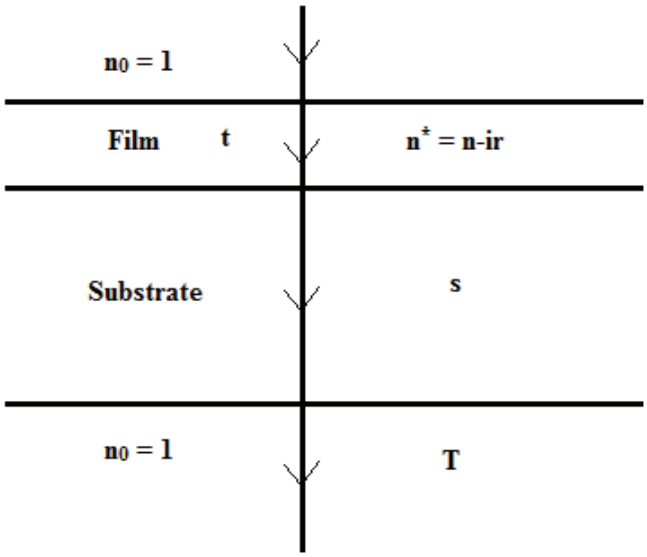

Fig 3.19 System of an absorbing thin film on a thick finite transparent substrate

The transparent substrate has a thickness of several orders of magnitude larger than t and has a refractive index s and absorption coefficient $\alpha_s = 0$. The system is surrounded by air with refractive index $n_0 = 1$. If the substrate and film surfaces are perfectly smooth and the film thickness t is uniform, interference effects give rise to a spectrum as shown in Fig 3.20.

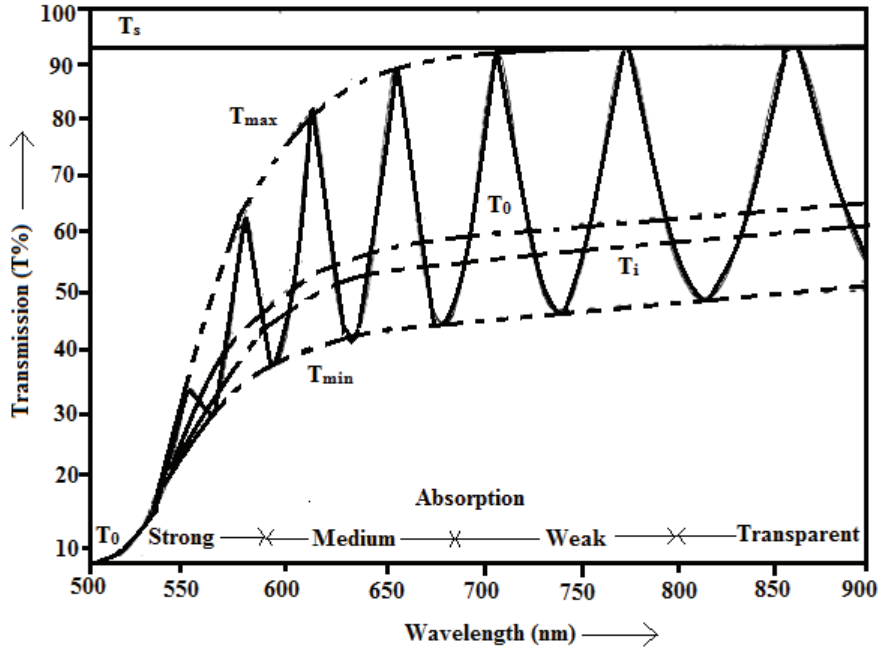

Fig 3.20 Transmission spectrum of a thin film of uniform thickness

These fringes of the transmission spectrum of a thin film surrounded by non absorbing media can be used to calculate the refractive index (n) and extinction coefficient (r) of the thin film sample using Swanepoel's method [18]. In this method, the interference fringes of the transmission spectrum alone are used to deduce the n and r of the thin films to an accuracy of the order of 1% which is much better than the accuracy of elaborate iteration methods.

The spectrum shown in Fig 3.20 is roughly divided into four regions, namely strong, medium and weak absorption regions and transparent regions [18]. In transparent region $\alpha = 0$ and the transmission is determined by n and s through multiple reflections. In the region of weak absorption α is small but starts to reduce the transmission. In the region of medium absorption α is large and the transmission decreases mainly due to the effect of α. In the region of

strong absorption, the transmission decreases drastically due to the influence of α [18]. A suitable envelope is drawn to find the interference maxima (T_{max}) and interference minima (T_{min}). In Fig 3.20, T_i denotes a curve passing through the inflection points of the fringes and it represents the interference free transmission. T_0 denotes a single curve to which T_{max}, T_i and T_{min} converge for very large α and T_S denotes the interference free transmission by considering the thick substrate alone in the absence of the film. The detailed procedure for the determination of n and r from the spectrum shown in Fig 3.20 using Swanepoel's method is given in the reference [18].

Knowing the values of n and r, it is possible to evaluate the following optical parameters:

- Real part (ε_1) and imaginary part (ε_2) of the complex dielectric constant is given by [19]

$$\varepsilon_1 = n^2 - r^2 \tag{3.34}$$

$$\varepsilon_2 = 2nr \tag{3.35}$$

- Loss factor or tan δ (measure of dissipation of electromagnetic energy into heat in the material) is given by [19]

$$\tan\delta = \frac{\varepsilon_2}{\varepsilon_1} \tag{3.36}$$

- Quality factor or Q factor (inverse of the measured tan δ) is given by [20]

$$\text{Q factor} = \frac{\varepsilon_1}{\varepsilon_2} \tag{3.37}$$

- Optical conductivity or $\sigma_{Optical}$ (measure of optical response of the material) is given by [21]

$$\sigma_{Optical} = \frac{\alpha n c}{4\pi} \tag{3.38}$$

In the present work, the optical absorption, transmission and reflection of the thin film samples are recorded in the wavelength range from 2500 nm to cut-off using JASCO V-570 UV-Vis-NIR spectrophotometer.

3.5.8 Photoconductivity measurement

When a light beam of energy hν greater than the band gap E_g is incident on a semiconductor, the electrons gets excited across the energy gap. This leads to an increase in the number of free charge carriers (electrons and holes) and hence an increase in electrical conductivity. This phenomenon is termed as photoconductivity [22]. Thus photoconductivity is the property by which a material becomes electrically conductive due to the absorption of electromagnetic radiation or it is the increase in the electrical conductivity in a material due to absorption of light. Photoconductivity depends on temperature, intensity of excitation source, internal electric field distribution, mobility and concentration of charge carriers and their recombination time [22]. The basic theory of photoconductivity has already been discussed in chapter 2. Measurement of photoconductivity gives information about recombination channels and traps. Schematic diagram of photoconductivity measurement setup is shown in Fig 3.21.

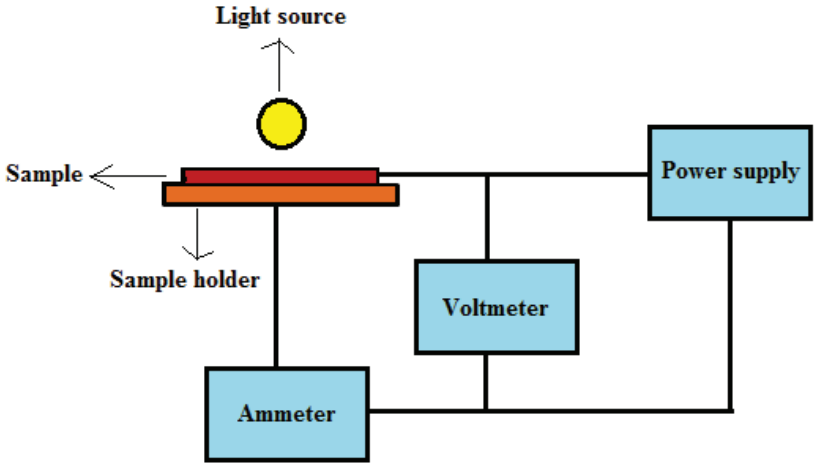

Fig 3.21 Schematic diagram of photoconductivity measurement setup

The sample is placed on a sample holder with silver paste applied at the ends of the sample for ohmic contact. A constant DC bias voltage is applied across the sample. Initially, the light source is switched OFF and the dark current (I_D) across the sample is measured for a given period of time. Later, the light source is switched ON. On illumination, the photocurrent (I_L) across the sample is measured for a given period of time. Then the light source is switched OFF and the decay current is measured for a given period of time. The rise and decay of photocurrent with time is given by Eq (3.39) and Eq (3.40) respectively.

$$I = I_0\left[1-\exp\left(-\frac{t}{\tau_d}\right)\right] \tag{3.39}$$

$$I = I_0\exp\left(-\frac{t}{\tau_d}\right) \tag{3.40}$$

where I is the photocurrent at time t, I_0 is the photocurrent at t = 0 and τ_d is the charge carrier lifetime [23]. The Eq (3.39) and Eq (3.40) holds good only when the charges are not trapped i.e., only when the decay of photocurrent is exponential. When the charge carriers are trapped, then the decay of photocurrent is non exponential. In such cases the decay curves are fitted by an expression of the type [23]

$$I = I_0(1+bt)^{-c} \tag{3.41}$$

where b and c are constants. The charge carrier life time is given by

$$\tau_d = -\left[\frac{1}{I^*_{ph}}\left(\frac{dI_{ph}}{dt}\right)\right]^{-1} \tag{3.42}$$

where I_{ph}^* is the maximum photocurrent at t = 0 for a given applied voltage [24]. The photoresponse of the sample is studied by plotting the time along the X axis and photocurrent along the Y axis. The photosensitivity (PS) of the sample is calculated as [25]

$$PS = \frac{I_L - I_D}{I_D} \tag{3.43}$$

In the present work, the photocurrent of the thin film sample is measured at room temperature using a Keithley 2611A source meter. An FSH lamp (82 V, 300 W) is used as the source of illumination.

3.5.9 Photoluminescence measurement

When light of sufficient energy is incident on a material, the electrons in the material absorb the incident photons and get excited to higher electronic

states. However, the distribution of electrons in the excited states is no longer in equilibrium. Eventually, these electrons in the excited states undergo a non radiative relaxation to conduction band and thereafter make a radiative relaxation to valence band by emitting light. This spontaneous emission of light from a material under optical excitation is referred to as photoluminescence [26] and it is illustrated in Fig 3.22. Photoluminescence depends on the nature of the optical excitation and the density of photoexcited electrons. Various types of luminescence mechanisms are already discussed in chapter 2.

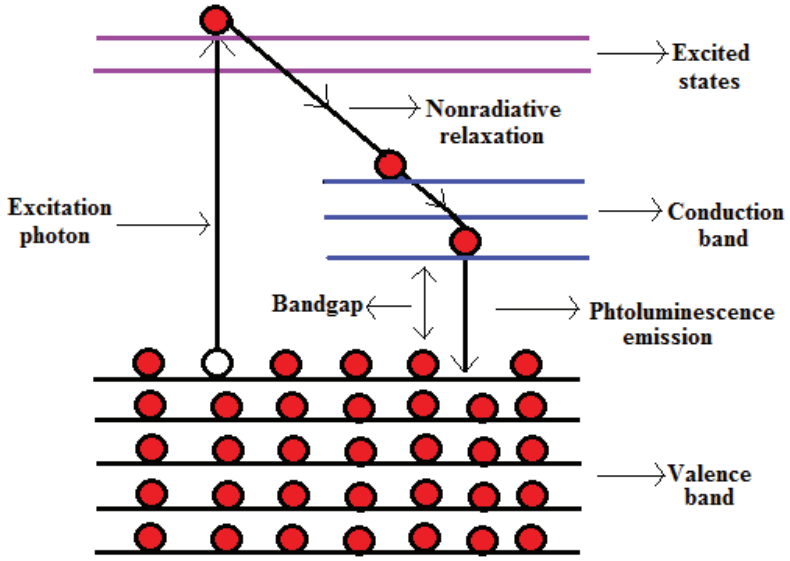

Fig 3.22 Principle of photoluminescence emission

Photoluminescence spectroscopy is a very simple, versatile and non-destructive method of probing the radiative levels and electronic structure of materials. It helps in the determination of band gap, detection of impurity levels and defects, identification of the surface and interface roughness and also the quantification of purity, crystalline quality and recombination

mechanism of semiconductors [26]. The output of photoluminescence spectroscopy is the photoluminescence spectrum that gives precise information on the transition energies, which can be used to determine energy levels available to electrons in the material. The intensity of photoluminescence signal is a measure of the relative rates of radiative and nonradiative recombination, which depends on the density of nonradiative interface states. A strong photoluminescence response corresponds to the high quality surface of the material [26]. Schematic diagram of photoluminescence measurement setup is given in Fig 3.23.

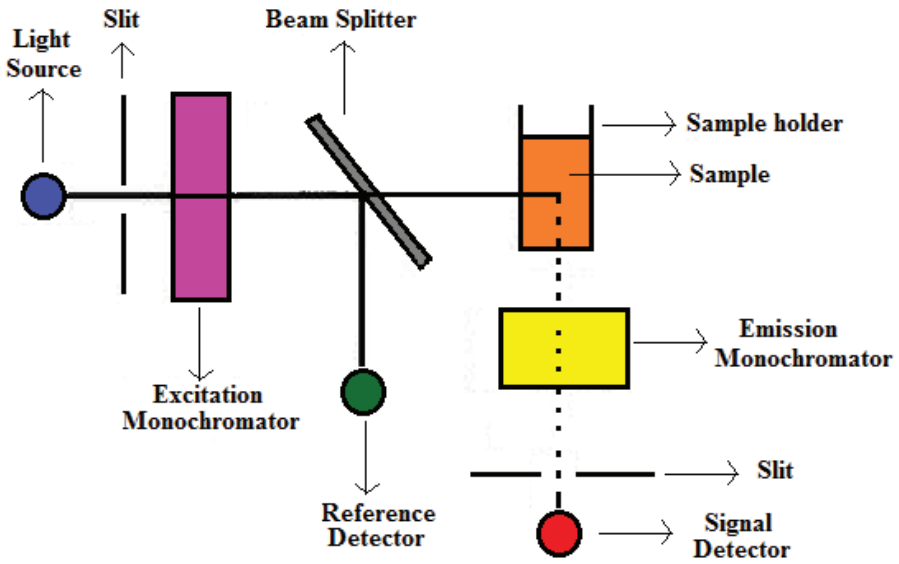

Fig 3.23 Schematic diagram of photoluminescence measurement setup

The source of light is a 150 W ozone free xenon arc lamp. A 180 W power supply supplies the start up voltage to the lamp and then holds the lamp steady at 12 V. The continuous light from the lamp is focused on the entrance slit of the excitation monochromator. The excitation monochromator selects a

band of wavelengths. This monochromatic excitation light is directed onto the sample and about 8% of the monochromatic excitation light is split off using a beam splitter to the reference detector. The reference detector is a UV enhanced silicon photodiode which monitors the xenon lamp in order to correct for wavelength and time dependent output of the lamp. The width of the slit on the excitation monochromator determines the bandpass of light incident on the sample [26].

When the monochromatic excitation light is incident on the sample, it emits luminescence. The luminescence is then directed onto the emission monochromator which selects a band of wavelengths and shines them onto a signal detector. The width of the slit on the emission monochromator controls the intensity of the luminescence signal recorded by the signal detector. The signal detector is a photomultiplier tube which sends the signal to a photocounting module. The signal from the detector is reported to a system controller and host computer with which data is recorded and presented using special software. The photoluminescence spectrum generated on the computer is obtained by rotating the grating and recording the intensity values at each wavelength [26].

In the present work, the photoluminescence spectrum of the thin film sample is recorded at room temperature using FluoroMax-3 spectrofluorometer that functions under the control of DataMax Spectroscopy software. The excitation source used is a 150 W Xenon arc lamp.

3.5.10 Conductivity type measurement

The hot probe method is a simple and convenient technique used to determine the type of conductivity of thin films. It is based on the thermoelectric principle [27] according to which when a temperature difference ΔT is applied between the ends of the sample, an emf of SΔT millivolts, where S is the Seebeck voltage is developed as shown in Fig 3.24. The type of conductivity of the sample is thereby determined by the sign of Seebeck voltage.

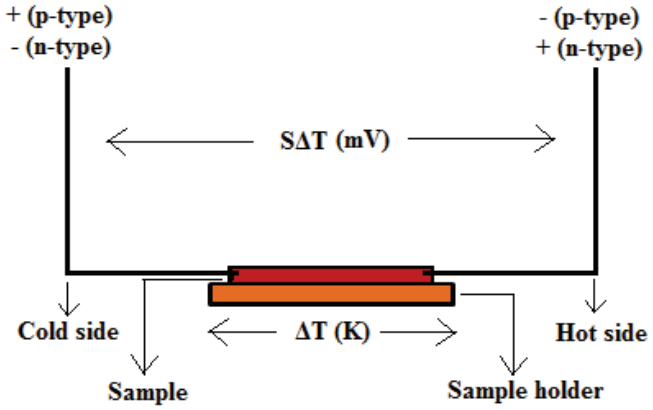

Fig 3.24 Schematic diagram of hot probe measurement setup

3.5.11 Hall measurement

When a magnetic field is applied perpendicular to a current carrying conductor, a voltage is developed across the sample in a direction perpendicular to both the current and the magnetic field. This phenomenon is called Hall effect. The voltage developed is called Hall voltage [28]. The origin

of Hall effect, determination of Hall coefficient and the applications of Hall measurement has already been discussed in chapter 2.

In the present study, the Van der Pauw method [29] is used to determine the Hall coefficient of the sample. This method can provide accurate measurements on the properties of the sample, provided the sample satisfies the following criteria [29]:

- The sample must have a flat shape of uniform thickness.
- The sample needs to be two dimensional i.e., thickness of the sample must be less than its length and width.
- The sample must not have any isolated holes.
- The sample must be homogeneous and isotropic.
- The sample must be a square shaped with all four ohmic contacts at the edges of the sample.
- The area of any individual contact must be an order of magnitude smaller than the area of the entire sample.

The objective of Hall measurement in the Van der Pauw method is to determine the Hall coefficient and hence the charge carrier concentration and charge carrier mobility in the material by measuring the Hall voltage V_H. The measurement of Hall voltage consists of a series of voltage measurements with a constant current I and a constant magnetic field B applied perpendicular to the plane of the sample [29]. Schematic diagram of Hall measurement setup in van der pauw method is shown in Fig 3.25.

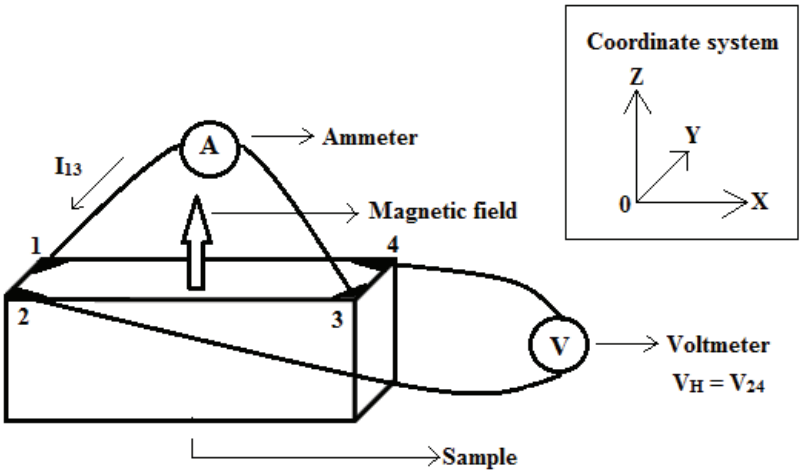

Fig 3.25 Schematic diagram of Hall measurement setup in Van der Pauw method

The sample of thickness t with silver paste applied at all the four corners 1, 2, 3 and 4 is subjected to a magnetic field B that acts perpendicular to the plane of the sample. To measure V_H, a current I is passed through the opposing pair of contacts 1 and 3 and the corresponding Hall voltage which is $V_H = V_{24}$ is measured across the remaining pair of contacts 2 and 4. Once V_H is measured, the Hall coefficient R_H can be calculated as [30]

$$R_H = \frac{V_H}{I}\frac{t}{B} \tag{3.44}$$

Using the value of R_H, the charge carrier concentration (p or n) can be calculated. By knowing the charge carrier concentration and electrical conductivity (σ) of the sample, the mobility (μ), effective mass (m^*), lifetime (τ) and mean free path (l) of the charge carrier can be calculated using the equations discussed in chapter 2.

In the present work, Hall measurement is performed on the thin film samples using ECOPIA HMS-3000 Hall measurement system. The system includes a software with I-V curve capability for checking the ohmic integrity of the sample contacts. The sample is square shaped with silver paste applied on all the four corners. The measurement is performed at room temperature under a magnetic field of 0.8 T.

3.5.12 Thermoelectric power measurement

The ratio of the voltage developed (ΔV) to the temperature gradient (ΔT) is called the thermoelectric power (S) or Seebeck coefficient and it is given by [31]

$$S_{Measured} = \frac{\Delta V}{\Delta T} \tag{3.45}$$

The principle of thermoelectrics for power generation and refrigeration has already been discussed in chapter 1. Schematic diagram of thermoelectric power measurement setup in the temperature range from 4 K to 300 K is given in Fig 3.26.

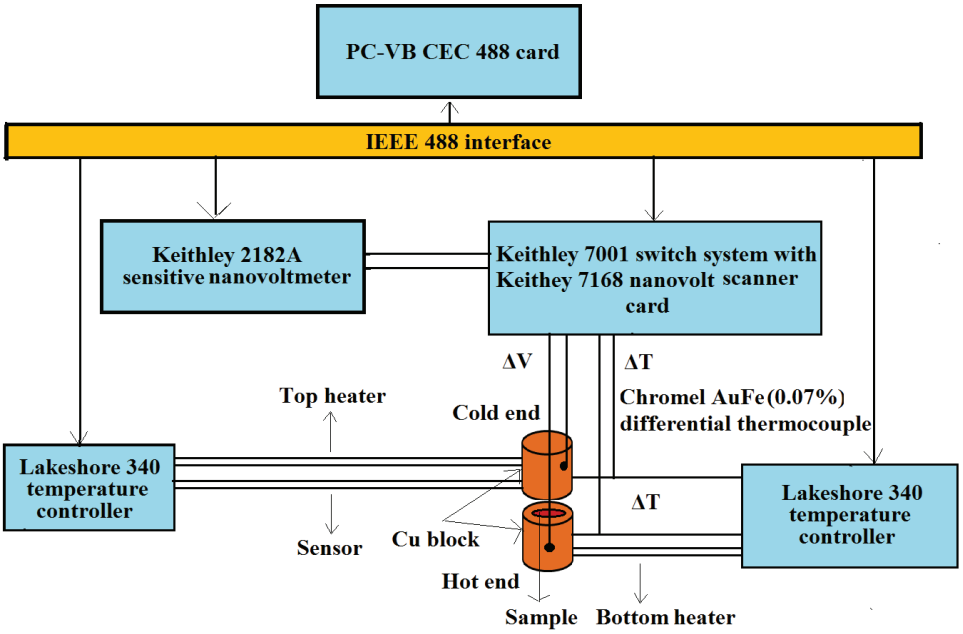

Fig 3.26 Schematic diagram of thermoelectric power measurement setup in the temperature range from 4 K to 300 K

The measurement system is configured for differential DC method with oxygen free highly conducting copper (OFHC) as reference. The main part of the system is a cryostat that can be fitted inside a liquid helium Dewar. The inside of the cryostat is maintained at a vacuum better than 10^{-6} mbar. The sample is placed between two cylindrical OFHC blocks [31]. The two junctions of the chromel-Au–Fe (0.07%) thermocouple are connected to the two OFHC blocks to which electrical leads are attached for potential difference (ΔV) measurements. A Lakeshore 340 temperature controller is used to maintain the temperature difference (ΔT) between the two OFHC blocks using the chromel-Au–Fe (0.07%) thermocouple and the bottom heater. The ΔT can be set to a desired value [31].

A calibrated silicon diode and the top heater are connected to another Lakeshore 340 temperature controller to sustain a desired controlled sample temperature (±10 mK). A Keithley 2182A sensitive nanovoltmeter coupled through a Keithley 7168 nanovolt scanner card measures ΔV and ΔT using a chromel-Au–Fe (0.07%) thermocouple. The sample holder is attached to a heat sink with a removable cylindrical OFHC jacket serving as a radiation shield. The sample holder is loaded in the cryostat. The TEP data ($S_{Measured}$) which is given by Eq (3.45) are recorded through a personal computer for a desired temperature step and range [31]. The absolute Seebeck coefficient S values of the sample is obtained by subtracting the Seebeck coefficient of the copper reference (S_{Cu}) from ($S_{Measured}$) such that the sample (S) is given by [31]

$$S = S_{Measured} - S_{Cu} \tag{3.46}$$

Schematic diagram of thermoelectric power measurement setup in the temperature range from 300 K to 425 K is given in Fig 3.27.

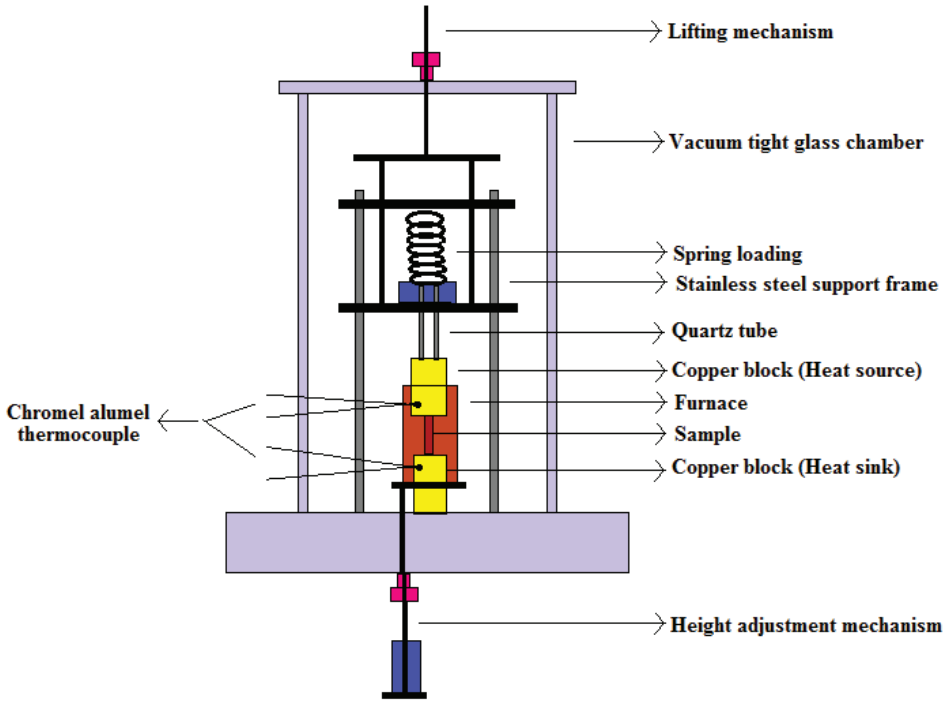

Fig 3.27 Schematic diagram of thermoelectric power measurement setup in the temperature range from 300 K to 425 K

The sample is placed inside a copper sample holder. The sample holder consists of two copper cylindrical blocks into which chromel-alumel thermocouples are embedded. The heater is wound on the upper heat source copper block. The bottom heat sink copper block is welded to the copper base plate. The quartz tube reduces the conductive heat loss from the heater block to the stainless steel support frame and the spring loading provides proper contact between the sample and the sample holder. The thermoelectric power is measured using two additional copper wires connected to the heater and base respectively [32]. The sample holder is placed inside a furnace. The height of the furnace can be adjusted from the bottom without disturbing the sample. A chromel-alumel thermocouple controls the furnace temperature through Toho

TTM-304 temperature controller. To minimize convective heat exchange, the whole arrangement is encapsulated in a vacuum tight glass chamber. The thermal contact between the heat source copper block and the sample is made or broken by a lifting mechanism [32]. A Keithley 228 constant current source is used to energize the heater. The temperature is measured as a function of time using a Keithley DMM 2700 scanner. The output of the current source and the multimeter are interfaced to a computer using an IEEE-488 interface and the data is collected in the hard disk [32]. The initial step in the measurement process is the evacuation of the glass chamber to a vacuum of 10^{-3} mbar followed by the heating and stabilization of the furnace to the desired temperature. The height of the furnace is adjusted such that the top and bottom thermocouples read the same value. Then, the constant current source is switched ON and the change in temperature is measured as a function of time. When the equilibrium value is reached, the heater is slightly lifted by using the lifting mechanism and the change in temperature is again measured [32].

For measuring the Seebeck coefficient, the sample is placed between the source-sink assembly as shown in Fig 3.27. A constant input power is applied and the corresponding rise in temperature (ΔT) and voltage developed across the sample (ΔV) is measured [32]. The Seebeck coefficient ($S_{Measured}$) can then be calculated using Eq (3.45). The TEP data ($S_{Measured}$) which is given by Eq (3.45) are recorded through a personal computer for a desired temperature step and range. The absolute Seebeck coefficient S values of the sample is obtained by using Eq (3.46).

3.5.13 Electrical conductivity measurement

At low temperatures, electrical conductivity of semiconductors is governed by Seto's classical grain boundary transport model which is dominant in the temperature region from 200 K to 270 K [33] and Mott's hopping model which is dominant in the temperature region less than 200 K [34]. The Seto's grain boundary model assumes the presence of trapping states at the grain boundaries which capture free charge carriers. These charged states create depleted regions and potential barriers which provide a resistance to the passage of charge carriers. As a result it is difficult for the charge carriers to cross the boundaries thus causing a reduction in electrical conduction [33]. On the other hand, when the temperature is low enough so that charge carriers cannot be excited into one of the allowed bands, the dominant conduction takes place by Mott's hopping model [34] where the charge carriers hop from occupied states to unoccupied states, which are located within the band gap. The hopping are of two types – nearest neighbour hopping (NNH) which is significant at higher temperatures and even at room temperature and the other is variable range hopping (VRH) which is dominant at still low temperatures [34].

Schematic diagram of electrical conductivity measurement setup in the temperature range from 4 K to 300 K is given in Fig 3.28. This measurement setup is capable of recording the resistivity of eight samples simultaneously.

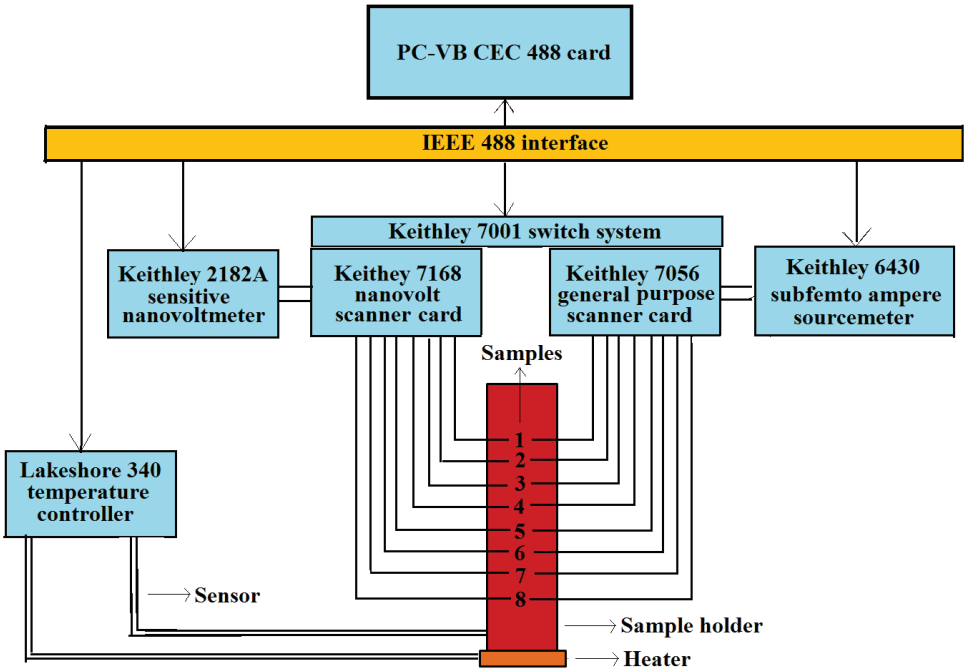

Fig 3.28 Schematic diagram of electrical conductivity measurement setup in the temperature range from 4 K to 300 K

The inside of the cryostat is maintained at a vacuum better than 10^{-6} mbar. The sample holder is kept inside the cryostat. The sample holder is a parallelepiped oxygen free highly conducting copper (OFHC) block and it is attached to a brass flange [31]. At the upper side of the brass flange, stainless steel feedthrough tube for various electrical wires is connected and at the bottom of the brass flange, a removable cylindrical OFHC jacket is fitted as a radiation shield. The samples are electrically isolated from the two opposite faces of the OFHC sample holder. Then, on the other remaining opposite faces, printed circuit board strips are fixed for electrical terminals. Two uninsulated copper wires each for current and voltage leads for each sample are taken from

these terminals for electrical contacts using a highly conducting silver paste [31].

The temperature is measured using a calibrated silicon diode (± 10 mK). The cartridge heater and the calibrated silicon diode are connected to a Lakeshore 340 temperature controller. At a selected temperature, a desired current is passed through the outer two terminals of the sample from a Keithley 6430 subfemto ampere sourcemeter and the resulting voltages in the inner two terminals are recorded by a Keithley 2182A sensitive nanovoltmeter. The data acquisition is enabled by a Keithley 7056 general purpose scanner card and a Keithley 7168 nanovolt scanner card both coupled to a Keithley 7001 switching system [31]. Using dimensions of the sample, the resistivity is calculated. Thereafter, the electrical conductivity is calculated from the inverse of the resistivity values. The typical error estimated in the measurement is about 3%.

At high temperatures, greater than 300 K, semiconductors usually exhibit thermally activated electrical conductivity described by Arrhenious model [35]. Schematic diagram of electrical conductivity measurement setup in the temperature range from 300 K to 425 K is given in Fig 3.29.

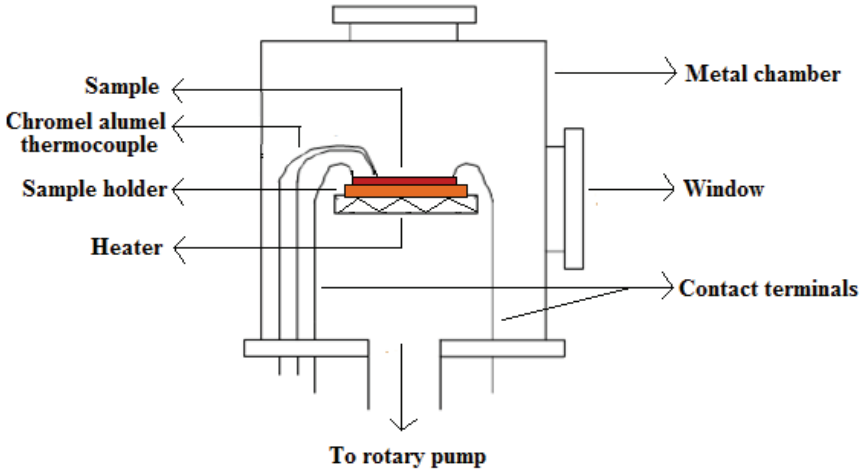

Fig 3.29 Schematic diagram of electrical conductivity measurement setup in the temperature range from 300 K to 425 K

To study the electrical conductivity, the ends of the thin film sample are applied with silver paste to ensure good ohmic contact. The film is then placed on a heater inside a metal chamber coupled with a rotary pump to pump down to 10^{-3} mbar. The measurement is made in vacuum to avoid the possibility of short circuiting of the sample due to the humidity present in the atmosphere. A DC regulated single output variable power supply is used as the voltage source and an APLAB 1015 digital multimeter is used for measuring the current.

The circuit diagram for the measurement of electrical conductivity is shown in Fig 3.30.

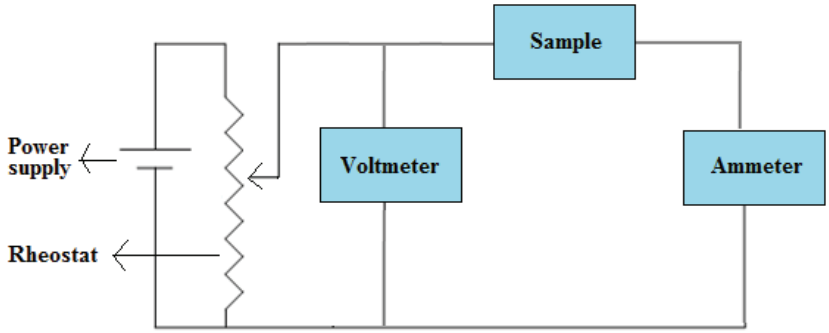

Fig 3.30 Circuit diagram for the measurement of electrical conductivity

3.5.14 Thermal conductivity measurement

Thermal conductivity is defined as the property of a material to conduct heat. It is measured in watts per meter kelvin ($Wm^{-1}K^{-1}$). Thermal conductivity measurement reveals information about the various heat carriers in a material and it is of great importance in designing devices operating at cryogenic and very high temperatures.

Schematic diagram of thermal conductivity measurement setup in the temperature range from 4 K to 300 K is given in Fig 3.31.

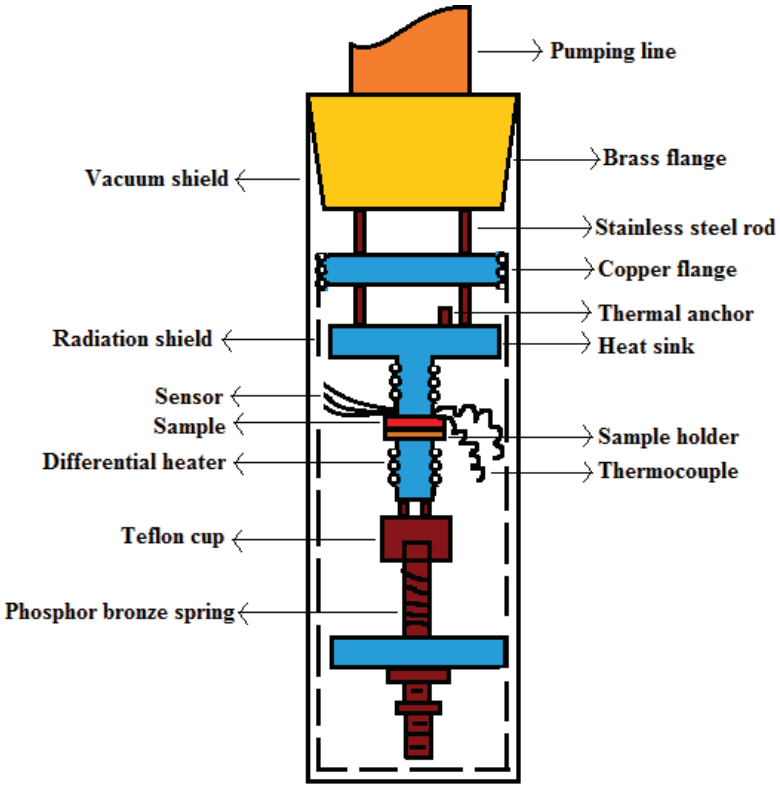

Fig 3.31 Schematic diagram of thermal conductivity measurement setup in the temperature range from 4 K to 300 K

The thermal conductivity data is obtained by conventional steady state method. A strain gauge resistor is thermally attached to the sample surface. The excitation of the strain gauge develops a temperature gradient (ΔT) at constant differential heater power. The temperature of the sample is controlled using a Lakeshore DRC-93CA controller. The details of the experimental setup is given in reference [36].

Schematic diagram of thermal conductivity measurement setup in the temperature range from 300 K to 425 K is same as that given in Fig 3.27. The

thermal conductivity is measured by steady state method where the thermal conductivity (k) of the material is given by

$$k = \frac{\left(\frac{Q_S}{A}\right)}{\left(\frac{\Delta T}{\Delta L}\right)} \tag{3.47}$$

where Q_S is the amount of heat passing per unit time through an area of cross section A and ΔT is the resulting temperature difference over a distance ΔL. Thus Q_S/A is the heat flux that cause the temperature gradient $\Delta T/\Delta L$. Thus in order to calculate k, the heat flux and temperature gradient must be measured. Q_S is given by [32]

$$Q_S = x\left(\Delta T_E - \Delta T_S\right) \tag{3.48}$$

where x is the heater constant, ΔT_E is the equilibrium temperature change in the heater block without the sample and ΔT_S is the equilibrium temperature change in the heater block with the sample. In order to evaluate x, ΔT_E is measured for different input power and the slope of the curve as ΔT_E tends to zero gives the value of x [32]. Using the value of x in Eq (3.48) gives Q_S. Once Q_S is known, k of the material can be calculated using Eq (3.47). Initially, a constant input power is supplied to the heater block without the sample. As temperature increases, heat loss also increases and finally the input power becomes equal to heat loss per unit time and the temperature of the heater block attains a constant value ΔT. Thus in this case, the heat input is the sum of heat gained by the source and heat dissipated to the surroundings. Later, the sample is placed between the source-sink assembly so that a part of the heat flows through the sample which depends on its k value. In this case, the heat input is distributed

to source, transferred through the sample and dissipated to the surroundings [32]. In both these cases, if the same heat input is maintained by assuming that the heat dissipation is also the same, then the k of the sample can be calculated.

References

[1] K. L. Chopra, Thin film phenomena (McGraw Hill, New York, 1969), pp. 10- 82.

[2] K. G. Gunther, The use of thin films in physical investigations, ed. by J. C. Anderson (Academic, London, 1966), pp. 213-232.

[3] R. Glang, Vacuum evaporation, ed. by L.I. Maissel and R. Glang (McGraw Hill, New York, 1970), pp. 1-130.

[4] R. K. Puri and V. K. Babbar, Solid state physics (S. Chand, New Delhi, 2003), pp. 34-74.

[5] B. D. Cullity, Elements of X-ray diffraction, ed. by M. Cohen (Addison Wesley, Philippines, 1978), pp. 81-106.

[6] W. A. Syed, S. Ahmed, M. S. Saleem and N. A. Shah, Chalcogenide Lett 12, 215 (2015).

[7] K. T. Saravana and B. S. Parveen, Int. J. Recent. Sci. Res 4, 1688 (2013).

[8] G. Ramanathan, R. J. Xavier and K. R. Murali, Thin. Film. Technol 50, 10588 (2012).

[9] W. Zhou, R. P. Apkarian, Z. L. Wang and D. Joy, Scanning microscopy for nanotechnology: Techniques and applications, ed. by W. Zhou and Z. L. Wang (Springer, Berlin, 2006), pp. 1- 40.

[10] P. C. Braga and D. Ricci, Atomic force microscopy: Biomedical methods and applications (Humana, USA, 2004), pp. 1-24.

[11] A. J. G. Reed and D. C. Bell, Energy dispersive X-ray analysis in the electron microscope (Taylor and Francis, USA, 2005), pp. 1-145.

[12] S. Hofmann, Auger and X-ray photoelectron spectroscopy in materials science, ed. by G. Ertl, H. Luth and D. L. Mills (Springer, Berlin, 2013), pp. 1-76.

[13] M. Schlesinger and M. Paunovic, Modern electroplating (Wiley, USA, 2010), pp. 545-546.

[14] R. C. Evans, P. Douglas and H. D. Burrows, Applied photochemistry, ed. by R. C. Evans, P. Douglas and H. D. Burrows (Springer, Berlin, 2013), pp. 502-504.

[15] J. Tauc, Amorphous and liquid semiconductors (Plenum, New York, 1974), pp. 159-220.

[16] D. J. Martin, Investigation into high efficiency visible light photocatalysts for water reduction and oxidation (Springer, Berlin, 2015), pp. 15-16.

[17] N. Sharma and R. Kumar, Adv. Appl. Sci. Res 5, 111 (2014).

[18] R. Swanepoel, J. Phys. E. Sci. Instrum 16, 1214 (1983).

[19] M. Dressel and G. Gruner, Electrodynamics of solids: Optical properties of electrons in matter (Cambridge, USA, 2002), pp. 21-28.

[20] B. Guigues, Ferroelectric dielectrics integrated on silicon, ed. by E. Defay (Wiley, USA, 2011), pp. 341-378.

[21] B. Jensen, Handbook of optical constants of solids, ed. by E. D. Palik (Academic, USA, 1985), pp. 169-188.

[22] N. V. Joshi, Photoconductivity art, science and technology (Marcel Dekker, New York, 1990), pp. 1-76.

[23] R. A. Smith, Semiconductors (Academic, Calcutta, 1978), pp. 342-350.

[24] W. Fuhs and J. Stuke, Phys. Status. Solidi B 27, 171 (1968).

[25] K. R. Murali and P. Thirumoorthy, Elec. Chem. Soc. Trans 28, 67 (2010).

[26] I. Pelant and J. Valenta, Luminescence spectroscopy of semiconductors (Oxford, New York, 2012), pp. 1-81.

[27] T. M. Tritt and M. A. Subramanian, Mater. Res. Soc. Bulletin 31, 188 (2006).

[28] R. Murugeshan, Modern physics (S. Chand, New Delhi, 2002), pp. 786-789.

[29] Y. Y. Peter and M. Cardona, Fundamentals of semiconductors: Physics and materials properties (Springer, Berlin, 1999), pp. 224-226.

[30] R. K. Rajput, Electronic measurements and instrumentation (S. Chand, New Delhi, 2009), pp. 404-405.

[31] A. Soni and G. S. Okram, Rev. Sci. Instrum 79, 1251031 (2008).

[32] T. Dasgupta and A. M. Umarji, Rev. Sci. Instrum 76, 0949011 (2005).

[33] J. Y. W. Seto, J. Appl. Phys 46, 5247 (1975).

[34] M. Eto and H. Kamimura, Comprehensive semiconductor science and technology, ed. by P. Bhattacharya, R. Fornari and H. Kamimura (Elsevier, USA, 2011), pp. 101-102.

[35] E. S. M. Farag and M. M. Sallam, Egypt. J. Solids 30, 1 (2007).

[36] V. P. S. Awana, A. Vajpayee, M. Mudgel, V. Ganesan, A. M. Awasthi, G. L. Bhalla and H. Kishan, Eur. Phys. J. B 62, 281 (2008).

Chapter 4

Preparation and Characterization of Degenerate Polycrystalline Cu_7Se_4 Thin Films

4.1 Introduction

Copper selenide is a well recognized chalcogenide belonging to the I-VI family of semiconductors. The most common phase of copper selenide is the CuSe or Klockmannite with hexagonal structure [1] as shown in Fig 4.1.

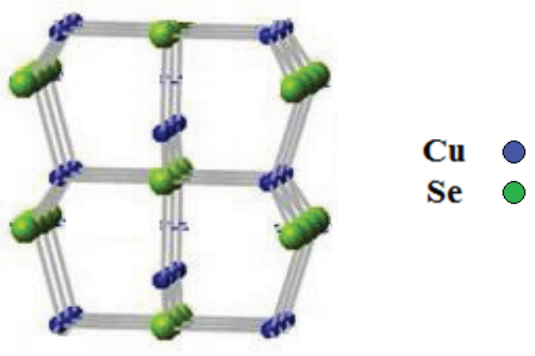

Fig 4.1 Crystal structure of CuSe

Thin films of copper selenide are of particular interest because of their optical and electrical properties suitable for applications in solar cells [2], superionic conductors [3], solar control coatings [4], thermoelectric converters [5], photodetectors [6], photoelectrochemical cells [7] and so on. The main attraction of this material lies in its feasibility of producing $CuInSe_2$ by incorporating indium which can then be used as an efficient absorber layer material in solar cells [8].

Copper selenide usually exists in a wide range of stoichiometric (CuSe, Cu_2Se, $CuSe_2$, Cu_3Se_2, Cu_7Se_4) and non stoichiometric ($Cu_{2-x}Se$) compositions. The thermal stability of these compounds varies depending on the composition but is stable over a wide range of departures from their stoichiometry [9]. Cu_2Se or $Cu_{2-x}Se$ are treated as copper (I) selenide and CuSe, $CuSe_2$ and Cu_3Se_2 are treated as copper (II) selenide [10]. At room temperature CuSe is reported as hexagonal which undergoes a transition to orthorhombic at 48 $^{\circ}$C and back to hexagonal at 120 $^{\circ}$C. At still higher temperatures, CuSe disproportionates into $Cu_{2-x}Se$ and Se [11]. $Cu_{2-x}Se$ phase of copper selenide is considered as a degenerate p-type semiconductor which exhibits a face centered cubic structure with $0.15 \leq x \geq 0.2$ at room temperature and ultimately reaches the tetragonal structure of Cu_2Se phase [4].

Chen et al [12] used $Cu_{2-x}Se$ as an absorber layer material and has reported on a $Cu_{2-x}Se$/CdS heterojunction solar cell with an efficiency of 5.38%. On the other hand Okimura et al [13] used $Cu_{2-x}Se$ as a window layer material in the heterojunction solar cell, which showed conversion efficiency of 8.8 % and good stability. Recently copper selenide has been recalled by

thermoelectric society due to its very high thermoelectric figure of merit. Liu et al [14] has reported on $Cu_{2-x}Se$ that reaches a thermoelectric figure of merit of 1.5 at 1000 K, which is among the highest values for any bulk materials. Copper selenide thin films of varying stoichiometries and different crystalline modifications can be prepared by chemical bath deposition [15], spray pyrolysis [16], brush electrodeposition [17], pulsed laser deposition [18], metal organic chemical vapour deposition [19] sputtering [20] and so on.

The studies on copper selenide thin films of various compositions prepared using several deposition techniques are well documented. Some of them include tetragonal-Cu_3Se_2 (Umangite), Cubic-$Cu_{2-x}Se$ (Berzelianite) [15] and hexagonal-CuSe (Klockmannite), orthorhombic-Cu_2Se (Bellidoite), cubic-$CuSe_2$ (Krutaite) [18]. But to the best of our knowledge, there are no reports on the properties of Cu_7Se_4 which is a rare phase of copper selenide. Hence in the present work, a systematic investigation is carried out on the structural, compositional, morphological, optical, electrical and thermoelectric power properties of reactive evaporated Cu_7Se_4 thin films, about which no reports are available in literature to date. The results of the studies are discussed in the following sections.

4.2 Experimental technique

In the present study, reactive evaporation - a variant of Gunther's three temperature method [21], described in section 3.3, is used to prepare Cu_7Se_4 thin films. The experimental setup and the detailed process of thin film deposition have already been discussed in section 3.4. Briefly, high purity Cu (99.999%) and Se (99.999%) are evaporated simultaneously at suitable rates

from two independently heated sources. Cu is evaporated from a molybdenum boat whereas Se is evaporated from a glass crucible kept in a molybdenum basket. The vapours are allowed to deposit on glass substrates kept at an elevated temperature of 498±5 K after attaining a pressure of the order of 10^{-5} mbar in the coating unit. The optimized conditions used to deposit Cu_7Se_4 thin films are:

Impingement rate of Cu : 3.5×10^{15} atoms $cm^{-2}s^{-1}$
Impingement rate of Se : 2.3×10^{15} atoms $cm^{-2}s^{-1}$
Substrate temperature : 498±5 K

The as-prepared Cu_7Se_4 thin films are characterized for their structural properties using Rigaku D MaxC X-ray diffractometer (XRD) for 2θ varying from 10° to 70° with CuK_{α} (1.5404 Å) as the radiation source. The elemental composition is verified from energy dispersive analysis of X-rays (EDAX) and X-ray photoelectron spectroscopy (XPS). The surface morphology is studied using scanning electron microscopy (SEM) and atomic force microscopy (AFM). The optical properties are analyzed using UV-Vis-NIR spectrophotometer in the wavelength range from 2000 nm to cut-off. The thickness of the film is measured using Veeco Dektak 6M stylus profiler and is found to be ≈ 350 nm. The Hall and photoluminescence measurements are performed at room temperature. The Seebeck coefficient, electrical conductivity and thermal conductivity of the as-prepared thin films are measured in the temperature range from 4 K to 425 K to evaluate the thermoelectric figure of merit. The details of the aforementioned

characterization tools have already been described in section 3.5 and the results obtained are presented in the following sections.

4.3 Results and Discussions

4.3.1 Structural analysis

The XRD pattern of the as-prepared Cu_7Se_4 thin film is shown in Fig 4.2. The observed interplanar spacing and (hkl) plane of the prepared thin film matches well with that of cubic Cu_7Se_4 (JCPDS Card. 26-0557).

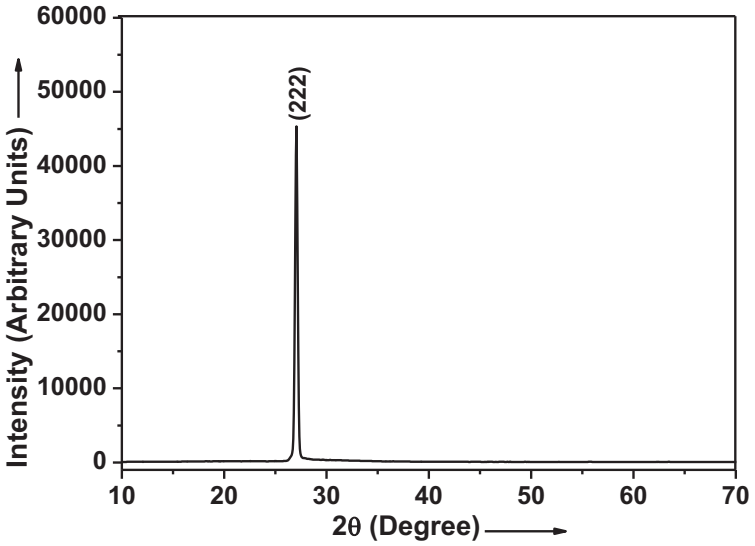

Fig 4.2 XRD pattern of the as-prepared Cu_7Se_4 thin film

The XRD pattern shows a well defined peak with very high intensity at $2\theta = 27.03^{\circ}$. Cu_7Se_4 thin film with such a good crystallinity has not so far been

reported. The absence of other peaks with significant relative intensities is due to the preferential orientation of crystallites along the (222) plane. No elemental peaks or unassigned peaks are observed indicating that the prepared Cu_7Se_4 thin film is pure without the existence of any impurity. The calculated value of lattice constant is a = 11.39 Å. The average crystallite size of the prepared Cu_7Se_4 thin film is calculated using Scherrer formula [22] and is obtained as 60 nm. The structural parameters such as dislocation density, number of crystallites per unit area and lattice strain in the film are estimated as 2.8×10^{10} lines cm^{-2}, 16×10^{10} cm^{-2} and 1×10^{-3} respectively using the equations described in section 3.5.1.

4.3.2 Compositional analysis

The EDAX spectrum of the as-prepared Cu_7Se_4 thin film is shown in Fig 4.3. The analysis of EDAX spectrum reveals the near stoichiometric composition of the film with an average atomic percentage of the elements as Cu = 63.37% and Se = 36.63%. The peaks obtained for the elements in the spectrum are strong and no unassigned peaks are observed which confirms the purity of the prepared film.

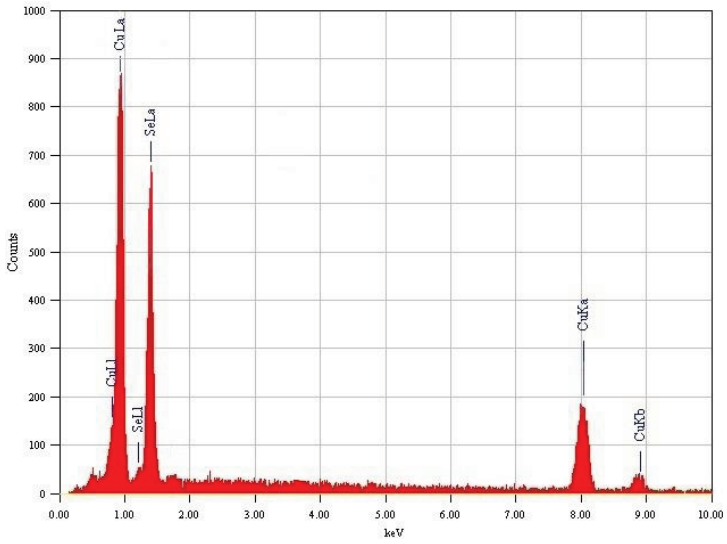

Fig 4.3 EDAX spectrum of Cu_7Se_4 thin film

Fig 4.4 depicts the binding energy (B.E) versus counts per second (CPS) of Cu2p peaks and Se3d peak obtained from the XPS spectrum of the prepared Cu_7Se_4 thin film. The composition of the prepared film determined from the XPS spectrum is found to be near stoichiometric with an average atomic percentage of Cu and Se as 64.15% and 35.85% respectively. These results are in accordance with the observation from EDAX analysis.

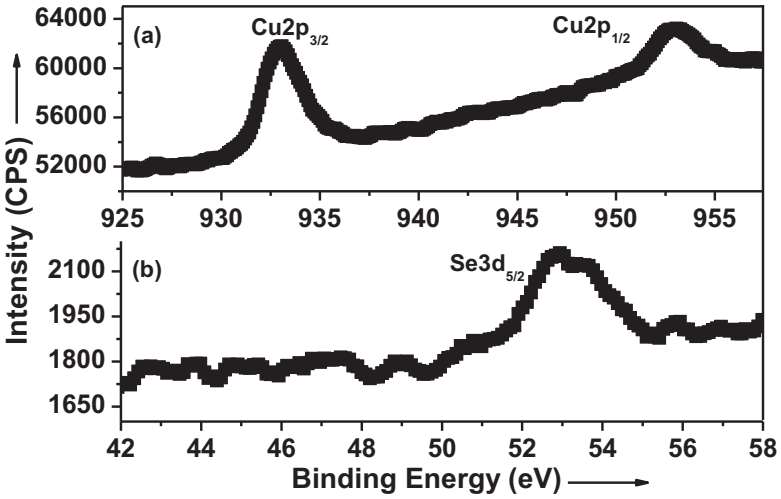

Fig 4.4 XPS spectrum of Cu_7Se_4 thin film

The observed shift in the B.E of Cu and Se from their elemental peak position, shown in Table 4.1, is a clear evidence of the formation of Cu_7Se_4 compound where the elements Cu and Se exist in a chemically bonded state.

Table 4.1 Comparison of the observed peak positions of Cu and Se from the XPS spectrum with their standard elemental peak positions

Peak position (eV)	$Cu2p_{3/2}$	$Cu2p_{1/2}$	$Se3d_{5/2}$
Observed peak position	933.1	953.2	53.1
Elemental peak position [23]	932.6	952.2	54.9

4.3.3 Morphological analysis

The SEM image of the as-prepared Cu_7Se_4 thin film shown in Fig 4.5, suggests the significantly smooth surface of the prepared film.

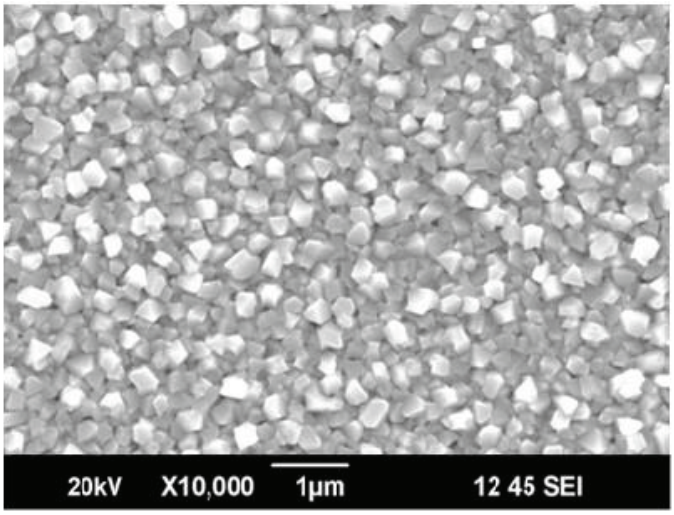

Fig 4.5 SEM image of Cu_7Se_4 thin film

The surface of the film is densely packed with crystallites without having any discontinuity. The grain size calculated from SEM is in the range from 200 nm to 230 nm, an outcome of clustering or agglomeration of particles. This can be ascribed to the fact that the grain size measured from SEM will lead to a value greater than the crystallite size measured from XRD. The surface morphology of the film is further analyzed by 2D AFM and 3D AFM shown in Fig 4.6(a) and (b) respectively. The scan area is 2 µm x 2 µm and scan rate is 10.172 Hz.

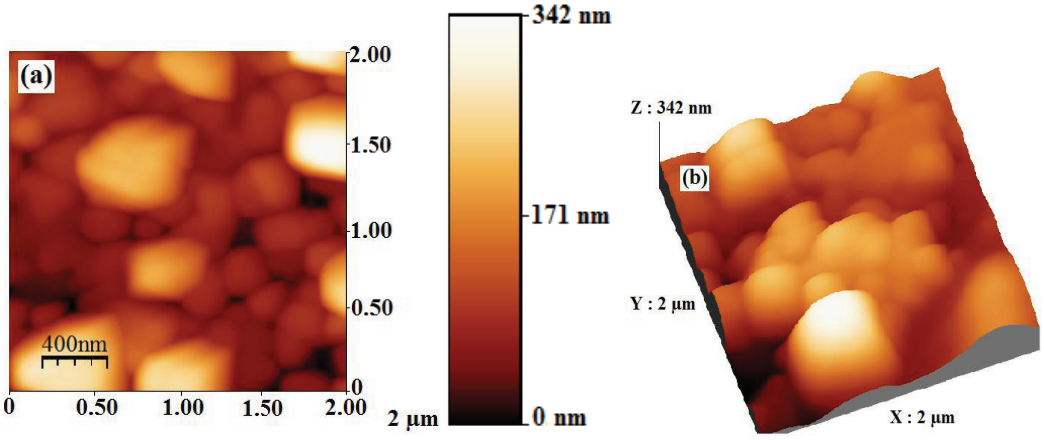

Fig 4.6(a) 2D AFM (b) 3D AFM of Cu_7Se_4 thin film

It can be seen from Fig 4.6(a) that the film exhibits clusters of sizes in the range from 330 nm to 360 nm in diameter, indicating the agglomeration of particles. The root mean square (RMS) value of surface roughness of the film determined from Fig 4.6(b) is 15 nm, suggesting a significantly smooth surface.

4.3.4 Hall measurement

The positive value of Hall coefficient indicates that the prepared films are of p-type. Hole mobility (μ_p) and hole concentration (p) are 2.4 $cm^2V^{-1}s^{-1}$ and 8×10^{21} cm^{-3} respectively. Hole mobility ≈ 2 $cm^2V^{-1}s^{-1}$ to 5 $cm^2V^{-1}s^{-1}$ and 8 $cm^2V^{-1}s^{-1}$ to 15 $cm^2V^{-1}s^{-1}$ has been reported [13] for p-type degenerate $Cu_{2-x}Se$ thin films prepared on substrates at a temperature of 40 °C and 200 °C respectively with charge carrier density of the former ≈ 10^{22} cm^{-3}, which is one order of magnitude higher than that obtained for Cu_7Se_4. The as-prepared

Cu_7Se_4 shows a high electrical conductivity $\sigma \approx 3\times10^3$ Scm^{-1} at room temperature consistent with the high charge carrier concentration. This high charge carrier concentration makes the prepared Cu_7Se_4 thin film a degenerate semiconductor. This is in agreement with the charge carrier concentration of degenerate semiconductors which is evaluated to be above 10^{18} cm^{-3} at room temperature [24]. Hence the prepared film can be considered as a degenerate semiconductor. Certain phases of copper selenides such as CuSe, Cu_2Se, Cu_3Se_2 and $Cu_{2-x}Se$ are reported as degenerate p-type semiconductors with relatively large numbers of holes in their valence band [25].

4.3.5 Optical analysis

The transmission spectrum and reflection spectrum of the as-prepared Cu_7Se_4 thin film are shown in Fig 4.7 and Fig 4.8 respectively.

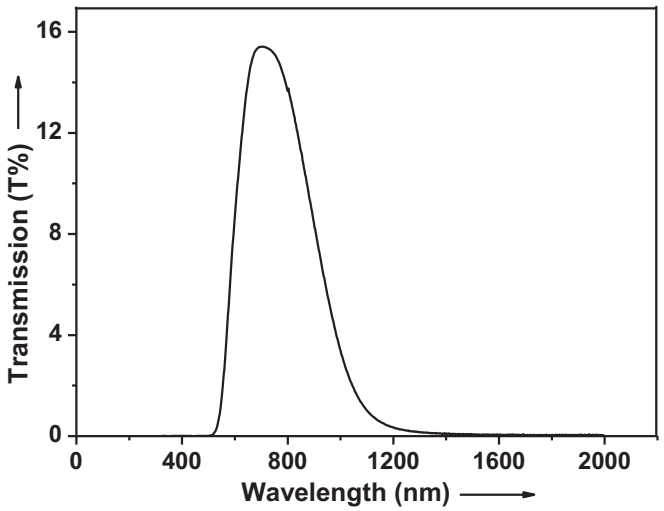

Fig 4.7 Transmission spectrum of Cu_7Se_4 thin film

In the visible region, transmission of the film is moderate but drops substantially in the near infrared (NIR) region. This is due to high NIR reflection (≈ 60%) of the film, shown in Fig 4.8. The high NIR reflection is attributed to the high electrical conductivity of the film, a typical feature of degenerate thin films that can be associated with the theory of free charge carrier absorption of electromagnetic radiation [26]. The free charge carrier absorption is evident from the absorption spectrum of Cu_7Se_4 thin film shown in Fig. 4.9.

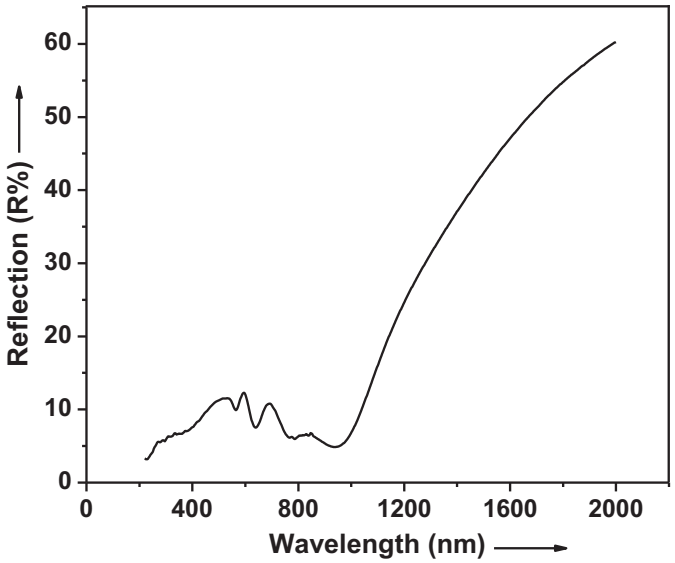

Fig 4.8 Reflection spectrum of Cu_7Se_4 thin film

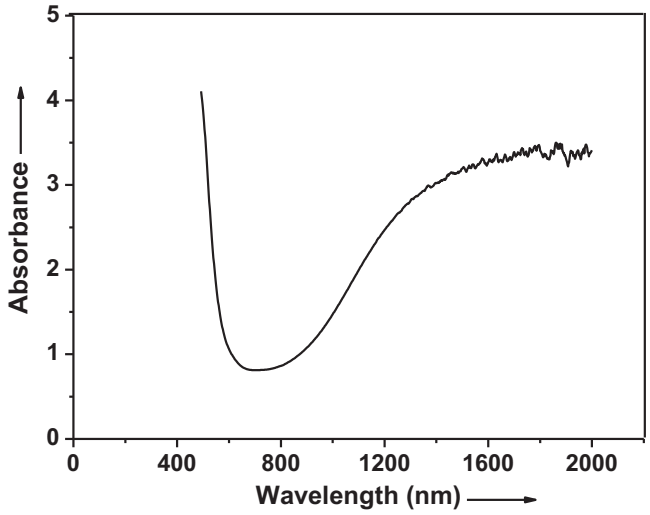

Fig 4.9 Absorption spectrum of Cu_7Se_4 thin film

In order to determine the absorption coefficient (α) and optical band gap (E_g) of the as-prepared Cu_7Se_4 thin film, the transmission spectrum shown in Fig 4.7 is corrected for loss due to reflection using the relation

$$T_{Corrected} = \left\{ \frac{T(\%)}{100 - R(\%)} \right\} \times 100 \tag{4.1}$$

The absorption coefficient for band to band transition across the gap at different wavelengths is calculated using the values of corrected transmission ($T_{Corrected}$) given by

$$\alpha = \frac{1}{t} \ln\left(\frac{100}{T_{Corrected}} \right) \tag{4.2}$$

The absorption coefficient is found to be 10^5 cm^{-1}. The optical band gap is analyzed using Tauc relation [27] described in section 3.5.7. The plot of $(\alpha h\nu)^2$ versus hν of the as-prepared Cu_7Se_4 thin film is shown in Fig 4.10.

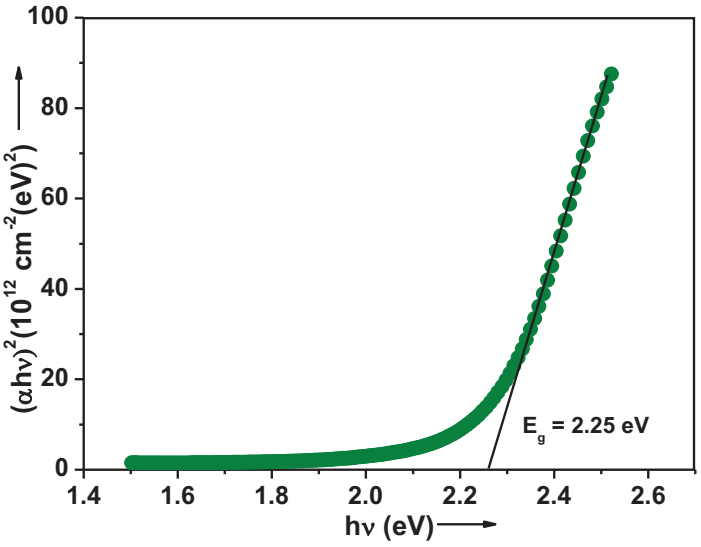

Fig 4.10 Plot of $(\alpha h\nu)^2$ versus hν of Cu_7Se_4 thin film

The linear nature of the plot indicates the existence of direct transition. The optical band gap of the film is found to be 2.25 eV which is in good agreement with those reported for materials used in solar cells [28]. The prepared film being a degenerate semiconductor, the measured band gap is equal to its actual band gap plus the Moss Burstein shift [29]. For degenerate semiconductors since all the states around the conduction band minimum are filled, it is not possible to absorb photons with energies exactly of the band gap energy. Hence, to excite electrons into free states higher up in the conduction band a little extra energy is needed. Thus in the optical absorption

measurements, the band gap appears to be increased. This phenomenon is called as the Moss Burstein shift. Hence the actual band gap of the film is less than the optical energy gap determined in the present study.

The free charge carrier absorption observed in Fig 4.9, leads to low NIR transmission, and hence the typical transmission spectrum of non degenerate semiconductors is not attained. It is reported that along with the optical absorption due to free charge carriers and charge carrier generation across the band, an inverted bell type transmission curve is obtained for degenerate semiconductor thin films [30] and it is consistent with the observation from Fig. 4.7. This is a characteristic feature of wide band gap degenerate semiconductors, some among them includes SnO_2:F, SnO_2:Sb, In_2O_3:Sn that are used in heat mirror coatings [31] and CuS that is used in solar control coatings [32].

The analysis of transmission and reflection spectra suggests that the prepared thin film shows moderate transmission in the visible region, low transmission in the near infrared region, low reflection in the visible region and relatively high reflection in the near infrared region. These properties are close to those desired for near ideal solar control coatings [4] and are typical features of degenerate thin films.

Therefore, on further work, the prepared thin film can be considered for applications in solar control coatings and also in microwave (infrared) shielding coatings. The highly conductive Cu_7Se_4 thin films thus prepared may also be used as radiation filters. The optical properties of the prepared film is almost similar to that of conductive $Cu_{2-x}Se$ films that show excellent

photovoltaic properties both as an absorber layer material and also as a window layer material in heterojunction solar cells.

Photoluminescence measurement

The photoluminescence spectrum of the as-prepared Cu_7Se_4 thin film recorded at room temperature under an excitation wavelength of 500 nm is shown in Fig 4.11.

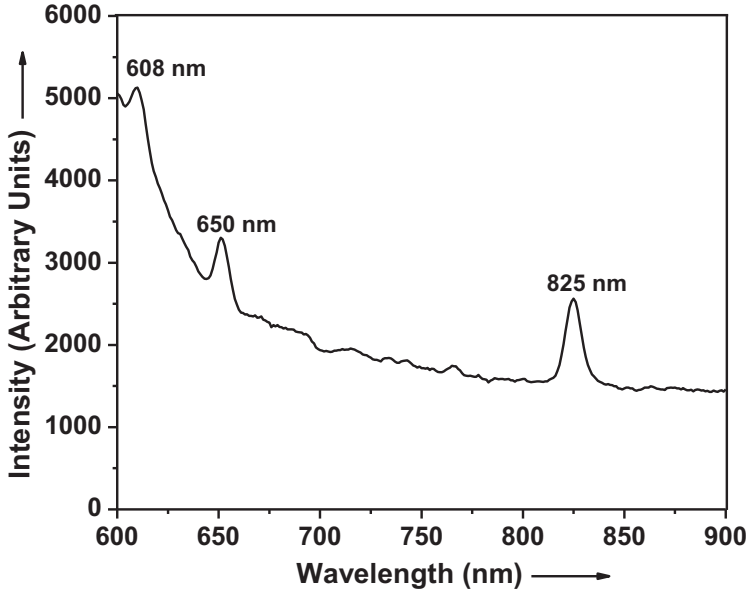

Fig 4.11 Photoluminescence spectrum of Cu_7Se_4 thin film

As observed from Fig 4.11, photoluminescence emission is observed at wavelengths 608 nm, 650 nm and 825 nm which correspond to energies 2.04 eV, 1.91 eV and 1.51 eV respectively. The difference in energies is considered

to have its origin from a radiative donor-acceptor pair recombination at defect levels with energies 2.04 eV, 1.91 eV and 1.51 eV within the band gap of the film [33]. It can be concluded that there is a non radiative transition from conduction band to defect levels with energies 2.04 eV, 1.91 eV and 1.51 eV and from these defect levels radiative transitions occurred with energies 2.04 eV, 1.91 eV and 1.51 eV to valence band. The photoluminescence emission of the film is due to these radiative transitions from defect levels to valence band. Hence photoluminescence studies can be used as one sensitive method to detect the defect states present in the film.

4.3.6 Electrical analysis

Electrical conductivity measurement

Fig 4.12 shows the variation of ln(I) with inverse of temperature of the as-prepared Cu_7Se_4 thin film for three continuous heating-cooling cycles.

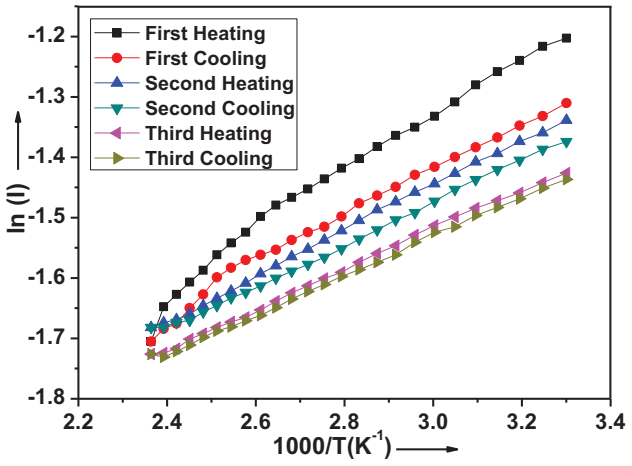

Fig 4.12 Variation of ln(I) with inverse of temperature of Cu_7Se_4 thin film

From Fig 4.12, it is seen that electrical conductivity shows an irreversible variation during the first heating-cooling cycles. But after the first heating-cooling cycle, the film attained thermal stability and the dependence of electrical conductivity becomes reversible. This is due to removal of frozen-in equilibrium defects formed during very fast evaporation process involved in film deposition and to some extent homogenization of the film due to the annealing effect [34]. It is observed that the electrical conductivity of the thin film decreases with an increase in temperature, which is again a typical trait of a degenerate semiconductor and hence consistent with the results of optical analysis. The metallic conduction exhibited by the film may be attributed to its high electrical conductivity arising from the degenerate nature.

Determination of thermoelectric power factor and figure of merit in the temperature range from 4 K to 425 K

Fig 4.13 shows the variation of thermoelectric power (TEP) or Seebeck coefficient (S) in the temperature range from 4 K to 425 K of the as-prepared Cu_7Se_4 thin film. The positive value of S observed from Fig 4.13 confirms that the as-prepared Cu_7Se_4 thin films are of p-type. The hot probe and Hall measurements on the film corroborate this observation.

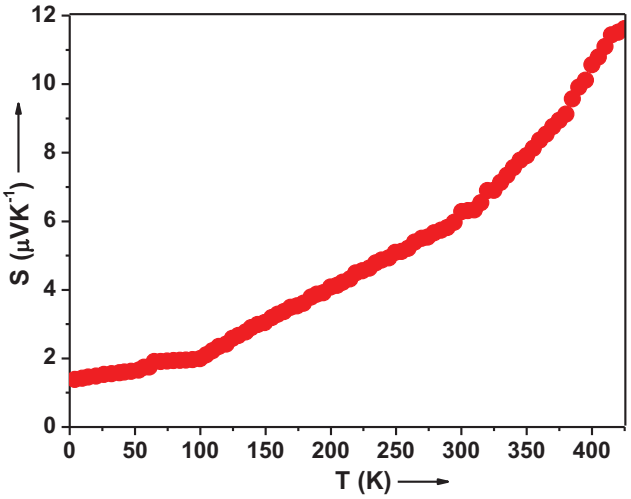

Fig 4.13 Variation of S with temperature of Cu_7Se_4 thin film

It is observed from Fig 4.13 that S of the prepared film increases with increase in temperature, which is a typical trait of a degenerate semiconductor. Being a degenerate semiconductor, the values of S observed in the measured temperature range is low and it varies from 1.4 μVK^{-1} to 11.6 μVK^{-1} with S ≈ 6 μVK^{-1} at 300 K like metals do [35]. This observation is in agreement with the generally accepted fact that higher the electrical conductivity lower will be the thermoelectric power [36]. Fig 4.14 and Fig 4.15 shows the variation of electrical conductivity (σ) and thermal conductivity (k) in the temperature range from 4 K to 425 K of the as-prepared Cu_7Se_4 thin film respectively. The value of σ of the film is high of the order of 10^3 Scm^{-1}, an optimum value for thermoelectric applications [37]. The k value decreases from 0.0057 $Wm^{-1}K^{-1}$ to 0.004 $Wm^{-1}K^{-1}$ with increase in temperature, indicative of the degenerate semiconducting nature of the film.

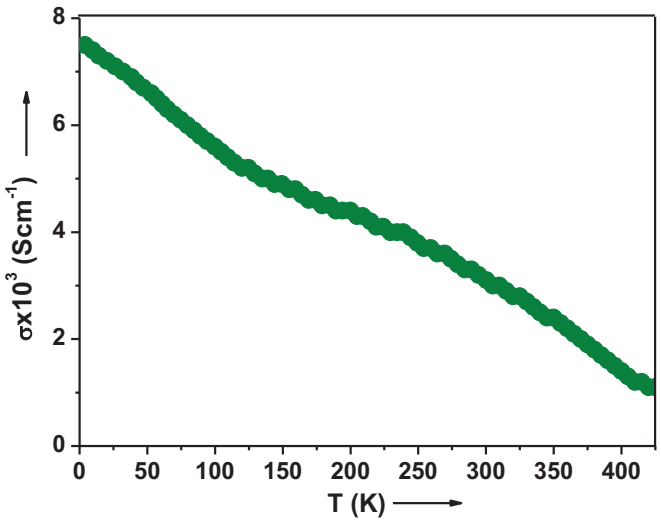

Fig 4.14 Variation of σ with temperature of Cu_7Se_4 thin film

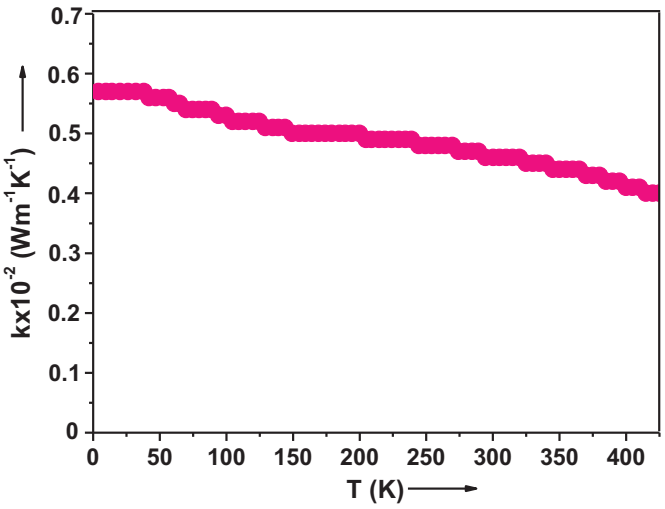

Fig 4.15 Variation of k with temperature of Cu_7Se_4 thin film

Using the values of S and σ, the thermoelectric power factor ($S^2\sigma$) of the film is calculated and its variation in the temperature range from 4 K to 425 K is shown in Fig 4.16.

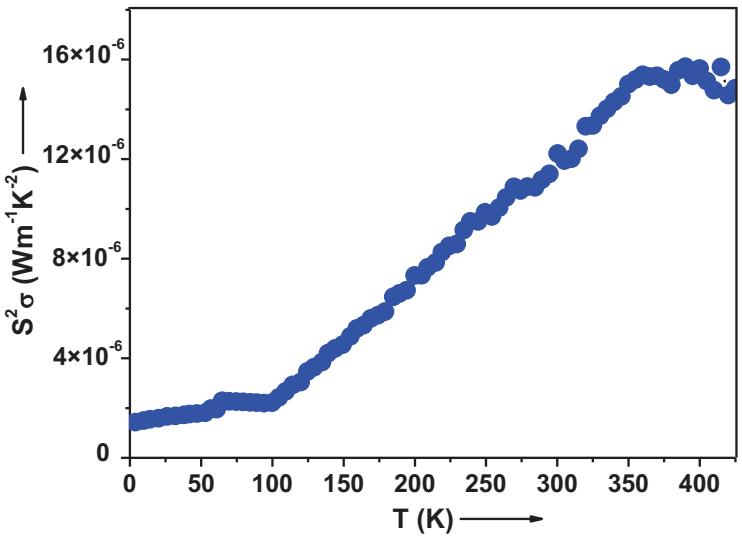

Fig 4.16 Variation of $S^2\sigma$ with temperature of Cu_7Se_4 thin film

As seen from Fig 4.16, the $S^2\sigma$ of the film varies from 10^{-6} $Wm^{-1}K^{-2}$ to 10^{-5} $Wm^{-1}K^{-2}$. These values are low compared to efficient thermoelectric materials ($\approx 10^{-3}$ $Wm^{-1}K^{-2}$ to 10^{-5} $Wm^{-1}K^{-2}$). But agree with those reported for reasonably good thermoelectric materials such as ZnO ($\approx 8.8\times10^{-6}$ $Wm^{-1}K^{-2}$) [38]. The value of $S^2\sigma \approx 1.2 \times 10^{-5}$ $Wm^{-1}K^{-2}$ at room temperature is close to those reported for certain potential thermoelectric materials such as Bi_2Te_3 based composite thin films [39], Bi_2Se_3 nanostructures [40] and $Nd_{1.95}Ce_{0.05}CuO_4$ [41] that are recently being developed.

Moreover, the thermoelectric efficiency of the as-prepared Cu_7Se_4 thin film is evaluated by calculating the thermoelectric figure of merit (ZT) given by [42]

$$ZT = \frac{S^2 \sigma T}{k} \tag{4.3}$$

The variation of ZT in the temperature range from 4 K to 425 K is shown in Fig 4.17.

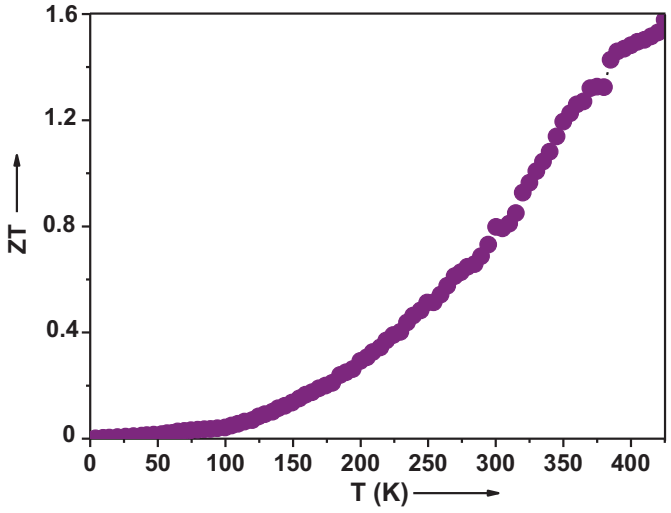

Fig 4.17 Variation of ZT with temperature of Cu_7Se_4 thin film

As observed from Fig. 4.17, the as-prepared Cu_7Se_4 thin film exhibits a maximum ZT ≈ 1.6 at 425 K, a reasonably high value suitable for thermoelectric applications and comparable to the best of the novel thermoelectric materials [43]. Also, the observed ZT ≈ 1.6 is in good agreement with that exhibited by certain efficient thermoelectric materials such

as $Na_{0.05}Pb_{0.95}Te_{0.85}Se_{0.15}$ [44], $K_{0.02}Pb_{0.98}Te_{0.75}Se_{0.25}$[45] and $K_{0.95}Pb_{20}Sb_{1.2}Te_{22}$ [46] that are actively being investigated. Moreover, $Cu_{2-x}Se$ has been reported to have ZT ≈ 1.5 at 1000 K. In this regard, the as-prepared Cu_7Se_4 thin film which exhibits a comparable ZT ≈ 1.6 at much lower temperatures ≈ 425 K are expected to provide higher values of ZT towards higher temperatures due to its degenerate semiconducting nature. The degenerate semiconductors with Seebeck coefficient of the order of a few tens or hundreds of microvolts per degree are the most commonly used materials in thermoelectric applications [47]. Hence further optimization of $S^2\sigma$ and ZT through nanostructuring and electronic band engineering [47], could possibly make Cu_7Se_4 even more competitive with the prominent materials for high temperature thermoelectric applications. Since no reports are found related to the thermoelectric measurements of Cu_7Se_4 thin films, a comparison of our results with literature is not possible.

Evaluation of material parameters

The data from the analysis of Hall and thermoelectric power measurements have been combined to evaluate important material parameters such as Fermi energy (E_F), electron affinity (EA), effective mass (m_p*), relaxation time (τ) and mean free path (l). The results obtained are presented in the following sections.

For metals and degenerate semiconductors, the Seebeck coefficient (S) is related to Fermi energy (E_F) as [48]

$$S = \frac{\pi^2 K_B^2 T}{3eE_F}\left(\frac{3}{2} + A\right) \tag{4.4}$$

where A is the scattering parameter and can take the values A = -1/2 for acoustic phonon scattering which is dominant at high temperatures T ≥ 300 K and also A = 3/2 for ionized impurity scattering which is dominant at low temperatures T≤ 300 K [49]. With A = 3/2, the above equation reduces to the well known expression for the thermoelectric power of metals given by

$$S = \frac{\pi^2 K_B^2 T}{eE_F} \tag{4.5}$$

Using the measured value of S at 300 K, the above equation gives E_F = 3.7 eV at T = 300 K. This value is found to be close to E_F = 3.2 eV at T = 300 K, determined for CuSe thin film which showed metallic nature [50]. CuSe is a degenerate p-type semiconductor with a band gap of 2.1 eV [51]. The high value of E_F of the as-prepared Cu_7Se_4 thin film when compared to its band gap is indicative of its degenerate character. The electron affinity (EA) of the compound is calculated by using the equation [52]

$$EA = \chi - \frac{1}{2}E_g \tag{4.6}$$

where χ is the bulk electronegativity of the compound and E_g is the band gap energy. Using this equation and the postulate of geometric mean, EA of Cu_7Se_4 is determined as 3.8 eV relative to the vacuum level, which is high as usually reported for SnO_2 [52] which is a wide band gap degenerate semiconductor [31]. The prepared film being a p-type degenerate semiconductor, the effective

mass of holes (m_p*) at room temperature is estimated using the equation [43]

$$S = \frac{8\pi^2 K_B^2 T}{3eh^2} m_p^* \left(\frac{\pi}{3p}\right)^{\frac{2}{3}} \tag{4.7}$$

where S is the Seebeck coefficient, K_B is the Boltzmann constant, T is the absolute temperature, e is the electronic charge, h is the Plank's constant, m_p* is the effective mass of hole and p is the hole concentration. Using the measured value of S and p at 300 K, the above equation gives m_p* as $1.2m_0$ at T = 300 K where m_0 is the rest mass of electron. It has been reported that the m_p* value of a single crystal with p $>10^{20}$ cm^{-3} is $1.1m_0$ [53], which is consistent with the m_p* value obtained for the as-prepared Cu_7Se_4 thin film. The relaxation time (τ) and mean free path (l) of charge carriers in the film are calculated as 1.6×10^{-15} s^{-1} and 17 Å using the equations described in chapter 2.

4.4 Summary and Conclusions

Polycrystalline thin films of Cu_7Se_4 are successfully prepared by reactive evaporation and a comprehensive characterization of its optoelectronic and thermoelectric power properties has been carried out for the first time. Hall measurement suggests the degenerate nature of the prepared film with high charge carrier concentration $\approx 10^{21}$ cm^{-3}. The film exhibits a direct allowed transition with an optical band gap of 2.25 eV. The positive value of Seebeck coefficient reveals the p-type conductivity of the film. The results of optical, electrical conductivity and thermoelectric power measurements support the degenerate semiconducting nature of the prepared film and the possible reasons for its metallic conduction are discussed in the context of relevant experimental

findings. Thus the as-prepared Cu_7Se_4 belongs to the category of degenerate p-type semiconductors like that of CuSe, Cu_2Se, Cu_3Se_2 and $Cu_{2-x}Se$ which are discussed in detail in the literature. The high value of electrical conductivity ≈ 10^3 Scm^{-1} and figure of merit ≈ 1.6 exhibited by the film at 425 K is well within the range reported for efficient thermoelectric materials for high temperature thermoelectric applications. This shows the potential of Cu_7Se_4 and hence that of degenerate semiconductors for future thermoelectric energy conversions. Table 4.2 summarizes a few notable material parameters of the as-prepared degenerate Cu_7Se_4 thin film.

Table 4.2 Material parameters of the as-prepared Cu_7Se_4 thin film

Material Parameters	Cu_7Se_4
Type of conductivity	p-type degenerate
Optical band gap	2.25 eV
Photosensitivity	No photoresponse
Charge carrier concentration at 300 K	$8x10^{21}$ cm^{-3}
Electrical conductivity at 300 K	$3x10^3$ Scm^{-1}
Effective mass at 300 K	$1.2m_0$
Mobility at 300 K	2.4 $cm^2V^{-1}s^{-1}$
Maximum Seebeck coefficient	11.6 μVK^{-1} at 425 K
Maximum electrical conductivity	7.5 $x10^3$ Scm^{-1} at 4 K
Maximum thermal conductivity	0.0057 $Wm^{-1}K^{-1}$ at 4 K
Maximum power factor	$1.5x10^{-5}$ $Wm^{-1}K^{-2}$ at 425 K
Maximum figure of merit	1.6 at 425 K

References

[1] V. Milman, Acta. Cryst B 58, 437 (2002).

[2] P. K. Nair, M. T. S. Nair, V. M. Garcia, O. L. Arenas, Y. Pena, A. Castillo, I. T. Ayala, O. Gomezdaza, A. Sanchez, J. Campos, H. Hu, R. Suarez and M. E. Rincon, Sol. Energy. Mater. Sol. Cells 52, 313 (1998).

[3] M. A. Korzhuev, Phys. Solid. State 40, 217 (1998).

[4] V. M. Garcia, L. Guerrero, M. T. S. Nair and P. K. Nair, Superficies y Vacio 9, 213 (1999).

[5] V. M. Bhuse, P. P. Hankare, K. M. Garadkar and A. S. Khomane, Mater. Chem. Phys 80, 82 (2003).

[6] H. M. Pathan, C. D. Lokhande, D. P. Amalnerkar and T. Seth, Appl. Surf. Sci 211, 48 (2003).

[7] A. A. Yadav, J. Mater. Sci. Mater. Electron 25, 3096 (2014).

[8] I. A. Ezenwa, N. A. Okereke and L. N. Okoli, Int. J. Eng. Sci. Tech. Inn 2, 82 (2013).

[9] P. Peranantham, Y. L. Jeyachandran, C. Viswanathan, N. N. Praveena, P. C. Chitra, D. Mangalaraj and S. K. Narayandass, Mater. Charact 58, 756 (2007).

[10] C. L. Clement, M. N. Spallart, S. K. Haram and K. S. V. Santhanam, Thin Solid Films 302, 12 (1997).

[11] A. L. N. Stevels and F. Jellinek, Recl. Trav. Chim. Pays. Bas 90, 273 (1971).

[12] W. S. Chen, J. M. Stewart and R. A. Mickelsen, Appl. Phys. Lett 46, 1095 (1985).

[13] H. Okimura, T. Matsumae and R. Makabe, Thin Solid Films 71, 53 (1980).

[14] H. Liu, X. Shi, F. Xu, L. Zhang, W. Zhang, L. Chen, Q. Li, C. Uher, T. Day and G. J. Snyder, Nature. Mater 11, 422 (2012).

[15] V. M. Garcia, P. K. Nair and M. T. S. Nair, J. Crystal. Growth 203, 113 (1999).

[16] B. Guzeldir and M. Saglam, Spectrochimica. Acta A 150, 111 (2015).

[17] K. R. Murali and R. J. Xavier, Chalcogenide Lett 6, 683 (2009).

[18] M. Z. Xue, Y. N. Zhou, B. Zhang, L. Yu, H. Zhang and Z. W. Fu, J. Electrochem. Soc 153, A2262 (2006).

[19] M. Kemmler, M. Lazell, P. O. Brien, D. J. Otway, J. H. Park and J. R. Walsh, J. Mater. Sci. Mater. Electron 13, 531 (2002).

[20] Y. D. Li, P. Fan, Z. H. Zheng, J. T. Luo, G. X. Liang and S. Z. Guo, J. Alloys Compd 658, 880 (2016).

[21] K. G. Gunther, The use of thin films in physical investigations, ed. by J. C. Anderson (Academic, London, 1966), pp. 213-232.

[22] B. D. Cullity, Elements of X-ray diffraction, ed. by M. Cohen (Addison Wesley, Philippines, 1978), pp. 81-106.

[23] C. D. Wagner, Handbook of X-ray photoelectron spectroscopy: a reference book of standard data for use in X-ray photoelectron spectroscopy, ed. by G. E. Muilenberg (Perkin Elmer, USA, 1979), pp. 1-190.

[24] I. Terasaki, Comprehensive semiconductor science and technology, ed. by P. Bhattacharya, R. Fornari and H. Kamimura (Elsevier, USA, 2011), pp. 326-358.

[25] R. S. Mane, S. P. Kajve, C. D. Lokhande and S. H. Han, Vacuum 80, 631 (2006).

[26] R. G. Hunsperger, Integrated optics theory and technology (Springer, Berlin, 1995), pp. 74-92.

[27] J. Tauc, Amorphous and liquid semiconductors (Plenum, London, 1974), pp. 159-220.

[28] A. M. Hermann and L. Fabick, J. Cryst. Growth 61, 658 (1983).

[29] E. Burstein, Phys. Rev. 93, 632 (1953).

[30] P. K. Nair, J. O. Aguilar, O. G. Daza and M. T. S. Nair, Chemical solution deposition of semiconducting and non metallic films, ed. by D. Lincot and G. Hodes (Electrochemical Society, USA, 2006), pp. 22-30.

[31] C. M. Lampert, Sol. Energy. Mater 6, 1 (1981).

[32] M. T. S. Nair and P. K. Nair, Semicond. Sci. Technol 4, 599 (1989).

[33] S. Prabahar, N. Suryanarayanan, V. Balasubramanian, S. Srikanth and D. Kathirvel, Archives. Appl. Sci. Res 2, 292 (2010).

[34] V. D. Das, J. Appl. Phys 55, 1023 (1984).

[35] K. Matsuura and D. M. Rowe, Chemical rubber company handbook of thermoelectrics, ed. by D. M. Rowe (Chemical Rubber Company, USA, 1995), pp. 573-594.

[36] R. Matsumoto, Y. Hoshina and N. Akuzawa, Mater. Trans 50, 1607 (2009).

[37] T. M. Tritt and M. A. Subramanian, Mater. Res. Soc. Bulletin 31, 188 (2006).

[38] K. Mahmood, M. Asghar, A. Ali, M. A. U. Nabi, M. I. Arshad, N. Amin and M. A. Hasan, Adv. Energy. Res 3, 117 (2015).

[39] Y. Du, K. F. Cai, S. Chen, P. Cizek and T. Lin, American. Chem. Soc. Appl. Mater. Interfaces 6, 5735 (2014).

[40] K. Kadel, L. Kumari, W. Z. Li, J. Y. Huang and P. P. Provencio, Nanoscale. Res. Lett 6, 57 (2011).

[41] M. Yasukawa and N. Murayama, J. Mater. Sci 32, 6489 (1997).

[42] M. Fardy, A. I. Hochbaum, J. Goldberger, M. M. Zhang and P. Yang, Adv. Mater 19, 3047 (2007).

[43] G. J. Snyder and E. S. Toberer, Nature. Mater 7, 105 (2008).

[44] C. Kang, H. Wang, H. Kim, S. J. Kim and W. Kim, J. Electronic. Mater 43, 353 (2014).

[45] Q. Zhang, F. Cao, W. Liu, K. Lukas, B. Yo, S. Chen, C. Opeil, D. Broido, G. Chen and Z. Ren, J. American. Chem. Soc 134, 10031 (2012).

[46] P. F. P. Poudeu, A. Gueguen, C. I. Wu, T. Hogan and M. G. Kanatzidis, Chem. Mater 22, 1046 (2010).

[47] J. R. Szczech, J. M. Higgins and S. Jin, J. Mater. Chem 21, 4037 (2011).

[48] H. Arabshahi and F. Sarlak, Res. J. Appl. Sci 6, 232 (2011).

[49] H. J. Goldsmid, Introduction to thermoelectricity, ed. by R. Hull, J. Parisi, R. M. Osgood and H. Warlimont (Springer, Berlin, 2010), pp. 45-66.

[50] Z. Ogorelec and D. Selinger, J. Mater. Sci 6, 136 (1971).

[51] A. Mondal and P. Pramanik, J.Solid. State. Chem 47, 81 (1983).

[52] M. A. Butler and D. S. Ginley, J. Electrochem. Soc 125, 228 (1978).

[53] G. B. Abdullaev, Z. A. Aliyarova and G. A. Asadov, Phys. Status. Solidi B 21, 461 (1967).

Chapter 5

Preparation and Characterization of Polycrystalline $CuInSe_2$ Thin Films

5.1 Introduction

Copper Indium Selenide ($CuInSe_2$ or CISe) is a compound belonging to I-III-VI family of semiconductors with a tetragonal chalcopyrite structure [1] as shown in Fig 5.1.

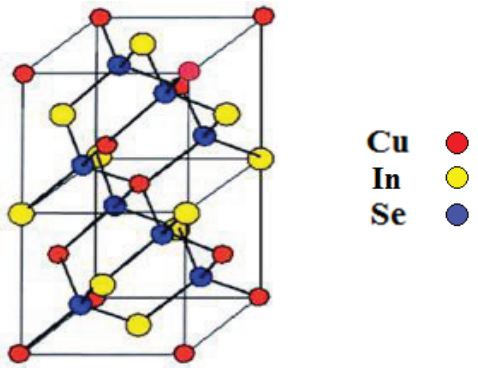

Fig 5.1 Crystal structure of $CuInSe_2$

$CuInSe_2$ is an attractive material for researchers because it allows tuning of properties in a desired manner for required applications by means of doping [2]. $CuInSe_2$ is a renowned highly efficient, low cost, radiation resistant and stable absorber layer material for use in thin film solar cells due to its near optimum band gap for harvesting solar energy, high optical absorption coefficient, long term thermal, environmental and electrical stability, reasonable work function and potential low cost methods in its preparation [3]. Solar cells based on alloys between $CuInSe_2$ and $Cu(In,Ga)Se_2$ have already demonstrated record conversion efficiency which exceed 19.2% [4]. A wide variety of preparation techniques such as pulsed laser deposition [5], sputtering [6], chemical bath deposition [7], flash evaporation [8], spray pyrolysis [9] have been employed for the deposition of $CuInSe_2$ with varying degrees of success.

Most interestingly, it is possible to dope $CuInSe_2$ as p-type and n-type simply by the introduction of native defects and thereby forming stable homojunctions in solar cells [10]. However, deviations from the ideal stoichiometry of $CuInSe_2$ give rise to several donor and acceptor levels which influence its optoelectronic properties [11]. The presence of intrinsic point defects such as vacancies, interstitials and antisite defects plays a dominant role on the optical and electrical properties of $CuInSe_2$. The cation vacancies or anion interstitials leads to p-type conductivity, whereas, the anion vacancies or cation interstitials leads to n-type conductivity of the film [12]. Therefore, depending on the deposition methods, especially for vacuum evaporated thin films, there are possibilities for the incorporation of a number of such defects that contribute significantly to optoelectronic properties of $CuInSe_2$ [13]. Thus

it is desirable to have knowledge on the origin and nature of these defects for a better understanding of the performance of $CuInSe_2$ based solar cells.

In literature, although considerable work on $CuInSe_2$ has been done, there are only a few studies devoted to the analysis of intrinsic point defects, photoconductivity and thermoelectric power in $CuInSe_2$. Therefore in the present work, special emphasis is given to the characterization of defect levels, evaluation of thermoelectric power factor and figure of merit in the temperature range from 4 K to 425 K of $CuInSe_2$ thin films. The as-prepared $CuInSe_2$ thin films are characterized for their structural, compositional, morphological, optical, electrical and thermoelectric power properties and the results of the studies are discussed in the following sections.

5.2 Experimental technique

In the present study, reactive evaporation - a variant of Gunther's three temperature method [14], described in section 3.3, is used to prepare $CuInSe_2$ thin films. The experimental setup and the detailed process of thin film deposition have already been discussed in section 3.4. Briefly, high purity Cu (99.999%), In (99.999%) and Se (99.999%) are evaporated simultaneously at suitable rates from independently heated sources. Cu and In are evaporated from two separate molybdenum boats whereas Se is evaporated from a glass crucible kept in a molybdenum basket. The vapours are allowed to deposit on glass substrates kept at an elevated temperature of 473±5 K after attaining a pressure of the order of 10^{-5} mbar in the coating unit. The optimized conditions used to deposit $CuInSe_2$ thin films are:

Impingement rate of Cu : 3.5×10^{15} atoms $cm^{-2}s^{-1}$
Impingement rate of In : 3.3×10^{15} atoms $cm^{-2}s^{-1}$
Impingement rate of Se : 4.1×10^{15} atoms $cm^{-2}s^{-1}$
Substrate temperature : 473±5 K

The as-prepared $CuInSe_2$ thin films are characterized for their structural properties using Rigaku D MaxC X-ray diffractometer (XRD) for 2θ varying from 10° to 70° with CuK_{α} (1.5404 Å) as the radiation source. The elemental composition is verified from energy dispersive analysis of X-rays (EDAX) and X-ray photoelectron spectroscopy (XPS). The surface morphology is studied using scanning electron microscopy (SEM) and atomic force microscopy (AFM). The optical properties are analyzed using UV-Vis-NIR spectrophotometer in the wavelength range from 2500 nm to cut-off. The thickness of the film is measured using Veeco Dektak 6M stylus profiler and is found to be ≈ 150 nm. The Hall and photoconductivity measurements are performed at room temperature. The Seebeck coefficient, electrical conductivity and thermal conductivity of the as-prepared thin films are measured in the temperature range from 4 K to 425 K to evaluate the thermoelectric figure of merit. The details of the aforementioned characterization tools have already been described in section 3.5 and the results obtained are presented in the following sections.

5.3 Results and Discussions

5.3.1 Structural analysis

The XRD pattern of the as-prepared $CuInSe_2$ thin film is shown in Fig 5.2. The observed interplanar spacings and (hkl) planes of the prepared thin film match well with that of tetragonal $CuInSe_2$ (JCPDS Card. 40-1487).

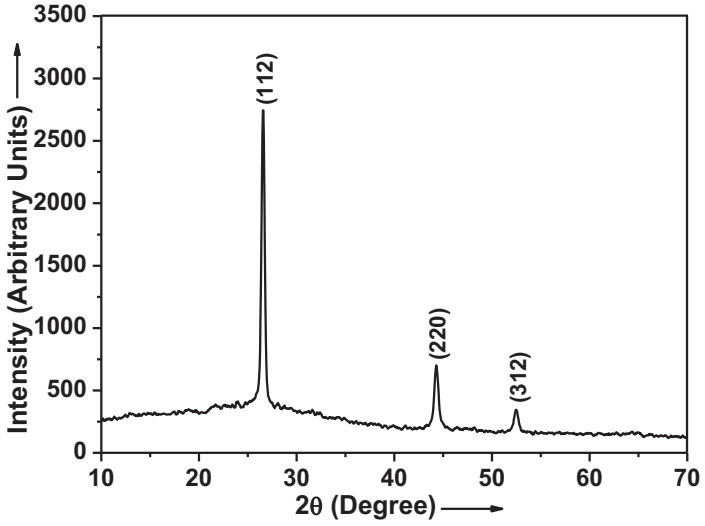

Fig 5.2 XRD pattern of the as-prepared $CuInSe_2$ thin film

The XRD pattern indicates the formation of polycrystalline $CuInSe_2$ thin film. The reflection from (112), (220) and (312) planes are typical of the chalcopyrite structure. The lattice constants are obtained as a = 5.79 Å and c = 11.68 Å. These values agree well with those listed in the (JCPDS Card. 40-1487). The average crystallite size is calculated using Scherrer formula [15] and is obtained as 52 nm. The structural parameters of the film such as

dislocation density, number of crystallites per unit area and lattice strain are obtained as 3.7×10^{10} lines cm^{-2}, 11×10^{10} cm^{-2} and 1.3×10^{-3} respectively using the equations described in section 3.5.1.

5.3.2 Compositional analysis

The EDAX spectrum of the as-prepared $CuInSe_2$ thin film is shown in Fig 5.3. The analysis of EDAX spectrum reveals a slightly Cu rich and non Se deficient composition with an average atomic percentage of the elements as Cu = 25.75%, In = 23.87% and Se = 50.38%.

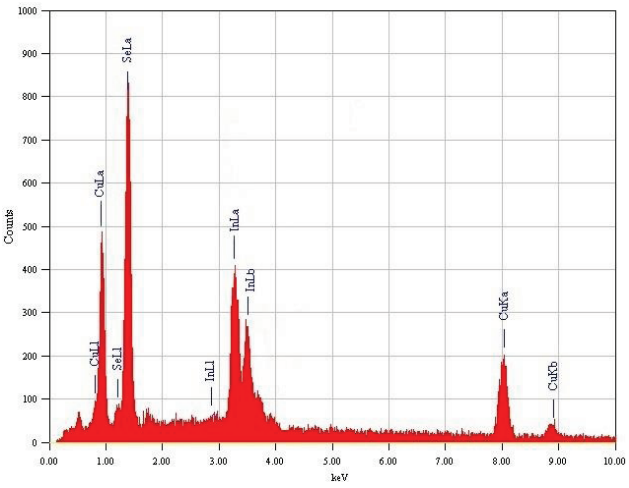

Fig 5.3 EDAX spectrum of $CuInSe_2$ thin film

Fig 5.4 depicts the binding energy (B.E) versus counts per second (CPS) of Cu2p, In3d and Se3d peaks obtained from the XPS spectrum of the as-prepared $CuInSe_2$ thin film. The XPS data reveals an average atomic percentage of Cu = 25.68%, In = 23.71% and Se = 50.61%, thereby suggesting

a slightly Cu rich and non Se deficient composition consistent with EDAX results.

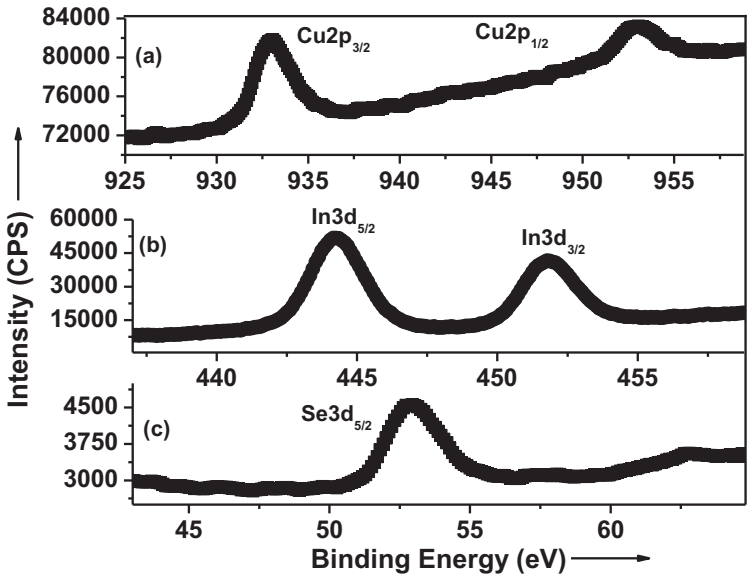

Fig 5.4 XPS spectrum of $CuInSe_2$ thin film

The observed shift in the B.E of Cu, In and Se from their elemental peak position, shown in Table 5.1, is a clear evidence of the formation of $CuInSe_2$ compound where the elements Cu, In and Se exist in a chemically bonded state.

Table 5.1 Comparison of the observed peak positions of Cu, In and Se from the XPS spectrum with their standard elemental peak positions

Peak position (eV)	$Cu2p_{3/2}$	$Cu2p_{1/2}$	$In3d_{5/2}$	$In3d_{3/2}$	$Se3d_{5/2}$
Observed peak position	933.1	953.1	444.3	451.8	53.1
Elemental peak position [16]	932.6	952.2	443.8	451.4	54.9

The slightly Cu rich and non Se deficient composition of the film observed from EDAX and XPS analysis is further verified by applying bond length calculations and also by determining the molecularity and stoichiometry deviation parameters which are discussed in the following sections.

Calculation of bond lengths

The chalcopyrite $CuInSe_2$ possesses a tetragonal crystal structure. In this structure, each cation A and B is tetrahedrally coordinated by four anions C and each anion C is coordinated by two A cations and two B cations. Thus there are two cation sublattices and in the equilibrium condition the anion is found to be slightly displaced towards one cation, thereby leading to unequal bond lengths $R_{AC} \neq R_{BC}$ [17], where R_{AC} represents Cu-Se bond length and R_{BC} represents In-Se bond length.

In chalcopyrites, the displacement of anions from their ideal tetrahedral sites is denoted by anion displacement parameter (u) given by [18]

$$u = \frac{1}{2} - \frac{1}{4}\left(2\eta^2 - 1\right)^{1/2} \tag{5.1}$$

The unit cell is tetragonally distorted by a parameter η called distortion parameter given by [17]

$$\eta = \frac{c}{2a} \tag{5.2}$$

where a and c are lattice constants.

Using the rule of conservation of tetrahedral bonds, the values of η and u of the as-prepared $CuInSe_2$ are calculated as 1.009 and 0.246 respectively [18]. The observed decrease in u from that of the equilibrium value of 0.248 in $CuInSe_2$ is explained as due to the slight increase in Cu content in the films from that of stoichiometric composition, which is quite evident from the EDAX and XPS analysis. The increase in Cu content will increase the charge concentration on Cu-Se bond simultaneously producing a shortening of Cu-Se bond length. Since u is proportional to the difference in squares of (Cu-Se) and (In-Se) bond lengths [17], a decrease in Cu-Se bond length lowers u value. Bond lengths are calculated as R_{AC} = 2.501 Å and R_{BC} = 2.528 Å using Eq (5.3) and Eq (5.4)

$$R_{AC} = a\left[u^2 + \left(1+\eta^2\right)/16\right]^{1/2} \tag{5. 3}$$

$$R_{BC} = a\left[\left(u-1/2\right)^2 + \left(1+\eta^2\right)/16\right]^{1/2} \tag{5. 4}$$

As per the bond length calculations, $R_{AC} < R_{BC}$, which means that the anion Se is slightly displaced towards the cation Cu and away from cation In, resulting in a slightly stretched unit cell. The values of R_{AC} and R_{BC} thus obtained are compared with the calculated values of R_{AC} (2.500 Å) and R_{BC} (2.514 Å) for $CuInSe_2$ from the (JCPDS card Card No. 40-1487) and it agrees with the interpretation that in the prepared compound, Se atoms are slightly displaced toward the Cu atoms, which is in conformity with the results of EDAX and XPS analysis where a slightly increased atomic percentage of Cu is observed. The bond length mismatch δ [17] is estimated as -0.136 $(Å)^2$ using

$$\delta = R_{AC}^2 - R_{BC}^2 \tag{5.5}$$

Thus the bond length calculations reveal the slightly Cu rich and non Se deficient composition of the as-prepared $CuInSe_2$ thin film.

Determination of molecularity (Δm) and stoichiometry (Δs) deviation parameters

Based on EDAX and XPS studies, the deviations from stoichiometric composition of $CuInSe_2$ are described by two parameters proposed by Groenink et al [12]. These parameters are Δm and Δs given by Eq (5.6) and Eq (5.7) and they determine the deviations from molecularity and stoichiometry respectively.

$$\Delta m = \frac{[Cu]}{[In]} - 1 \tag{5.6}$$

$$\Delta s = \frac{2[Se]}{[Cu] + 3[In]} - 1 \tag{5.7}$$

The deviations of these parameters from zero indicate:

1. $\Delta m > 0 \rightarrow$ Cu rich films, $\Delta m < 0 \rightarrow$ In rich films
2. $\Delta s > 0 \rightarrow$ excess of selenium, $\Delta s < 0 \rightarrow$ deficiency of selenium.

The value of Δm and Δs are found to be 0.08 and 0.04 respectively, suggesting that the as-prepared $CuInSe_2$ thin film is slightly Cu rich with an excess of Se, consistent with EDAX and XPS analysis.

5.3.3 Morphological analysis

The SEM image of the $CuInSe_2$ thin film shown in Fig 5.5 suggests the significantly smooth surface with densely packed needle shaped crystallites.

The average grain size calculated from SEM ranges from about 120 nm to 150 nm.

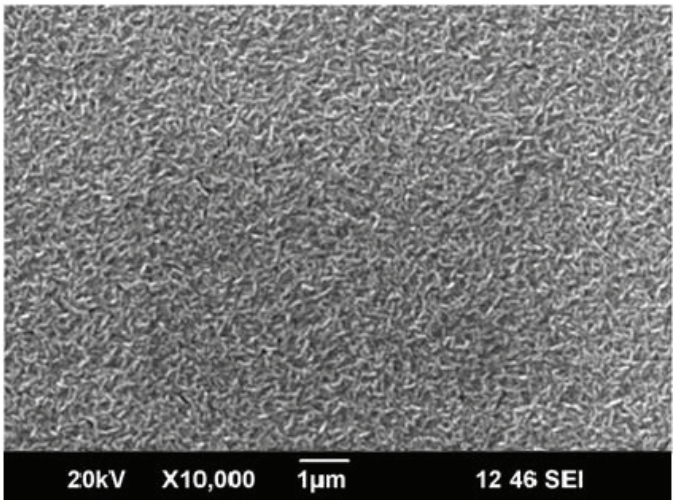

Fig 5.5 SEM image of $CuInSe_2$ thin film

The 2D AFM and 3D AFM is shown in Fig 5.6(a) and (b) respectively. The scan area is 1 µm x 1 µm and scan rate is 10.172 Hz.

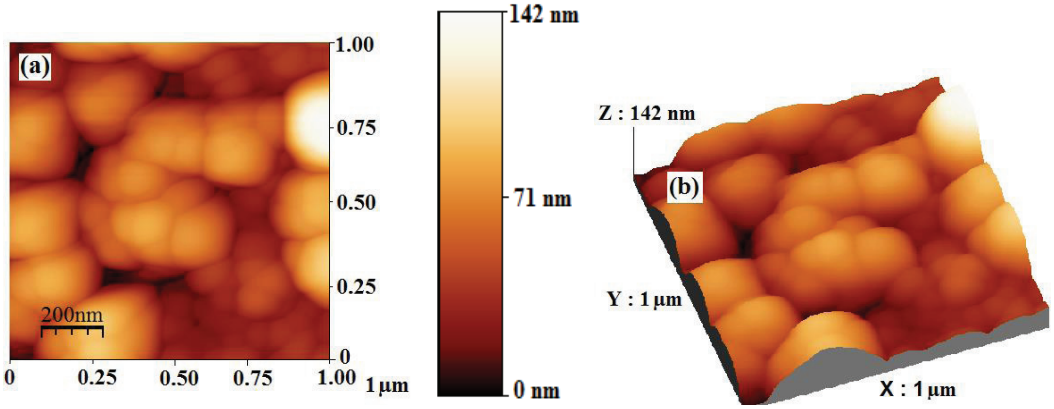

Fig 5.6(a) 2D AFM (b) 3D AFM of $CuInSe_2$ thin film

It can be seen from Fig 5.6(a) that the film exhibits clusters of sizes in the range from 140 nm to 170 nm in diameter, indicating the agglomeration of particles. The root mean square (RMS) value of surface roughness of the film determined from Fig 5.6(b) is 20 nm, indicating a significantly smooth surface.

5.3.4 Optical analysis

Determination of optical band gap

The interference fringes in the transmission spectrum of the as-prepared $CuInSe_2$ thin film shown in Fig 5.7 indicates the uniformity and quality of the film.

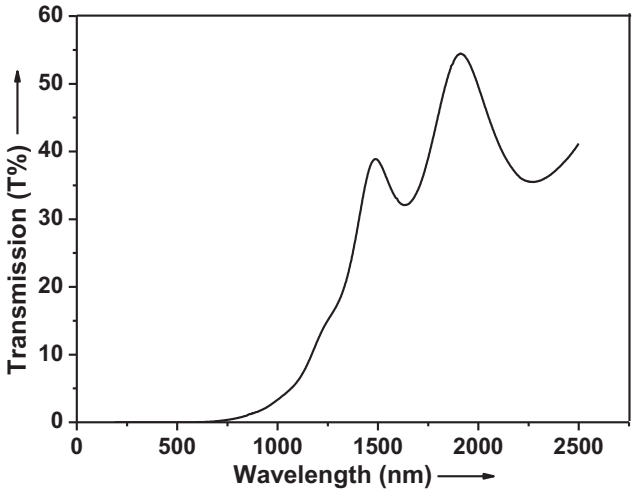

Fig 5.7 Transmission spectrum of $CuInSe_2$ thin film

The transmission spectrum is analyzed using Swanepoel's method [19] to determine the optical band gap (E_g) and absorption coefficient (α) of the

film. The optical band gap of the film is determined using the well known Tauc relation [20] described in section 3.5.7. The plot of $(\alpha h\nu)^2$ versus hν of the as-prepared $CuInSe_2$ thin film is shown in Fig 5.8.

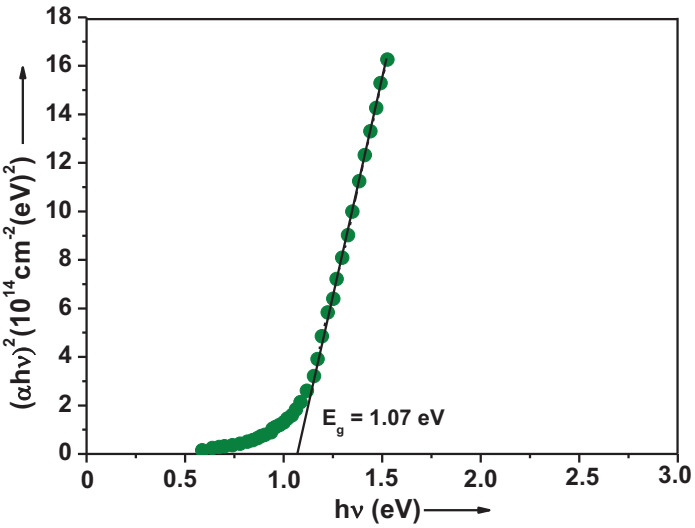

Fig 5.8 Plot of $(\alpha h\nu)^2$ versus hν of $CuInSe_2$ thin film

The film shows a direct allowed transition with an E_g of 1.07 eV and α of the order of 10^5 cm^{-1}, values well within the optimum range for harvesting solar energy. Hsu et al [21] has reported a band gap of 1.06 eV for $CuInSe_2$ thin films prepared by solid state reaction method.

Determination of optical constants

The refractive index (n) and extinction coefficient (r) of the prepared film are calculated using Swanepoel's method [19]. The real part (ε_1) and imaginary part (ε_2) of the dielectric constant of the film are calculated using the

equations described in section 3.5.7. The dependence of n, r, ε_1 and ε_2 on photon energy (hν) is presented in Fig 5.9.

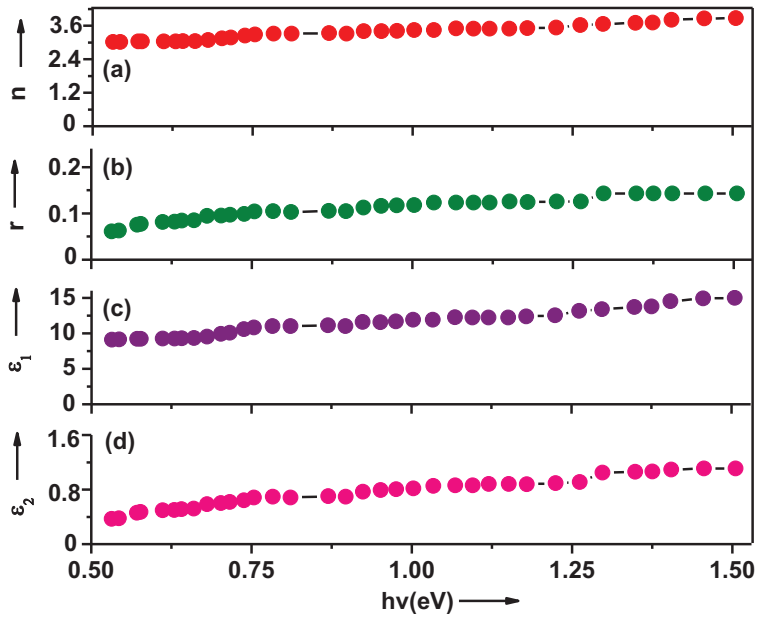

Fig 5.9 Variations of (a) n (b) r (c) ε_1 and (d) ε_2 with hν

The high refractive index and low extinction coefficient of the prepared film can be attributed to its better crystalline nature. It is observed from Fig. 5.9 that n varies from 3.0 to 3.9 and r varies from 0.06 to 0.14 in the photon energy range from 0.53 eV to 1.51 eV. It is clear that, ε_1 varies with photon energy in a similar manner as that of n whereas ε_2 varies with photon energy in a similar manner as that of r. Hence ε_1 can be related to dispersion and ε_2 can be related to the dissipation of electromagnetic wave.

Determination of dispersion parameters

The spectral dependence of the refractive index of the film is further analyzed using Wemple and DiDomenico (WD) model [22]. The WD model is a single effective oscillator model put forward by Wemple and DiDomenico in 1971 to analyze the spectral dependence of refractive index of amorphous and crystalline materials. According to WD model the dispersion of refractive index is given by

$$n^2 - 1 = \frac{E_0 E_d}{E_0^2 - (h\nu)^2} \tag{5.8}$$

where E_o is the single oscillator energy (average of optical band gap) and E_d is the dispersion energy (measure of strength of interband optical transitions). The parameters E_o and E_d are determined from the plot of $(n^2 - 1)^{-1}$ versus $(h\nu)^2$ shown in Fig 5.10, where E_o/E_d is the intercept of vertical axis and $(E_o\ E_d)^{-1}$ is the slope.

The E_o and E_d values of the prepared film are calculated as 2.17 eV and 17.19 eV respectively. Furthermore, the optical band gap is also calculated from the WD dispersion parameter E_0 by using $E_g \approx E_0/2$, a relation similar to that observed in chemical bath deposited $CdCr_2S_4$ thin films [23]. It is found that the value of E_g deduced from WD model is in good agreement with that determined from Tauc model.

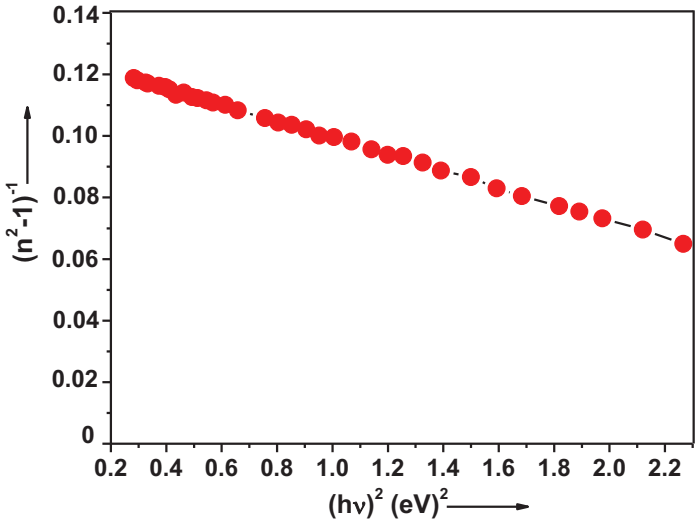

Fig 5.10 Plot of $(n^2 - 1)^{-1}$ versus $(h\nu)^2$

Using the values of E_o and E_d, the moments of the optical spectra (M_{-1} and M_{-3}), oscillator strength (f) and refractive index at infinite wavelength (n_∞) of the as-prepared thin film are calculated from the following equations [22]

$$E_0^2 = \frac{M_{-1}}{M_{-3}} \tag{5.9}$$

$$E_d^2 = \frac{M_{-1}^3}{M_{-3}} \tag{5.10}$$

$$f = E_0 E_d \tag{5.11}$$

$$n_\infty^2 - 1 = \frac{E_d}{E_0} \tag{5.12}$$

The calculated values of M_{-1}, M_{-3}, f and n_∞ are 7.91, 1.68 $(eV)^{-2}$, 37.3 $(eV)^2$ and 2.98 respectively. The moments M_{-1} and M_{-3} determine the average bond strength.

Determination of loss factor, quality factor and optical conductivity

To realize the suitability of the material for a specific optical application, the optical properties are further explored by evaluating the loss factor or tan δ (measure of dissipation of electromagnetic energy into heat in the material), quality factor or Q factor (inverse of the measured tan δ) and optical conductivity or $\sigma_{Optical}$ (measure of optical response of the material). These parameters are calculated using the equations described in section 3.5.7. The dependence of tan δ, Q factor and $\sigma_{Optical}$ on photon energy (hν) is presented in Fig 5.11.

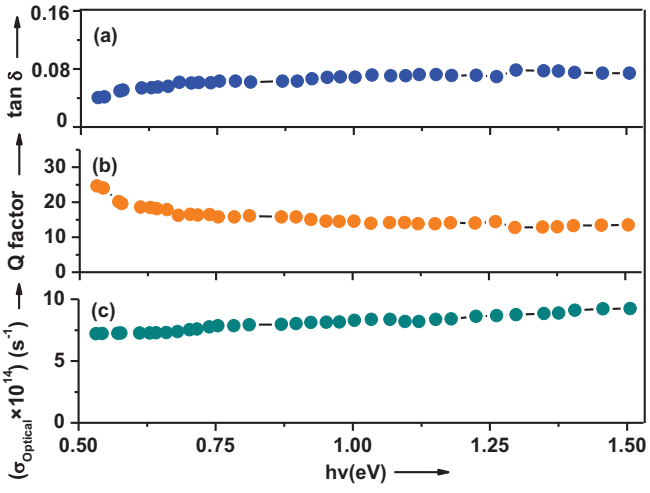

Fig 5.11 Variations of (a) tanδ (b) Q factor and (c) $\sigma_{Optical}$ with hν

Fig 5.11 shows that the loss factor of the film is too small in the measured photon energy range, suggestive of less dielectric loss. The Q factor ≈ 25 is observed at 0.53 eV and $\sigma_{Optical} \approx 9.2 \times 10^{14}\ s^{-1}$ is observed at 1.51 eV, reasonably high values suitable for optoelectronic applications and similar to that observed in chemical bath deposited $MgCdS_2$ thin films [24].

Photoconductivity measurement

The photoresponse curve of $CuInSe_2$ thin film at room temperature is given in Fig 5.12. The film shows a good photoresponse with a photocurrent ≈ 0.23 mA. The photosensitivity [25] of the film is calculated using the equation described in section 3.5.8 and is obtained as 0.6, suitable for photovoltaic applications.

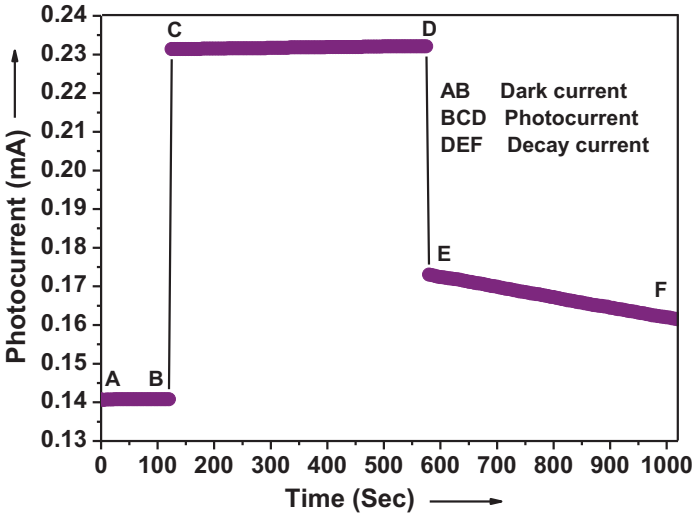

Fig 5.12 Photoresponse curve of $CuInSe_2$ thin film

As observed from Fig 5.12, the photocurrent is found to increase on illumination, indicating that the prepared film is photoconducting in nature thereby affirming the possible use of reactive evaporated $CuInSe_2$ thin films in photovoltaic devices. In Fig 5.12, the region AB represents the dark current. The region BCD represents the photocurrent resulting from the generation of charge carriers on illumination. The region DEF represents the decay current measured after cutting-off illumination. The region DEF involves two different regions, namely, the fast decay region from D to E and the slow decay region from E to F. The fast decay is due to the sudden drop in charge carriers reaching the grain barrier. The slow decay is due to the gradual emptying of charge carriers from defects (shallow traps) that are likely to be present in the film. The non exponential decay of photocurrent with time after cutting-off illumination and the observed decrease in slope of the curve with increase in decay time clearly manifests the effect of trapping of the charge carriers in the defects within the band gap of the film [26]. Using the differential lifetime concept as suggested by Fuhs et al [27] the lifetime (τ_d) is given by

$$\tau_d = -\left[\frac{1}{I^*_{ph}}\left(\frac{dI_{ph}}{dt}\right)\right]^{-1} \tag{5.13}$$

where I_{ph^*} is the maximum photocurrent at t = 0 for a given applied voltage and it is found to vary with time. The dependence of lifetime (τ_d) on time (t), depicted in Fig 5.13, shows an increase in differential lifetime with time. This confirms the presence of traps in the band gap of the material, having different time constants and thereby resulting in the non exponential decay of photocurrent.

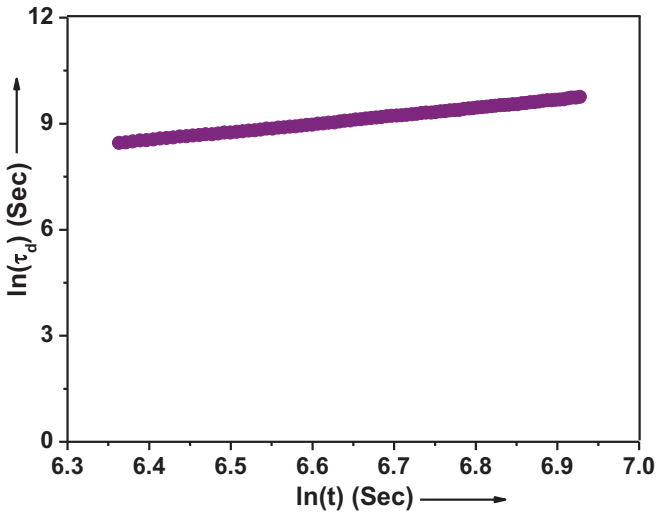

Fig 5.13 Variation of $\ln(\tau_d)$ with ln(t) of $CuInSe_2$ thin film

5.3.5 Electrical analysis

Hall measurement

The p-type conductivity of the film is verified from Hall measurements. The film shows a hole concentration $p \approx 6.2\times10^{16}$ cm^{-3}, hole mobility $\mu_p \approx 10.5$ $cm^2V^{-1}s^{-1}$ and electrical conductivity $\sigma \approx 0.1$ Scm^{-1} at room temperature.

Analysis of point defects: electrical conductivity measurement

Fig 5.14 shows the variation of ln(I) with inverse of temperature of the as-prepared $CuInSe_2$ thin film for three continuous heating-cooling cycles.

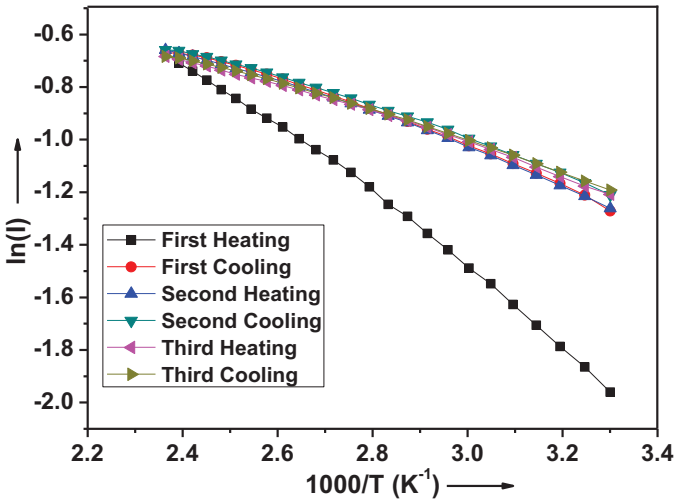

Fig 5.14 Variation of ln(I) with inverse of temperature of $CuInSe_2$ thin film

The increase in current with increase in temperature observed from Fig 5.14 ascertains the non degenerate semiconducting nature of the film. As already mentioned, for films deposited by vacuum evaporation, there are possibilities for the incorporation of a number of defects in the film during its formation. The prepared film being polycrystalline in nature, generally have lattice defects such as vacancies, interstitials and antisites [13]. The seven relevant defects that are possible to occur in $CuInSe_2$ are: the vacancies V_{Cu}, V_{In} and V_{Se} , the cation-cation antisites Cu_{In} and In_{Cu}, and the anion-cation antisites Cu_{Se} and In_{Se} [28]. The EDAX and XPS analysis shows that the prepared thin films are slightly Cu rich with an excess of Se. Since the films are of p-type, this deviation from ideal stoichiometry could lead to the existence of any of the acceptor type defects such as indium vacancy (V_{In}), selenium interstitial (Se_i), copper on indium antisite (Cu_{In}) or selenium on

indium antisite (Se_{In}). So a systematic analysis of defects that are possible to occur in the sample is carried out by an examination of activation energy. The activation energy [29] which is calculated from the ln(I) versus 1000/T plot is 0.05 eV. This value is in fairly good agreement with the energy of the defect level assigned to Cu_{In} (≈ 50 meV) by Polity et al [28] in their study of defects in electron irradiated $CuInSe_2$ by positron lifetime spectroscopy. Briefly, the Cu_{In} is a shallow acceptor defect responsible for p-type conductivity in slightly Cu rich, non Se deficient $CuInSe_2$ thin films [30]. Hence the p-type conductivity of the as-prepared $CuInSe_2$ thin film can be assigned to Cu_{In} defect, consistent with EDAX and XPS results.

The order of formation energies of the defects in stoichiometric/slightly Cu rich-In poor p-type $CuInSe_2$ thin films is calculated by Zhang et al [31] and is given as $Cu_{In}<V_{Cu}<V_{In}<Cu_i<In_{Cu}$. The defects such as Se_i and Se_{In} possess higher formation energies than Cu_{In}. Therefore, considering the order of formation energies, the possibilities of forming the Cu_{In} defect in the prepared film is higher than the other possible defects V_{In}, Se_i and Se_{In} [28]. Hence taking into account, the stoichiometry of the film and observation of defect transition energy level at energy consistent with literature data, the defect level observed at 50 meV in the present study is assigned to that of acceptor type antisite defect Cu_{In}. It is thus very likely that these defects are possible candidates that give rise to shallow traps in the band gap of the material. These shallow traps readily traps minority charge carriers to prevent recombination with majority charge carriers and enhances the photocurrent on illumination and also results in a non exponential decay of photocurrent after the illumination is cut-off. This phenomenon is quite evident from the

photoresponse curve of the film shown in Fig 5.12. Therefore, the electrical conductivity measurement can be used as one sensitive method to track predominant native point defects related to the deviations from ideal stoichiometry of compound thin films.

Determination of thermoelectric power factor and figure of merit in the temperature range from 4 K to 425 K

Fig 5.15 shows the variation of thermoelectric power (TEP) or Seebeck coefficient (S) in the temperature range from 4 K to 425 K of the as-prepared $CuInSe_2$ thin film. The positive value of S observed from Fig 5.15 confirms that the as-prepared $CuInSe_2$ thin films are of p-type. The hot probe and Hall measurements on the film corroborate this observation.

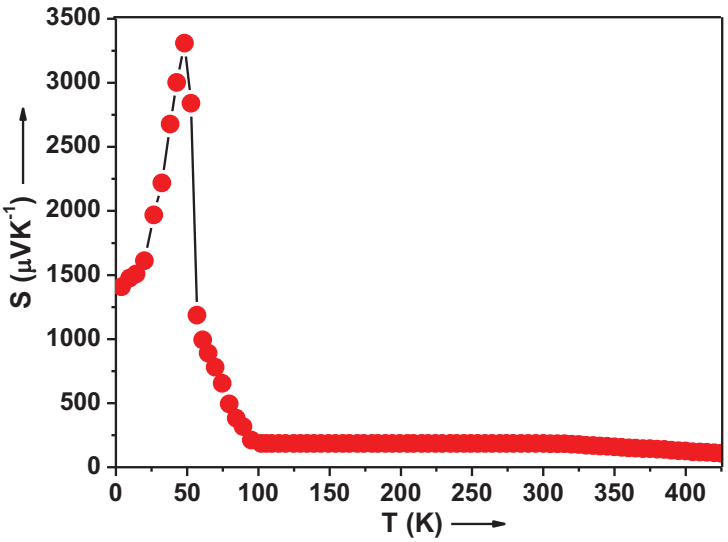

Fig 5.15 Variation of S with temperature of $CuInSe_2$ thin film

Fig 5.15 shows an increase in S from 107 μVK^{-1} to 183 μVK^{-1} with decrease in temperature from 425 K to 305 K, suggestive of the non degenerate semiconducting nature of the film. The observed value of S is well within the optimum range for thermoelectric applications [32]. Below 305 K, the value of S is constant ≈ 184 μVK^{-1} up to 100 K. But as the temperature is lowered from 100 K, there is a sudden and sharp increase in S whose onset is at around 95 K and reaches up to a maximum of ≈ 3309 μVK^{-1} at 48 K. This marked increase in S at low temperatures has been investigated theoretically by Herring [33] and is interpreted as due to the interaction of phonons with mobile charge carriers consequently resulting in the phonon drag on the charge carriers.

When a temperature gradient is established, an electric field is developed across the sample and more phonons carry energy from hot end to the cold end of the specimen. This prevents the isotropic scattering of electrons and more electrons are pushed towards the hot end by phonons. This process results in the development of an electric field in addition to the one already established by the temperature gradient. The final outcome is obviously a colossal Seebeck coefficient towards low temperatures - a phenomenon usually observed for specimens of high resistivity to moderate resistivity [33].

However, the amplitude of phonon drag effect depends on the number of phonons available to interact with the charge carriers. Towards very low temperatures (usually below about one-fifth of the Debye temperature θ_D), the relative number of phonons available for drag decreases. As a result the effect of phonon drag on the Seebeck coefficient also decreases. This can be a reason for the decrease in S observed in the film at temperatures below 48 K which is

about one fifth of the θ_D of $CuInSe_2$. The value of θ_D for $CuInSe_2$ is 244 K [34]. The value of S ≈ 1407 μVK^{-1} at 4 K obtained for the as-prepared $CuInSe_2$ thin films are typical of efficient materials used for thermoelectric applications [32].

Fig 5.16 and Fig 5.17 shows the variation of electrical conductivity (σ) and thermal conductivity (k) in the temperature range from 4 K to 425 K of the $CuInSe_2$ thin film respectively. As observed from Fig 5.16, the value of σ of the film varies from 0.06 Scm^{-1} to 0.25 Scm^{-1}.

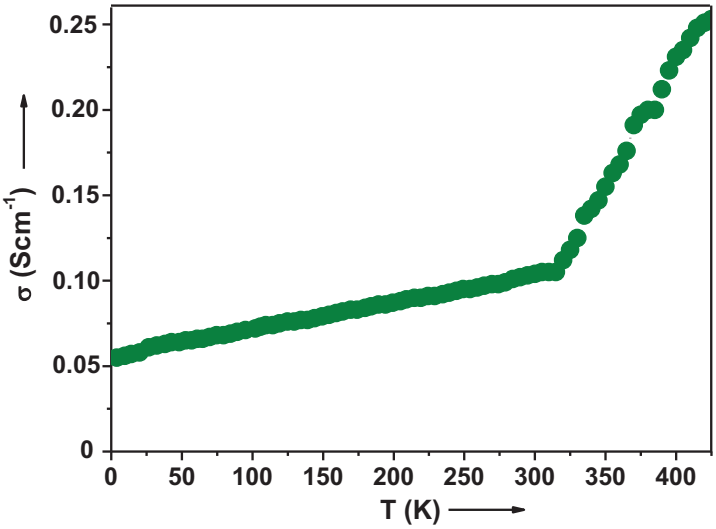

Fig 5.16 Variation of σ with temperature of $CuInSe_2$ thin film

As seen from Fig 5.17, the thermal conductivity of the film varies from 0.003 $Wm^{-1}K^{-1}$ to 0.006 $Wm^{-1}K^{-1}$. The variation of thermoelectric power factor ($S^2\sigma$) of the film in the temperature range from 4 K to 425 K is shown in Fig 5.18.

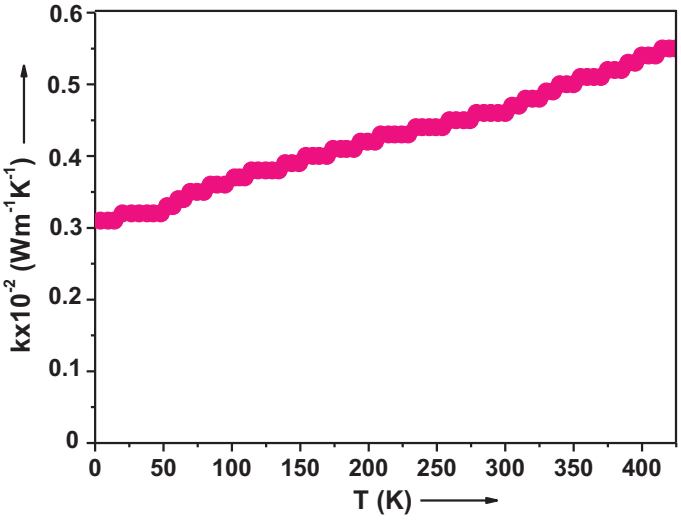

Fig 5.17 Variation of k with temperature of $CuInSe_2$ thin film

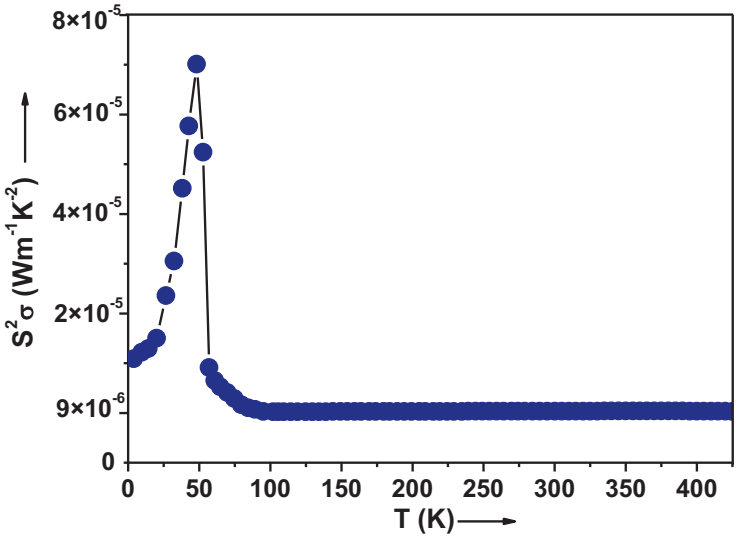

Fig 5.18 Variation of $S^2\sigma$ with temperature of $CuInSe_2$ thin film

As seen from Fig 5.18, the power factor of the film varies from 10^{-5} $Wm^{-1}K^{-2}$ to 10^{-7} $Wm^{-1}K^{-2}$ with a room temperature value ≈ 3.6 x 10^{-7} $Wm^{-1}K^{-2}$. These values are rather low compared to good thermoelectric materials (≈ 10^{-3} $Wm^{-1}K^{-2}$ to 10^{-5} $Wm^{-1}K^{-2}$) but comparable to emerging thermoelectric materials such as perovskite type $BaSn_{0.85}Co_{0.15}O_{2.85}$ (≈ 2.7 x 10^{-7} $Wm^{-1}K^{-2}$) [35]. The maximum value of $S^2\sigma$ is about 7 x 10^{-5} $Wm^{-1}K^{-2}$ observed at 48 K, which is approaching the useful range for thermoelectric applications (≈ 10^{-3} $Wm^{-1}K^{-2}$) [36] and comparable to those reported for some of the potential thermoelectric materials such as Bi_2Se_3 [37], $CuAlO_2$ [38] and $Nd_{1.95}Ce_{0.05}CuO_4$ [39] that are recently being developed. This provides an overwhelming optimism for the chalcopyrite $CuInSe_2$ to be considered as a possible candidate for thermoelectric applications, on further enhancement of its power factor by the optimization of charge carrier concentration [37] through nanostructuring and electronic band engineering. Moreover, the thermoelectric efficiency of the as-prepared $CuInSe_2$ thin film is evaluated by calculating the thermoelectric figure of merit (ZT) given by [40]

$$ZT = \frac{S^2 \sigma T}{k} \tag{5.14}$$

The variation of ZT in the temperature range from 4 K to 425 K is shown in Fig 5.19. The as-prepared $CuInSe_2$ exhibits a maximum ZT ≈ 1.1 at 48 K, comparable to that obtained for $Ge_{0.89}Te_{0.89}Ag_{0.88}Ge_{0.11}Te_{0.66}$ composites [41], Bi_2Te_3 nanopowders [42] and PbTe-PbS nanocomposites [43] which are state-of-the-art thermoelectric materials.

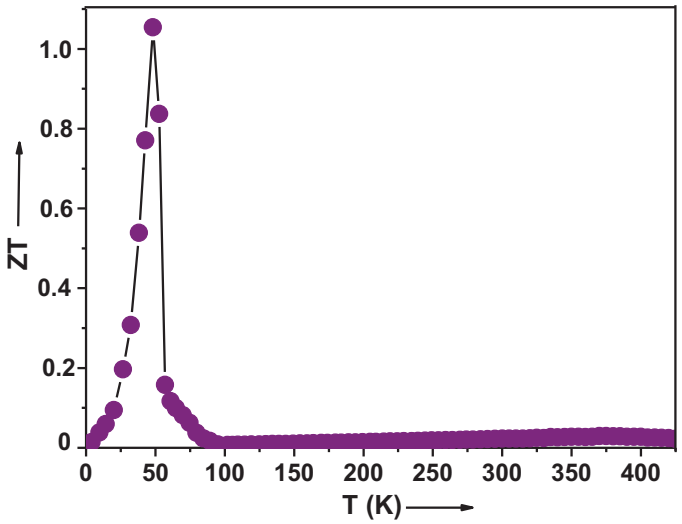

Fig 5.19 Variation of ZT with temperature of $CuInSe_2$ thin film

In general, materials with ZT ≥ 1 are recognized as efficient candidates for use in thermoelectric devices [32]. Hence the as-prepared $CuInSe_2$ thin film with ZT ≈ 1.1 at 48 K, on further work, can be regarded as a promising material for cryogenic thermoelectric applications.

Evaluation of material parameters

The data from the analysis of Hall and thermoelectric power measurements have been combined to evaluate important material parameters such as Fermi energy (E_F), effective mass (m_p*), density of states (N_V), relaxation time (τ) and mean free path (l). The results obtained are presented in the following sections.

For non degenerate semiconductors, the Seebeck coefficient (S) is related to Fermi energy (E_F) as

$$S = \pm \frac{K_B}{e}\left[A + \frac{E_F}{K_B T}\right] \tag{5.15}$$

where E_F is the separation of Fermi level from the top of the valence band edge, K_B is the Boltzmann constant, T is the temperature at which thermoelectric power is determined and A is the scattering parameter [44]. By using Eq (5.15), the position of Fermi level is determined as ≈ 0.02 eV above the valence band. The value of A is obtained as 3/2, indicating ionized impurity scattering [45]. The effective mass of holes (m_p*) is calculated by using the equations

$$p = N_V \exp\left[-\left(\frac{E_F - E_V}{K_B T}\right)\right] \tag{5.16}$$

$$N_V = 2\left(\frac{2\pi m_p^* K_B T}{h^2}\right)^{3/2} \tag{5.17}$$

where N_V is the effective density of states at the valence band edge, K_B is the Boltzmann constant, T is the temperature and h is the Planck's constant [46]. The values of N_V and m_p* are obtained as ≈ 4.6×10^{17} cm^{-3} and ≈ $0.07m_0$ respectively, where m_0 is the rest mass of electron. In the present study, the density of states (N_V) is found to be greater than the charge carrier concentration (p), i.e, $N_V >> p$, a relation that decides the non degenerate condition of semiconductors [47]. This observation once again confirms the

non degenerate semiconducting nature of the as-prepared $CuInSe_2$ thin film. The relaxation time (τ) is calculated by using the equation [48]

$$\tau = \frac{\mu m_p^*}{e} \tag{5.18}$$

where μ is the mobility of the charge carrier, m_p* is the effective mass of holes and e is the charge of electron. The mean free path (l) of charge carriers is calculated by using the equation [48]

$$l = \tau V_F \tag{5.19}$$

where V_F is the Fermi velocity and it is given by

$$V_F = \left(\frac{2E_F}{m_p^*} \right)^{1/2} \tag{5.20}$$

Thus τ and l are evaluated as $\approx 4.2 \times 10^{-16}$ s and ≈ 1.2 Å respectively, suggestive of high level of phonon interaction in polycrystalline thin films with innumerable grain boundaries.

5.4 Summary and Conclusions

Polycrystalline thin films of $CuInSe_2$ are successfully deposited under optimized deposition conditions by reactive evaporation. The interpretations based on bond length calculations and compositional analysis confirms the slightly Cu rich and non Se deficient nature of the film. The high absorption coefficient, near optimum optical band gap for solar energy harvesting and good photosensitivity suggests the possible use of the film as an absorber layer

material in solar cells. The temperature dependence of electrical conductivity and Seebeck coefficient reveals the non degenerate semiconducting nature of the film. The reasonably high value of Seebeck coefficient ≈ 3309 $\mu VK^{-1}$and figure of merit ≈ 1.1 at 48 K of the film, indicates its potential application in the field of low temperature thermoelectrics. Table 5.2 summarizes a few notable material parameters of the as-prepared $CuInSe_2$ thin film

Table 5.2 Material parameters of the as-prepared $CuInSe_2$ thin film

Material Parameters	$CuInSe_2$
Type of conductivity	p-type non degenerate
Optical band gap	1.07 eV
Photosensitivity	0.6
Charge carrier concentration at 300 K	$6.2x10^{16}$ cm^{-3}
Electrical conductivity at 300 K	0.1 Scm^{-1}
Effective mass at 300 K	$0.07m_0$
Mobility at 300 K	10.5 $cm^2V^{-1}s^{-1}$
Maximum Seebeck coefficient	3309 μVK^{-1} at 48 K
Maximum electrical conductivity	0.25 Scm^{-1} at 425 K
Maximum thermal conductivity	0.006 $Wm^{-1}K^{-1}$ at 425 K
Maximum power factor	$7x10^{-5}$ $Wm^{-1}K^{-2}$ at 48 K
Maximum figure of merit	1.1 at 48 K

References

[1] V. G. Lambrecht, Mater. Res. Bulletin 8, 1383 (1973).

[2] Z. Yan, W. Deng, X. Zhang, Q. Yuan, P. Deng, J. Liang and L. Sun, Phys. Status. Solidi A 211, 2546 (2014).

[3] U. Rau and H. W. Schock, Appl. Phys. A 69, 131 (1999).

[4] K. Ramanathan, M. A. Contreras, C. L. Perkins, S. Asher, F. S. Hasoon, J. Keane, D. Young, M. Romero, W. Metzger, R. Noufi, J. Ward and A. Duda, Prog. Photovolt. Res. Appl 11, 225 (2003).

[5] S. Kuranouchi and A. Yoshida, Thin Solid Films 343-344, 123 (1999).

[6] J. Muller, J. Nowoczin and H. Schmitt, Thin Solid Films 496, 364 (2006).

[7] K. R. Murali, Thin Solid Films 167, L19 (1988).

[8] B. Schumann, H. Neumann, E. Nowak and G. Kuhn, Cryst. Res. Technol 16, 675 (1981).

[9] B. Pamplin and R. S. Feigelson, Thin Solid Films 60, 141 (1979).

[10] K. L. Chopra and S. R. Das, Thin film solar cells (Plenum, New York, 1983), pp. 275-348.

[11] H. Neumann and R. D. Tomlinson, Sol. Cells 28, 301 (1990).

[12] J. A. Groenink, and P. H. Janse, Z. Phys. Chem 110, 17 (1978).

[13] V. D. Das, J. Appl. Phys 55, 1023 (1984).

[14] K. G. Gunther, The use of thin films in physical investigations, ed. by J. C. Anderson (Academic, London, 1966), pp. 213-232.

[15] B. D. Cullity, Elements of X-ray diffraction, ed. by M. Cohen (Addison Wesley, Philippines, 1978), pp. 81-106.

[16] C. D. Wagner, Handbook of X-ray photoelectron spectroscopy: a reference book of standard data for use in X-ray photoelectron

spectroscopy, ed. by G. E. Muilenberg (Perkin Elmer, USA, 1979), pp. 1-190.

[17] J. E. Jaffe and A. Zunger, Phys. Rev. B 28, 5822 (1983).

[18] J. E. Jaffe and A. Zunger, Phys. Rev. B 29, 1882 (1984).

[19] R. Swanepoel, J. Phys. E. Sci. Instrum 16, 1214 (1983).

[20] J. Tauc, Amorphous and liquid semiconductors (Plenum, New York, 1974), pp. 159-220.

[21] K. C. Hsu, Y. S. Fu, P. Y. Lin, I. T. Tang and J. D. Liao, Int. J. Photoenergy 156964, 1 (2013).

[22] S. H. Wemple and M. DiDomenico, Phys. Rev. B 3, 1338 (1971).

[23] A. M. Salem and M. E. E. Ghazzawi, Semicond. Sci. Technol 19, 236 (2004).

[24] F. I. Ezema and M. N. Nnabuchi, J. Res. 17, 115 (2006).

[25] K. R. Murali and P. Thirumoorthy, Elec. Chem. Soc. Trans 28, 67 (2010).

[26] R. A. Smith, Semiconductors (Academic, Calcutta, 1978), pp. 342-350.

[27] W. Fuhs and J. Stuke, Phys. Status. Solidi B 27, 171 (1968).

[28] A. Polity, R. K. Rehberg, T. E. M. Staab, M. J. Puska, J. Klais, H. J. Moller and B. K. Meyer, J. Appl. Phys 83, 71 (1998).

[29] E. S. M. Farag and M. M. Sallam, Egypt. J. Solids 30, 1 (2007).

[30] U. Rau and H. W. Schock, Practical handbook of photovoltaics: Fundamentals and applications, ed. by A. M. Evoy, T. Markvart, and L. Castaner (Elsevier,USA 2012), pp. 323-372.

[31] S. B. Zhang, S. H. Wei, A. Zunger and H. K. Yoshida, Phys. Rev. B 57, 9642 (1998).

[32] T. M. Tritt and M. A. Subramanian, Mater. Res. Soc. Bulletin 31, 188 (2006).

[33] C. Herring, Phys. Rev 96, 1163 (1954).

[34] O. Madelung, Semiconductors data handbook (Springer, Berlin, 2004), pp. 309-311.

[35] M. Yasukawa, Y. Hamada, T. Kono, K. Ueda, H. Yanagi, S. W. Kim and H. Hosono, J. Jpn. Soc. Powder. Metallurgy 58, 149 (2010).

[36] L. M. Goncalves, C. Couto, P. Alpuim, A. G. Rolo, F. Volklein and J. H. Correia, Thin Solid Films 518, 2816 (2010).

[37] K. Kadel, L. Kumari, W. Z. Li, J. Y. Huang and P. P. Provencio, Nanoscale. Res. Lett 6, 57 (2011).

[38] K. Koumoto, H. Koduka and W. S. Seo, J. Mater. Chem 11, 251 (2001).

[39] M. Yasukawa and N. Murayama, J. Mater. Sci 32, 6489 (1997).

[40] M. Fardy, A. I. Hochbaum, J. Goldberger, M. M. Zhang and P. Yang, Adv. Mater 19, 3047 (2007).

[41] J. Q. Li, L. F. Li, S. H. Song, F. S. Liu and W. Q. Ao, J. Alloys. Compd. 565, 144 (2013).

[42] F. Wu, H. Song, F. Gao, W. Shi, J. Jia and X. Hu, J. Elec. Mater 42, 1140 (2013).

[43] M. Ibanez, R. Zamani, S. Gorsse, J. Fan, S. Ortega, D. Cadavid, J. R. Morante, J. Arbiol and A. Cabot, American. Chem. Soc. Nano 7, 2573 (2013).

[44] H. B. Kwok, R. H. Bube, J. Appl. Phys 44, 138 (1973).

[45] H. J. Goldsmid, Introduction to thermoelectricity, ed. by R. Hull, J. Parisi, R. M. Osgood and H. Warlimont (Springer, Berlin, 2010), pp. 45-66.

[46] N. D. Gupta and A. D. Gupta, Semiconductor devices modelling and

technology, ed. by A. K. Ghosh (Prentice Hall of India, New Delhi, 2004), pp. 1-44.

[47] R. T Shuey, Semiconducting ore minerals (Elsevier, USA, 1975), pp. 41-77.

[48] M. A. Omar, Elementary solid state physics: Principles and applications (Addison Wesley, New Delhi, 2001), pp. 253-318.

…….ൠൠൠ…….

Chapter 6

Preparation and Characterization of Polycrystalline InSe Thin Films

6.1 Introduction

Indium monoselenide (InSe) is an important III-VI layered semiconductor with hexagonal structure [1] as shown in Fig 6.1.

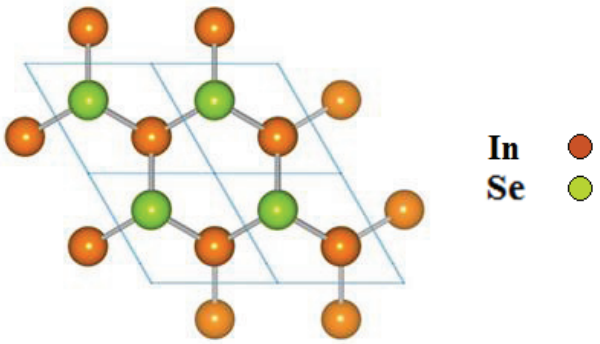

Fig 6.1 Crystal structure of InSe

Indium selenide is extensively studied in recent years due to its promising optical and electrical properties that are suitable for the fabrication of thin film solar cells [2], switching devices [3], radiation detectors [4], schottky diodes [5] and Li solid state batteries [6]. The layered structure of InSe allows the tuning of its electrical properties by means of intercalation so as to suit the processing of various semiconductor devices [7]. Moreover, the absence of dangling bonds on the surface layer makes InSe a promising candidate for application in heterojunction devices [8]. Researchers have successfully demonstrated the growth of InSe heterostructures such as ZnSe/InSe/Si [9] γ-In_2Se_3/TCO (SnO_2 or ZnO) [10] and InSe homojunction p-n photodiodes [11]. The conduction type and optoelectronic properties of InSe thin films are very sensitive to the growth parameters such as rate of evaporation and substrate temperature. Variations in the growth parameters yield different stoichiometric compositions of indium selenide such as InSe, In_2Se_3, In_4Se_3, In_6Se_7 and In_9Se_{11} [12]. InSe thin films can be prepared by several methods including chemical bath deposition [13], flash evaporation [14], metal organic chemical vapour deposition [15], spray pyrolysis [16] and pulsed laser deposition [17].

Recently, Kavitha et al. [13] reported that the mechanical weakness arising from the weak Van der Waals force between the layers of InSe hinders the use of InSe crystals in photovoltaic and optoelectronic devices. To overcome this difficulty, the preparation of InSe crystal in the form of thin film has emerged into a subject of active research. But one of the difficulties encountered in the preparation of InSe thin films is the existence of multi-phases in a single film due to the constriction in the formation energy range of

InSe in the phase diagram of In-Se system [12]. Due to the coexistence of different phases, there is inconsistency in literature on the properties of InSe thin films even of the same composition. Hence it is of great significance to study the properties of single phase or phase pure InSe thin film in view of its use in solar cells.

Hence, in the present work, an attempt is made to prepare phase pure p-type InSe thin films by reactive evaporation, about which research reports are comparatively less. The as-prepared InSe thin films are characterized for their structural, compositional, morphological, optical, electrical and thermoelectric power properties. To the best of our knowledge, this is the first report on the determination of thermoelectric power factor and figure of merit in the temperature range from 4 K to 425 K of phase pure InSe thin films. Moreover, the photosensitivity, optical constants and dispersion parameters of the films are calculated and the results are discussed in the following sections.

6.2 Experimental technique

In the present study, reactive evaporation - a variant of Gunther's three temperature method [18], described in section 3.3, is used to prepare InSe thin films. The experimental setup and the detailed process of thin film deposition have already been discussed in section 3.4. Briefly, high purity In (99.999%) and Se (99.999%) are evaporated simultaneously at suitable rates from independently heated sources. In is evaporated from a molybdenum boat whereas Se is evaporated from a glass crucible kept in a molybdenum basket. The vapours are allowed to deposit on glass substrates kept at an elevated

temperature of 473±5 K after attaining a pressure of the order of 10^{-5} mbar in the coating unit. The optimized conditions used to deposit InSe thin films are:

Impingement rate of In : 3.6×10^{15} atoms $cm^{-2}s^{-1}$

Impingement rate of Se : 3.8×10^{15} atoms $cm^{-2}s^{-1}$

Substrate temperature : 473±5 K

The as-prepared InSe thin films are characterized for their structural properties using Rigaku D MaxC X-ray diffractometer (XRD) for 2θ varying from 5° to 70° with CuK_{α} (1.5404 Å) as the radiation source. The elemental composition is verified from energy dispersive analysis of X-rays (EDAX) and X-ray photoelectron spectroscopy (XPS). The surface morphology is studied using scanning electron microscopy (SEM) and atomic force microscopy (AFM). The optical properties are analyzed using UV-Vis-NIR spectrophotometer in the wavelength range from 2500 nm to cut-off. The thickness of the film is measured using Veeco Dektak 6M stylus profiler and is found to be ≈ 170 nm. The Hall and photoconductivity measurements are performed at room temperature. The Seebeck coefficient, electrical conductivity and thermal conductivity of the as-prepared thin films are measured in the temperature range from 4 K to 425 K to evaluate the thermoelectric figure of merit. The details of the aforementioned characterization tools have already been described in section 3.5 and the results obtained are presented in the following sections.

6.3 Results and Discussions

6.3.1 Structural analysis

The XRD pattern of the as-prepared phase pure InSe thin film is shown in Fig 6.2. The observed interplanar spacings and (hkl) planes of the prepared thin film matches well with that of hexagonal InSe (JCPDS Card. 34-1431).

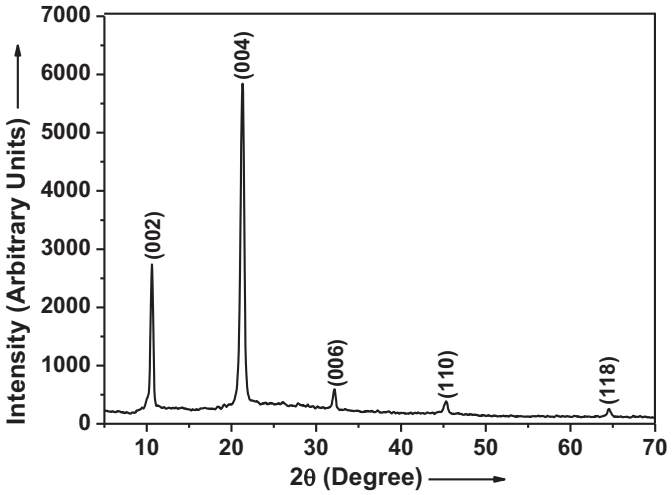

Fig 6.2 XRD pattern of the as-prepared phase pure InSe thin film

The prepared films are polycrystalline in nature and exhibits a well defined peak at $2\theta = 21.30^{\circ}$ corresponding to the (004) plane of InSe with hexagonal structure (JCPDS Card no. 34-1431). The lattice parameters of the InSe are calculated as a = 4.00 Å and c = 16.68 Å. These calculated values of lattice parameters agree with those listed in the (JCPDS Card. 34-1431). The average crystallite size of the prepared InSe thin film is calculated using

Scherrer formula [19] and is obtained as 48 nm. The structural parameters such as dislocation density, number of crystallites per unit area and lattice strain in the film are estimated as 4.34×10^{10} lines cm^{-2}, 15.37×10^{10} cm^{-2} and 1.8×10^{-3} respectively using the equations described in section 3.5.1.

6.3.2 Compositional analysis

The EDAX spectrum of the as-prepared InSe thin film is shown in Fig 6.3. The average atomic percentage of the elements is determined as In = 49.45% and Se = 50.55% respectively, indicating the near stoichiometric composition of the as-prepared phase pure InSe thin film.

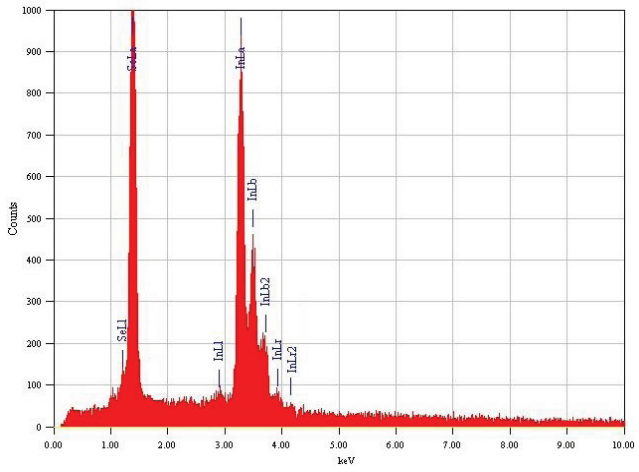

Fig 6.3 EDAX spectrum of InSe thin film

Fig 6.4 depicts the binding energy (B.E) versus counts per second (CPS) of In3d peaks and Se3d peak obtained from the XPS spectrum of the prepared InSe thin film. The composition of the prepared film determined from the XPS spectrum is found to be near stoichiometric with an average atomic

percentage of In and Se as 49.52% and 50.48% respectively. These results are in accordance with the observation from EDAX analysis.

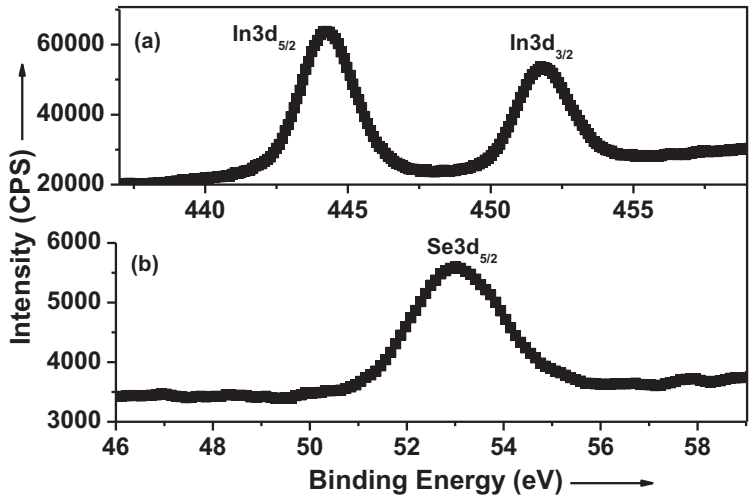

Fig 6.4 XPS spectrum of InSe thin film

The observed shift in the B.E of In and Se from their elemental peak position, shown in Table 6.1, is a clear evidence of the formation of InSe compound where the elements In and Se exist in a chemically bonded state.

Table 6.1 Comparison of the observed peak positions of In and Se from the XPS spectrum with their standard elemental peak positions

Peak position (eV)	$In3d_{5/2}$	$In3d_{3/2}$	$Se3d_{5/2}$
Observed peak position	444.3	451.8	53.1
Elemental peak position [20]	443.8	451.4	54.9

6.3.3 Morphological analysis

The SEM image of the InSe thin film shown in Fig 6.5 indicates that the surface of the film is densely packed with crystallites with average grain size in the range from 230 nm to 260 nm.

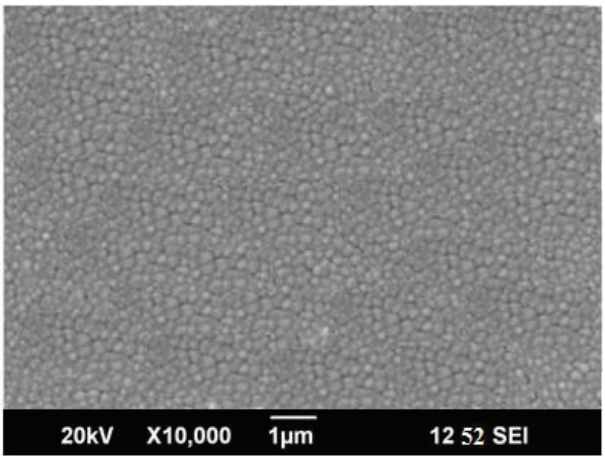

Fig 6.5 SEM image of InSe thin film

The 2D AFM and 3D AFM is shown in Fig 6.6 (a) and (b) respectively. The scan area is 2 µm x 2 µm and scan rate is 10.172 Hz.

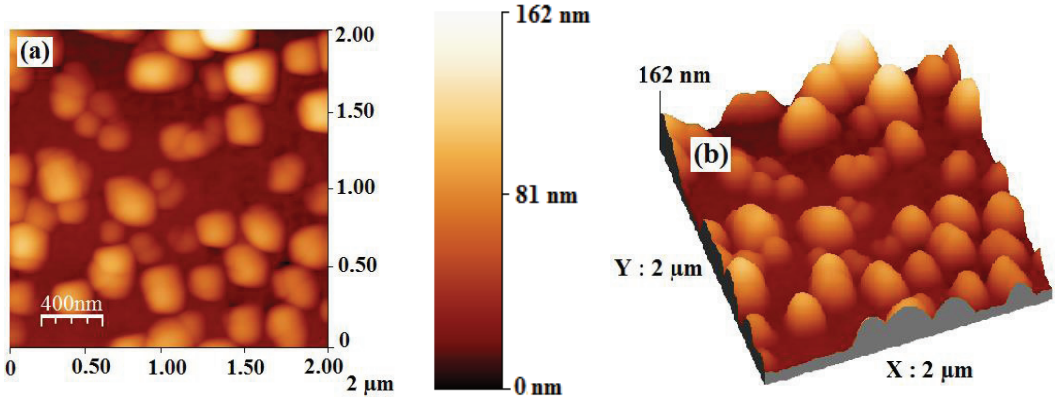

Fig 6.6 (a) 2D AFM (b) 3D AFM of InSe thin film

It can be seen from Fig 6.6 (a) that the film exhibits clusters of sizes in the range from 270 nm to 300 nm in diameter, indicating the agglomeration of particles. The root mean square (RMS) value of surface roughness of the film determined from Fig 6.6 (b) is 20 nm, suggesting a significantly smooth surface.

6.3.4 Optical analysis

Determination of optical band gap

The optical band gap, absorption coefficient and optical constants of the as-prepared film are evaluated from the transmission spectrum depicted in Fig 6.7 using Swanepoel's method [21].

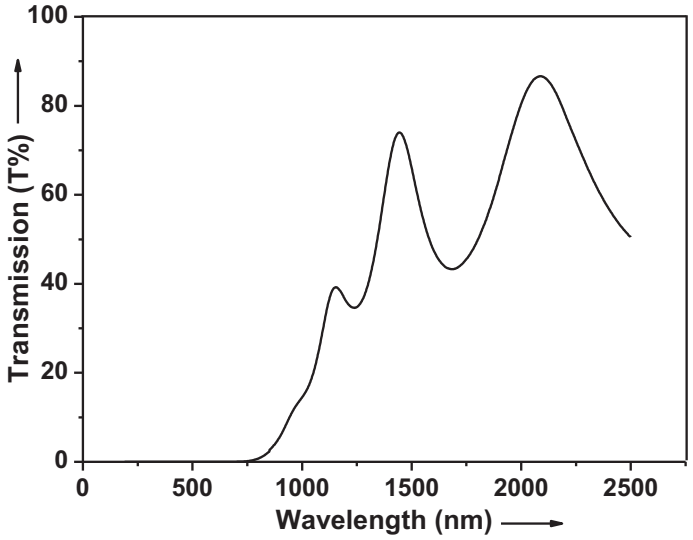

Fig 6.7 Transmission spectrum of InSe thin film

The optical band gap of the film is determined using the well known Tauc relation [22] described in section 3.5.7. Fig 6.8 illustrates the $(\alpha h\nu)^2$ versus hν plot of the as-prepared phase pure InSe thin film.

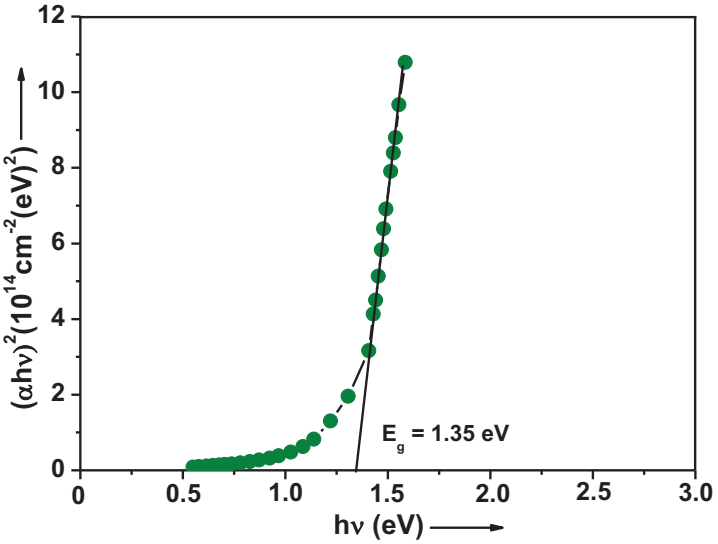

Fig 6.8 Plot of $(\alpha h\nu)^2$ versus hν of InSe thin film

The high absorption coefficient (α) of about 10^5 cm^{-1}, suggests the possible use of the film as an absorber layer material in solar cells. As seen from Fig 6.8, the film shows a direct allowed transition with an optical band gap (E_g) of 1.35 eV. The band gap thus obtained is in good agreement with 1.3 eV reported for single crystal InSe [23] and is also well within the optimum range for harvesting solar energy.

Determination of optical constants

The refractive index (n) and extinction coefficient (r) of the prepared film are calculated using Swanepoel's method [21]. The real part (ε_1) and imaginary part (ε_2) of the dielectric constant of the film are calculated using the equations described in section 3.5.7. The dependence of n, r, ε_1 and ε_2 on photon energy (hν) is presented in Fig 6.9.

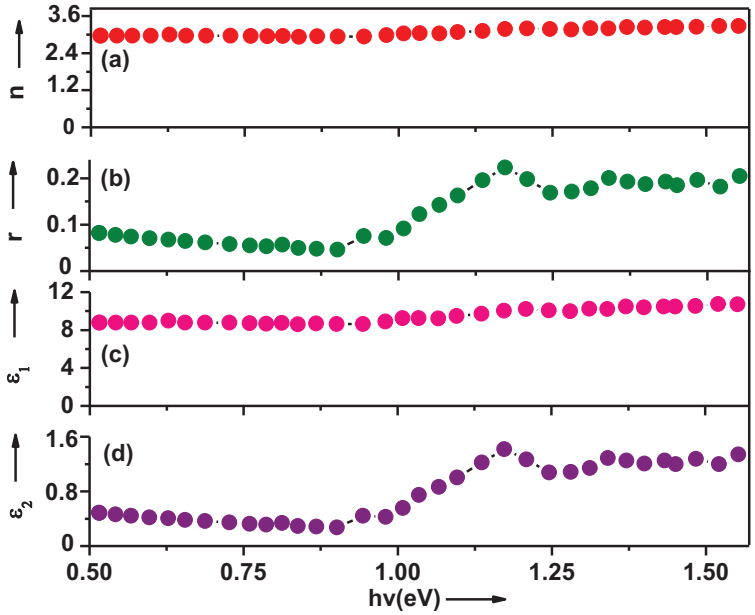

Fig 6.9 Variations of (a) n (b) r (c) ε_1 and (d) ε_2 with hν

The high refractive index and low extinction coefficient of the prepared film can be attributed to its better crystalline nature. This assumption is in accordance with the results reported by Senthil et al [24] for vacuum evaporated CdS thin films of grain size 24 nm. Furthermore, it is clear from Fig. 6.9 that, ε_1 varied with photon energy in a similar manner as that of n

whereas ε_2 varied with photon energy in a similar manner as that of r. Hence ε_1 can be related to dispersion and ε_2 can be related to the extinction coefficient r. The ratio of $\varepsilon_2/\varepsilon_1$ gives information on the loss factor of the material. In the present study, ε_2 is less than ε_1 and hence the loss factor is very small and is discussed in the later section.

Determination of dispersion parameters

The spectral dependence of the refractive index of the film is further analyzed using Wemple and DiDomenico (WD) model [25] which is described in detail in section 5.3.4. The single oscillator energy E_o and the dispersion energy E_d are calculated as 2.57 eV and 17.84 eV respectively from the plot of $(n^2 - 1)^{-1}$ versus $(h\nu)^2$ shown in Fig 6.10.

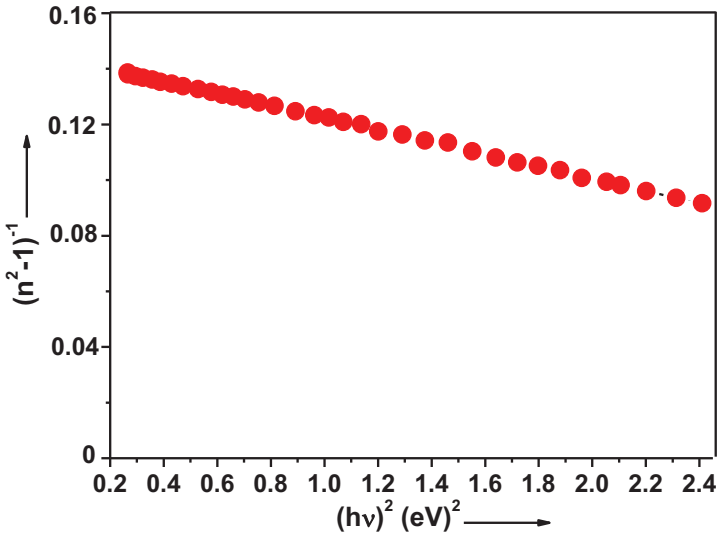

Fig 6.10 Plot of $(n^2 - 1)^{-1}$ versus $(h\nu)^2$

The optical band gap is also calculated from the WD dispersion parameter E_0 using $E_g \approx E_0/2$ relation. It is found that the value of E_g deduced from WD model is in good agreement with that determined from Tauc model and similar to that observed in thermal evaporated Sb_2S_3 thin films [26]. Moreover, the moments of optical spectra (M_{-1} and M_{-3}), oscillator strength (f) and refractive index at infinite wavelength (n_∞) [25] of the as-prepared thin film are calculated as 6.94, 1.05 $(eV)^{-2}$, 45.85 $(eV)^2$ and 2.82 respectively, using the equations described in section 5.3.4. The values of moments calculated for the as-prepared polycrystalline InSe thin film are found to be higher than that calculated for pulsed laser deposited amorphous InSe and InSeTe thin films [17]. As there are no reports on the calculation of single oscillator parameters of phase pure polycrystalline InSe thin films, a comparison of our results with literature is not possible.

Determination of loss factor, quality factor and optical conductivity

The loss factor or tan δ, quality factor or Q factor and optical conductivity or $\sigma_{Optical}$ of the as-prepared thin film are calculated using the equations described in section 3.5.7. The dependence of tan δ, Q factor and $\sigma_{Optical}$ on photon energy (hν) is presented in Fig 6.11.

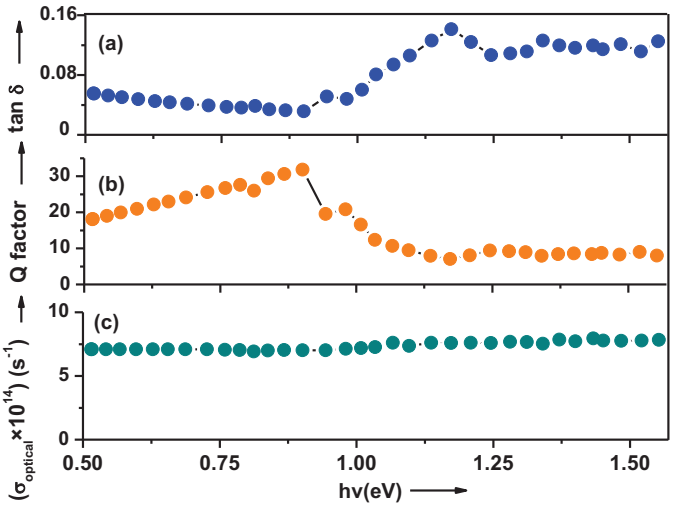

Fig 6.11 Variations of (a) tanδ (b) Q factor and (c) $\sigma_{Optical}$ with hν

It is clear from Fig 6.11 that the loss factor of the film is too small in the measured photon energy range, suggestive of less dielectric loss. The Q factor of the film reaches a maximum value of 31 at 0.9 eV. The $\sigma_{Optical}$ of the film is found to increase with increase in photon energies and attains a maximum of 7.8 $\times 10^{14}$ s^{-1} at 1.55 eV, a considerably high value suitable for optoelectronic applications and much higher than that reported for chemical bath deposited Ba_2S_3 thin films [27].

6.3.5 Electrical analysis

Hall measurement

The positive value of Hall coefficient reveals the p-type conductivity of the film. The sample exhibits a hole concentration p ≈ 9.8×10^{16} cm^{-3}, hole

mobility $\mu_p \approx 12.5$ $cm^2V^{-1}s^{-1}$ and electrical conductivity $\sigma \approx 0.2$ Scm^{-1} at room temperature.

Photoconductivity measurement

Fig 6.12 illustrates the photoresponse curve of InSe thin film. The measurement is performed at room temperature, first in the dark followed by illumination of the film and then after cutting-off illumination. The photosensitivity [28] of the as-prepared phase pure InSe thin film is calculated as 0.4 using the equation described in section 3.5.8.

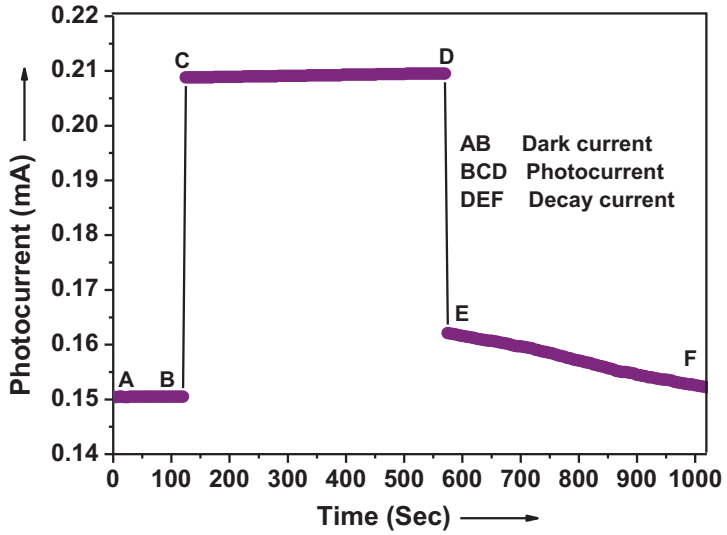

Fig 6.12 Photoresponse curve of InSe thin film

The increase in photocurrent on illumination is due to generation of electron-hole pairs in the film and it indicates the photoconducting nature of the prepared film.

Determination of activation energy

Fig 6.13 shows the variation of ln(I) with inverse of temperature of the as-prepared InSe thin film for three continuous heating-cooling cycles.

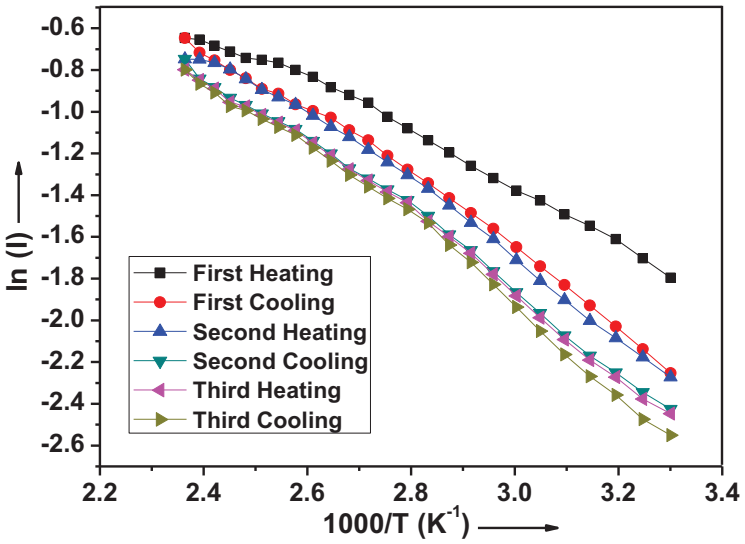

Fig 6.13 Variation of ln(I) with inverse of temperature of InSe thin film

The increase in current with increase in temperature shown in Fig 6.13 reveals the non degenerate semiconducting behaviour of the prepared film. The activation energy [29] is calculated from the slope of ln(I) versus 1000/T plot and is obtained as 0.11 eV.

Determination of thermoelectric power factor and figure of merit in the temperature range from 4 K to 425 K

Fig 6.14 shows the variation of thermoelectric power (TEP) or Seebeck coefficient (S) in the temperature range from 4 K to 425 K of the as-prepared InSe thin film. The positive value of S observed from Fig 6.14 confirms that the as-prepared InSe thin films are of p-type. The hot probe and Hall measurements on the film corroborate this observation.

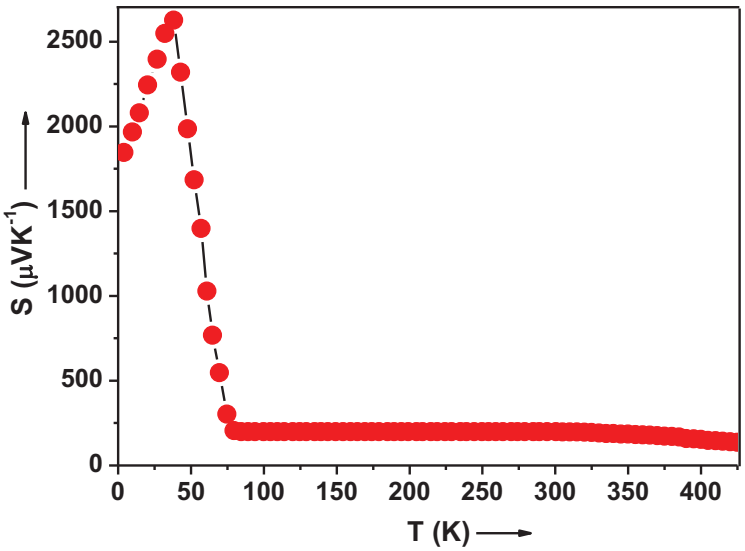

Fig 6.14 Variation of S with temperature of InSe thin film

Fig 6.14 shows an increase in S from 135 μVK^{-1} to 197 μVK^{-1} with decrease in temperature from 425 K to 305 K, suggestive of the non degenerate semiconducting nature of the film. The observed value of S is well within the optimum range for thermoelectric applications [30]. Below 305 K, the value of S is constant ≈ 198 μVK^{-1} up to 84 K. But as the temperature is lowered from

84 K, there is a sudden and sharp increase in S whose onset is at around 80 K and a peak is observed at 38 K. The prepared InSe thin film exhibits a reasonably high S ≈ 2626 μVK^{-1} at 38 K. In the present study, the rapid increase in S observed at low temperatures (80 K to 38 K) has been attributed to the effect of phonon drag on charge carriers resulting from the interaction of phonons with mobile charge carriers [31], which has already been discussed in detail in section 5.3.5.

It can also be seen from Fig 6.14 that, as the temperature is lowered from 38 K, S shows a decrease and attains a value of 1846 μVK^{-1} at 4 K. This decrease in S below 38 K is due to the fact that 38 K is about one fifth of Debye temperature (θ_D) of InSe. The θ_D for InSe is 190 K [32] below which phonons available for drag is less and consequently resulting in a decrease in S. To the best of our knowledge, this is the first report to investigate the thermoelectric properties of phase pure InSe thin films and hence it is not possible to present a comparative study of our results with literature. The InSe film demonstrates a considerably high S ≈ 2626 μVK^{-1} at 38 K, which on further work can possibly open up new advances in the field of cryogenic thermoelectric materials.

Fig 6.15 and Fig 6.16 shows the variation of electrical conductivity (σ) and thermal conductivity (k) in the temperature range from 4 K to 425 K of the as-prepared InSe thin film respectively. The value of σ of the film varies from 0.16 Scm^{-1} to 0.26 Scm^{-1} and the k value of the film varies from 0.004 $Wm^{-1}K^{-1}$ to 0.008 $Wm^{-1}K^{-1}$.

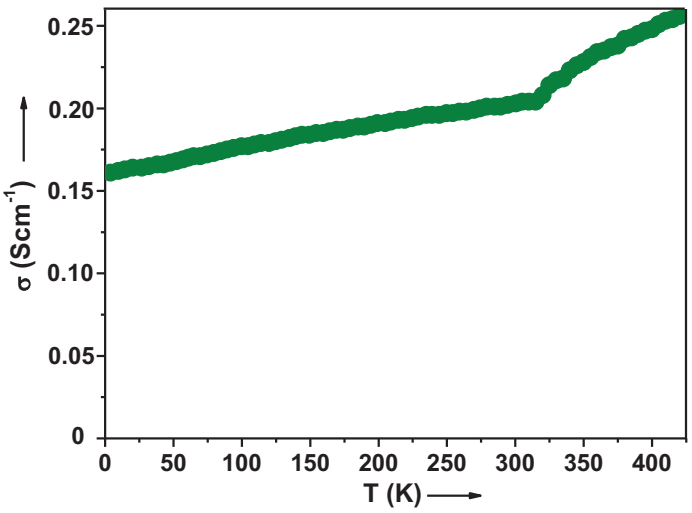

Fig 6.15 Variation of σ with temperature of InSe thin film

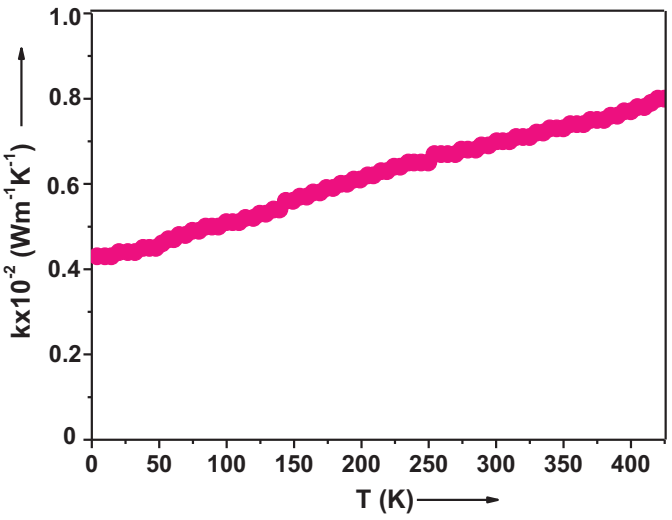

Fig 6.16 Variation of k with temperature of InSe thin film

Using the values of S and σ, the thermoelectric power factor ($S^2\sigma$) of the film is calculated and its variation in the temperature range from 4 K to 425 K is shown in Fig 6.17.

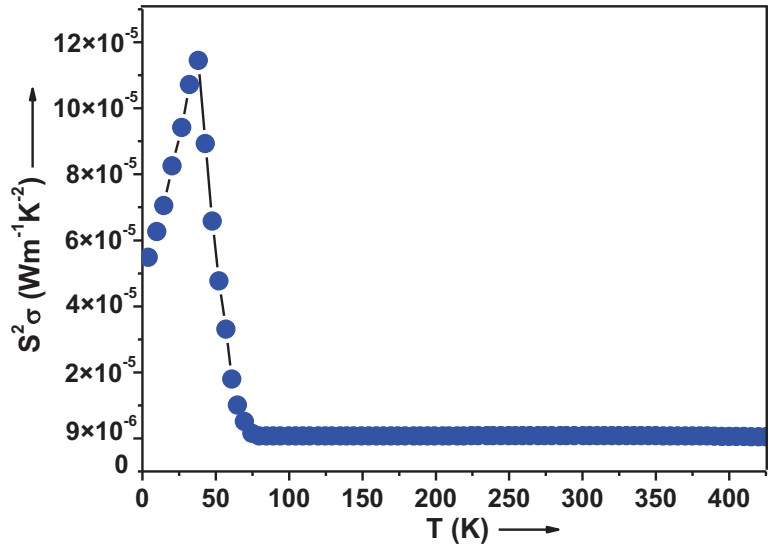

Fig 6.17 Variation of $S^2\sigma$ with temperature of InSe thin film

As seen from Fig 6.17, the power factor of the film varies from 10^{-4} $Wm^{-1}K^{-2}$ to 10^{-7} $Wm^{-1}K^{-2}$ with a room temperature value ≈ 8 x 10^{-7} $Wm^{-1}K^{-2}$. These values are rather low compared to good thermoelectric materials (≈ 10^{-3} $Wm^{-1}K^{-2}$ to 10^{-5} $Wm^{-1}K^{-2}$) but comparable to reasonably good thermoelectric materials such as rutile TiO_2 (≈ 3.52×10^{-7} $Wm^{-1}K^{-2}$) [33]. The maximum value of $S^2\sigma$ is about 1.1 x 10^{-4} $Wm^{-1}K^{-2}$ observed at 38 K, which is approaching the useful range for thermoelectric applications (≈ 10^{-3} $Wm^{-1}K^{-2}$) [34]. A similar power factor has been reported for certain potential thermoelectric materials such as $Ni_{0.8}Na_{0.15}Li_{0.05}O$ compacts [35], $Ca_{2.76}Cu_{0.24}Co_4O_9$ nanopowders [36]

and PbTe nanocomposites [37] that are recently being developed. This suggests that, on further optimization of power factor, the as-prepared InSe thin films possess the potential for low temperature thermoelectric applications. Moreover, the thermoelectric efficiency of the as-prepared InSe thin film is evaluated by calculating the thermoelectric figure of merit (ZT) given by [38]

$$ZT = \frac{S^2 \sigma T}{k} \tag{6.1}$$

The variation of ZT in the temperature range from 4 K to 425 K is shown in Fig 6.18.

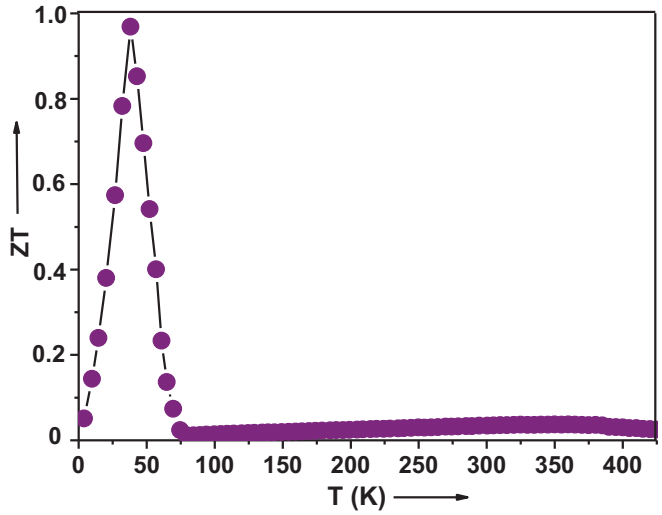

Fig 6.18 Variation of ZT with temperature of InSe thin film

The as-prepared InSe thin film shows a maximum ZT ≈ 0.97 at 38 K, which corresponds to the ZT of modern commercial Peltier devices at room temperature [39]. The ZT values of the as-prepared thin films are comparable

to that obtained for graphene/boron nitride heterostructures [40], Si doped $(In_{0.424}Ga_{0.376}As_{0.8})(In_{0.104}Al_{0.096}As_{0.2})$ III-V semiconductor alloys [41] and also to the state-of-the-art thermoelectric material Bi_2Te_3 [34]. Also, the ZT observed is much higher than those reported for certain emerging potential thermoelectric materials such as Bi_2Se_3 [42]. Hence the as-prepared InSe thin film with ZT ≈ 0.97 at 38 K, on further work, can be regarded as a promising material for cryogenic thermoelectric applications.

Evaluation of material parameters

The data from the analysis of Hall and TEP measurements have been combined to evaluate important material parameters such as Fermi energy (E_F), effective mass (m_p*), density of states (N_V), relaxation time (τ) and mean free path (l) using the equations described in section 5.3.5.

The position of Fermi level is determined as ≈ 0.02 eV above the valence band. The values of N_V and m_p* are obtained as ≈ 5.7×10^{17} cm^{-3} and ≈ $0.08m_0$ respectively, where m_0 is the rest mass of electron. The density of states (N_V) is found to be greater than the charge carrier concentration (p), i.e, $N_V >> p$, indicating the non degenerate semiconducting nature of the film [43]. The relaxation time (τ) and mean free path (l) of charge carriers in the film are evaluated as ≈ 5.7×10^{-16} s and ≈ 1.7 Å respectively.

6.4 Summary and Conclusions

Polycrystalline phase pure p-type InSe thin films are successfully deposited on glass substrates under optimized deposition conditions by reactive evaporation. The near optimum band gap for harvesting solar energy, high

absorption coefficient and reasonably good photosensitivity of the prepared film suggests its possible use as an absorber layer material in solar cells. On further work, the prepared InSe thin films can also be considered for low temperature thermoelectric applications because of its considerably high Seebeck coefficient ≈ 2626 μVK^{-1} and thermoelectric figure of merit ≈ 0.97 observed at 38 K. Table 6.2 summarizes a few notable material parameters of the as-prepared phase pure InSe thin film.

Table 6.2 Material parameters of the as-prepared phase pure InSe thin film

Material Parameters	InSe
Type of conductivity	p-type non degenerate
Optical band gap	1.35 eV
Photosensitivity	0.4
Charge carrier concentration at 300 K	$9.8x10^{16}$ cm^{-3}
Electrical conductivity at 300 K	0.2 Scm^{-1}
Effective mass at 300 K	$0.08m_0$
Mobility at 300 K	12.5 $cm^2V^{-1}s^{-1}$
Maximum Seebeck coefficient	2626 μVK^{-1} at 38 K
Maximum electrical conductivity	0.26 Scm^{-1} at 425 K
Maximum thermal conductivity	0.008 $Wm^{-1}K^{-1}$ at 425 K
Maximum power factor	$1.1x10^{-4}$ $Wm^{-1}K^{-2}$ at 38 K
Maximum figure of merit	0.97 at 38 K

References

[1] B. Gurbulak, M. Sata, S. Dogan, S. Duman, A. Ashkhasi and E. F. Keskenler, Physica E 64, 106 (2014).

[2] G. Gordillo and C. Calderon, Sol. Energy Mater. Sol. Cells 77, 163 (2003).

[3] M. A. Kenawy, A. F. E. Shazly, M. A. Afifi, H. A. Zayed and H. A. E. Zahid, Thin Solid Films 200, 203 (1991).

[4] V. M. Koshkin, L. P. Galchinetskii, V. N. Kulik , B. I. Minkov and U. A. Ulmanis, Solid State Commun 13, 1 (1973).

[5] P. Matheswaran, R. Sathyamoorthy and K. Asokan, Electron. Mater. Lett 8, 621 (2012).

[6] M. Balkanski, P. G. D. Costa and R. F. Wallis, Phys. Status Solidi B 194, 175 (1996).

[7] V. B. Boledzyuk, Z. D. Kovalyuk and M. N. Pyrlya, Inorg. Mater 45, 1222 (2009).

[8] T. Matsushita, T. T. Nang, M. Okuda, A. Suzuki and S. Yokota, Japan. J. Appl. Phys 15, 901 (1976).

[9] B. Ullrich, Mater. Sci. Eng B 56, 69 (1998).

[10] S. Marsillac and J. C. Bernede, Thin Solid Films 315, 5 (1998).

[11] Z. D. Kovalyuk, V. N. Katerynchuk , O. A. Politanska, O. N. Sydor and V. V. Khomyak, Tech. Phys. Lett 31, 359 (2005).

[12] H. Okamoto, J. Phase. Equilib. Diff 25, 201 (2004).

[13] B. Kavitha and M. Dhanam, J. Ovonic. Res 6, 75 (2010).

[14] M. Persin, A. Persin, B. Celustka and B. Etlinger, Thin Solid Films 11, 153 (1972).

[15] S. S. Lee, K. W. Seo and I. W. Shim, Bulletin. Korean. Chem. Soc 27, 147 (2006).

[16] H. Bouzouita, N. Bouguila, S. Duchemin, S. Fiechter and A. Dhouib, Renewable Energy 25, 131 (2002).

[17] M. Hrdlicka, J. Prikryl, M. Pavlista, L. Benes, M. Vlcek and M. Frumar, J. Phys. Chem. Solids 68, 846 (2007).

[18] K. G. Gunther, The use of thin films in physical investigations, ed. by J. C. Anderson (Academic, London, 1966), pp. 213-232.

[19] B. D. Cullity, Elements of X-ray diffraction, ed. by M. Cohen (Addison Wesley, Philippines, 1978), pp. 81-106.

[20] C. D. Wagner, Handbook of X-ray photoelectron spectroscopy: a reference book of standard data for use in X-ray photoelectron spectroscopy, ed. by G. E. Muilenberg (Perkin Elmer, USA, 1979), pp. 1-190.

[21] R. Swanepoel, J. Phys. E. Sci. Instrum 16, 1214 (1983).

[22] J. Tauc, Amorphous and liquid semiconductors (Plenum, New York, 1974), pp. 159-220.

[23] A. Mandelis, Handbook of optical constants of solids, ed. by E. D. Palik (Academic Press, USA, 1998), pp. 59-98.

[24] K. Senthil, D. Mangalaraj, S. K. Narayandass and S. Adachi, Mater. Sci. Eng. B 78, 53 (2000).

[25] S. H. Wemple and M. DiDomenico, Phys. Rev. B 3, 1338 (1971).

[26] N. Tigau, Cryst. Res. Technol 42, 281 (2007).

[27] O. D. Nnanyere, Int. Org. Sci. Res. J. Appl. Phys 7, 10 (2015).

[28] K. R. Murali and P. Thirumoorthy, Elec. Chem. Soc. Trans 28, 67 (2010).

[29] E. S. M. Farag and M. M. Sallam, Egypt. J. Solids 30, 1 (2007).

[30] T. M. Tritt and M. A. Subramanian, Mater. Res. Soc. Bulletin 31, 188 (2006).

[31] C. Herring, Phys. Rev 96, 1163 (1954).

[32] O. Madelung, Semiconductors data handbook (Springer, Berlin, 2004), pp. 530- 533.

[33] Y. C. Lai, H. J. Tsai, C. I. Hung, H. Fujishiro, T. Naito and W. K. Hsu Phys. Chem. Chem. Phys 17, 8120 (2015).

[34] L. M. Goncalves, C. Couto, P. Alpuim, A. G. Rolo, F. Volklein and J. H. Correia, Thin Solid Films 518, 2816 (2010).

[35] Y. Lu, L. Hao, H. Yoshida and M. Hirohashi, J. Mater. Sci. Mater. Electron 23, 315 (2012).

[36] S. W. Nam, Y. S. Lim, S. M. Choi, W. S. Seo and K. Park, J. Nanoscience. Nanotechnol 11, 1734 (2011).

[37] B. Paul and P. Banerji, Nanosci. Nanotechnol. Lett 1, 208 (2009).

[38] M. Fardy, A. I. Hochbaum, J. Goldberger, M. M. Zhang and P. Yang, Adv. Mater 19, 3047 (2007).

[39] J. Androulakis, P. Migiakis and J. Giapintzakis, Appl. Phys. Lett 84, 1099 (2004).

[40] L. A. Algharagholy, Q. A. Galiby, H. A. Marhoon, H. Sadeghi, H. M. Abduljalil and C. J. Lambert, Nanotechnology 26, 4754011 (2015).

[41] J. H. Bahk, Z. Bian, M. Zebarjadi, J. M. O. Zide, H. Lu, D. Xu, J. P. Feser, G. Zeng, A. Majumdar, A. C. Gossard, A. Shakouri and J. E. Bowers, Phys. Rev B 81, 2352091 (2010).

[42] K. Kadel, L. Kumari, W. Z. Li, J. Y. Huang and P. P. Provencio, Nanoscale. Res. Lett 6, 57 (2011).

[43] R. T. Shuey, Semiconducting ore minerals (Elsevier, USA, 1975), pp. 41-77.

Chapter 7

Preparation and Characterization of Polycrystalline $InSbSe_3$ Thin Films

7.1 Introduction

Investigations on the III-VI and V-VI group of semiconductors have recently gained substantial attention due to their remarkable structural and optoelectronic properties suitable for a wide range of energy related applications. Among the III-VI group, the hexagonal structured indium selenide (In_2Se_3) is an interesting layered semiconductor with attractive optical, electrical and photoconducting properties suitable for photovoltaic applications [1] and among the V-VI group, the orthorhombic structured antimony selenide (Sb_2Se_3) is a well known layered semiconductor widely studied for their excellent photovoltaic and thermoelectric properties [2]. Consequently, several researchers have carried out elaborate studies on the synthesis and characterization of In_2Se_3 and Sb_2Se_3 thin films and the results are well

documented. However, studies on the combination of In_2Se_3-Sb_2Se_3 are very few.

Recently, it has been reported that a direct fusion of stoichiometric quantities of In_2Se_3 and Sb_2Se_3 at 1273 K can form indium antimony selenide ($InSbSe_3$) - a rarely studied III-V-VI compound belonging to triclinic crystal system with space group P_1 and lattice parameters a = 6.032 Å, b = 7.040 Å, c = 12.1869 Å, angles α = 95.783 Å, β = 51.808 Å, γ = 95.852 Å and unit cell volume of 402.496 $Å^3$ [3]. The crystal structure of $InSbSe_3$ [3] is shown in Fig 7.1.

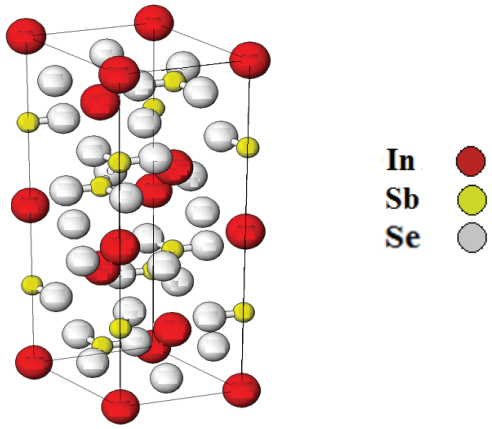

Fig 7.1 Crystal structure of $InSbSe_3$

However, systematic investigations on the properties of $InSbSe_3$ are not sufficient in literature, except for a few dealing with its optical [3] and electrical [4] properties. Therefore, in the application point of view, it is of utmost interest to explore and optimize the properties of $InSbSe_3$ prepared by various experimental techniques. Hence in the present work, a detailed analysis is carried out on the structural, compositional, morphological, optical, electrical

and thermoelectric power properties of reactive evaporated $InSbSe_3$ thin films, with special focus on its high photosensitivity and determination of thermoelectric power factor and figure of merit in the temperature range from 4 K to 425 K about which no reports are available in literature to date, to the best of our knowledge. This is the first report to deduce the material parameters of $InSbSe_3$ thin films by correlating the results of Hall and thermoelectric power measurements. The results of the studies are discussed in the following sections.

7.2 Experimental technique

In the present study, reactive evaporation - a variant of Gunther's three temperature method [5], described in section 3.3, is used to prepare $InSbSe_3$ thin films. The experimental setup and the detailed process of thin film deposition have already been discussed in section 3.4. Briefly, high purity In (99.999%), Sb (99.999%) and Se (99.999%) are evaporated simultaneously at suitable rates from independently heated sources. In is evaporated from a molybdenum boat whereas Sb and Se are evaporated from two separate glass crucibles kept in molybdenum baskets. The vapours are allowed to deposit on glass substrates kept at an elevated temperature of 523±5 K after attaining a pressure of the order of 10^{-5} mbar in the coating unit. The optimized conditions used to deposit $InSbSe_3$ thin films are:

Impingement rate of In : 3.6×10^{15} atoms $cm^{-2}s^{-1}$
Impingement rate of Sb : 3.1×10^{15} atoms $cm^{-2}s^{-1}$
Impingement rate of Se : 3.8×10^{15} atoms $cm^{-2}s^{-1}$
Substrate temperature : 523±5 K

The as-prepared $InSbSe_3$ thin films are characterized for their structural properties using Rigaku D MaxC X-ray diffractometer (XRD) for 2θ varying from 10° to 60° with CuK_{α} (1.5404 Å) as the radiation source. The elemental composition is verified from energy dispersive analysis of X-rays (EDAX) and X-ray photoelectron spectroscopy (XPS). The surface morphology is studied using scanning electron microscopy (SEM) and atomic force microscopy (AFM). The optical properties are analyzed using UV-Vis-NIR spectrophotometer in the wavelength range from 2500 nm to cut-off. The thickness of the film is measured using Veeco Dektak 6M stylus profiler and is found to be ≈ 180 nm. The Hall and photoconductivity measurements are performed at room temperature. The Seebeck coefficient, electrical conductivity and thermal conductivity of the as-prepared thin films are measured in the temperature range from 4 K to 425 K to evaluate the thermoelectric figure of merit. The details of the aforementioned characterization tools have already been described in section 3.5 and the results obtained are presented in the following sections.

7.3 Results and Discussions

7.3.1 Structural analysis

The XRD pattern of the as-prepared $InSbSe_3$ thin film is shown in Fig 7.2. The presence of well defined sharp diffraction peaks in the XRD pattern confirms the polycrystalline nature of the prepared film.

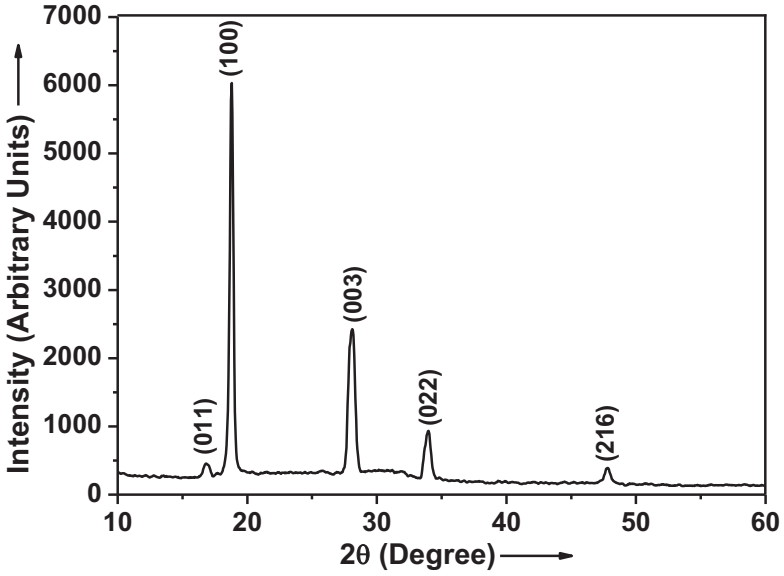

Fig 7.2 XRD pattern of the as-prepared $InSbSe_3$ thin film

The considerably high intensity of the XRD peaks indicates the good crystalline quality of the film. All the XRD peaks observed in the present study are indexed according to the experimentally obtained database for $InSbSe_3$ in powder form suggested by Soliman et al [3]. The calculated values of interplanar spacings and (hkl) planes matches very well with those mentioned in the aforesaid reference, thereby suggesting the formation of $InSbSe_3$. The average crystallite size is calculated using Scherrer formula [6] and is obtained as 75 nm. The structural parameters such as dislocation density, number of crystallites per unit area and lattice strain in the film are evaluated as 1.78×10^{10} lines cm^{-2}, 4.27×10^{10} cm^{-2} and 1.5×10^{-3} respectively using the equations described in section 3.5.1.

7.3.2 Compositional analysis

The EDAX spectrum of the as-prepared $InSbSe_3$ thin film is shown in Fig 7.3. The average atomic percentage of the elements obtained from EDAX is that of near stoichiometric $InSbSe_3$ with In = 20.48%, Sb = 19.21% and Se = 60.31%.

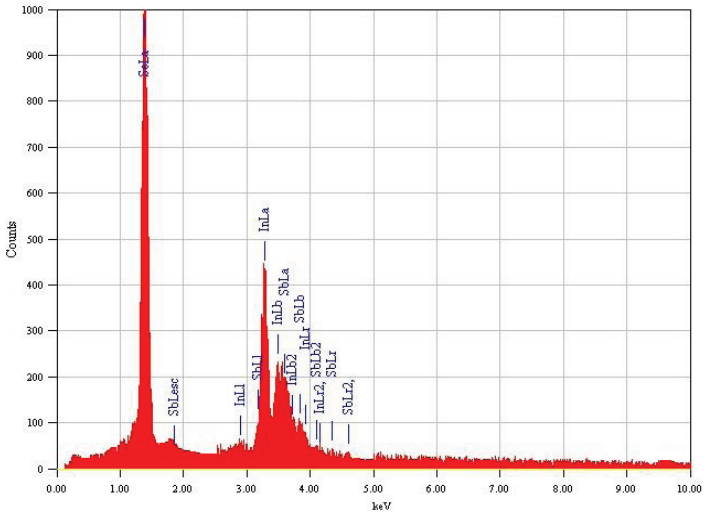

Fig 7.3 EDAX spectrum of $InSbSe_3$ thin film

The elemental composition of the as-prepared $InSbSe_3$ thin film is further verified by XPS. Fig 7.4 depicts the binding energy (B.E) versus counts per second (CPS) of In3d, Sb3d and Se3d peaks obtained from the XPS spectrum of the $InSbSe_3$ thin film. The XPS data ascertains the near stoichiometric composition of the film with In = 20.51%, Sb = 19.26% and Se = 60.23%, consistent with EDAX results.

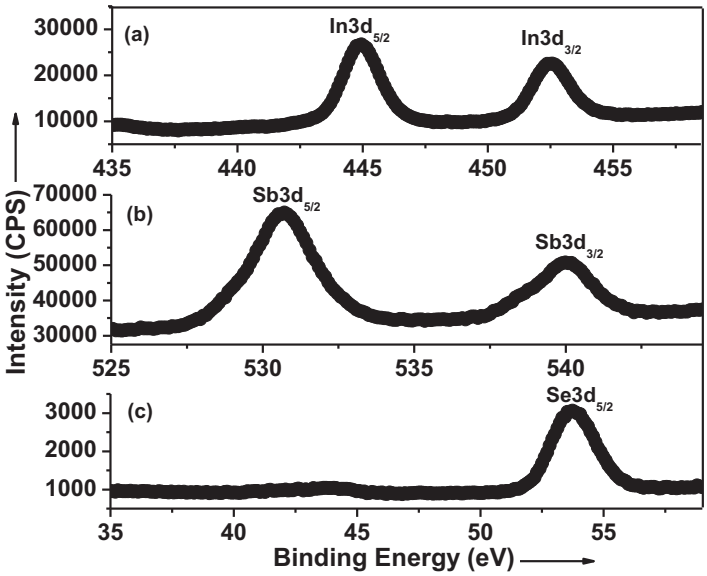

Fig 7.4 XPS spectrum of $InSbSe_3$ thin film

The observed XPS peak positions of the constituent elements in the sample are compared with their standard elemental peak positions and are given in Table 7.1.

Table 7.1 Comparison of the observed peak positions of In, Sb and Se from the XPS spectrum with their standard elemental peak positions

Peak position (eV)	$In3d_{5/2}$	$In3d_{3/2}$	$Sb3d_{5/2}$	$Sb3d_{3/2}$	$Se3d_{5/2}$
Observed peak position	444.8	452.5	530.8	540.1	53.8
Elemental peak position [7]	443.8	451.4	528.2	537.6	54.9

The slight difference between the observed and standard elemental peak position substantiate the formation of $InSbSe_3$ compound where the elements In, Sb and Se exist in a chemically bonded state.

7.3.3 Morphological analysis

The SEM image of the as-prepared $InSbSe_3$ thin film is shown in Fig 7.5. The surface of the film is densely packed with crystallites with an average grain size in the range from 280 nm to 310 nm.

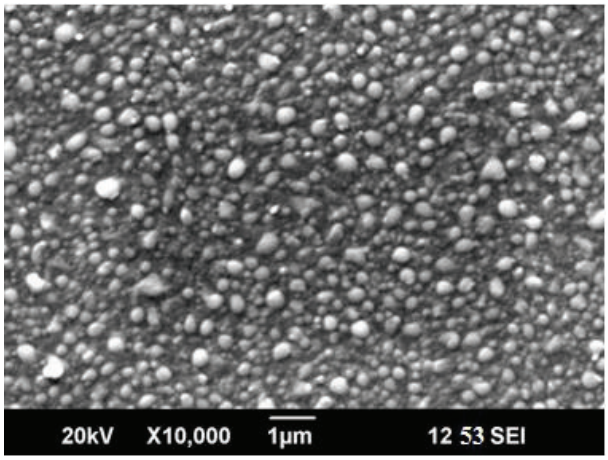

Fig 7.5 SEM image of $InSbSe_3$ thin film

The 2D AFM and 3D AFM is shown in Fig 7.6(a) and (b) respectively. The scan area is 2 μm x 2 μm and scan rate is 10.172 Hz.

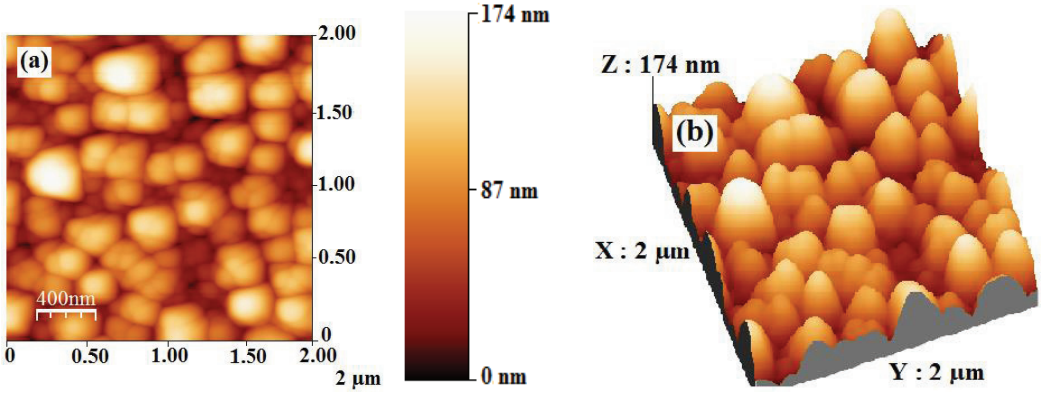

Fig 7.6 (a) 2D AFM (b) 3D AFM of $InSbSe_3$ thin film

It can be seen from Fig 7.6(a) that the film exhibits clusters of sizes in the range from 350 nm to 380 nm in diameter, indicating the agglomeration of particles. The root mean square (RMS) value of surface roughness of the film determined from Fig 7.6(b) is 25 nm, suggesting a significantly smooth surface.

7.3.4 Optical analysis

Determination of optical band gap

The absorption coefficient (α) of the film is evaluated from the transmission spectrum shown in Fig 7.7 using Swanepoel's method [8] and is found to be high of the order of 10^5 cm^{-1}.

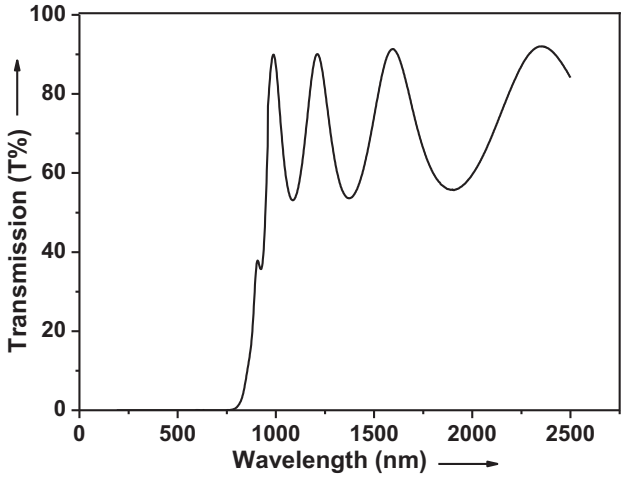

Fig 7.7 Transmission spectrum of $InSbSe_3$ thin film

A detailed analysis of the dependence of α on photon energy (hν) using Tauc relation [9] described in section 3.5.7 shows that the $(\alpha h\nu)^2$ curve of the

prepared film is linear, indicative of direct allowed transition. The optical band gap of the film which is obtained by the subsequent extrapolation of $(\alpha h\nu)^2$ versus hν curve at X-axis depicted in Fig 7.8 is 1.52 eV, a value well within the optimum range for efficient solar energy harvesting structures.

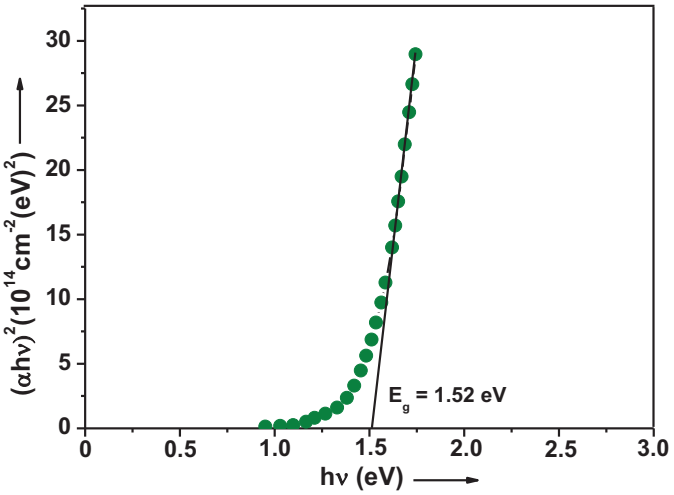

Fig 7.8 Plot of $(\alpha h\nu)^2$ versus hν of $InSbSe_3$ thin film

It is noteworthy that, $InSbSe_3$ thin films with direct optical band gap are not so far been reported. Soliman et al [3] and Atiya [10] have reported an indirect band gap of 1.46 eV and 1.13 eV respectively, for thermally evaporated $InSbSe_3$ thin films. However, it is well known that materials with direct band gap are preferred to those with indirect band gap, because absorption is much stronger in direct band gap materials as it involves only the simple electron-photon interaction thereby leading to high conversion efficiency in photovoltaic devices. Hence on further work, the prepared $InSbSe_3$ thin film that shows a direct allowed transition with an optimum band

gap can be considered for use as an absorber layer material in thin film solar cells.

Determination of optical constants

The refractive index (n) and extinction coefficient (r) of the film are evaluated from the transmission spectrum [8] and their dependence on photon energy (hv) is illustrated in Fig 7.9 (a) and (b). It is observed that n varies from 3.1 to 3.3 and r varies from 0.08 to 0.07 in the photon energy range from 0.52 eV to 1.55 eV. The high value of n thus obtained provides an additional confirmation of the better crystalline nature of the film.

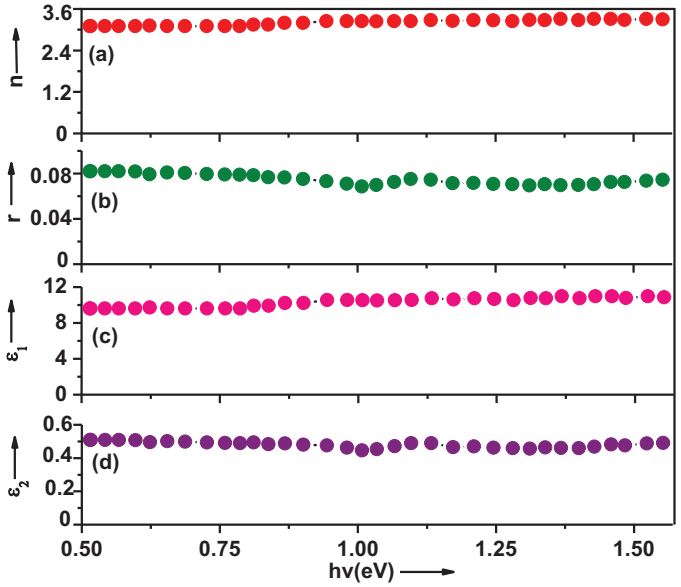

Fig 7.9 Variations of (a) n (b) r (c) ε_1 and (d) ε_2 with hν

The values of n and r is further utilized to evaluate the real part (ε_1) and imaginary part (ε_2) of the complex dielectric constant of the prepared film

using the equations described in section 3.5.7, and their dependence on photon energy are depicted in Fig 7.9 (c) and (d). It is noticed that, the spectral variation of n is similar to ε_1 and that of r is similar to ε_2. Hence, certainly ε_1 can be related to dispersion and ε_2 can be associated with the dissipation of electromagnetic wave.

Determination of dispersion parameters

Optical analysis is further extended to the estimation of dispersion parameters of the film, namely, the oscillator energy E_0 and the dispersion energy E_d using the well known Wemple and DiDomenico single oscillator model [11] which is discussed in detail in section 5.3.4. The plot $(n^2 - 1)^{-1}$ versus $(h\nu)^2$ is shown in Fig 7.10.

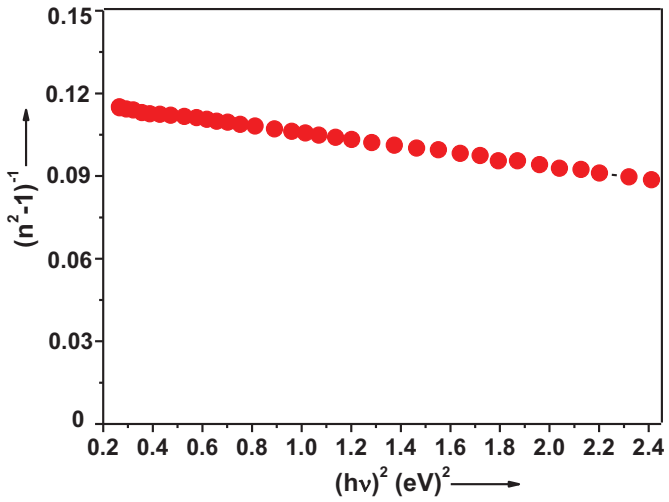

Fig 7.10 Plot of $(n^2 - 1)^{-1}$ versus $(h\nu)^2$

The values of E_0 and E_d calculated from Fig 7.10 are found to be 3.12 eV and 26.48 eV repectively. Thus the oscillator energy of the prepared $InSbSe_3$ thin film is found to be twice its optical band gap ($E_0 \approx 2E_g$) which in good agreement with the relation deduced for polycrystalline thermal evaporated $Zn_{0.9}Cd_{0.1}Te$ thin films [12]. Furthermore, the value of E_g deduced from WD model is in good agreement with that determined from Tauc model. The dispersion energy is considerably high indicating strong optical transitions. The moments of optical spectra (M_{-1} and M_{-3}), oscillator strength (f) and refractive index at infinite wavelength (n_∞) of the film are calculated using the equations described in section 5.3.4 and are obtained as 8.47, 0.87 $(eV)^{-2}$, 82.62 $(eV)^2$ and 3.08 respectively [11]. As there are no reports on the calculation of single oscillator parameters of polycrystalline $InSbSe_3$ thin films, a comparison of our results with literature is not possible.

Determination of loss factor, quality factor and optical conductivity

The loss factor or tan δ, quality factor or Q factor and optical conductivity or $\sigma_{Optical}$ of the as-prepared film are calculated using the equations described in section 3.5.7. The dependence of tan δ, Q factor and $\sigma_{Optical}$ on photon energy (hν) is presented in Fig 7.11.

It is observed from Fig 7.11 that the calculated values of tan δ are small varying from 0.05 to 0.04 in the measured photon energy range, indicative of less dielectric loss in the prepared film. The Q factor is found to increase towards high frequencies, which implies the possible use of the film for high frequency optical applications on further optimization.

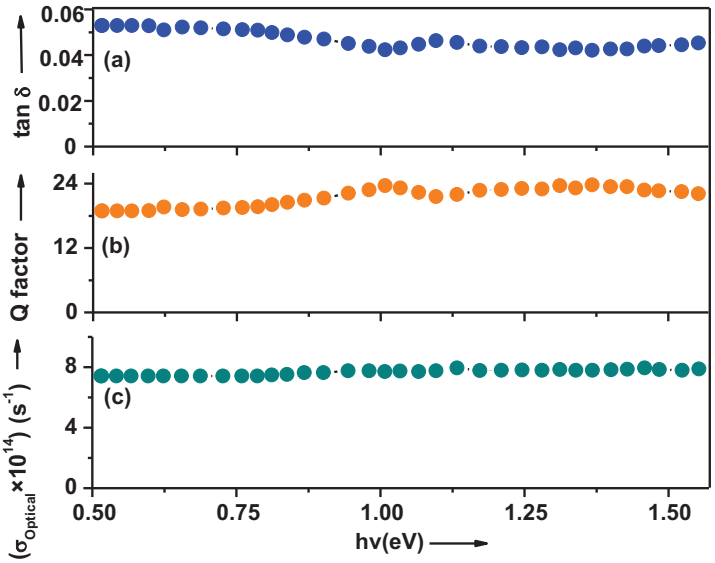

Fig 7.11 Variations of (a) tan δ (b) Q factor and (c) $\sigma_{Optical}$ with hν

The $\sigma_{Optical}$ of the film is fairly constant in the photon energy range from 0.52 eV to 0.78 eV and then increase up to 7.8 $\times 10^{14}$ s^{-1} at 1.55 eV, a significantly high value adequate for optoelectronic applications and comparable to that obtained for chemical bath deposited $AgAlS_2$ thin films [13].

7.3.5 Electrical analysis

Hall measurement

The positive value of Hall coefficient confirms the p-type conductivity of the film. At room temperature, the prepared $InSbSe_3$ thin film shows a hole concentration $p \approx 9.1 \times 10^{16}$ cm^{-3}, hole mobility $\mu_p \approx 21.3$ $cm^2V^{-1}s^{-1}$ and

electrical conductivity $\sigma \approx 0.3$ Scm^{-1}, quite suitable for photovoltaic applications.

Photoconductivity measurement

Moreover, for the categorization of the optoelectronic properties of the film, it becomes necessary to realize the photoconducting properties in addition to the charge carrier transport properties. Hence the photocurrent of the as-prepared $InSbSe_3$ thin film is measured and is shown in Fig 7.12. No such study has been reported so far for $InSbSe_3$ thin film. The photosensitivity [14] of the prepared film is calculated using the equation described in section 3.5.8 and is found to be 4.8, a reasonably high value signifying the good photosensitive nature of the film appropriate for photovoltaic applications.

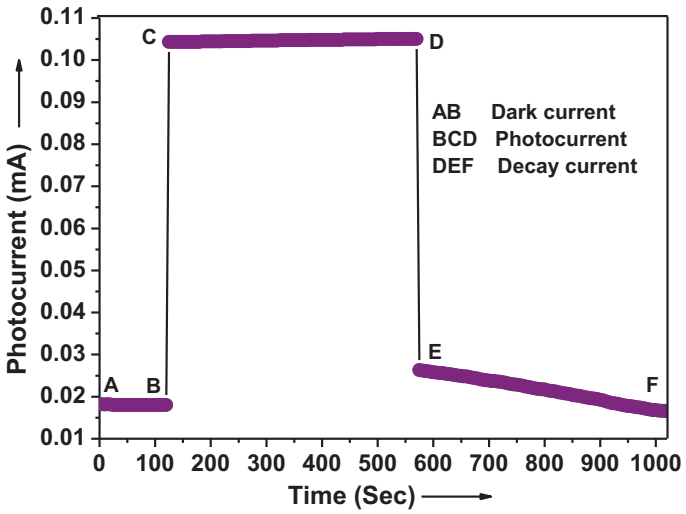

Fig 7.12 Photoresponse curve of $InSbSe_3$ thin film

The increase in photocurrent on illumination is due to generation of electron-hole pairs in the film and it indicates the photoconducting nature of the prepared film.

Determination of activation energy

Fig 7.13 shows the variation of ln(I) with inverse of temperature of the as-prepared $InSbSe_3$ thin film for three continuous heating-cooling cycles.

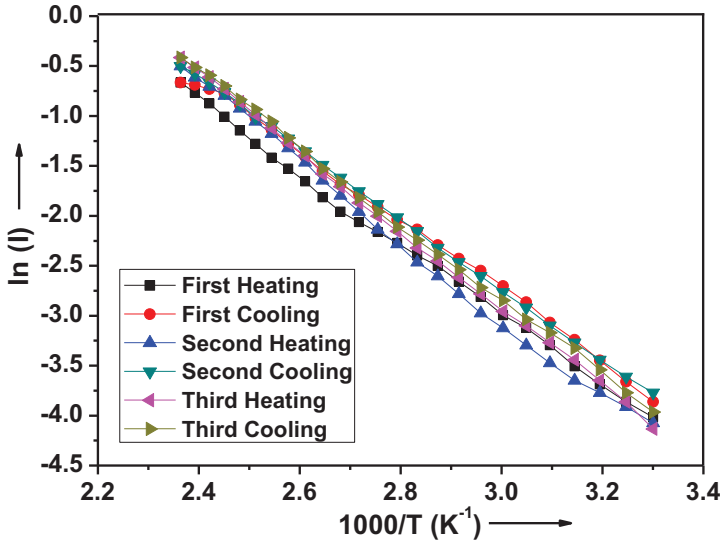

Fig 7.13 Variation of ln(I) with inverse of temperature of $InSbSe_3$ thin film

The observed increase in current with increase in temperature, shown in Fig 7.13, substantiates the non degenerate semiconducting nature of the film. The activation energy is calculated from the slope of ln(I) versus 1000/T plot using the Arrhenius relation [15] and is obtained as 0.3 eV.

Determination of thermoelectric power factor and figure of merit in the temperature range from 4 K to 425 K

The thermoelectric power properties of $InSbSe_3$ thin film is investigated in the temperature range from 4 K to 425 K for the first time in literature in view of their use in thermoelectric devices. Fig 7.14 shows the variation of thermoelectric power (TEP) or Seebeck coefficient (S) in the temperature range from 4 K to 425 K of the as-prepared $InSbSe_3$ thin film. The positive value of S observed from Fig 7.14 confirms that the as-prepared $InSbSe_3$ thin films are of p-type. The hot probe and Hall measurements on the film corroborate this observation.

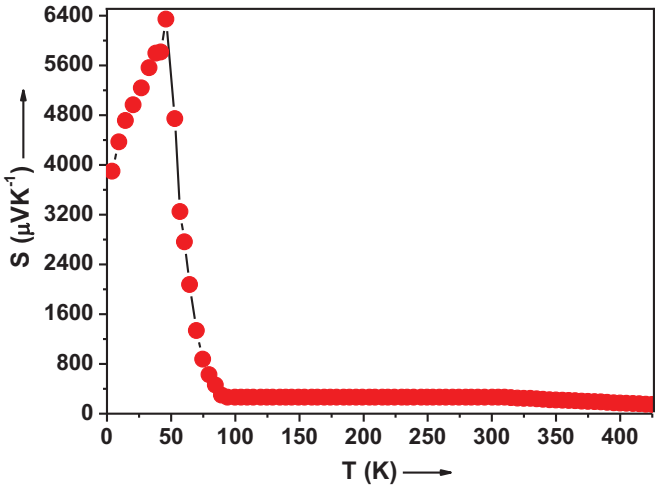

Fig 7.14 Variation of S with temperature of $InSbSe_3$ thin film

It is observed from Fig 7.14 that S of the prepared film shows an increase from 145 μVK^{-1} to 257 μVK^{-1} with decrease in temperature from 425 K to 315 K, suggestive of the non degenerate semiconducting nature of the

film. The value of S is well within the optimum range for thermoelectric applications [16]. Below 315 K, a constant value of S ≈ 262 μVK^{-1} is observed up to 94 K. Later, S shows an unexpected and rapid increase which reaches up to a maximum of ≈ 6342 μVK^{-1} at 46 K. This unusual increase is explained as an outcome of the influence of phonon drag on charge carriers resulting from the interaction of phonons with mobile charge carriers [17], which has already been discussed in detail in section 5.3.5.

However, the amplitude of phonon drag effect depends on the number of phonons available to interact with the charge carriers. Towards very low temperatures (usually below about one-fifth of the Debye temperature θ_D), the relative number of phonons available for drag decreases. As a result the effect of phonon drag on the Seebeck coefficient also decreases. This can be a reason for the decrease in S observed in the film at temperatures below 46 K. Below 46 K, S shows a sudden drop and attains a value ≈ 3896 μVK^{-1} at 4 K. Thus θ_D of the as-prepared $InSbSe_3$ thin film can be estimated as ≈ 230 K. Therefore, thermoelectric power measurement can be considered as a sensitive tool to estimate θ_D. To the best of our knowledge, this is the first report to investigate the thermoelectric properties of $InSbSe_3$ thin films and hence it is not possible to present a comparative study of our results with literature. The high value of S ≈ 6342 μVK^{-1} at 46 K, obtained for the prepared $InSbSe_3$ thin film is suggestive of its potential use as an efficient thermoelectric material at low temperatures.

Fig 7.15 and Fig 7.16 shows the variation of electrical conductivity (σ) and thermal conductivity (k) in the temperature range from 4 K to 425 K of the $InSbSe_3$ thin film respectively. The value of σ of the film varies from 0.26

Scm^{-1} to 0.41 Scm^{-1} and the value of k of the film varies from 0.042 $Wm^{-1}K^{-1}$ to 0.075 $Wm^{-1}K^{-1}$.

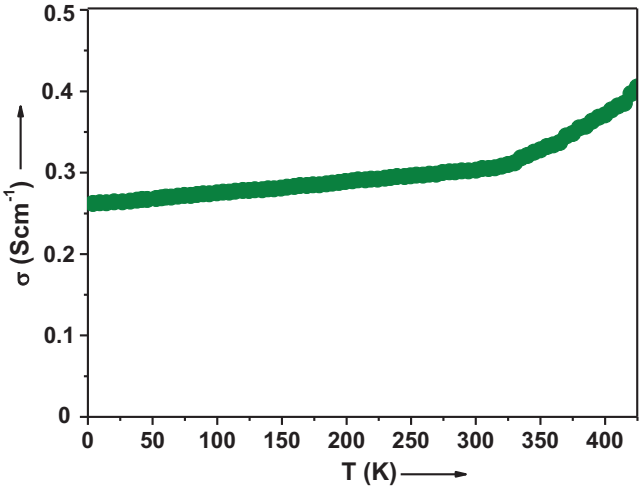

Fig 7.15 Variation of σ with temperature of $InSbSe_3$ thin film

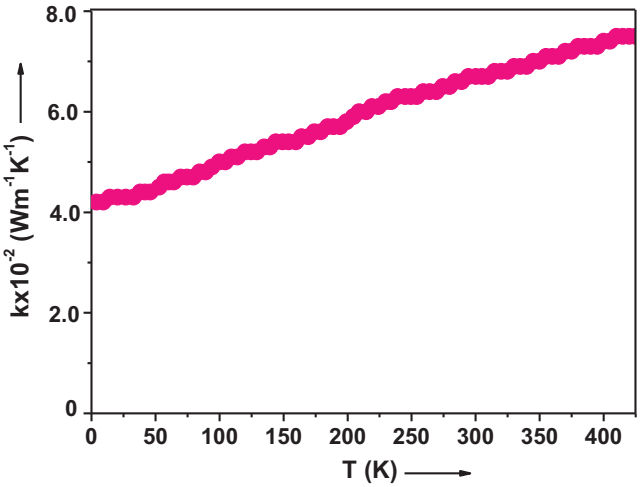

Fig 7.16 Variation of k with temperature of $InSbSe_3$ thin film

Using the values of S and σ, the thermoelectric power factor ($S^2\sigma$) of the film is calculated and its variation in the temperature range from 4 K to 425 K is shown in Fig 7.17.

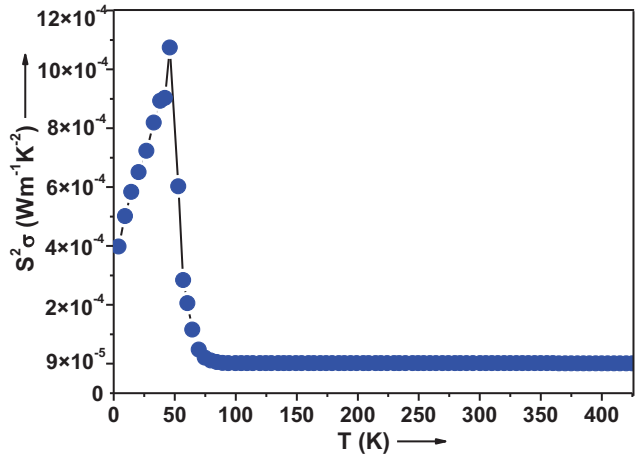

Fig 7.17 Variation of $S^2\sigma$ with temperature of $InSbSe_3$ thin film

The power factor of the film varies from 10^{-3} $Wm^{-1}K^{-2}$ to 10^{-7} $Wm^{-1}K^{-2}$ with a room temperature value ≈ 2.1 x 10^{-6} $Wm^{-1}K^{-2}$. This value is rather low compared to good thermoelectric materials (≈ 10^{-3} $Wm^{-1}K^{-2}$ to 10^{-5} $Wm^{-1}K^{-2}$) but comparable to reasonably good thermoelectric materials such as TiO_2 ceramics (≈ 3.3 x 10^{-6} $Wm^{-1}K^{-2}$) [18]. The maximum value of $S^2\sigma$ is about 1.1 x 10^{-3} $Wm^{-1}K^{-2}$ observed at 46 K, which is in good agreement with that reported for today's state-of-the-art thermoelectric materials such as Sb_2Te_3 [19], $AgSbTe_2$ [20] and Bi_2Te_3 [21]. This suggests that, on further optimization of power factor, the as-prepared $InSbSe_3$ thin films can possibly open up new advances in the field of cryogenic thermoelectric materials. To determine the

thermoelectric efficiency of the as-prepared $InSbSe_3$ thin film, the thermoelectric figure of merit (ZT) is calculated using the equation [22]

$$ZT = \frac{S^2 \sigma T}{k} \tag{7.1}$$

The variation of ZT in the temperature range from 4 K to 425 K is shown in Fig 7.18.

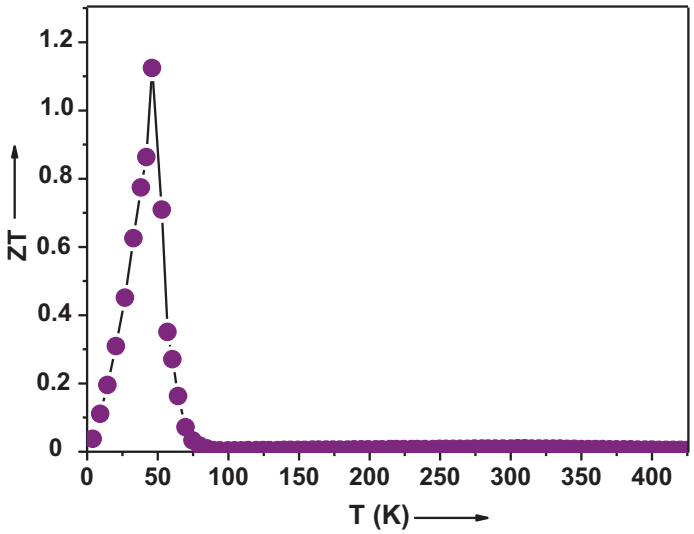

Fig 7.18 Variation of ZT with temperature of $InSbSe_3$ thin film

The film exhibits a maximum ZT ≈ 1.1 at 46 K, which is comparable to recently developed efficient thermoelectric materials such as $In_{0.0025}Sn_{0.9975}Te$ nanostructures [23], Na doped PbTe [24] and $Bi_{0.875}Ba_{0.125}CuSeO$ oxyselenides [25]. The thermoelectric devices with ZT ≈ 1 can operate at a power conversion efficiency of 4% to 5% [26]. In general, materials with ZT ≥ 1 are recognized as efficient candidates for use in thermoelectric devices [16].

However, it is noteworthy to mention that for thermoelectric refrigeration, materials with ZT ≥ 4 are needed [27]. Hence, on further optimization of power factor and thermal conductivity by the introduction of new technologies and concepts of nanostructuring, the as-prepared $InSbSe_3$ with ZT ≈ 1.1 at 46 K can be regarded as a novel promising material for cryogenic thermoelectric applications in the near future.

Evaluation of material parameters

The data from the analysis of Hall and thermoelectric power measurements have been combined to evaluate important material parameters such as Fermi energy (E_F), effective mass (m_p*), density of states (N_V), relaxation time (τ) and mean free path (l) using the equations described in section 5.3.5. The position of Fermi level is determined as ≈ 0.04 eV above the valence band. The values of N_V and m_p* are obtained as ≈ 2×10^{17} cm^{-3} and ≈ $0.04m_0$ respectively, where m_0 is the rest mass of electron. The density of states (N_V) is found to be greater than the charge carrier concentration (p), i.e, $N_V >> p$, indicating the non degenerate semiconducting nature of the film [28]. The relaxation time (τ) and mean free path (l) of charge carriers in the film are evaluated as ≈ 4.8×10^{-16} s and ≈ 4 Å respectively.

7.4 Summary and Conclusions

Polycrystalline p-type $InSbSe_3$ thin films are successfully deposited on glass substrates under optimized deposition conditions by reactive evaporation. The film shows a direct allowed transition with an optimum band gap of 1.52 eV and high absorption coefficient ≈ 10^5 cm^{-1}, suitable for use as an absorber

layer material in solar cells. The films are photoconducting and exhibit a high photosensitivity of 4.8 and hence can also be considered as a plausible substitute for smart materials. Interestingly, the considerably high value of Seebeck coefficient ≈ 6342 μVK^{-1} and thermoelectric figure of merit ≈ 1.1 observed at 46 K demands further research on $InSbSe_3$ thin films to make them competitive with other state-of-the-art thermoelectric materials for cryogenic thermoelectric applications. Briefly, the prepared $InSbSe_3$ thin film shows potentially useful photovoltaic and thermoelectric power properties that call for further investigation and optimization. Table 7.2 summarizes a few notable material parameters of the as-prepared $InSbSe_3$ thin film.

Table 7.2 Material parameters of the as-prepared $InSbSe_3$ thin film

Material Parameters	$InSbSe_3$
Type of conductivity	p-type non degenerate
Optical band gap	1.52 eV
Photosensitivity	4.8
Charge carrier concentration at 300 K	$9.1x10^{16}$ cm^{-3}
Electrical conductivity at 300 K	0.3 Scm^{-1}
Effective mass at 300 K	$0.04m_0$
Mobility at 300 K	21.3 $cm^2V^{-1}s^{-1}$
Maximum Seebeck coefficient	6342 μVK^{-1} at 46 K
Maximum electrical conductivity	0.41 Scm^{-1} at 425 K
Maximum thermal conductivity	0.075 $Wm^{-1}K^{-1}$ at 425 K
Maximum power factor	$1.1x10^{-3}$ $Wm^{-1}K^{-2}$ at 46 K
Maximum figure of merit	1.1 at 46 K

References

[1] S. S. Lee, K. W. Seo and I. W. Shim, Bulletin. Korean. Chem. Soc 27, 147 (2006).

[2] K. Y. Rajpure, C. D. Lokhande, and C. H. Bhosale, Thin Solid Films 311, 114 (1997).

[3] H. S. Soliman, B. A. Khalifa, M. M. E. Nahass, and E. M. Ibrahim, Physica B 351, 11 (2004).

[4] M. A. Afifi, E. A. E. Wahabb, A. E. Bekheet, and H. E. Atyia, J. Mater. Sci 41, 7969 (2006).

[5] K. G. Gunther, The use of thin films in physical investigations, ed. by J. C. Anderson (Academic, London, 1966), pp. 213-232.

[6] B. D. Cullity, Elements of X-ray diffraction, ed. by M. Cohen (Addison Wesley, Philippines, 1978), pp. 81-106.

[7] C. D. Wagner, Handbook of X-ray photoelectron spectroscopy: a reference book of standard data for use in X-ray photoelectron spectroscopy, ed. by G. E. Muilenberg (Perkin Elmer, USA, 1979), pp. 1-190.

[8] R. Swanepoel, J. Phys. E. Sci. Instrum 16, 1214 (1983).

[9] J. Tauc, Amorphous and liquid semiconductors (Plenum, New York, 1974), pp. 159-220.

[10] H. E. Atyia, J. Optoelec. Adv. Mater 8, 1359 (2006).

[11] S. H. Wemple and M. DiDomenico, Phys. Rev. B 3, 1338 (1971).

[12] A. H. Ammar, Appl. Surface. Sci 201, 9 (2002).

[13] E. E. Ezeobele and I. A. Ezenwa, Int. J. Sci. Technol 4, 45 (2015).

[14] K. R. Murali and P. Thirumoorthy, Elec. Chem. Soc. Trans 28, 67 (2010).

[15] E. S. M. Farag and M. M. Sallam, Egypt. J. Solids 30, 1 (2007).

[16] T. M. Tritt and M. A. Subramanian, Mater. Res. Soc. Bulletin 31, 188 (2006).

[17] C. Herring, Phys. Rev 96, 1163 (1954).

[18] K. Rubenis, V. Teteris, J. Locs, J. Barloti and L. B. Cimdina, Mater. Sci. Appl. Chem 28, 34 (2013).

[19] Z. K. Cai, P. Fan, Z. H. Zheng, X. M. Cai, D. P. Zhang, T. B. Chen and P. J. Liu, Adv. Mater. Res 538-541, 60 (2012).

[20] J. Xu, H. Li, B. Du, X. Tang, Q. Zhang and C. Uher, J. Mater. Chem 20, 6138 (2010).

[21] L. M. Goncalves, C. Couto, P. Alpuim, A. G. Rolo, F. Volklein and J. H. Correia, Thin Solid Films 518, 2816 (2010).

[22] M. Fardy, A. I. Hochbaum, J. Goldberger, M. M. Zhang and P. Yang, Adv. Mater 19, 3047 (2007).

[23] Q. Zhang, B. Liao, Y. Lan, K. Lukas, W. Liu, K. Esfarjani, C. Opeil, D. Broido, G. Chen and Z. Ren, Proc. National. Academy. Sci 110, 13261 (2013).

[24] K. Biswas, J. He, I. D. Blum, C. I. Wu, T. P. Hogan, D. N. Seidman, V. P. Dravid and M. G. Kanatzidis, Nature 489, 414 (2012).

[25] J. Li, J. Sui, Y. Pei, C. Barreteau, D. Berardan, N. Dragoe, W. Cai, J. He and L. D. Zhao, Energy. Environ. Sci 5, 8543 (2012).

[26] X. Zhang and L. D. Zhao, J. Materiomics 1, 92 (2015).

[27] J. Androulakis, P. Migiakis and J. Giapintzakis, Appl. Phys. Lett 84, 1099 (2004).

[28] R. T. Shuey, Semiconducting ore minerals (Elsevier, USA, 1975), pp. 41-77.

…….ൟൟൟ…….

Chapter 8

Preparation and Characterization of Polycrystalline SnSe Thin Films

8.1 Introduction

Tin monoselenide (SnSe) is an important narrow band gap IV-VI layered semiconductor compound [1] with orthorhombic structure [2] as shown in Fig 8.1.

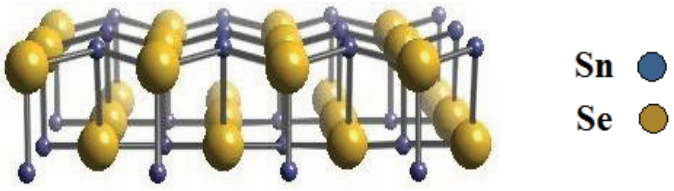

Fig 8.1 Crystal structure of SnSe

In recent years, SnSe thin films have been intensively studied due to the abundance and non toxicity of its constituent elements, near optimum band gap

for absorbing solar energy suitable for thin film solar cells and high absorption coefficient. SnSe undergoes phase transitions from orthorhomic to cubic at a temperature of 540 $^{\circ}$C [3] and from orthorhombic to tetragonal at very high temperatures of about 860 $^{\circ}$C. SnSe is a potential candidate for application in solar cells. Recently Nair et al [4] developed and characterized a heterojunction solar cell of configuration $InSnO_2$:F/CdS/Sb_2S_3/SnSe with a conversion efficiency of 0.61% using evaporated SnSe thin film. SnSe has been widely used in memory switching devices [5], schottky diodes [6], radiation detectors [7] and photoelectrochemical cells [8]. SnSe thin films have been successfully prepared by researchers using different deposition techniques such as chemical bath deposition [9], thermal evaporation [10], laser ablation [11], electrochemical atomic layer epitaxy [12] and spray pyrolysis [13].

Recently, it has been found that SnSe demonstrates the highest thermoelectric figure of merit (ZT) ever found, thereby making it a possible material for use in thermoelectric generators. Stevens et al [14] carried out a systematic investigation on the high temperature thermoelectric power properties of metal chalcogenides with SnSe for the three systems: namely, PbTe-SnSe, PbSe-SnSe and SnTe-SnSe and found that the SnTe-SnSe system showed a very high ZT with a maximum of 0.45 at 700 K. Later on, Zhao et al [15] reported an ZT of 2.6 ± 0.3 at 923 K, the highest value ever found in SnSe single crystals. They have attributed the high value of ZT to the low lattice thermal conductivity which arise from the anharmonicity of SnSe resulting from its layered structure. SnSe is thus proved to be a promising compound for further research in the field of thermoelectrics, as it is of p-type and less toxic than the commonly used toxic lead based thermoelectric materials.

It is therefore thought worthwhile to also explore the thermoelectric power properties of SnSe thin films at low temperatures, about which no reports are available in literature, to the best of our knowledge. Hence the present work elucidates the low temperature thermoelectric power properties of SnSe thin films and evaluates the thermoelectric power factor and figure of merit in the temperature range from 4 K to 425 K in view of their possible applications in thermoelectric devices functioning at low temperatures. The as-prepared SnSe thin films are characterized for their structural, compositional, morphological, optical, electrical and thermoelectric power properties and the results are discussed in the following sections.

8.2 Experimental technique

In the present study, reactive evaporation - a variant of Gunther's three temperature method [16], described in section 3.3, is used to prepare SnSe thin films. The experimental setup and the detailed process of thin film deposition have already been discussed in section 3.4. Briefly, high purity Sn (99.999%) and Se (99.999%) are evaporated simultaneously at suitable rates from independently heated sources. Sn is evaporated from a molybdenum boat whereas Se is evaporated from a glass crucible kept in a molybdenum basket. The vapours are allowed to deposit on glass substrates kept at an elevated temperature of 523±5 K after attaining a pressure of the order of 10^{-5} mbar in the coating unit. The optimized conditions used to deposit SnSe thin films are:

Impingement rate of Sn : 4.2×10^{15} atoms $cm^{-2}s^{-1}$
Impingement rate of Se : 4.8×10^{15} atoms $cm^{-2}s^{-1}$
Substrate temperature : 523±5 K

The as-prepared SnSe thin films are characterized for their structural properties using Rigaku D MaxC X-ray diffractometer (XRD) for 2θ varying from 10° to 70° with CuK_α (1.5404 Å) as the radiation source. The elemental composition is verified from energy dispersive analysis of X-rays (EDAX) and X-ray photoelectron spectroscopy (XPS). The surface morphology is studied using scanning electron microscopy (SEM) and atomic force microscopy (AFM). The optical properties are analyzed using UV-Vis-NIR spectrophotometer in the wavelength range from 2500 nm to cut-off. The thickness of the film is measured using Veeco Dektak 6M stylus profiler and is found to be ≈ 180 nm. The Hall and photoconductivity measurements are performed at room temperature. The Seebeck coefficient, electrical conductivity and thermal conductivity of the as-prepared thin films are measured in the temperature range from 4 K to 425 K to evaluate the thermoelectric figure of merit. The details of the aforementioned characterization tools have already been described in section 3.5 and the results obtained are presented in the following sections.

8.3 Results and Discussions

8.3.1 Structural analysis

The XRD pattern of the as-prepared SnSe thin film is shown in Fig 8.2. The observed interplanar spacings and (hkl) planes of the prepared thin film matches well with that of orthorhombic SnSe (JCPDS Card. 53-0527).

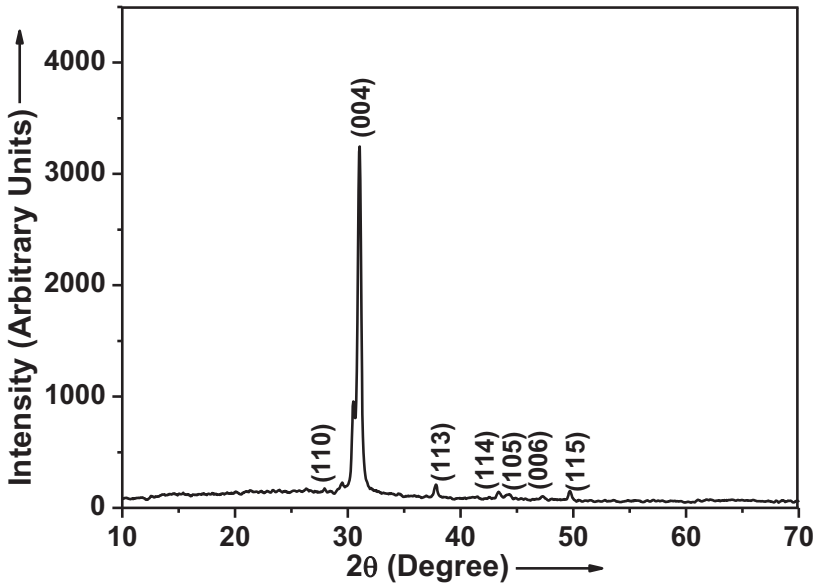

Fig 8.2 XRD pattern of the as-prepared SnSe thin film

The XRD pattern indicates the polycrystalline nature of the as-prepared SnSe thin film. All the diffraction peaks observed in the XRD pattern are indexed according to the orthorhombic phase SnSe (JCPDS Card. 53-0527). The lattice parameters of the SnSe are calculated as a = 4.48 Å, b = 4.11 Å and c = 11.52 Å. These calculated values of lattice parameters very well match with those listed in the (JCPDS Card no. 53-0527). The average crystallite size of the as-prepared SnSe thin film is calculated using Scherrer formula [17] and is obtained as 52 nm. The dislocation density, number of crystallites per unit area and lattice strain in the film are calculated as 3.69×10^{10} lines cm^{-2}, 12.8×10^{10} cm^{-2} and 1.08×10^{-3} respectively using the equations described in section 3.5.1.

8.3.2 Compositional analysis

The EDAX spectrum of the as-prepared SnSe thin film is shown in Fig 8.3. The average atomic percentage is determined as Sn = 49.38% and Se = 50.62%, which indicate that the composition of the as-prepared SnSe thin film is nearly stoichiometric.

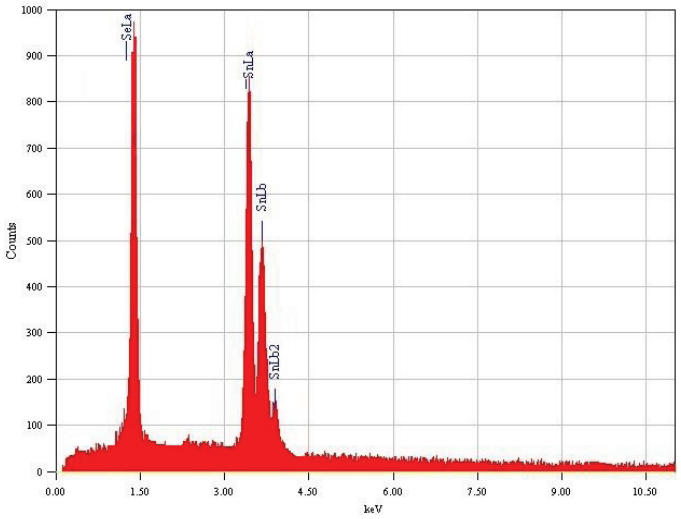

Fig 8.3 EDAX spectrum of SnSe thin film

Fig 8.4 depicts the binding energy (B.E) versus counts per second (CPS) of Sn3d peaks and Se3d peak obtained from the XPS spectrum of the prepared SnSe thin film. The composition of the prepared film determined from the XPS spectrum is found to be near stoichiometric with an average atomic percentage of Sn = 49.43% and Se = 50.57%, consistent with EDAX results.

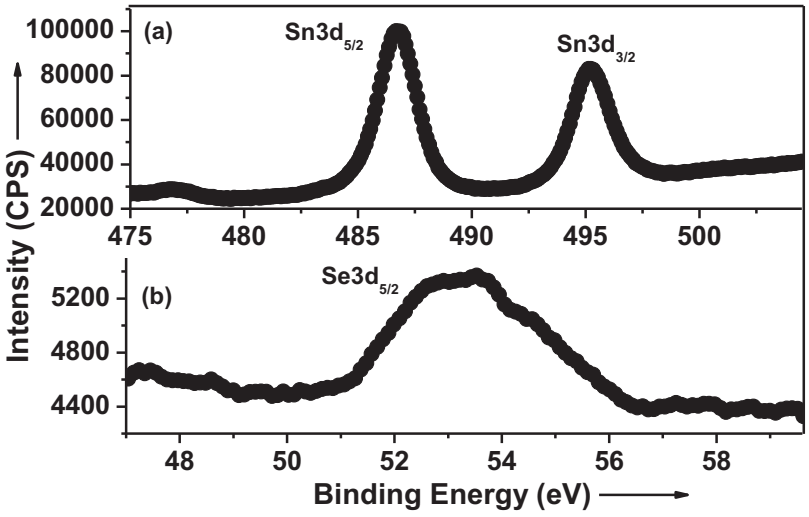

Fig 8.4 XPS spectrum of SnSe thin film

The observed shift in the B.E of Sn and Se from their elemental peak position shown in Table 8.1 is a clear evidence of the formation of SnSe compound where the elements Sn and Se exist in a chemically bonded state.

Table 8.1 Comparison of the observed peak positions of Sn and Se from the XPS spectrum with their standard elemental peak positions

Peak position (eV)	$Sn3d_{5/2}$	$Sn3d_{3/2}$	$Se3d_{5/2}$
Observed peak position	486.8	495.3	53.2
Elemental peak position [18]	484.9	493.3	54.9

8.3.3 Morphological analysis

The SEM image of the SnSe thin film shown in Fig 8.5 indicates that the surface of the film is densely packed with crystallites with an average grain size in the range from 240 nm to 270 nm.

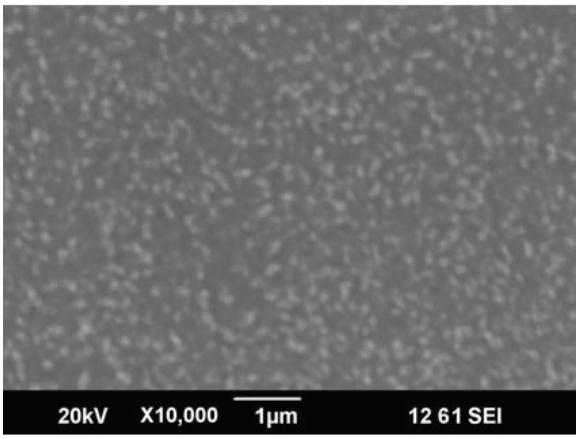

Fig 8.5 SEM image of SnSe thin film

The 2D AFM and 3D AFM is shown in Fig 8.6(a) and (b) respectively. The scan area is 2 µm x 2 µm and scan rate is 10.172 Hz.

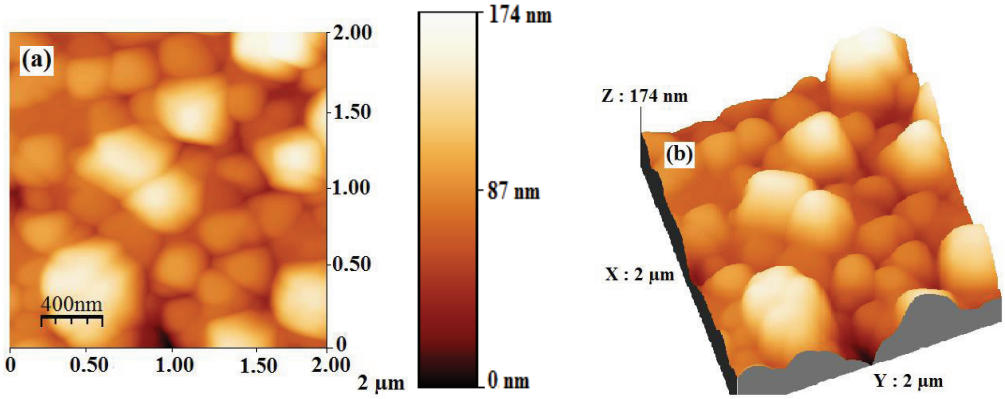

Fig 8.6(a) 2D AFM (b) 3D AFM of SnSe thin film

It can be seen from Fig 8.6(a) that the film is densely packed with crystallites with an average diameter in the range from 280 nm to 310 nm, indicating the agglomeration of particles. The root mean square (RMS) value of surface roughness of the film determined from Fig 8.6(b) is 23 nm, indicating that the overall film surface is significantly smooth.

8.3.4 Optical analysis

Determination of optical band gap

The absorption coefficient (α) of the film is evaluated from the transmission spectrum shown in Fig 8.7 using Swanepoel's method [19] and is found to be 10^5 cm^{-1}.

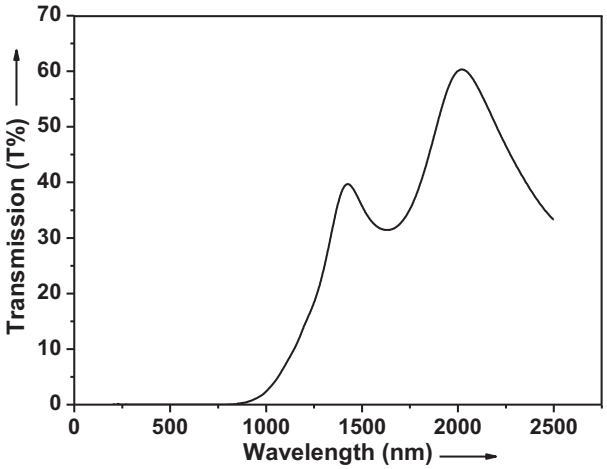

Fig 8.7 Transmission spectrum of SnSe thin film

The optical band gap of the film is determined using the Tauc relation [20] described in section 3.5.7. Fig 8.8 shows the $(\alpha h\nu)^2$ versus hν plot of SnSe thin film.

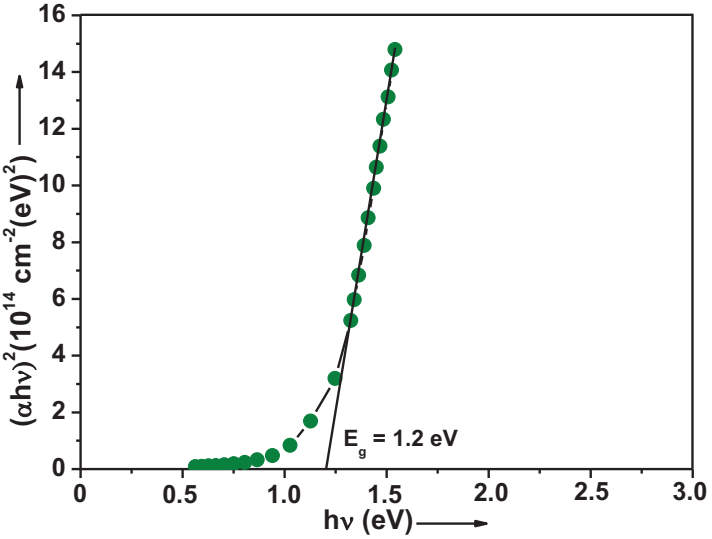

Fig 8.8 Plot of $(\alpha h\nu)^2$ versus $h\nu$ of SnSe thin film

The film shows a direct allowed transition with an optical band gap of 1.2 eV. This value is in good agreement with earlier reports [10] and well within the optimum range for harvesting solar energy.

Determination of optical constants

Fig 8.9 (a) and (b) shows the variation of refractive index (n) and extinction coefficient (r) of the as-prepared SnSe thin film as a function of photon energy ($h\nu$) calculated using Swanepoel's method [19]. The observed high refractive index and small extinction coefficient can be correlated to the better crystalline nature of the prepared film. The real part (ε_1) and imaginary part (ε_2) of the complex dielectric constant of the film are calculated by using the values of n and r using the equations described in section 3.5.7.

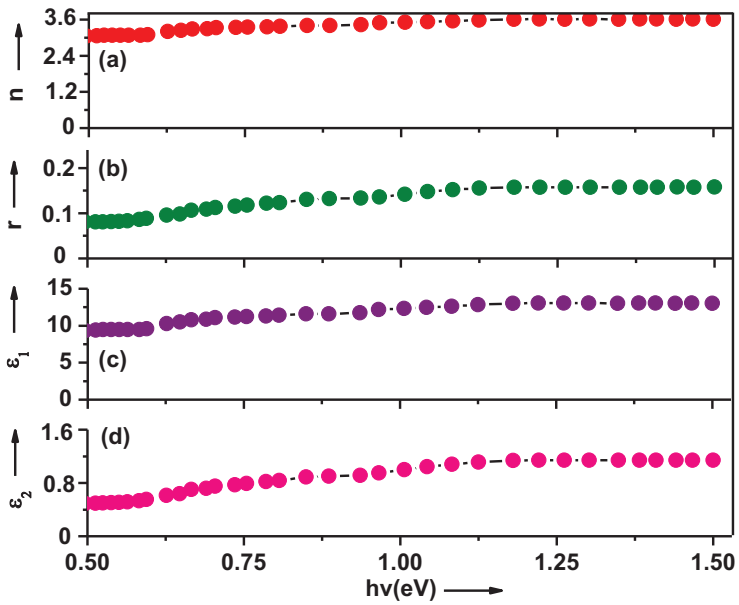

Fig 8.9 Variations of (a) n (b) r (c) ε_1 and (d) ε_2 with hν

Fig. 8.9 (c) and (d) shows the variation of ε_1 and ε_2 of the film with hν. A similar variation with hν is observed between n and ε_1 and that between r and ε_2. Hence ε_1 can be related to n (dispersion) and ε_2 to r (the rate of dissipation of electromagnetic wave).

Determination of dispersion parameters

The single oscillator energy (E_o) and the dispersion energy (E_d) of the prepared thin films are determined using Wemple and DiDomenico single oscillator model [21] which is described in detail in section 5.3.4. The values of E_o and E_d are calculated as 2.62 eV and 19.63 eV respectively from the plot of $(n^2 - 1)^{-1}$ versus $(h\nu)^2$ shown in Fig 8.10.

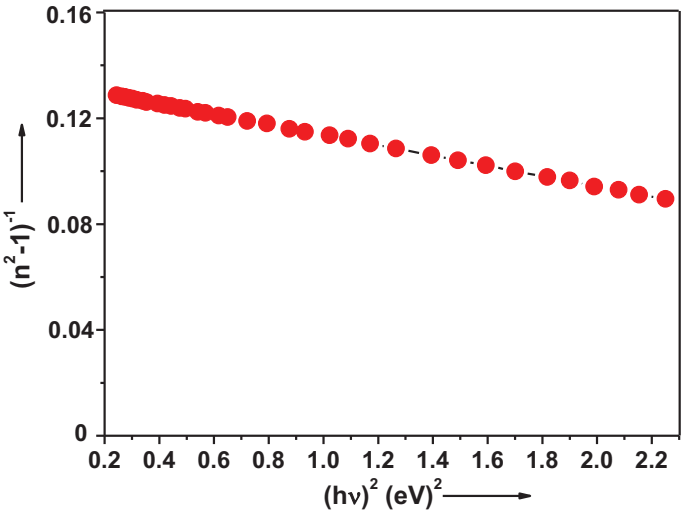

Fig 8.10 Plot of $(n^2 - 1)^{-1}$ versus $(h\nu)^2$

It is found that $E_0 \approx 2E_g$ similar to the relation obtained for thermal evaporated SnS thin films [22]. The E_g deduced from WD model is in good agreement with that determined from Tauc model. Moreover, the moments of optical spectra (M_{-1} and M_{-3}), oscillator strength (f) and refractive index at infinite wavelength (n_∞) [21] of the as-prepared thin films are calculated as 7.48, 1.09 $(eV)^{-2}$, 51.43 $(eV)^2$ and 2.91 respectively using the equations described in section 5.3.4. As there are no reports on the calculation of single oscillator parameters of polycrystalline SnSe thin films, a comparison of our results with literature is not possible.

Determination of loss factor, quality factor and optical conductivity

The loss factor or tan δ, quality factor or Q factor and optical conductivity or $\sigma_{Optical}$ of the as-prepared thin films are calculated using the

equations described in section 3.5.7. The dependence of tan δ, Q factor and $\sigma_{Optical}$ on photon energy (hv) is presented in Fig 8.11.

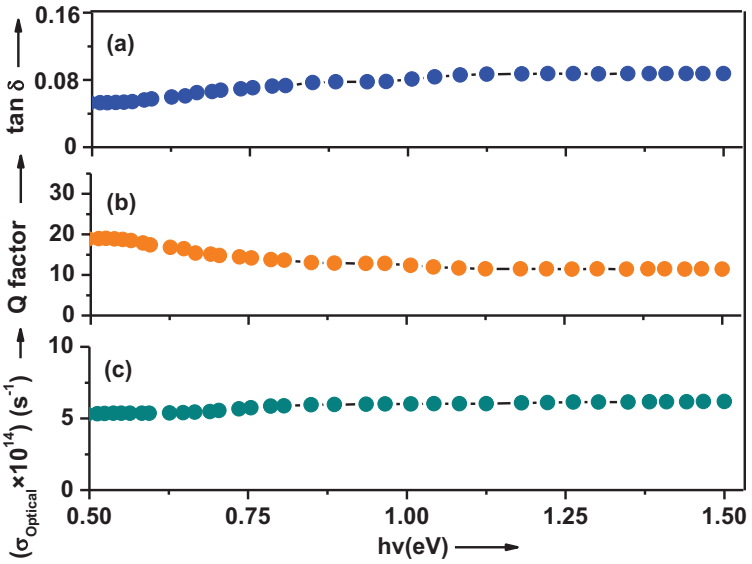

Fig 8.11 Variations of (a) tanδ (b) Q factor and (c) $\sigma_{Optical}$ with hν

The loss factor or tan δ of the film represents the inherent dissipation of electromagnetic energy into heat in the film. It depends on the grain size, lattice strain and structural defects in the film. It can be seen from Fig 8.11 (a) that, in the photon energy range from 0.5 eV to 1.5 eV, the tan δ values varies from 0.05 to 0.08, which is slightly high as expected for thin films compared to their bulk counterparts. The Q factor varied from 18 to 11 as shown in Fig 8.11 (b). The high value of Q factor obtained is in accordance with the general fact that polycrystalline films possess high Q factor than amorphous films. It is observed from Fig. 8.11(c) that $\sigma_{Optical}$ increases with increase in photon energy and attains a maximum value ≈ 6.2×10^{14} s^{-1} at 1.5 eV, a reasonably high value

suitable for optoelectronic applications and similar to that reported for flash evaporated ZnS thin films [23].

8.3.5 Electrical analysis

Hall measurement

The positive value of Hall coefficient confirms the p-type conductivity of the film. At room temperature, the as-prepared SnSe thin film shows a hole concentration of $p \approx 8.7\times10^{16}$ cm^{-3}, hole mobility $\mu_p \approx 10.8$ $cm^2V^{-1}s^{-1}$ and electrical conductivity $\sigma \approx 0.15$ Scm^{-1}.

Photoconductivity measurement

Fig 8.12 shows the photoresponse curve of SnSe thin film. The room temperature photosensitivity [24] is ≈ 1.5, indicating that the SnSe thin film is photosensitive in nature and hence suitable for photovoltaic applications.

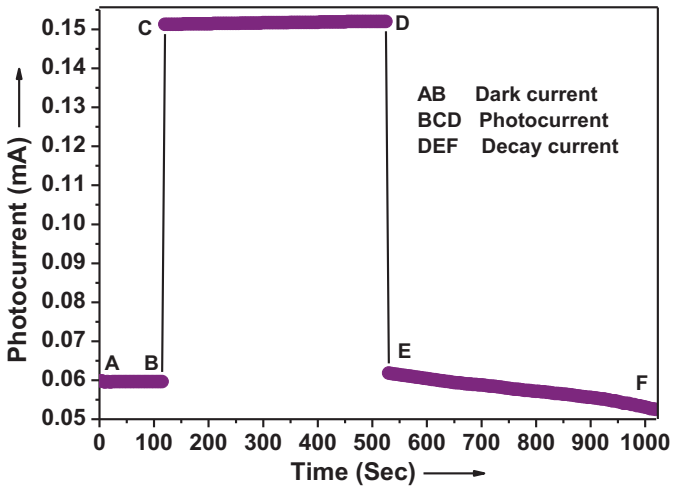

Fig 8.12 Photoresponse curve of SnSe thin film

The increase in photocurrent on illumination is due to generation of electron-hole pairs in the film and it indicates the photoconducting nature of the prepared film.

Determination of activation energy

Fig 8.13 shows the variation of ln(I) with inverse of temperature of the as-prepared SnSe thin film for three continuous heating-cooling cycles.

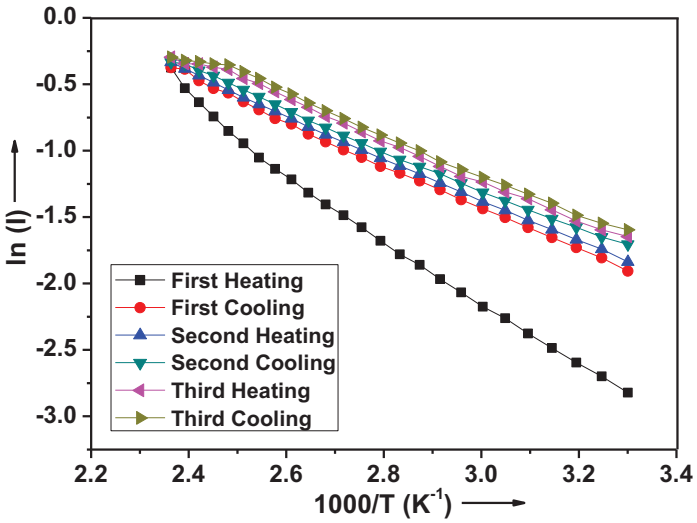

Fig 8.13 Variation of ln(I) with inverse of temperature of SnSe thin film

The observed increase in current with increase in temperature, shown in Fig 8.13, confirms the non degenerate semiconducting nature of the film. The activation energy is calculated from the slope of ln(I) versus 1000/T plot using the Arrhenius relation [25] and is obtained as 0.14 eV.

Determination of thermoelectric power factor and figure of merit in the temperature range from 4 K to 425 K

Fig 8.14 shows the variation of thermoelectric power (TEP) or Seebeck coefficient (S) in the temperature range from 4 K to 425 K of the as-prepared SnSe thin film. The positive value of S observed from Fig 8.14 confirms that the as-prepared SnSe thin films are of p-type. The hot probe and Hall measurements on the film corroborate this observation.

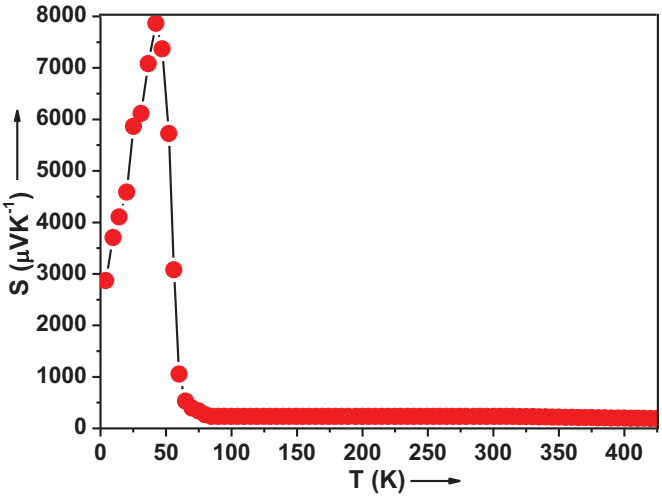

Fig 8.14 Variation of S with temperature of SnSe thin film

Fig 8.14 shows an increase in S from 191 μVK^{-1} to 230 μVK^{-1} with decrease in temperature from 425 K to 305 K, suggestive of the non degenerate semiconducting nature of the film. The observed value of S is well within the optimum range for thermoelectric applications [26]. Below 305 K, the value of S is constant ≈ 231 μVK^{-1} up to 84 K. But as the temperature is lowered from 84 K, there is a sudden and sharp increase in S whose onset is at around 80 K

and a peak is observed at 42 K. The prepared SnSe thin film exhibits a reasonably high S ≈ 7863 μVK^{-1} at 42 K. In the present study, the rapid increase in S observed at low temperatures (80 K to 42 K) has been attributed to the effect of phonon drag on charge carriers resulting from the interaction of phonons with mobile charge carriers [27], which has already been discussed in detail in section 5.3.5.

It can also be seen from Fig 8.14 that, as the temperature is lowered from 42 K, S shows a decrease and attains a value of 2871 μVK^{-1} at 4 K. This decrease in S below 42 K is due to the fact that 42 K is about one fifth of Debye temperature (θ_D) of InSe. The θ_D for SnSe is 210 K [28] below which phonons available for drag is less and consequently resulting in a decrease in S. In the present study, the colossal Seebeck coefficient ~ 7863 μVK^{-1} at 42 K, obtained for the prepared SnSe thin film is suggestive of the possible use of the film as an alternative thermoelectric material at low temperatures. Thus SnSe thin films which are recently being recognized as an efficient thermoelectric material at high temperature can also be considered for cryogenic thermoelectric applications, on further work. Since no low temperature thermoelectric power studies are reported to date on SnSe thin films, a comparison of our results to that extent is not possible.

Fig 8.15 and Fig 8.16 shows the variation of electrical conductivity (σ) and thermal conductivity (k) in the temperature range from 4 K to 425 K of the as-prepared SnSe thin film respectively. The value of σ of the film varies from 0.11 Scm^{-1} to 0.19 Scm^{-1} and the k value of the film varies from 0.023 $Wm^{-1}K^{-1}$ to 0.055 $Wm^{-1}K^{-1}$.

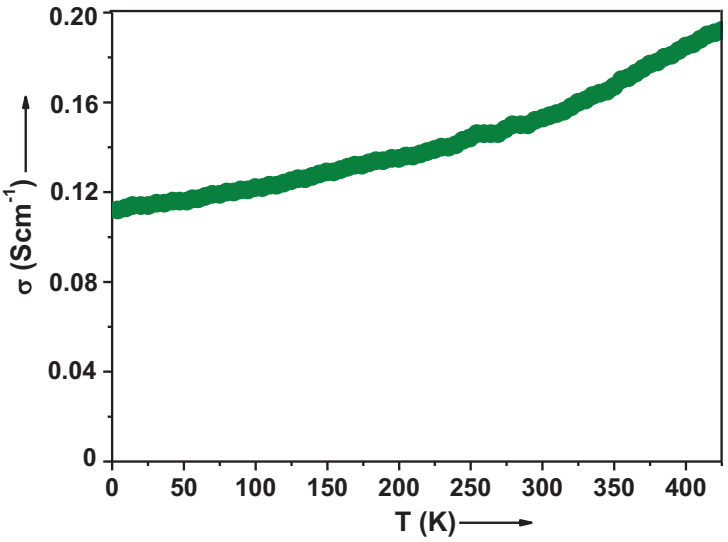

Fig 8.15 Variation of σ with temperature of SnSe thin film

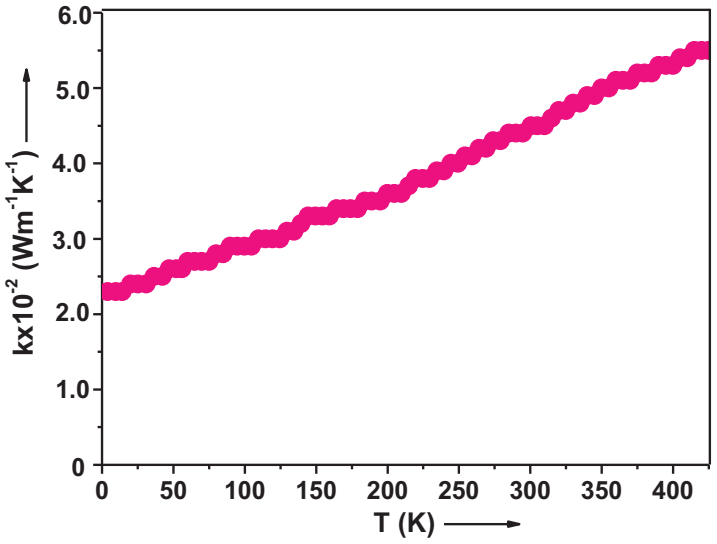

Fig 8.16 Variation of k with temperature of SnSe thin film

Using the values of S and σ, the thermoelectric power factor ($S^2\sigma$) of the film is calculated and its variation in the temperature range from 4 K to 425 K is shown in Fig 8.17.

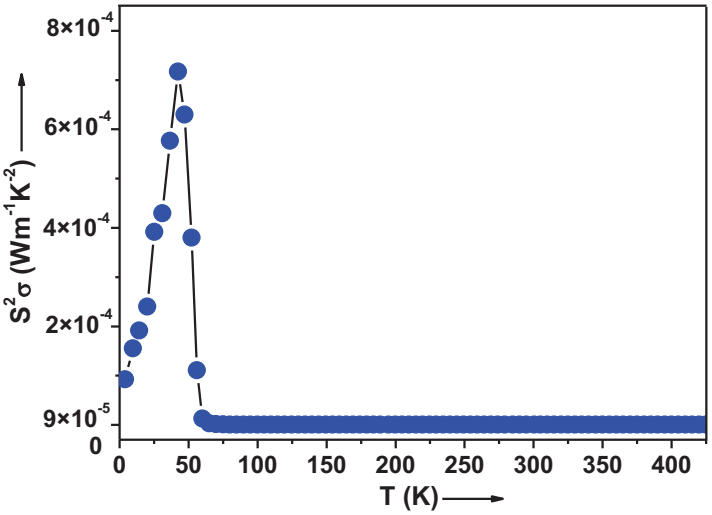

Fig 8.17 Variation of $S^2\sigma$ with temperature of SnSe thin film

As seen from Fig 8.17, the power factor of the film varies from 10^{-4} $Wm^{-1}K^{-2}$ to 10^{-7} $Wm^{-1}K^{-2}$ with a room temperature value ≈ 8.2 x 10^{-7} $Wm^{-1}K^{-2}$. These values are rather low compared to good thermoelectric materials (≈ 10^{-3} $Wm^{-1}K^{-2}$ to 10^{-5} $Wm^{-1}K^{-2}$) but similar to the reasonably good thermoelectric materials such as organic conducting polymers (≈ 10^{-7} $Wm^{-1}K^{-2}$) [29]. The maximum value of $S^2\sigma$ is about 7.2 x 10^{-4} $Wm^{-1}K^{-2}$ observed at 42 K, which is approaching the useful range for thermoelectric applications (≈ 10^{-3} $Wm^{-1}K^{-2}$) [30]. A similar power factor has been reported for certain potential thermoelectric materials such as $CuAgSe_{0.95}Te_{0.05}$ [31], $Zn_{9.993}Ga_{0.0023}In_{0.0047}O$

[32] and PbTe nanocomposites [33] that are recently being developed. This suggests that, on further optimization of power factor, the as-prepared SnSe thin films possess the potential for low temperature thermoelectric applications. Moreover, the thermoelectric efficiency of the as-prepared SnSe thin film is evaluated by calculating the thermoelectric figure of merit (ZT) given by [34]

$$ZT = \frac{S^2 \sigma T}{k} \tag{8.1}$$

The variation of ZT in the temperature range from 4 K to 425 K is shown in Fig 8.18.

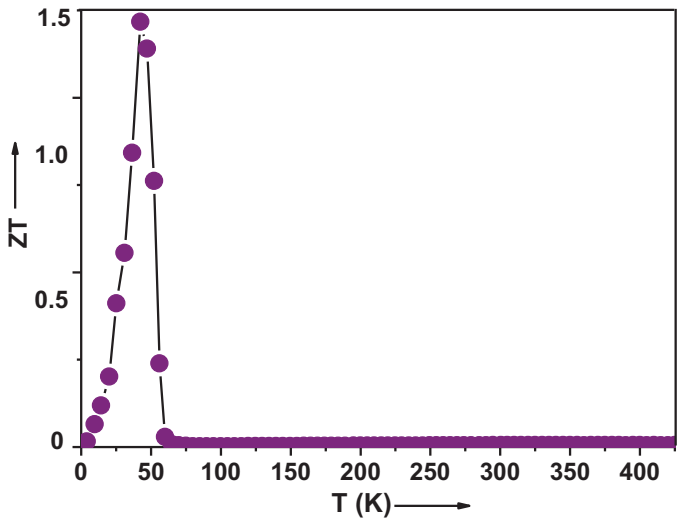

Fig 8.18 Variation of ZT with temperature of SnSe thin film

The as-prepared SnSe thin film shows a maximum ZT ≈ 1.2 at 42 K which is well within the optimum value for thermoelectric applications. The ZT values of the as-prepared thin films are comparable to that obtained for

half-heusler alloys [35], $Bi_{0.5}Sb_{1.5}Te_3$ nanocomposites [36] and $Yb_{0.35}Co_4Sb_{12}$ [37] which are state-of-the-art thermoelectric materials. Hence the as-prepared SnSe thin film with ZT ≈ 1.2 at 42 K, on further work, can be regarded as a promising material for cryogenic thermoelectric applications.

Evaluation of material parameters

The data from the analysis of Hall and thermoelectric power measurements have been combined to evaluate important material parameters such as Fermi energy (E_F), effective mass (m_p*), density of states (N_V), relaxation time (τ) and mean free path (l) using the equations described in section 5.3.5.

The position of Fermi level is determined as ≈ 0.03 eV above the valence band. The values of N_V and m_p* are obtained as ≈ 2.8×10^{17} cm^{-3} and ≈ $0.05m_0$ respectively, where m_0 is the rest mass of electron. The density of states (N_V) is found to be greater than the charge carrier concentration (p), i.e, $N_V >>$ p, indicating the non degenerate semiconducting nature of the film [38]. The relaxation time (τ) and mean free path (l) of charge carriers in the film are evaluated as ≈ 3.1×10^{-16} s and ≈ 1.4 Å respectively.

8.4 Summary and Conclusions

Polycrystalline thin films of p-type SnSe have been successfully deposited onto glass substrates under optimized deposition conditions by reactive evaporation. The film shows a direct allowed transition with an optical band gap of 1.2 eV. The high absorption coefficient and high photosensitivity confirms the potential use of the reactive evaporated SnSe thin films as an

absorber layer material in solar cells. The optimum value of Seebeck coefficient ≈ 7863 μVK^{-1} and reasonably high thermoelectric figure of merit ≈ 1.2 observed at 42 K, indicates that, on further work, the as-prepared SnSe thin film can be considered as an ideal material for cryogenic thermoelectric applications. Table 8.2 summarizes a few notable material parameters of the as-prepared SnSe thin film.

Table 8.2 Material parameters of the as-prepared SnSe thin film

Material Parameters	SnSe
Type of conductivity	p-type non degenerate
Optical band gap	1.2 eV
Photosensitivity	1.5
Charge carrier concentration at 300 K	$8.7x10^{16}$ cm^{-3}
Electrical conductivity at 300 K	0.15 Scm^{-1}
Effective mass at 300 K	$0.05m_0$
Mobility at 300 K	10.8 $cm^2V^{-1}s^{-1}$
Maximum Seebeck coefficient	7863 μVK^{-1} at 42 K
Maximum electrical conductivity	0.19 Scm^{-1} at 425 K
Maximum thermal conductivity	0.055 $Wm^{-1}K^{-1}$ at 425 K
Maximum power factor	$7.2x10^{-4}$ $Wm^{-1}K^{-2}$ at 42 K
Maximum figure of merit	1.2 at 42 K

References

[1] A. Agarwal, M. N. Vashi, D. Lakshminarayana and N. M. Batra, J. Mater. Sci. Mater. Electron 11, 67 (2000).

[2] G. H. Chandra, J. N. Kumar, N. M. Rao and S. Uthanna, J. Crystal. Growth 306, 68 (2007).

[3] T. Chattopadhyay, J. Pannetier and H. G. V. Schnering, J. Phys. Chem. Solids 47, 879 (1986).

[4] M. T. S. Nair, E. B. Salgado, A. R. Garcia, M. R. A. Silva, J. Campos and P. K. Nair, Elec. Chem. Soc. Trans 41, 177 (2011).

[5] K. A. Campbell and C. M. Anderson, Microelectron J 38, 52 (2007).

[6] N. Tugluoglu, S. Karadeniz, M. Sahin and H. Safak, Semicond. Sci. Technol 19, 1092 (2004).

[7] L. S. Wang, B. Niu, Y. T. Lee, D. A. Shirley and K. Balasubramanian, J. Chem. Phys 92, 899 (1990).

[8] Z. Zainal, S. Nagalingam, A. Kassim, M. Z. Hussein and W. M. M. Yunus, Mater. Sci 21, 225 (2003).

[9] N. A. Okereke and A. J. Ekpunobi, Chalcogenide. Lett 7, 531 (2010).

[10] R. Indirajith, T. P. Srinivasan, K. Ramamurthi and R. Gopalakrishnan, Current. Appl. Phys 10, 1402 (2010).

[11] R. Teghil, A. Santagata, V. Marotta, S. Orlando, G. Pizzella, A. G. Guidoni and A. Mele, Appl. Surf. Sci 90, 505 (1995).

[12] Z. Qiao, W. Shang and C. Wang, J. Electroanal. Chem 576, 171 (2005).

[13] J. S. N. Rios, M. Ramachandran, D. M. Escobar and A. S. Suarez, J. Semicond 34, 0130011 (2013).

[14] K. R. Stevens, M. G. Kanatzidis, S. Johnsen and S. N. Girard, Nanoscape 7, 52 (2010).

[15] L. D. Zhao, S. H. Lo, Y. Zhang, H. Sun, G. Tan, C. Uher, C. Wolverton, V. P. Dravid and M. G. Kanatzidis, Nature 508, 373 (2014).

[16] K. G. Gunther, The use of thin films in physical investigations, ed. by J. C. Anderson (Academic, London, 1966), pp. 213-232.

[17] B. D. Cullity, Elements of X-ray diffraction, ed. by M. Cohen (Addison Wesley, Philippines, 1978), pp. 81-106.

[18] C. D. Wagner, Handbook of X-ray photoelectron spectroscopy: a reference book of standard data for use in X-ray photoelectron spectroscopy, ed. by G. E. Muilenberg (Perkin Elmer, USA, 1979), pp. 1-190.

[19] R. Swanepoel, J. Phys. E. Sci. Instrum 16, 1214 (1983).

[20] J. Tauc, Amorphous and liquid semiconductors (Plenum, New York, 1974), pp. 159-220.

[21] S. H. Wemple and M. DiDomenico, Phys. Rev. B 3, 1338 (1971).

[22] M. M. E. Nahass, H. M. Zeyada, M. S. Aziz and N. A. E. Ghamaz, Optical. Mater 20, 159 (2002).

[23] N. A. Bakr, N. N. Jandow and N. F. Habubi, Int. Lett. Chem. Phys. Astronomy 39, 52 (2014).

[24] K. R. Murali and P. Thirumoorthy, Elec. Chem. Soc. Trans 28, 67 (2010).

[25] E. S. M. Farag and M. M. Sallam, Egypt. J. Solids 30, 1 (2007).

[26] T. M. Tritt and M. A. Subramanian, Mater. Res. Soc. Bulletin 31, 188 (2006).

[27] C. Herring, Phys. Rev 96, 1163 (1954).

[28] O. Madelung, Semiconductors data handbook (Springer, Berlin, 2004), pp. 580- 582.

[29] O. Bubnova and X. Crispin, Energy. Environ. Sci 5, 9345 (2012).

[30] L. M. Goncalves, C. Couto, P. Alpuim, A. G. Rolo, F. Volklein and J. H. Correia, Thin Solid Films 518, 2816 (2010).

[31] P. F. Qiu, X. B. Wang, T. S. Zhang, X. Shi and L. D. Chen, J. Mater. Chem. A 3, 22454 (2015).

[32] H. Takemoto, H. Kawakami, M. Saito and H. Yamamura, Procedia. Eng 36, 434 (2012).

[33] B. Paul and P. Banerji, J. Nano. Electron. Phys 3, 691 (2011).

[34] M. Fardy, A. I. Hochbaum, J. Goldberger, M. M. Zhang and P. Yang, Adv. Mater 19, 3047 (2007).

[35] L. Chen, S. Gao, X. Zeng, A. M. Dehkordi, T. M. Tritt and S. J. Poon, Appl. Phys. Lett 107, 0419021 (2015).

[36] H. C. Hsu, J. Y. Huang and T. K. Huang, China. Steel. Tech. Report 27, 57 (2014).

[37] J. Yang, Q. Hao, H. Wang, Y. C. Lan, Q. Y. He, A. Minnich, D. Z. Wang, J. A. Harriman, V. M. Varki, M. S. Dresselhaus, G. Chen and Z. F. Ren, Phys. Rev. B 80, 1153291 (2009).

[38] R. T. Shuey, Semiconducting ore minerals (Elsevier, USA, 1975), pp. 41-77.

Chapter 9

Preparation and Characterization of Polycrystalline $Sn_2Sb_4Se_8$ Thin Films

9.1 Introduction

In the past few decades, the search for novel thin film semiconductors with better properties for specific applications has emerged into an active field of basic and applied solid state research. However, a substantial progress in this field is achieved with the advent of the chalcogenide (Group VI) based semiconducting compounds either in bulk or thin film forms. To date, several metal chalcogenide semiconductors have been synthesized and investigated for their structural modifications and electro-optical properties suitable for energy storage and conversion applications [1]. Among them, the IV-VI and V-VI group of compounds have recently gained more attention owing to their promising properties in the field of photovoltaics and thermoelectrics. One of the prominent candidates of IV-VI group is the orthorhombic layered semiconductor SnSe – a good photovoltaic material [2] and an excellent

thermoelectric material with a figure of merit ZT of 2.6 ± 0.3 at 923 K [3]. On the other hand, one of the prominent compounds of V-VI family is Sb_2Se_3 – an orthorhombic layered semiconductor with good photovoltaic and thermoelectric properties [4].

Hence it is of particular interest to synthesize a semiconducting compound that integrates the properties of SnSe and Sb_2Se_3 and to optimize its properties for energy related applications. Intensive research works in this direction has lead to the successful development of tin antimony selenide of composition $Sn_2Sb_4Se_8$ – a compound belonging to the ternary Sn-Sb-Se system or TAS system and an interesting material for future research due to the relative abundance and low cost of its constituent elements. The $Sn_2Sb_4Se_8$ is a IV-V-VI group semiconductor with orthorhombic structure [5] as shown in Fig 9.1.

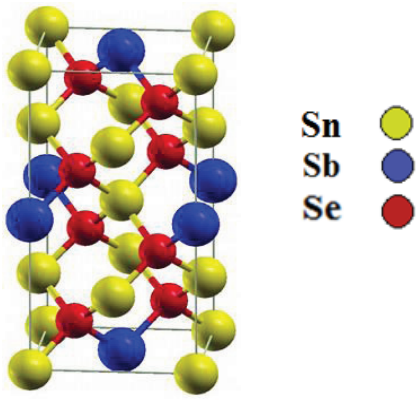

Fig 9.1 Crystal structure of $Sn_2Sb_4Se_8$

With literature search up to now, there is unfortunately a noticeable lack of systematic work on Sn-Sb-Se system except for a few dealing with their

glass crystalline boundary forming regions [6] and Poole Frenkel conduction [7]. Adam et al [8] have reported on certain stoichiometric and non stoichiometric compositions of Sn-Sb-Se system formed by melt quenching technique. Recently, a detailed analysis is carried out by Kumar et al [9] on melt quenched $Sn_{10}Sb_{20}Se_{60}$, $Sn_{11}Sb_{20}Se_{59}$ and $Sn_{12.5}Sb_{20}Se_{57.5}$ glassy films which contain different phases of SnSe, SbSe and Sn-Sb-Se systems. Also, Hasbi et al [10] and Harea et al [11] have reported on the optical properties of amorphous thin films of Sn-Sb-Se. However, no critical evaluation has been carried out, to date, on a particular crystalline phase of Sn-Sb-Se system. Consequently, most of the properties of Sn-Sb-Se system and their thin films still remain unexplored due to scarcity of sufficient literature. Therefore, it should be emphasized that, the novel and unique family of Sn-Sb-Se system and their thin films demand further investigation and optimization to prove their potential in the field of photovoltaics and thermoelectrics.

Hence, in the present work, a systematic investigation is carried out, for the first time, on the structural, compositional, morphological, optical, electrical and thermoelectric power properties of reactive evaporated phase pure polycrystalline thin films of $Sn_2Sb_4Se_8$ – the most commonly encountered crystalline phases of the Sn-Sb-Se system [6] but surprisingly, not yet studied in detail in literature. To the best of our knowledge, this is the first report on the analysis of photoconductivity and determination of thermoelectric figure of merit in the temperature range from 4 K to 425 K of $Sn_2Sb_4Se_8$ thin films. Moreover, the optical constants and dispersion parameters of the films are calculated and the results are discussed in the following sections. To provide an insight into the charge carrier transport properties and conduction mechanism,

the effective mass and mobility of charge carriers, density of states and position of Fermi level have been evaluated by correlating the results of Hall and thermoelectric power measurements. The results of the studies are discussed in the following sections.

9.2 Experimental technique

In the present study, reactive evaporation - a variant of Gunther's three temperature method [12], described in section 3.3, is used to prepare $Sn_2Sb_4Se_8$ thin films. The experimental setup and the detailed process of thin film deposition have already been discussed in section 3.4. Briefly, high purity Sn (99.999%), Sb (99.999%) and Se (99.999%) are evaporated simultaneously at suitable rates from independently heated sources. Sn is evaporated from a molybdenum boat whereas Sb and Se are evaporated from two separate glass crucibles kept in molybdenum baskets. The vapours are allowed to deposit on glass substrates kept at an elevated temperature of 548±5 K after attaining a pressure of the order of 10^{-5} mbar in the coating unit. The optimized conditions used to deposit $Sn_2Sb_4Se_8$ thin films are:

Impingement rate of Sn : 4.2×10^{15} atoms cm^{-2} s^{-1}
Impingement rate of Sb : 4.5×10^{15} atoms cm^{-2} s^{-1}
Impingement rate of Se : 4.8×10^{15} atoms cm^{-2} s^{-1}
Substrate temperature : 548±5 K

The as-prepared $Sn_2Sb_4Se_8$ thin films are characterized for their structural properties using Rigaku D MaxC X-ray diffractometer (XRD) for 2θ varying from 10° to 70° with CuK_α (1.5404 Å) as the radiation source. The

elemental composition is verified from energy dispersive analysis of X-rays (EDAX) and X-ray photoelectron spectroscopy (XPS). The surface morphology is studied using scanning electron microscopy (SEM) and atomic force microscopy (AFM). The optical properties are analyzed using UV-Vis-NIR spectrophotometer in the wavelength range from 2500 nm to cut-off. The thickness of the film is measured using Veeco Dektak 6M stylus profiler and is found to be ≈ 200 nm. The Hall and photoconductivity measurements are performed at room temperature. The Seebeck coefficient, electrical conductivity and thermal conductivity of the as-prepared thin films are measured in the temperature range from 4 K to 425 K to evaluate the thermoelectric figure of merit. The details of the aforementioned characterization tools have already been described in section 3.5 and the results obtained are presented in the following sections.

9.3 Results and Discussions

9.3.1 Structural analysis

The XRD pattern of the as-prepared $Sn_2Sb_4Se_8$ thin film is shown in Fig 9.2. The XRD pattern suggests the polycrystalline nature of the as-prepared $Sn_2Sb_4Se_8$ thin film.

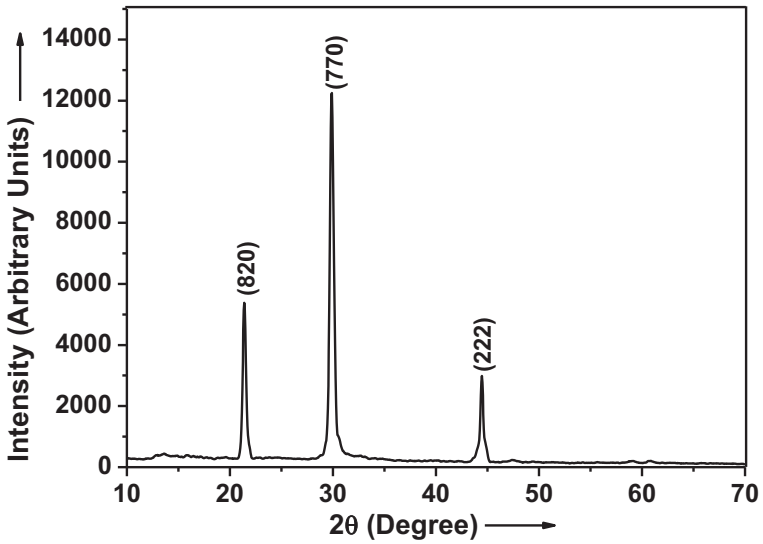

Fig 9.2 XRD pattern of the as-prepared $Sn_2Sb_4Se_8$ thin film

The interplanar spacings and (hkl) planes corresponding to the diffraction peaks matches well with $Sn_2Sb_4Se_8$ (JCPDS Card. 36-1206). The average crystallite size calculated using Scherrer formula [13] is obtained as 84 nm. The structural parameters such as dislocation density, number of crystallites per unit area and lattice strain in the film are evaluated as 1.42×10^{10} lines cm^{-2}, 3.37×10^{10} cm^{-2} and 1.08×10^{-2} respectively using the equations described in section 3.5.1.

9.3.2 Compositional analysis

The presence of Sn, Sb and Se is evident from EDAX spectrum of the as-prepared $Sn_2Sb_4Se_8$ thin film shown in Fig 9.3.

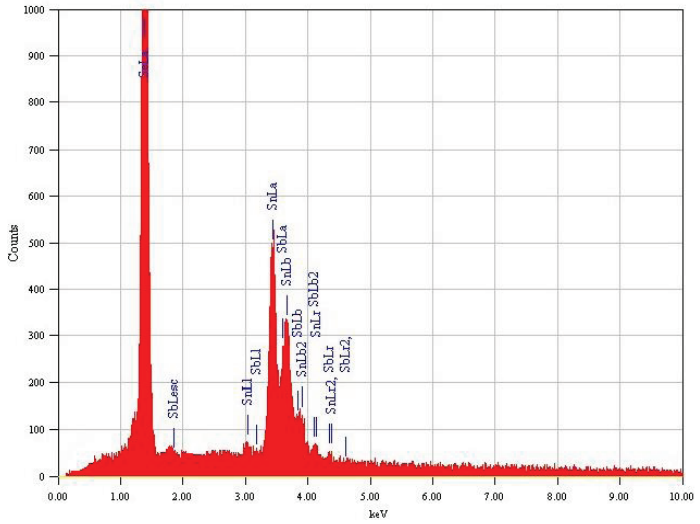

Fig 9.3 EDAX spectrum of $Sn_2Sb_4Se_8$ thin film

No peaks corresponding to any impurity is observed, thereby confirming the purity of the as-prepared film. The average atomic percentage of the elements determined from EDAX is Sn = 15.62%, Sb = 28.15% and Se = 56.23%. The stoichiometric deviation is comparable to experimental errors, consequently the composition of the as-prepared film can be considered as nearly stoichiometric.

The elemental composition of the film is further verified by XPS. Fig 9.4 depicts the binding energy (B.E) versus counts per second (CPS) of Sn3d, Sb3d and Se3d peaks obtained from the XPS spectrum of the $Sn_2Sb_4Se_8$ thin film. The XPS data confirms the near stoichiometric composition of the film with Sn = 15.67%, Sb = 28.21% and Se = 56.12%, consistent with EDAX results.

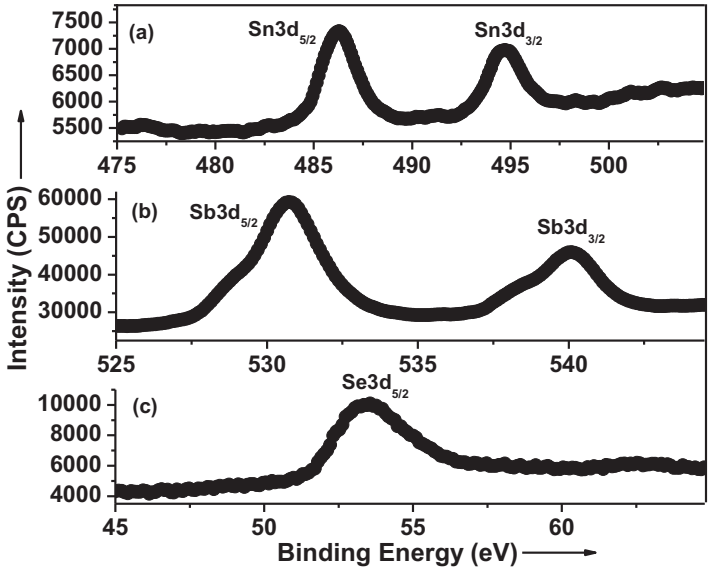

Fig 9.4 XPS spectrum of $Sn_2Sb_4Se_8$ thin film

The observed XPS peak positions of the elements in the compound are compared with their standard elemental peak positions and are presented in Table 9.1.

Table 9.1 Comparison of the observed peak positions of Sn, Sb and Se from the XPS spectrum with their standard elemental peak positions

Peak position (eV)	$Sn3d_{5/2}$	$Sn3d_{3/2}$	$Sb3d_{5/2}$	$Sb3d_{3/2}$	$Se3d_{5/2}$
Observed peak position	486.2	494.7	530.7	540.1	53.5
Elemental peak position [14]	484.9	493.3	528.2	537.6	54.9

The observed shift in the binding energies of the constituent elements from their elemental peak positions has been ascribed to the existence of an intact chemical bonding between the elements in the film, thereby affirming the formation of $Sn_2Sb_4Se_8$ compound.

9.3.3 Morphological analysis

The SEM image of the as-prepared $Sn_2Sb_4Se_8$ thin film is shown in Fig 9.5. The surface of the film is densely packed with crystallites with an average grain size in the range from 300 nm to 330 nm.

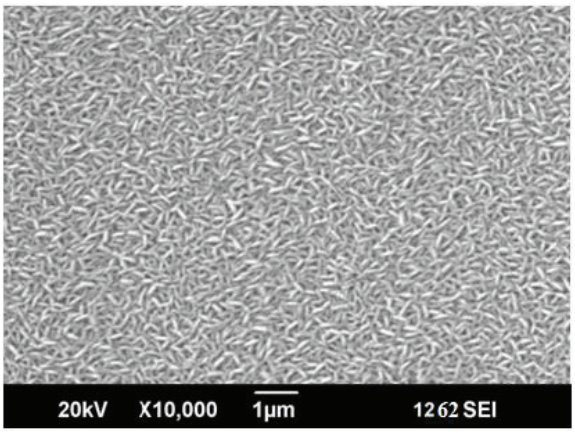

Fig 9.5 SEM image of $Sn_2Sb_4Se_8$ thin film

The 2D AFM and 3D AFM is shown in Fig 9.6(a) and (b) respectively. The scan area is 2 µm x 2 µm and scan rate is 10.172 Hz.

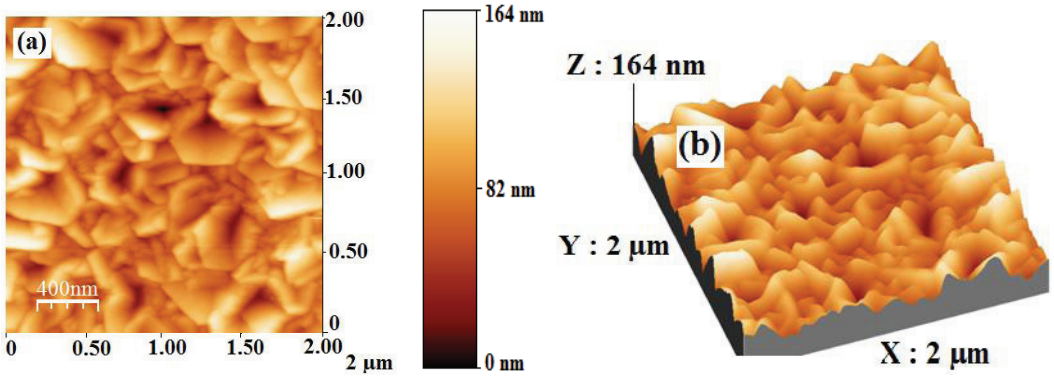

Fig 9.6(a) 2D AFM (b) 3D AFM of $Sn_2Sb_4Se_8$ thin film

The 2D AFM images clearly exhibits the uniform distribution of particles with an average size of about 350 nm to 380 nm agglomerated to form petal like structure of a flower. The root mean square (RMS) value of surface roughness of the film is estimated from the 3D AFM image as 32 nm, indicating a significantly smooth surface.

9.3.4 Optical analysis

Determination of optical band gap

The transmission spectrum shown in Fig 9.7 is analyzed using Swanepoel's method [15] to obtain the absorption coefficient (α) and optical band gap (E_g) of the as-prepared $Sn_2Sb_4Se_8$ thin film.

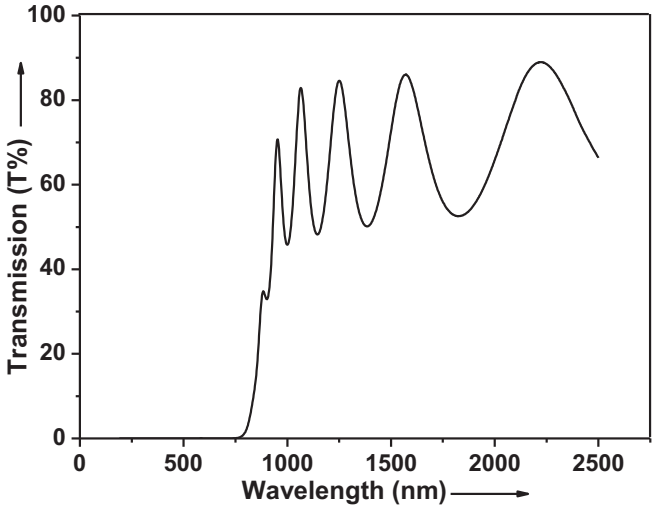

Fig 9.7 Transmission spectrum of $Sn_2Sb_4Se_8$ thin film

The value of α is found to be high of the order of 10^5 cm^{-1}, indicating the possible use of the film as an absorber layer material in solar cells. On

analysis using Tauc relation [16], the prepared film is found to exhibit a direct allowed transition with an optical band gap of 1.54 eV, obtained by the extrapolation of the $(\alpha h\nu)^2$ versus hν curve at X-axis shown in Fig 9.8.

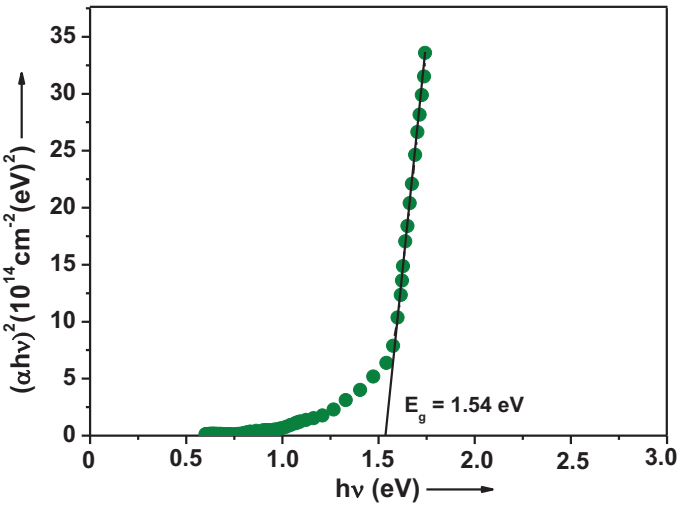

Fig 9.8 Plot of $(\alpha h\nu)^2$ versus hν of $Sn_2Sb_4Se_8$ thin film

The value of band gap thus obtained is well within the ideal range for solar energy harvesting. Moreover, the direct band gap of the film allows strong absorption compared to indirect band gap materials. Taken together, this finding further confirms the possible application of $Sn_2Sb_4Se_8$ thin film as an absorber layer material in the fabrication of thin film solar cells.

Determination of optical constants

The optical constants (refractive index (n), extinction coefficient (r), real part (ε_1) and imaginary part (ε_2) of the complex dielectric constant) are the key factors that decide the application of a material in optical communication

and device design. Hence n and r of the film are evaluated from the transmission spectrum shown in Fig 9.7 using Swanepoel's method [15] and their dependence on photon energy (hν) is illustrated in Fig 9.9 (a) and (b). It is observed that n varies from 2.7 to 2.9 and r varies from 0.006 to 0.03 in the photon energy range from 0.51 eV to 1.53 eV. The high value of n thus obtained provides an additional confirmation of the better crystalline nature of the film.

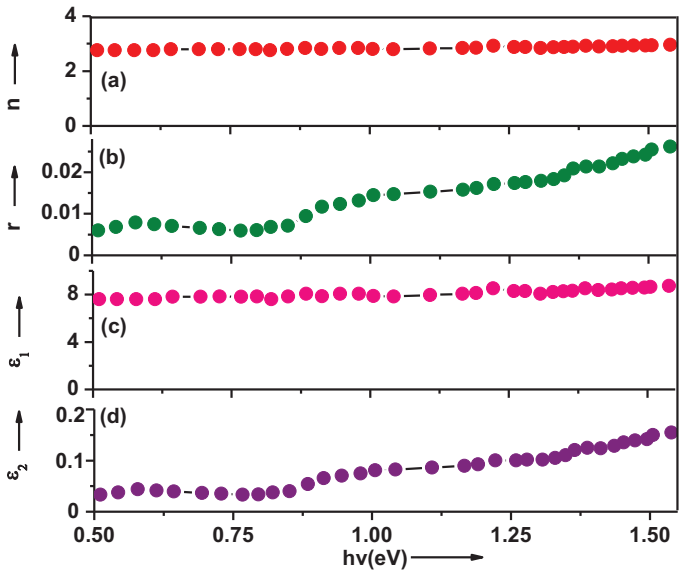

Fig 9.9 Variations of (a) n (b) r (c) ε_1 and (d) ε_2 with hν

The values of n and r are used to determine ε_1 and ε_2 using the equations described in section 3.5.7, and their dependence on photon energy are depicted in Fig 9.9 (c) and (d). It is noticed that, the spectral variation of n is similar to ε_1 and that of r is similar to ε_2. Hence, undoubtedly ε_1 can be related to

dispersion and ε_2 can be associated with the dissipation of electromagnetic wave.

Determination of dispersion parameters

The oscillator energy E_0 and the dispersion energy E_d of the prepared film are determined from the plot of $(n^2 - 1)^{-1}$ versus $(h\nu)^2$ shown in Fig 9.10 by applying Wemple and DiDomenico single oscillator model [17] which is discussed in detail in section 5.3.4.

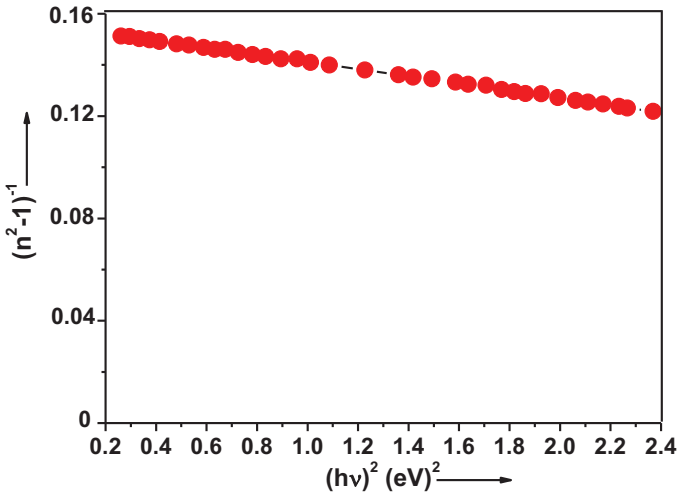

Fig 9.10 Plot of $(n^2 - 1)^{-1}$ versus $(h\nu)^2$

The values of E_0 and E_d are determined as 3.33 eV and 21.49 eV, with E_0 approximately two times the optical band gap (E_g). Thus the oscillator energy of the prepared $Sn_2Sb_4Se_8$ thin film is found to be twice its optical band gap ($E_0 \approx 2E_g$) which in good agreement with the relation deduced for thermal evaporated polycrystalline $Sn_3Sb_2S_6$ thin films [18]. Furthermore, the value of

E_g deduced from WD model is in good agreement with that determined from Tauc model. In addition, the moments of optical spectra (M_{-1} and M_{-3}), oscillator strength (f) and refractive index at infinite wavelength (n_∞) of the film are calculated using the equations described in section 5.3.4 and are obtained as 6.43 eV, 0.58 $(eV)^{-2}$, 71.56 $(eV)^2$ and 2.73 respectively [17]. As there are no reports on the calculation of single oscillator parameters of polycrystalline $Sn_2Sb_4Se_8$ thin films, a comparison of our results with literature is not possible.

Determination of loss factor, quality factor and optical conductivity

The optical properties are further explored by evaluating the loss factor or tan δ, quality factor or Q factor and optical conductivity or $\sigma_{Optical}$ of the as-prepared film using the equations described in section 3.5.7. The dependence of tan δ, Q factor and $\sigma_{Optical}$ on photon energy (hν) is presented in Fig 9.11.

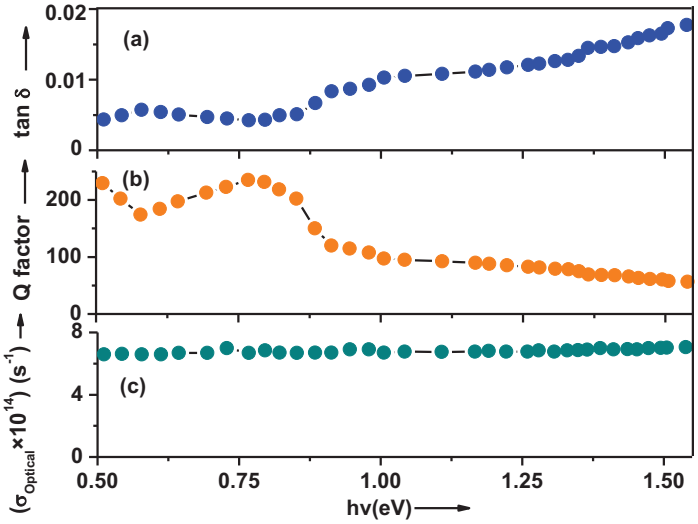

Fig 9.11 Variations of (a) tanδ (b) Q factor and (c) $\sigma_{Optical}$ with hν

It is clear from Fig 9.11 that the loss factor of the film is too small in the measured photon energy range, suggestive of less dielectric loss. The Q factor of the film is found to increase towards low energies, attaining a maximum of 230 at 0.51 eV. The $\sigma_{Optical}$ of the film is found to increase with increase in photon energies, exhibiting a maximum value of 7.05 $\times 10^{14}$ s^{-1} at 1.53 eV, a considerably high value suitable for optoelectronic applications. This value is high compared to the optical conductivity of thermal evaporated α-$(As_2Se_3)_{90}$ Ge_{10} thin film [19].

9.3.5 Electrical analysis

Hall measurement

The positive value of Hall coefficient reveals the p-type conductivity of the film. The film shows a hole concentration p ~ 8.1×10^{16} cm^{-3}, hole mobility

μ_p ~33.2 $cm^2V^{-1}s^{-1}$ and electrical conductivity σ ~ 0.43 Scm^{-1} at room temperature.

Photoconductivity measurement

The photocurrent of the prepared film is measured and is illustrated in Fig 9.12. No such studies are reported to date on $Sn_2Sb_4Se_8$ thin films. The photosensitivity [20] of the prepared film is calculated using the equation described in section 3.5.8 and is found to be 8.4, a reasonably high value signifying the good photosensive nature of the film appropriate for photovoltaic applications.

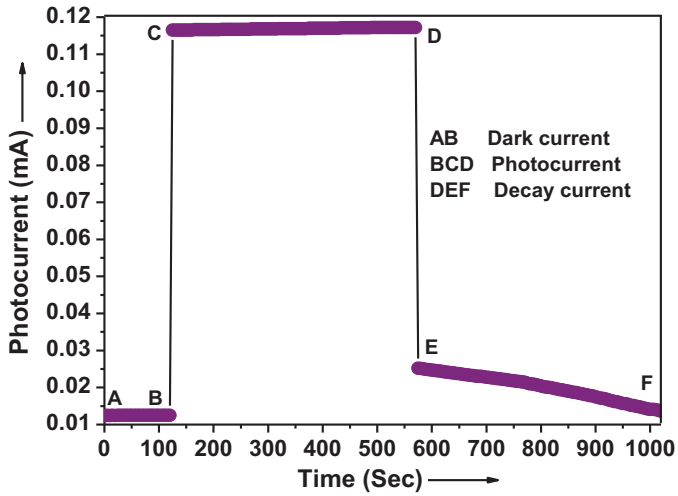

Fig 9.12 Photoresponse curve of $Sn_2Sb_4Se_8$ thin film

On illumination, an increase in photocurrent is observed due to electron-hole pair generation in the film. This obviously reveals that $Sn_2Sb_4Se_8$

thin films are photoconducting in nature and can possibly open up new advances in the field of photovoltaic materials.

Determination of activation energy

Fig 9.13 shows the variation of ln(I) with inverse of temperature of the as-prepared $Sn_2Sb_4Se_8$ thin film for three continuous heating-cooling cycles. The observed increase in current with increase in temperature, shown in Fig 9.13, validates the non degenerate semiconducting nature of the film. The activation energy is calculated from the slope of ln(I) versus 1000/T plot using the Arrhenius relation [21] and is obtained as 0.16 eV.

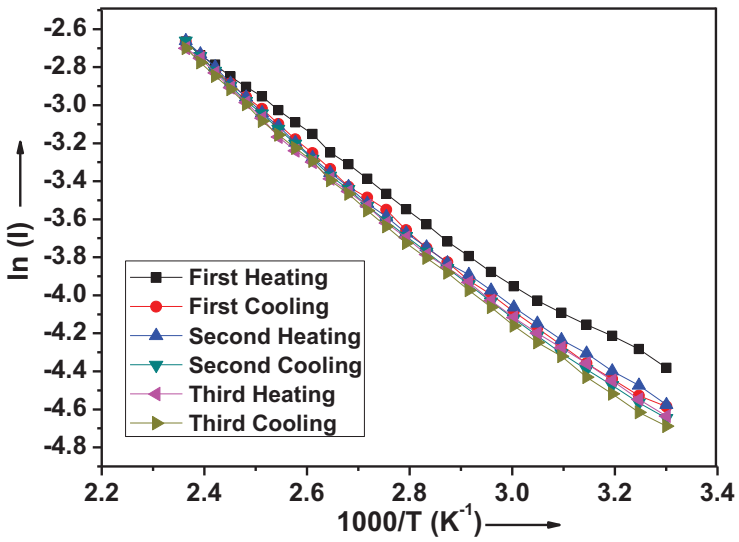

Fig 9.13 Variation of ln(I) with inverse of temperature of $Sn_2Sb_4Se_8$ thin film

Determination of thermoelectric power factor and figure of merit in the temperature range from 4 K to 425 K

The thermoelectric power properties of $Sn_2Sb_4Se_8$ thin film is investigated in the temperature range from 4 K to 425 K for the first time in literature in view of their use in thermoelectric devices. Fig 9.14 shows the variation of thermoelectric power (TEP) or Seebeck coefficient (S) in the temperature range from 4 K to 425 K of the as-prepared $Sn_2Sb_4Se_8$ thin film. The positive value of S observed from Fig 9.14 confirms that the as-prepared $Sn_2Sb_4Se_8$ thin films are of p-type. The hot probe and Hall measurements on the film corroborate this observation.

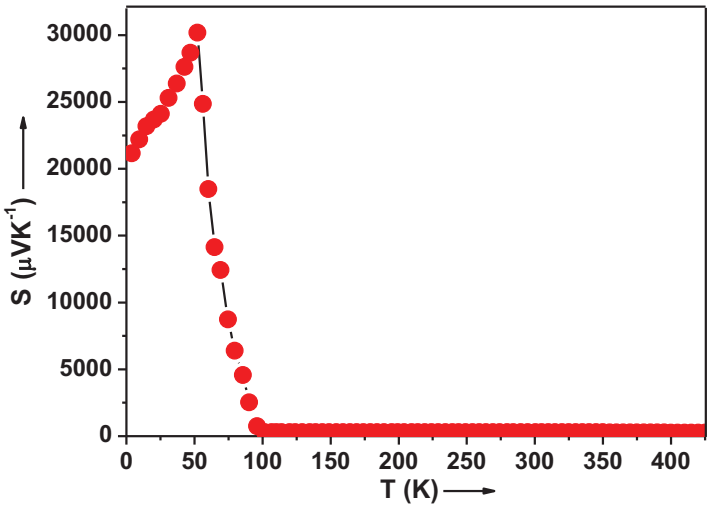

Fig 9.14 Variation of S with temperature of $Sn_2Sb_4Se_8$ thin film

It is observed from Fig 9.14 that S of the prepared film increase from 257 μVK^{-1} to 304 μVK^{-1} with decrease in temperature from 425 K to 305 K,

suggestive of the non degenerate semiconducting nature of the film. The value of S is well within the optimum range for thermoelectric applications [22]. Below 305 K, a constant value of S ≈ 305 μVK^{-1} is observed up to 100 K. Later, S shows an unexpected and rapid increase which reaches up to a maximum of ≈ 30174 μVK^{-1} at 52 K. This unusual increase is explained as an outcome of the influence of phonon drag on charge carriers resulting from the interaction of phonons with mobile charge carriers [23], which has already been in discussed in detail in section 5.3.5.

However, the amplitude of phonon drag effect depends on the number of phonons available to interact with the charge carriers. Towards very low temperatures (usually below about one-fifth of the Debye temperature θ_D), the relative number of phonons available for drag decreases. As a result the effect of phonon drag on the Seebeck coefficient also decreases. This can be a reason for the decrease in S observed in the film at temperatures below 52 K. Below 52 K, S shows a sudden drop and attains a value ≈ 21157 μVK^{-1} at 4 K. Thus θ_D of the as-prepared $Sn_2Sb_4Se_8$ thin film can be estimated as ≈ 260 K. Therefore, thermoelectric power measurement can be considered as a sensitive tool to estimate θ_D. To the best of our knowledge, this is the first report to investigate the thermoelectric properties of $Sn_2Sb_4Se_8$ thin films and hence it is not possible to present a comparative study of our results with literature. It is noteworthy that the high S ≈ 30174 μVK^{-1} at 52 K, exhibited by the $Sn_2Sb_4Se_8$ thin film is indicative of its prospective application in the field low temperature thermoelectrics, on further optimization.

Fig 9.15 and Fig 9.16 shows the variation of electrical conductivity (σ) and thermal conductivity (k) in the temperature range from 4 K to 425 K of the

$Sn_2Sb_4Se_8$ thin film respectively. The value of σ of the film varies from 0.38 Scm^{-1} to 0.48 Scm^{-1} and the k value varies from 1.42 $Wm^{-1}K^{-1}$ to 1.72 $Wm^{-1}K^{-1}$.

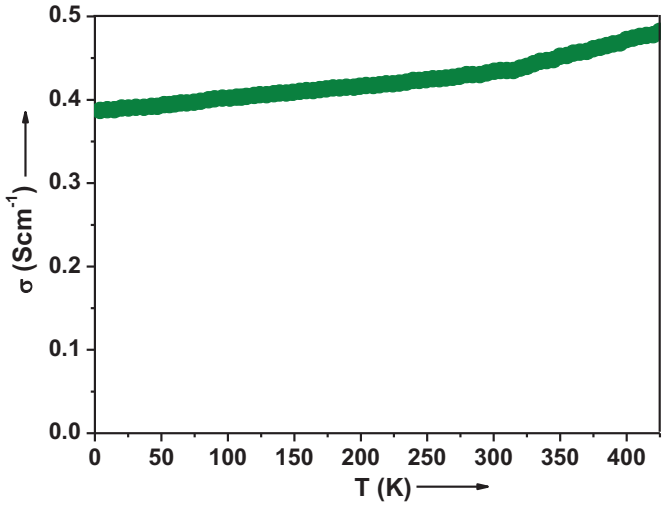

Fig 9.15 Variation of σ with temperature of $Sn_2Sb_4Se_8$ thin film

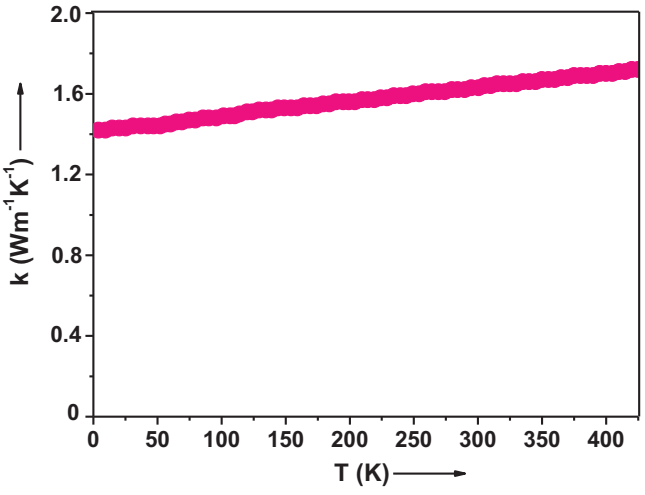

Fig 9.16 Variation of k with temperature of $Sn_2Sb_4Se_8$ thin film

Using the values of S and σ, the thermoelectric power factor ($S^2\sigma$) of the film is calculated and its variation in the temperature range from 4 K to 425 K is shown in Fig 9.17.

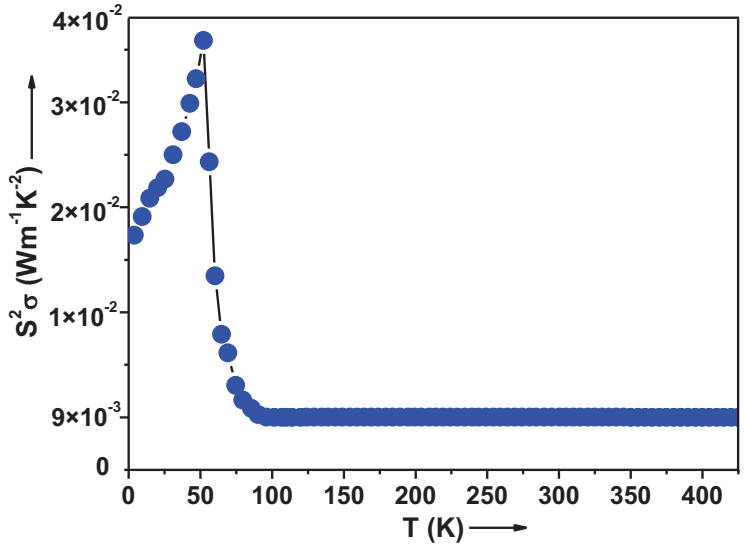

Fig 9.17 Variation of $S^2\sigma$ with temperature of $Sn_2Sb_4Se_8$ thin film

The power factor of the film varies from 10^{-2} $Wm^{-1}K^{-2}$ to 10^{-6} $Wm^{-1}K^{-2}$ with a room temperature value ≈ 4 x 10^{-6} $Wm^{-1}K^{-2}$. This value is rather low compared to good thermoelectric materials (≈ 10^{-3} $Wm^{-1}K^{-2}$ to 10^{-5} $Wm^{-1}K^{-2}$) but comparable to reasonably good thermoelectric materials such as La doped $BaSnO_3$ [24]. The maximum value of $S^2\sigma$ is about 3.5 x 10^{-2} $Wm^{-1}K^{-2}$ observed at 52 K, which is higher than the state-of-the-art thermoelectric material Bi_2Te_3 [25] and today's emerging potential thermoelectric materials such as Te doped ZnSb [26] and $Bi_{0.5}Sb_{1.5}Te_3$ [27]. This suggests that, on further optimization of power factor, the as-prepared $Sn_2Sb_4Se_8$ thin films can possibly open up new

advances in the field of cryogenic thermoelectric materials. To determine the thermoelectric efficiency of the as-prepared $Sn_2Sb_4Se_8$ thin film, the thermoelectric figure of merit (ZT) is calculated using the equation [28]

$$ZT = \frac{S^2 \sigma T}{k} \tag{9.1}$$

The variation of ZT in the temperature range from 4 K to 425 K is shown in Fig 9.18.

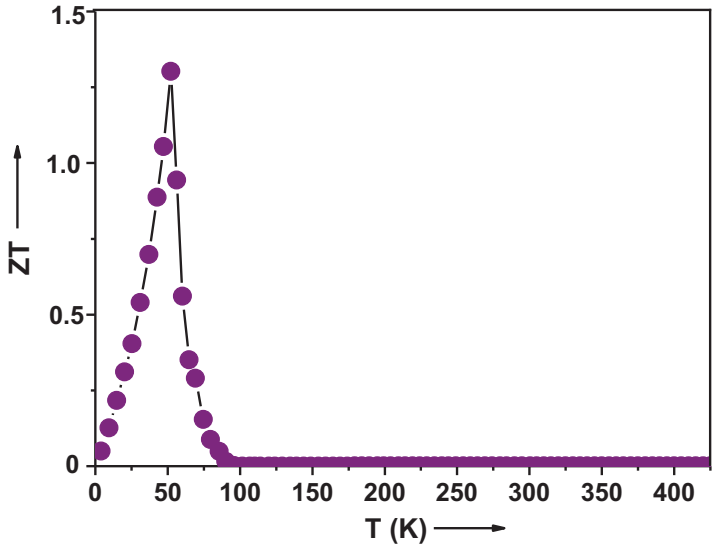

Fig 9.18 Variation of ZT with temperature of $Sn_2Sb_4Se_8$ thin film

The as-prepared $Sn_2Sb_4Se_8$ thin film exhibits a maximum ZT ≈ 1.3 at 52 K, which is comparable to recently developed efficient thermoelectric materials such as $Ge_{0.94}Bi_{0.06}Te$ [29], $Ce_{0.14}Co_4Sb_{12}$ skutterudites [30] and SiGe bulk alloy [31]. In general, materials with ZT ≥ 1 are recognized as efficient candidates for use in thermoelectric devices [22]. Hence, on further

optimization, the as-prepared $Sn_2Sb_4Se_8$ with ZT ≈ 1.3 at 52 K can be regarded as a novel promising material for cryogenic thermoelectric applications in the near future.

Evaluation of material parameters

The data from the analysis of Hall and thermoelectric power measurements have been combined to evaluate important material parameters such as Fermi energy (E_F), effective mass (m_p*), density of states (N_V), relaxation time (τ) and mean free path (l) using the equations described in section 5.3.5. The position of Fermi level is determined as ≈ 0.05 eV above the valence band. The values of N_V and m_p* are obtained as ≈ 1.3×10^{17} cm^{-3} and ≈ $0.03m_0$ respectively, where m_0 is the rest mass of electron. The density of states (N_V) is found to be greater than the charge carrier concentration (p), i.e, $N_V >>$ p, indicating the non degenerate semiconducting nature of the film [32]. The relaxation time (τ) and mean free path (l) of charge carriers in the film are evaluated as ≈ 5.7×10^{-16} s and ≈ 4 Å respectively.

9.4 Summary and Conclusions

Thin films of p-type $Sn_2Sb_4Se_8$ are successfully prepared under optimized deposition conditions by reactive evaporation. A comprehensive characterization of the structural, compositional, morphological, optical, electrical and thermoelectric power properties of the as-prepared $Sn_2Sb_4Se_8$ thin films is carried out for the first time with the goal of providing a platform to highlight the unique properties of this novel material. The films are photosensitive in nature and exhibit a direct allowed transition with an optical

band gap of 1.54 eV and high absorption coefficient ≈ 10^5 cm^{-1}, thereby indicating its possible use as an absorber layer material in thin film solar cells. The considerably high value of Seebeck coefficient ≈ 30174 μVK^{-1} and thermoelectric figure of merit ≈ 1.3 observed at 52 K can possibly open up novel opportunities for $Sn_2Sb_4Se_8$ in the field of cryogenic thermoelectrics. Thus, on further optimization, the $Sn_2Sb_4Se_8$ thin films prepared herein can be considered as a prospective material for photovoltaic and thermoelectric applications. Table 9.2 summarizes a few notable material parameters of the as-prepared $Sn_2Sb_4Se_8$ thin film.

Table 9.2 Material parameters of the as-prepared $Sn_2Sb_4Se_8$ thin film

Material Parameters	$Sn_2Sb_4Se_8$
Type of conductivity	p-type non degenerate
Optical band gap	1.54 eV
Photosensitivity	8.4
Charge carrier concentration at 300 K	$8.1x10^{16}$ cm^{-3}
Electrical conductivity at 300 K	0.43 Scm^{-1}
Effective mass at 300 K	$0.03m_0$
Mobility at 300 K	33.2 $cm^2V^{-1}s^{-1}$
Maximum Seebeck coefficient	30174 μVK^{-1} at 52 K
Maximum electrical conductivity	0.48 Scm^{-1} at 425 K
Maximum thermal conductivity	1.72 $Wm^{-1}K^{-1}$ at 425 K
Maximum power factor	$3.5x10^{-2}$ $Wm^{-1}K^{-2}$ at 52 K
Maximum figure of merit	1.3 at 52 K

References

[1] H. M. Pathan and C. D. Lokhande, Bulletin. Mater. Sci 27, 85 (2004).

[2] M. T. S. Nair, E. B. Salgado, A. R. Garcia, M. R. A. Silva, J. Campos and P. K. Nair, Elec. Chem. Soc. Trans 41, 177 (2011).

[3] L. D. Zhao, S. H. Lo, Y. Zhang, H. Sun, G. Tan, C. Uher, C. Wolverton, V. P. Dravid and M. G. Kanatzidis, Nature 508, 373 (2014).

[4] K. Y. Rajpure, C. D. Lokhande and C. H. Bhosale, Thin Solid Films 311, 114 (1997).

[5] U. Dhawan, A. K. Mukherjee, K. D. Kundra, M. Mondal and S. Z. Ali, Indian. J. Pure. Appl. Phys 20, 681 (1982).

[6] A. B. Adam, S. Sakrani and Y. Wahab, J. Mater. Sci. 40, 1571 (2005).

[7] S. B. Sakrani, S. A. Sakena and A. Jabar, Proc. Soc. Optics. Photonics 3175, 280 (1998).

[8] A. B. Adam, S. Sakrani and Y. Wahab, J. Mater. Sci. 41, 5797 (2006).

[9] P. Kumar, R. Thagaraj and T. S. Sathiaraj, Phys. Status Solidi A 206, 1465 (2009).

[10] H. A. Hasbi, S. Sakrani and N. A. Ahmad, Solid. State. Sci. Tecnol. 13, 46 (2005).

[11] D. V. Harea, M. A. Iovu, O. Iaseniuc, E. P. Colomeico, A. Meshalkin and M.S. Iovu, J. Optoelectronics. Adv. Mater. 11, 2039 (2009).

[12] K. G. Gunther, The use of thin films in physical investigations, ed. by J. C. Anderson (Academic, London, 1966), pp. 213-232.

[13] B. D. Cullity, Elements of X-ray diffraction, ed. by M. Cohen (Addison Wesley, Philippines, 1978), pp. 81-106.

[14] C. D. Wagner, Handbook of X-ray photoelectron spectroscopy: a reference book of standard data for use in X-ray photoelectron spectroscopy, ed. by G. E. Muilenberg (Perkin Elmer, USA, 1979), pp. 1-190.

[15] R. Swanepoel, J. Phys. E. Sci. Instrum 16, 1214 (1983).

[16] J. Tauc, Amorphous and liquid semiconductors (Plenum, New York, 1974), pp. 159-220.

[17] S. H. Wemple and M. DiDomenico, Phys. Rev. B 3, 1338 (1971).

[18] A. Larbi, H. Dahman and M. Kanzari, Vacuum 110, 34 (2014).

[19] P. Sharma and S. C. Katyal, J. Phys. D. Appl. Phys 40, 2115 (2007).

[20] K. R. Murali and P. Thirumoorthy, Elec. Chem. Soc. Trans 28, 67 (2010).

[21] E. S. M. Farag and M.M. Sallam, Egypt. J. Solids 30, 1 (2007).

[22] T. M. Tritt and M. A. Subramanian, Mater. Res. Soc. Bulletin 31, 188 (2006).

[23] C. Herring, Phys. Rev 96, 1163 (1954).

[24] M. Yasukawa, K. Ikeuchi, T. Kono, H. Yanagi and H. Hosono, J. Jpn. Soc. Powder. Metallurgy 54, 639 (2007).

[25] L.M. Goncalves, C. Couto, P. Alpuim, A. G. Rolo, F. Volklein and J. H. Correia, Thin Solid Films 518, 2816 (2010).

[26] T. Ueda, C. Okamura, Y. Noda and K. Hasezaki, Mater. Trans 74, 110 (2010).

[27] S. H. Wei, H. Chen, Z. Wang, Y. Chu, L. Zhu, X. Y. Jian and H. J. Yu, Mater. Sci. Forum 610-613, 394 (2009).

[28] M. Fardy, A. I. Hochbaum, J. Goldberger, M. M. Zhang and P. Yang, Adv. Mater 19, 3047 (2007).

[29] S. Perumal, S. Roychowdhury and K. Biswas, Inorg. Chem. Front 3, 125 (2016).

[30] Y. Tang, R. Hanus, S. W. Chen and G. J. Snyder, Nature Commun 6, 7584 (2015).

[31] X. W. Wang, H. Lee, Y. C. Lan, G. H. Zhu, G. Joshi, D. Z. Wang, J. Yang, A. J. Muto, M. Y. Tang, J. Klatsky, S. Song, M. S. Dresselhaus, G. Chen and Z. F. Ren, Appl. Phys. Lett 93, 1931211 (2008).

[32] R. T. Shuey, Semiconducting ore minerals (Elsevier, USA, 1975), pp. 41-77.

Chapter 10

Summary and Scope for Future Studies

10.1 Summary

The research on photovoltaic and thermoelectric materials has achieved remarkable progress over the past few years. Among the various materials investigated, compound semiconductors based on oxides, sulphides, selenides and tellurides have demonstrated promising photovoltaic and thermoelectric performances and they are one among the critical materials for today's leading photovoltaic and thermoelectric technologies. However, the development of cadmium free materials for thin film solar cells that can offer reasonably high photovoltaic efficiency and the development of toxic lead and scarce tellurium free materials for thermoelectric power generation and refrigeration that can offer reasonably high thermoelectric efficiency is an ongoing and challenging area of research.

In the present thesis, preparation, optimization of deposition conditions and characterization of certain degenerate and non degenerate p-type semiconducting compound selenide thin films that exhibit promising properties for photovoltaic and thermoelectric applications are discussed. The study highlights the possibility of investigating further into the optoelectronic and thermoelectric properties of these compounds in view of their applications in solar cells and thermoelectric devices. The major findings and conclusions are presented in this chapter with the scope for future studies.

Thin films of Cu_7Se_4, InSe, SnSe, $CuInSe_2$, $InSbSe_3$, $Sn_2Sb_4Se_8$ are successfully prepared under optimized deposition conditions using reactive evaporation - a well established technique used to deposit crystalline thin films with high reproducibility. The as-prepared thin films are characterized for their structural, compositional, morphological, optical, electrical and thermoelectric properties. Thin films of Cu_7Se_4 is found to be a degenerate p-type semiconductor with promising properties for use in solar control coatings, microwave shielding coatings, radiation filters and high temperature thermoelectric devices. The non degenerate p-type semiconducting thin films of InSe, SnSe, $CuInSe_2$ exhibits optoelectronic properties suitable for photovoltaic applications and a reasonably good thermoelectric figure of merit suitable for low temperature thermoelectric applications, thereby proving their potential in photovoltaic and thermoelectric technologies, on further optimization. The as-prepared non degenerate p-type semiconducting thin films of $InSbSe_3$ and $Sn_2Sb_4Se_8$ are found to be prospective materials for photovoltaic and cryogenic thermoelectric applications with excellent optoelectronic and thermoelectric properties which are not so far been reported

in literature to date, to the best of our knowledge, and hence demand further research to make them competitive with the other state-of-the-art photovoltaic and thermoelectric materials.

10.2 Scope for future studies

The present work suggests the possibility of fabricating a heterojunction solar cell by developing a pn junction between the as-prepared p-type counterparts and an n-type wide band gap material with suitable lattice matching. The p-type $CuInSe_2$ can also be prepared as n-type which suggests the possibility of fabricating a $CuInSe_2$ based homojunction solar cell. The thermoelectric figure of merit of the as-prepared thin films can be enhanced on further optimization of power factor through nanostructuring and electronic band engineering. The $InSbSe_3$ and $Sn_2Sb_4Se_8$ demonstrate promising photovoltaic and thermoelectric properties. But most of their properties remain unexplored due to the scarcity of sufficient literature. A systematic investigation of these compounds can open up new advances in photovoltaic and thermoelectric research. The preparation of the aforesaid binary and ternary compounds recommends the possibility for innovative research on the preparation of novel quaternary compounds with optimum optoelectronic and thermoelectric properties that can be suitably selected for fabricating thin film solar cells and thermoelectric modules. A well focussed investigation in this direction also seems to yield promising results.

Today, lot of research are being directed towards thermophotovoltaics – a new area of research which focuses on the generation of power from the heat generated in a photovoltaic cell by combining the principles of photovoltaic

and thermoelectric technologies. It is well known that solar cells can convert only a small portion of solar energy into electric power and the remaining solar radiation produces heat energy which heat up the rear side of the solar cell and thereby reducing the open circuit voltage, conversion efficiency and lifetime of the solar cell. A thermophotovoltaic module as shown in Fig 10.1 consists of a photovoltaic cell, thermoelectric module and a thermal heating system [1].

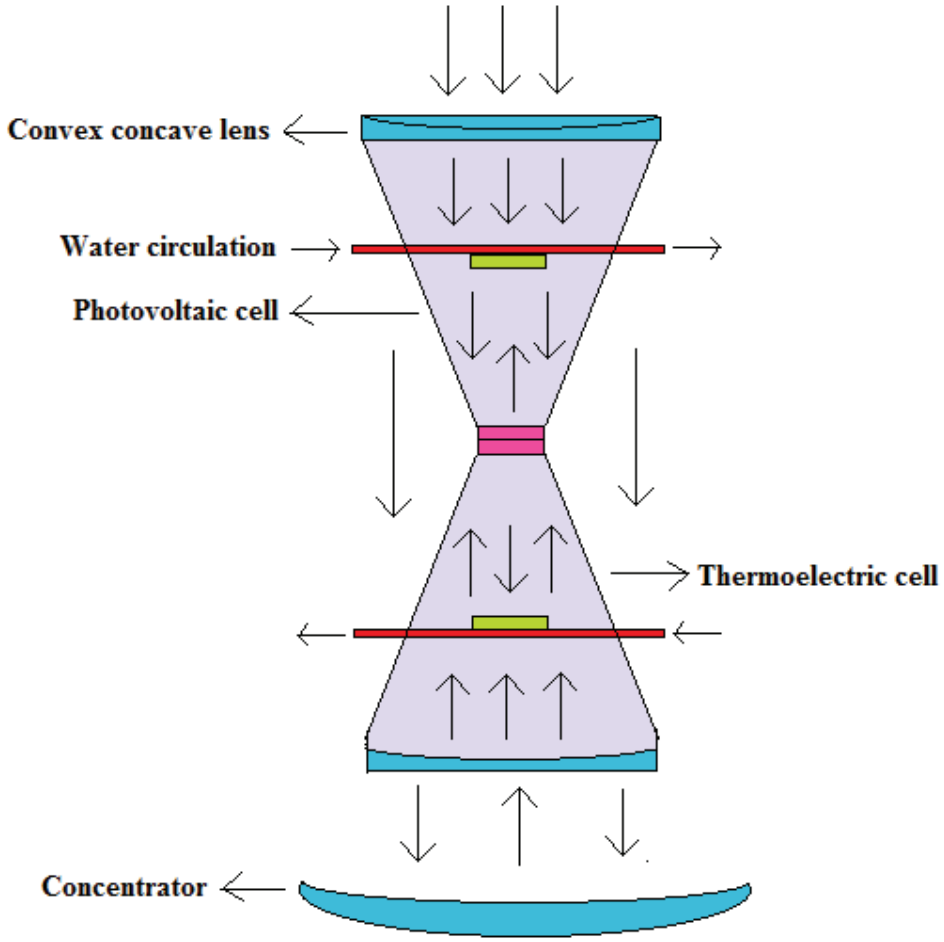

Fig 10.1 Thermophotovoltaic module

The convex concave lens concentrates and also split the incident solar radiation. The solar radiation which splits falls on the copper pipes carrying water. Since the housing is made up of glass, the incident radiation gets reflected back to the photovoltaic cell which is kept at the edge of the glass housing. It absorbs high wavelength energies while the less wavelength energies are reflected to the thermoelectric cell which is kept contradictory to the photovoltaic cell and at the rear of the copper pipes. These two arrangements carry heat from the photovoltaic cell and convert them into electricity. The water in the copper pipes gets heated to produce steam that can be used to run the turbine. The concentrator collects the radiations and concentrates at a mid point.

The as-prepared thin films can be used in thermophotovoltaic modules either as a material for photovoltaic cell or thermoelectric cell, thereby proving their potential for future energy scenarios.

References

[1] P. Arunkumar, K. Arunprakash, P. Rajarajan, G. Balaji and V.A. Saravanan, International proceedings of chemical, biological and environmental engineering 6, V21 (2011).